NTNU – Trondheim
Norwegian University of
Science and Technology

Porous Silicon as Anode Material for Li-ion Batteries

Structure and Performance

Asbjørn Ulvestad

Materials Science and Engineering
Submission date: June 2013
Supervisor: Volodymyr Yartys, IMTE
Co-supervisor: Jan Ketil Solberg, IMT
Martin Kirkengen, Institutt for Energiteknikk

Norwegian University of Science and Technology
Department of Materials Science and Engineering

Abstract

Silicon has proven to have a great potential as anode material in lithium-ion batteries due to its high theoretical electrochemical capacity. However, silicon anodes deteriorate quickly during cyclic charging and discharging, rendering them useless in only a few cycles. This has been attributed to the stresses induced by the large volume change of the material during cycling. By using finely structured silicon, these stresses can be effectively reduced, in what is aptly called dimensional stabilization. Numerous attempts have been made to exploit this effect, e.g. by using nanoparticles, nanorods and nanowires, with a varying degree of success. This study is an investigation into the use of porous silicon for anodes with reduced level of stress. The work consists of two main phases; the formation and characterization of porous silicon, and the testing of the resulting porous structures in electrochemical cells. In addition, an investigation into the use of prelithiated silicon as base material for composite electrodes has been conducted.

Porous silicon was obtained by electrochemical etching of n- and p-type silicon wafers in hydrofluoric acid (HF) at different current densities and for different durations. The resulting material was analyzed by SEM to characterize its morphology and pore size. One n-type and one p-type structure were selected for electrochemical testing, involving cyclic charge and discharge in half cells with lithium metal as a counter electrode. The chosen samples were tested both as-etched and with a carbon coating made by a pyrolization procedure with polyacrylonitrile (PAN) as precursor. In a different part of the work, composite electrodes were made from an alloy consisting of the intermetallic phase Li_7Si_3, carbon black and PAN. These were tested using the same conditions as the porous electrodes.

From the SEM analysis, it was determined that porous silicon structures were indeed formed on the wafer surfaces. The p-type wafers are believed to form structures with pores <10 nm. These were too small to be observed in SEM, but other collected data indicate that they do exist. The n-type wafers formed a double-layer structure, which was not expected for the parameters used. The bottom layer was found to be highly porous and consisting of vertically aligned, branched pores, several tens of nanometer wide. The top layer consisted of a framework of random pores less than 10 nm in diameter.

The electrochemical testing of the wafer-based electrodes showed that within 8 cycles they reached a capacity close to 3000 mAh/g which remains unchanged on further cycling. The performance is in some part attributed to the solid silicon in the bulk wafers. The porous electrodes exhibited a rather low Coulombic efficiency for the initial cycles, particularly the first, and generally lower efficiency than the non-porous reference. Carbon coating primarily enhanced the Coulombic efficiency of the electrodes, having most pronounced effect on the large surfaced p-type electrode. The n-type structure is believed to have been destroyed in the coating process due to the fragility of the highly porous lower layer.

The electrochemical testing of the prelithiated composite electrodes revealed that reversible capacity was very limited. It was concluded that this was due to contamination of the base material, Li_7Si_3, during its handling after synthesis, despite the extensive preventive measures that were taken. It is thus concluded that extreme care must thus be taken when characterizing the electrochemical capacity of such materials due to their high chemical reactivity.

Sammendrag

Silisium har vist seg å ha et enormt potensiale som anodemateriale i litium-ion batterier, først og fremst på grunn av sin høye teoretiske elektrokjemiske kapasitet. Imidlertid forsvinner denne egenskapen raskt ved syklisk opp- og utladning etter bare noen få sykluser. Dette skyldes spenninger forårsaket den store volumendringen materialet gjennomgår i løpet av denne syklingen. Ved å bruke finstrukturerte materialer kan disse spenningene effektiv reduseres, i det som er treffende kalt dimensjoneringsstabilisering. Det er blitt gjort mange forsøk på å utnytte dette, for eksempel ved bruk an nanopartikler, -staver og -tråder, med varierende suksess. Denne oppgaven er en studie i bruken av porøs silisium til dette formålet. Arbeidet består i hovedsak at to deler; produksjon og karakterisering av porøs silisium, og testing av disse porøse strukturene som elektroder i elektrokjemiske celler. I tillegg er det gjort en studie på effekten av å bruke prelitiert silisium i form av legeringer som basematerial i kompositt-elektroder.

Porøs silisium ble laget ved elektrokjemisk etsning av n- og p-type silisium-wafere i flussyre (HF) ved forskjellige strømtettheter og etsetider. Det produserte materialet ble så analysert i SEM for å karakterisere morfologien og størrelsen til porene. Én n og én p-type struktur ble valgt ut til testing ved syklisk opp- og utladning i halvceller med litium-metall som mot-elektrode. De valgte prøvene ble testet i sin naturlige etsede form og med karbon-belegg, lagt på ved hjelp av en pyroliseringsprosess med polyakrylonitril (PAN) som startmateriale. I testingen av prelitierte elektroder ble kompositt-elektroder laget av en legering bestående av den intermetalliske fasen Li_7Si_3, carbon black og PAN. Disse elektrodene ble testet under samme forutsetninger som de porøse elektrodene.

Fra SEM-analysen ble det bestemt at porøs silisium hadde blitt laget. Strukturene laget av p-type materiale er antatt å bestå av porer mindre enn 10 nm. Disse var for små til å se i SEM-instrumentet som ble brukt, men andre resultater indikerer at de eksisterer. Av n-type-materialet ble det laget tolags-strukturer, noe som ikke var forventet for etseparameterne som ble brukt. Det ble observert at det nederste laget hadde veldig høy porøsitet og bestod hovedsakelig av vertikale forgrenede porer med diameter på flere titalls nanometer. Det øverste laget bestod hovedsakelig av tilfeldig orienterte porer med diameter mindre enn 10 nm.

Den elektrokjemiske testingen av de wafer-baserte elektrodene viste at de stabiliserte seg i nærheten av 3000 mAh/g innen de første 8 syklusene og holdt seg der gjennom syklingen. Den gode ytelsen er til dels tilskrevet det store depotet av silisium i den underliggende waferen. De porøse elektrodene hadde lavere Coulombisk effektivitet enn en ikke-porøs referanseelektrode, hovedsakelig i de første syklene, men også til en mindre grad i resten av syklene. Karbonbelegg hadde først og fremst en forbedrende virkning på den Coulombiske effektiviteten, med størst effekt på p-type-elektroden, pga. den store overflaten. N-type-prøven er antatt at ble ødelagt under karbonbelegningen på grunn av det skjøre, høyporøse, nederste laget.

Den elektrokjemiske testingen av de prelitierte kompositteelektrodene viste at disse bare så vidt fungerte. Det er konkludert med at det aktive basematerialet, Li_7Si_3, ble ødelagt under produksjonen av elektroden, på tross av de omfattende tiltakene som ble gjennomført for å unngå det. Det er dermed vist at ekstreme hensyn må tas for å karakterisere slike materialer på grunn av deres høye kjemiske reaktivitet.

Acknowledgements

First and foremost I would like to express my gratitude to my head supervisor Professor Volodymyr Yartys, who have guided me through this work, providing me with valuable insight and encouragement during my time at IFE. I would also like to thank my co-supervisors Dr. Martin Kirkengen at IFE and Professor Jan Ketil Solberg at NTNU for advice and support along the way.

I am very grateful to Sean Erik Foss, head of the solar energy department at IFE, for facilitating my use of his departments laboratories, as well as the numerous people from whom I acquired help with the various tasks performed there; Ørnulf Nordseth and Junjie Zhu for providing me with silicon wafers of different types; Josefine Selj for sharing her expertise in porous silicon formation; Bent Thomassen for help with handling and use of chemicals in relation to the HF etch bath; and Chang Chuan You and Rune Søndenå for introducing me to the laser cutter and four point probe, respectively.

Collaboration on the SEM characterization of the porous silicon samples with Dr. Fermin Cuecas, Dr. Michel Latroche and Dr. Stéphane Bastide at Institut de Chimie et des Materiaux Paris Est, CNRS, Thiais (France) is greatly appreciated.

In the battery-lab at IFE I have had the pleasure of working alongside, and having the invaluable assistance of, Dr. Jan Petter Mæhlen, Dr. Preben J. S. Vie and Dr. Roman V. Denys, without whom there would be little to show for of electrochemical testing data or lithium silicon alloys.

Finally, I would like to thank my family and friends for their encouragement and care. In particular I would like to mention Charlotte Lund, my significant other, for her unwavering support and company through late evenings spent working.

Abbreviations

AIT	Advanced Instrument Technology
AIST	National Institute of Advanced Industrial Science and Technology, Japan
AMMT	Advanced Micromachining Tools
BET	Brunauer–Emmett–Teller
CB	Carbon black
CMC	Carboxyl methyl cellulose
CNRS	National Center for Scientific Research, France
CNT	Carbon nanotube
CVD	Chemical vapor deposition
DEC	Diethylene carbonate
DEE	1,2-diethoxy ethane
DMC	Dimethyl carbonate
DME	1,2-dimethoxy ethane
DMF	Dimethylformamide
EC	Ethylene carbonate
EDS	Energy Dispersive Spectroscopy
EELS	Electron Energy Loss Spectroscopy
EMC	ethyl methyl carbonate
HF	Hydrofluoric Acid
ICMPE	East Paris Institute of Chemistry and Material Science
IFE	Institute for Energy Technology
IR	Internal resistance
IUPAC	International Union of Pure and Applied Chemistry
LiBOB	Lithium bis(oxalato)borate
LiFAP	Lithium tris(pentafluoroethyl)trifluorophosphate
MWCNT	Multi-walled carbon nanotube
NAA	Neutron Activation Analysis
NTNU	Norwegian University of Science and Technology
OVC	Open circuit voltage
PC	Propylene carbonate
PS	Porous silicon
SBR	Styrene-butadiene rubber
SEI	Solid Electrolyte Interface
SEM	Scanning Electron Microscopy
SHE	Standard Hydrogen Electrode
PAN	Polyacrylonitrile
PPAN	Pyrolyzed polyacrylonitrile
PVdF	Polyvinylidene fluoride
TEM	Transmission Electron Microscopy
VCR	Vacuum coupling radiation
XRD	X-ray Diffraction

Table of Contents

1 Introduction

1.1 Motivation

Modern society stands before a great challenge in meeting the increasing demand of large scale and high efficiency energy storage. In the mobility sector, the number of electric and hybrid-electric vehicles steadily increases as technology and infrastructure are improved. However, in making such vehicles energetically and economically competitive to traditional internal combustion vehicles, battery technology should be drastically improved (Gerssen-Gondelach and Faaij, 2012). In consumer electronics, increased computational power, screen size and battery life in laptop computers and other mobile devices place ever higher demands on capacity with strict limitations on weight (Whittingham, 2012). The increased environmental awareness of the last decades together with the returning distrust of the safety of nuclear energy after the Fukushima Daiichi disaster has led to an increased interest in renewable energy sources. Because of the notoriously variable and unpredictable power output associated with many of these sources, large scale grid storage will undoubtedly be needed in the near future (Ummels et al., 2008, Connolly et al., 2012)

For many of these applications, electrochemical batteries are the best option. Batteries are divided into two main categories; primary and secondary cells. Based on non-reversible reactions, primary batteries are made for single use and not rechargeable, e.g. alkaline batteries. Secondary cells, on the other hand, are based on electrically reversible reactions and the batteries can therefore be recharged by applying a reversed potential larger than that of the cell. Examples of secondary battery chemistries are the NiMH (nickel metal hydride), lead-acid and Li-ion (lithium-ion) batteries. This introduction is mainly concerned with the latter type of batteries and focuses specifically on the anode material for the Li-ion batteries.

Electrodes of carbonaceous materials are regarded as the standard anode for the lithium-ion battery. Usually made of graphite, these electrodes have a theoretical capacity of 372 mAh/g, low operating voltage and good cycle lifetime (Scrosati, 2000). Alternative anode materials include a variety of alloying metals, e.g. tin and silicon, the latter of which is the subject of this work. Silicon anodes have a theoretical capacity of over 4000 mAh/g (Ng et al., 2006), making them an attractive alternative. Why, then, is silicon not the standard anode material for Li-ion batteries? While silicon anodes start out with a high capacity, close to the theoretical limit, it quickly drops during cycling. After only a few cycles the electrode capacity falls below that of a corresponding graphite electrode and after a few more the electrode stop working altogether.

At the time of writing it is widely agreed that the performance drop is due to the large volume expansion and contraction that the electrode experiences during lithiation and delithiation. Silicon, being a brittle material, cannot withstand the resulting stresses and cracks, causing material to fall away from the rest of the electrode. In addition and of the same reason, the interface between the electrode and its connector plate can be compromised, causing entire sections of the electrode to loosen. Even though the material is contained inside the battery, both of these effects cause parts of the electrode to loose electrical contact with the rest of the electrode. When loosing electrical contact, the energy stored in these fragments no longer can be harvested, rendering them dead weight and thereby decreasing the specific capacity of the

electrode. Even if electrical contact is sustained, the increased surface area created by cracks presents additional problems which will be discussed in detail later.

Several solutions to these issues have been proposed and tested, some more successfully than others. The most common approach has been to minimize the stresses caused by the volume change by altering the morphology of the silicon. Pure silicon anodes made from nanotubes and thin-films of nanometer thickness have shown good initial capacity and degrade more slowly than their bulk-silicon counterparts, but still too rapidly to be commercially viable. Another approach is to incorporate silicon particles into a matrix, forming a composite electrode. The matrix serves to both increase the conductivity of the electrode and to accommodate the volume expansion of the silicon particles without losing mechanical integrity. While having a lower initial capacity due to the lower silicon content, these electrodes tend to show reasonably good capacity retention for some cycles before a sudden capacity fade occurs. The number of cycles before this fade occurs depends on the preparation of the electrode; the initial size and morphology of the silicon, what kind of matrix and binder were used, and if any surface treatment of the particles was performed. (Kasavajjula et al., 2007)

A large number of different particle morphologies and sizes have been tested, including spherical particles, rods and wires (Etacheri et al., 2011a). Table 1 shows an overview of some of the silicon anode designs and their reported performance in terms of specific capacity and cycle stability. Recently, there have been reports of porous silicon of different varieties being used for this purpose. This research, having shown exceptional results (Ge et al., 2012, Thakur et al., 2012a, Thakur et al., 2012b, Thakur et al., 2012c, Zhao et al., 2012, Ge et al., 2013), constitutes the motivation for this study.

Table 1: A list of silicon anode designs and their reported performance

Design	Reported performance
Nanowires (Chan et al., 2008)	3,500 mAh/g for 20 cycles
Carbon-silicon core-shell nanowires (Cui et al., 2009)	2,000 mAh/g for 30 cycles
Particles+Carbon nanotubes (Zhang et al., 2006b)	584 mAh/g for 20 cycles
Thin films (Maranchi et al., 2003)	3500 mAh/g for 30 cycles
50 nm thin films (Takamura et al., 2004)	2000mAh/g for 3000 cycles
Crystalline-amorphous core-shell nanowires (Cui et al., 2008)	1000 mAh/g for 100 cycles
Gold coated porous silicon films (Thakur et al., 2012a)	3000 mAh/g for 50 cycles
Hierarchical micro/nano porous particles (Zhao et al., 2012)	1500 mAh/g for 50 cycles
Porous silicon particulates (Thakur et al., 2012c)	3000 mAh/g for 600+ cycles
Porous silicon nanowires (Ge et al., 2012)	2000 mAh/g for 250 cycles
Porous silicon nanoparticles (Ge et al., 2013)	1400 mAh/g for 200 cycles

1.2 Thesis Outline

This study consists of two main parts; porous silicon formation by anodic etching and electrochemical testing of the formed structures. During a project work performed by the author in collaboration with IFE during the fall of 2012, lithium-silicon alloys were made and characterized for the purpose of determining the effects of using prelithiated silicon in composite electrodes. However, due to difficulties handling and characterizing lithium compounds, insufficient time was left to run the electrochemical testing before the end of the project. An effort has therefore been made to incorporate those tests in the current work.

Porous silicon was formed using anodic etching in hydrofluoric acid (HF) at a range of etching times and current densities. The formed structures were characterized using scanning electron microscopy (SEM) to determine their morphology and pore sizes. These results were used to determine which samples were most suitable for electrochemical testing. The selected samples were cut into pieces of suitable electrode size, and two pieces from each sample were tested as electrodes, one as-etched and one coated by pyrolyzed polyacrylonitrile (PPAN). Composite electrodes were prepared using the lithium-silicon alloys as active material, carbon black as conductive matrix and polyacrylonitrile as binder. The electrodes were tested under conditions designed to evaluate different aspects of their performance.

In order to provide the reader with the necessary knowledge base to utilize the content of this thesis, a review of current status of the R&D will be given first. Due to the broad spectrum of the main topics, this review is rather extensive, and contains three main parts; the lithium-ion battery in general, the silicon anode, and fundamentals of porous silicon. This is followed by an account of the state of the art, the art in this case being the use of porous silicon as anode material.

The experimental section gives an account of the experiments performed during the course of this work. It includes a detailed description of the fabrication and characterization of the porous silicon and lithium-silicon alloys, the production of both porous silicon and prelithiated composite electrodes, the electrochemical testing performed and the post-cycling characterization. After this section, the most relevant results are presented, including but not limited to SEM studies of the porous structures and data from the electrochemical testing. These results are then discussed in relation to the previously presented theory, and possible weaknesses of the experimental procedure are evaluated, before conclusions are drawn.

2 Theory

2.1 The Li-ion Battery

As one of the most effective and energy dense secondary battery chemistries, the Li-ion battery has become an important part of energy storage technology, being used in various applications and scales, from cell phones and laptop computers to power tools and electric vehicles. Emerging from research based on the lithium metal primary battery, the current Li-ion battery was proposed in a patent filed in May 1985 by Akira Yoshino and a working prototype was assembled the following year (Yoshino, 2012). A comparison of the specific power and energy of different battery technologies can be seen in Figure 1, showing the very good performance of two of the most common lithium-ion technologies. The difference between these lies in the use of different cathode materials, a topic that will be described in detail later.

This section will provide an introduction to the field of lithium-ion batteries, beginning with a brief explanation of the working principle of the lithium-ion battery. An overview of important characteristics of batteries will then be given, explaining and defining some expressions that are used later in the thesis. An important aspect of the lithium-ion battery, especially with regard to anode materials; the solid electrolyte interface or SEI, will then be explained. In addition, while the research performed in this study mainly concerns the silicon anode, a review of materials used for other components and purposes in lithium-ion battery is also deemed prudent due to the high degree of interaction between the different parts of the system.

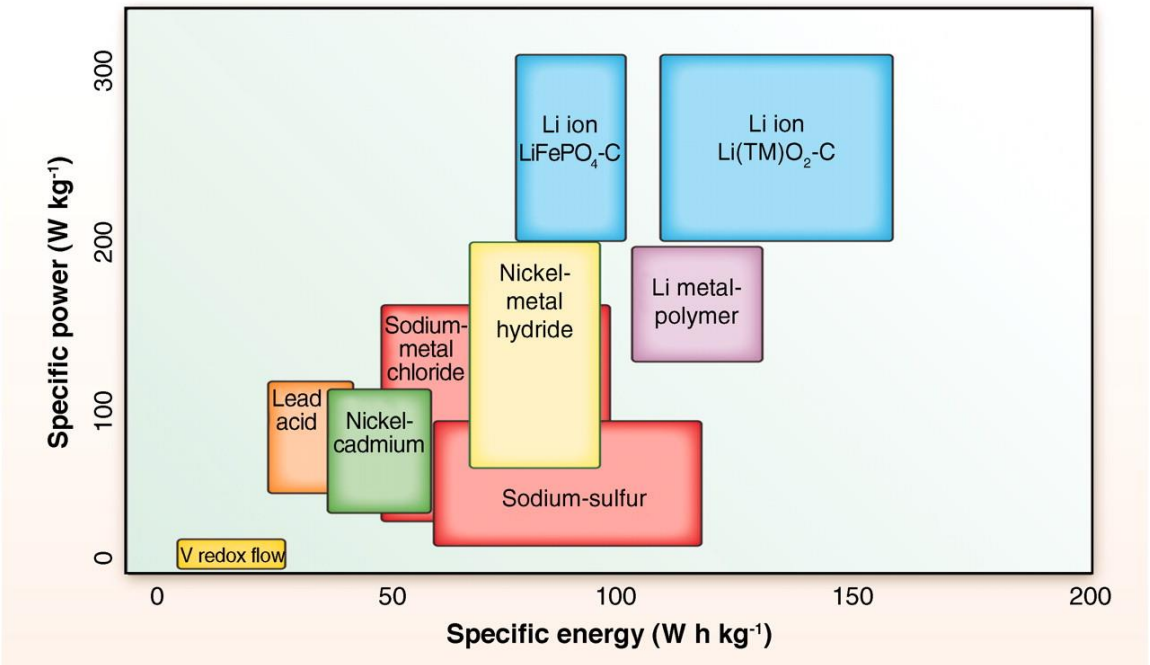

Figure 1: A comparison of the specific power and energy capacity of different battery technologies, showing the superior performance of different lithium-ion technologies (Dunn et al., 2011).

2.1.1 Working Principle

The structure of the lithium-ion battery does not differ notably from other secondary battery systems, and is, in its simplest form, an electrochemical cell as any other; two electrodes immersed in an ionically conducting electrolyte and electronically connected through an external circuit. During discharge, the battery converts chemical energy to electrical energy through a redox reaction. The reduction and oxidation reactions happen on different electrodes, and as these are separated by a non-electronically conducting electrolyte, the electrons are forced through the external circuit, where a load can be applied. During charging, electrical energy is converted into chemical energy by driving this redox reaction in the opposite direction. The cathode and anode are by definition the electrodes where the reduction and oxidation reactions happen, respectively, and which electrode is which therefore changes depending on whether the battery is charged or discharged. In battery science the convention is to designate the electrodes by their function during discharge. (Haas and Cairns, 1999)

In addition to the many similarities between the lithium-ion battery and other battery chemistries, there are some important differences, the most obvious being the use of lithium ions. Lithium is one of the most reductive elements, the Li/Li^+ couple having a reduction potential of -3.04 volts vs. the SHE (Bard et al., 1985). In combination with a low atomic weight of only 6.94 u (Wieser, 2006), this makes lithium metal ideal for energy storage, yielding both a high number of electrons per mass and high energy per electron. Ideally, to obtain the highest possible capacity, the anode should be pure lithium, as is the case for the lithium metal primary battery. However, several problems were quickly discovered when attempting to charge a lithium metal battery. In addition to the inherent risk stemming from the high chemical reactivity of metallic lithium, one also encountered issues with lithium being deposited on the anode in the form of sharp dendrites able to pierce the separator and cause a short circuit. While severely reducing the reliability of the batteries, these problems also present a risk for thermal runaway reactions, and in cases where lithium is involved these can be most violent and pose a serious safety hazard (Yoshino, 2012).

This was the motivation behind the research that led to the Li-ion battery, which solves these problems by using so called intercalation electrodes as both anode and cathode, meaning that lithium ions can be reversibly inserted and extracted from the electrodes, rather than deposited on their surfaces. A potential-difference between the electrodes causes lithium ions to spontaneously move from the anode to the cathode through the

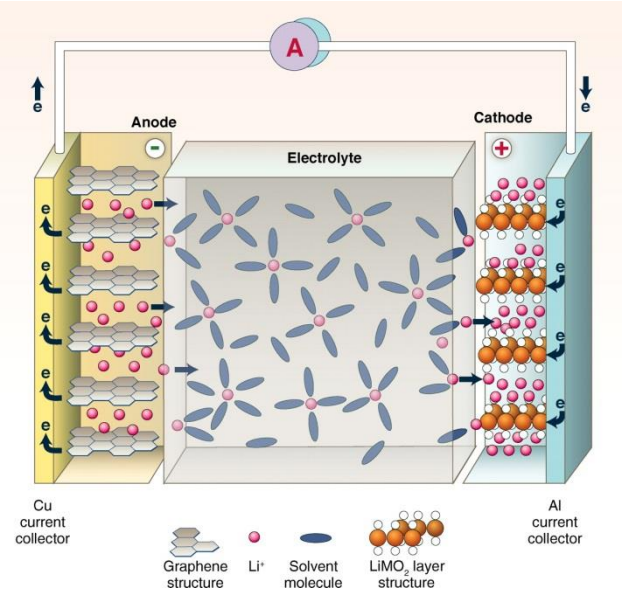

Figure 2: Schematic of a lithium-ion battery. In this case, graphitic carbon is used as an anode and a relevant transition metal oxide as cathode. On charging, Li ions are removed or deintercalated from the layered oxide compound and intercalated into the graphite layers. The process is reversed on discharge. (Dunn et al., 2011)

electrolyte. As the electrolyte is electronically isolating, the electrons are left to travel through the external cycle, where their energy can be harvested. During charging, an applied voltage forces the electrons and lithium ions to move in the opposite direction. Figure 2 shows a schematic representation of a lithium-ion battery using a common combination of intercalation electrodes; a graphite anode and a layered transition metal oxide cathode. The half-cell reactions and full cell reaction for this example can be seen in Figure 3, along with the schematic structures for the charged and discharged anode and cathode. The factor x in these reactions vary depending on which transition metal oxide is used, but is usually between 0.5 and 1. At open circuit conditions the electrons are hindered from moving, hence the transport of ions will establish an electric field nullifying the potential difference between the electrodes and halting the reaction. As soon as the external circuit is closed, however, the reaction is free to continue and energy can be released.

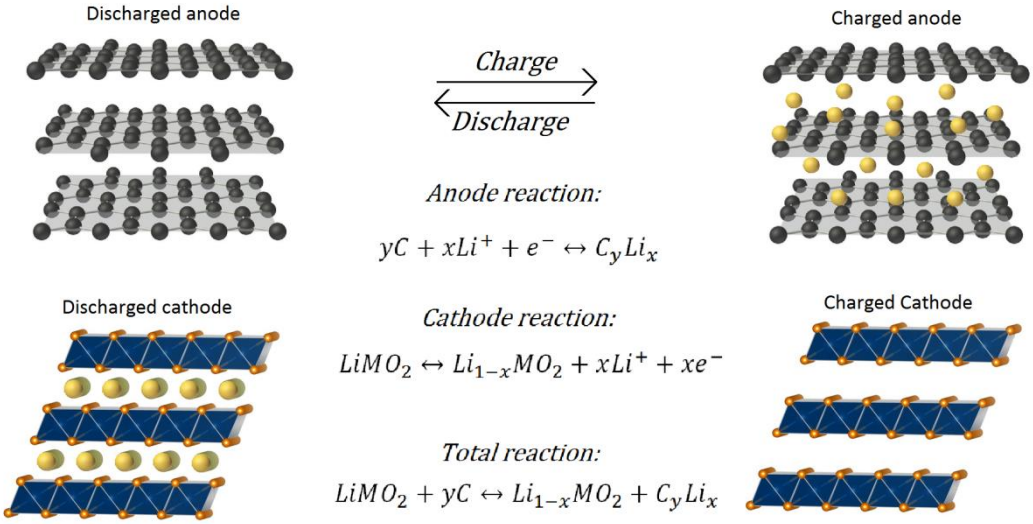

Figure 3: Schematic presentation of the charged and discharged structure of a graphite anode and a layered oxide cathode, in addition to the half-cell reactions and full cell reaction.

2.1.2 Important Characteristics

- Specific capacity is one of the most common ways to express cell or electrode capacity and is given in mAh/g. The relationship between the capacity of the entire cell and the capacities of its components is commonly expressed as

$$C_{Cell} = \frac{1}{1/C_A + 1/C_C + 1/Q_M} \qquad \text{Equation 1}$$

  Where C_A is the anode capacity, C_C is the cathode capacity and $1/Q_M$ is the capacity specific mass of the remaining cell components; electrolyte, casing etc.
- Charge density is another expression of capacity, but relative to volume rather than weight, and is usually given in mAh/cm^3.
- Cycle stability is a measure of how well the battery copes with being charged and discharged. There is no convention for how to express the cycle stability for a battery,

but it is commonly given as the number of cycles before the capacity falls below the designated capacity of the battery or electrode, or a certain percentage of its initial capacity.

- C-rate is a normalized charge/discharge rate that depends on the electrode or battery capacity. It is defined as the rate at which the entire capacity of the electrode is charged or discharged in one hour. Charge/discharge rate during cycling is usually given as a fraction or multiple of the C-rate. E.g. for a 2 gram electrode with specific capacity of 1000mAh/g the C-rate is 2000mA, and if cycled at for instance C/4 the current is set to 500mA.
- Coulombic efficiency is defined as the ratio between the amount of charge that can be extracted from the battery and the amount of charge that was put in during charging, typically given in percent.
- Charge and discharge can be used by different conventions. The traditional definition amongst electrochemists is that discharge means the loss of positive charge by combination with an electron. It is also possible to define the filling of an electrode with ions as charging the electrode. As this means that the ions are combined with electrons, these conventions are inherently opposite. In battery science, the most common, which is known from daily life, is that a spontaneous reaction is denoted discharging, while a forced reaction is denoted charging. For an anode in a full cell, this means that lithium intercalation would be denoted charging. However, when coupled with lithium metal counter electrodes in half cells, anode materials will in fact act as cathode, hence lithiation would constitute discharging. To prevent ambiguity, in this work, lithiation of anode materials will always be denoted charging and delithiation discharging, regardless of its actual role in the cell.

2.1.3 SEI Formation

All compounds are stable in a certain range of redox potentials, below this range the compound is reduced and above it is oxidized. Intercalation of lithium into the anode of the Li-ion battery happens at a very low potential, e.g. for a standard graphite anode most of the intercalation happens <0.1 volt relative to the Li/Li^+ redox couple (Bruce et al., 2008), and decomposition of the electrolyte solution constituents is thus virtually inevitable and will happen to at least some degree. This problem is circumvented by using an electrolyte that together with the electrode material and lithium decomposes into stable solid compounds that form a coating around the electrode. The coating, commonly referred to as the solid electrolyte interphase (SEI), should ideally prevent further decomposition of solvent by forming an impermeable as well as electronically isolating layer, but still be ionically conducting to allow lithium ions to pass from the electrolyte to the electrode.

The formation of the SEI happens by a number of parallel and competing reactions, resulting in a layer of inhomogeneous composition and varying thickness, complicating the characterization and evaluation of the coating. A schematic representation of SEI formed on a graphite particle of a standard carbon anode can be seen in Figure 4. Needless to say, the composition and efficiency of the SEI is greatly influenced by the composition of the electrolyte, but the complexity of the formation makes it sensitive to external influence as well, e.g. varying

operating conditions in different laboratories. This has resulted in some controversy regarding the composition, distribution of constituents and the structure of the SEI, even for apparently similar cases. However, for carbon anodes, which are the most extensively researched, most groups agree that the SEI is composed of multiple layers; a layer consisting mostly of inorganic salt reduction products closest to the electrode followed by a layer of organic reaction products from the decomposition of the solvents (Verma et al., 2010).

While being essential for the successful operation of the Li-ion battery, the SEI also has some adverse effects on the battery performance. The most notable is the capacity loss caused by lithium being irreversibly bound in compounds during the formation of the interphase, observed as a reduced Coulombic efficiency for the first few charge/discharge cycles. The magnitude of this reduction is related to the thickness and composition of the SEI, which in turn can be manipulated by tuning the composition of the electrolyte (Etacheri et al., 2011a).

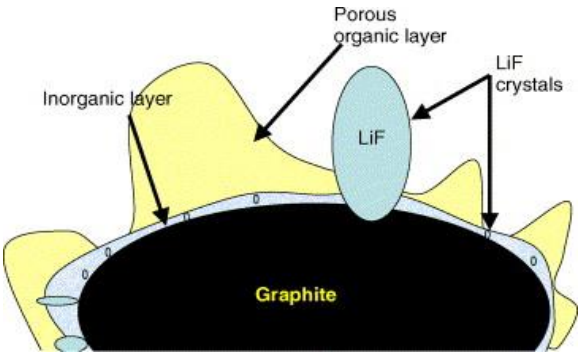

Figure 4: Schematic representation of SEI forming on the surface of graphite particles in an anode (Verma et al., 2010).

2.1.4 Components and Commonly Used Materials

2.1.4.1 Electrolyte solvents

The primary role of the electrolyte in any electrochemical cell is to conduct ions from one electrode to the other while being electronically insulating and thermodynamically stable. The last property can either be intrinsic for the electrolyte or a result of the decomposition products passivating the electrode surface by formation of a SEI. For lithium-ion batteries, the latter is usually the case, of reasons discussed in the previous section. The choice of a proper electrolyte therefore has a great impact on the cycle stability and Coulombic efficiency of the battery.

A vast number of different electrolytes have been designed for use in the lithium-ion battery, most of which fit into one of three main groups; ionic liquids, polymer electrolytes and liquid electrolytes. Only the latter is used in the experiments for this work, but a short introduction to the other classes seems prudent. Ionic liquids are based on salts that are in their molten state at ambient temperature, in which lithium salts can be dissolved. These salts have a broad stability window and very low volatility, making them non-flammable. However, research in this area has in the past largely been based on $AlCl_3$, whose extremely corrosive nature has resulted in a very limited use. In later years, however, a renewed interest has been sparked by the discovery of new low melting temperature salts, mainly based on the quaternary ammonium cation (Lewandowski and Świderska-Mocek, 2009).

Of the polymer electrolytes, gel polymers are by far the most common. Gel polymers possess both the physical properties of a solid and the diffusive properties of a liquid. These properties

are a result of the electrolyte consisting of a polymer host material imbued with an organic solvent, into which a lithium salt is dissolved (Manuel Stephan, 2006). While generally regarded as having a smaller charge capacity than conventional Li-ion batteries, lithium polymer batteries are cheaper and simpler in construction, more rugged and resistant to short circuiting. In addition, the absence of a free liquid removes the need for a metal housing and increases flexibility when it comes to battery shape and packaging (van Schalkwijk and Scrosati, 2002).

Liquid electrolytes are made by dissolution of a lithium salt (e.g. $LiPF_6$) in a nonaqueous solvent. Different groups of solvents are outlined by van Schalkwijk and Scrosati (2002) and include ethers, esters, alkyl carbonates and inorganic solvents. The most commonly used are propylene carbonate (PC), ethylene carbonate (EC), dimethyl carbonate (DMC), diethylene carbonate (DEC), 1,2-dimethoxy ethane (DME), ethyl methyl carbonate (EMC) and 1,2-diethoxy ethane (DEE) (van Schalkwijk and Scrosati, 2002). PC was used in early research, but was found to be incompatible with graphitic electrodes due to co-intercalation phenomena. This happens because the PC molecules fail to create a stable SEI and intercalate into the electrode, causing a continuous break down of the electrodes by exfoliation of graphite layers. EC, while having a very similar molecular structure to PC, does not cause these problems and has proven to be a more suitable solvent. A binary electrolyte of EC and one of the less viscous DEC, DMC and EMC is commonly found in commercial batteries (Etacheri et al., 2011b).

2.1.4.2 Solutes

When evaluating a lithium-salt's aptitude as electrolyte solute for lithium-ion batteries, there are two main requirements that must be satisfied; 1) as the primary purpose of the solute is to provide a sufficient concentration of lithium ions, the salt must have a high solubility in non-aqueous solvents and 2) the anion must be stable in relation to the other components of the battery, either by being inherently so or by passivation. Examples of salts that fulfill these requirements are $LiClO_4$, $LiAsF_6$, $LiPF_6$ and $LiSO_3CF_3$. In addition to these requirements, there are a number of other properties that should be taken into account, e.g. toxicity ($LiAsF_6$), fire or explosion hazard ($LiClO_4$), low conductivity ($LiSO_3CF_3$) and cost, which narrows down the number of practical candidates considerably (Aurbach et al., 2004). Indeed, the vast majority of lithium-ion batteries both in production and research use the same salt as primary solute, namely lithium hexafluorophosphate ($LiPF_6$). While this salt was proposed as early as in the patent for the first ever lithium-ion battery (Yoshino et al., 1987), it has yet to be superseded as the standard solute. This must not, however, be interpreted as it being a perfect solute, but rather as being a good compromise of properties. For applications where demands are more extreme, $LiPF_6$ can leave something to be desired. For instance, at high temperatures, the decomposition of $LiPF_6$ into LiF and PF_5 becomes a major problem, as PF_5 readily hydrolyses to form HF, which is devastating for the electrode performance (Aurbach et al., 2004). This has led to research into alternative solutes, like lithium tris(pentafluoroethyl)trifluorophosphate and lithium bis(oxalato)borate, commonly known as LiFAP (Gnanaraj et al., 2003) and LiBOB (Xu et al., 2002), respectively. These have shown great potential, but are not yet commercialized on a large scale.

2.1.4.3 Electrolyte additives

Many of the processes occurring in the lithium-ion battery can be influenced by introducing additives to the electrolyte. There are hundreds of publications and patents in this field; hence a thorough examination would be far too extensive for this thesis. However, an introduction is given based on the reviews by (Zhang, 2006) and (Verma et al., 2010), with the additives divided into a set of groups based on their intended function proposed by (Zhang, 2006) (where other sources than these two are used, they are referred);

1. SEI formation improver:
   As established earlier, the formation of the SEI happens through a series of competing reactions. Additives that catalyze or inhibit the more beneficial or unfavorable of these reactions, respectively, would be counted as SEI formation improvers, as would compounds that reduce to stable SEI constituents themselves. LiBOB would be an example of the latter.
2. Cathode protection agent:
   Water and acidic impurities in the electrolyte, mainly HF formed from the reaction between water and $LiPF_6$, effectively dissolve most cathode materials. This dissolution can be reduced by adding water and acid scavenging compounds to the electrolyte, an example of which is N,N-diethylamino trimethylsilane.
3. $LiPF_6$ salt stabilizer:
   The continuous decomposition of $LiPF_6$ into LiF and PF_5 is a recurring problem in lithium-ion batteries of several reasons, most of them stemming from the high reactivity of PF_5. As mentioned, hydrolysis of PF_5 leads to formation of HF, which is detrimental to electrode performance. In addition, reactions between PF_5 and a number of known SEI components produce LiF and CO_2, both of which are undesirable, CO_2 for increasing the internal pressure of the battery and LiF for decreasing the stability of the SEI. PF_5 also react readily with the organic solvents, causing deterioration of the electrolyte itself. Additives that inhibit the decomposition of the salt is thus advantageous, particularly at elevated temperatures, examples of which can be found in (Zhang, 2006).
4. Safety protection agents
   There are two main types of safety protecting agents in Li-ion batteries; the aptly named overcharge protectors and fire retardants. Overcharge protectors come in many forms and can be separated into redox shuttles and shutdown additives, the former being reversible, while the latter permanently shuts down the battery. The purpose of the redox shuttle is to provide a secondary discharge route that is activated over a certain potential, which should ideally lie just above the end-of-charge potential of the cell. At the given potential, the species is oxidized at the cathode before it diffuses to the anode where it is reduced, trapping the battery in an endless charging cycle at that potential. An example of such a redox shuttle is the I_2/I_3^- redox couple, which activates at about 3 volts. A shutdown additive relies on an entirely different mechanism which is based on high charging potentials causing a gas emitting polymerization of the additive. The increased pressure exerted by the gas triggers a so-called current interrupt device (often mechanical) while the polymer coats and isolates the electrode.

One of the factors limiting the use of lithium-ion batteries in vehicles is the fire hazard posed by the reactivity of lithium and flammability of the electrolyte solvents. While the former is reduced considerably by proper use of intercalation electrodes, the latter can be lowered by additives. These additives have different ways of working. Some form a charred layer during combustion, isolating the liquid and gas phases and thus reducing evaporation and limiting the flow of combustible material to the reaction. Others work by scavenging radicals in the gas phase, thereby terminating the combustion chain reaction. Most additives of this kind work by a combination of these processes, an example of a proven fire retarder being hexamethoxycyclotriphosphazene.

5. Lithium deposition improver

   A significant part of the irreversible capacity lost in cycling a lithium-ion battery is caused by lithium being plated on the anode during charging. The deposed lithium disturbs the formation of the SEI as this happens mostly during the late stages of charging. In addition to being inherently reactive, lithium metal also tends to deposit as high surface area structures, like dendrites or porous sponges, making it increasingly unstable. While the chemical reactivity of metallic lithium is difficult to change, there are additives that influence the structure that it forms during deposition. These are described in detail in (Zhang, 2006).

6. Ionic solvation improvers

   The solubility of lithium salts in the electrolyte is imperative for high ionic conductivity. Increased solubility can be achieved by additives that complex either of the salt ions, thereby shifting the equilibrium. Complexion of the lithium cat-ions has been found to be unfavorable, as it increases the bulkiness of the ion, leading to decreased ion mobility in the electrolyte and slower kinetics at the electrode-electrolyte interface. Hence, a number of compounds with an electron deficient boron or chlorine atom have been developed, e.g. tris(pentafluorophenyl)borane, to selectively coordinate the anions in the electrolyte, thereby increasing the solubility of many lithium salts, for instance the lithium halides.

7. Corrosion inhibitors

   Aluminum is frequently used in current collectors for lithium-ion batteries due to its electronic and mechanical properties. However, the corrosion resistance of aluminum is dependent on a passivating layer being formed on the metal surface. The stability of this layer has been found to vary greatly with the anion of the lithium salt dissolved in the electrolyte. Some salts, like those based on the bis(oxalato) borate-anion, form a very stable and dense passivating layer, even when used as an additive in relatively small quantities (<5 mol%).

8. Wetting agents and viscosity diluters

   In cases where the electrolyte is not able to wet the separator sufficiently, a wetting agent must be used to ensure the best possible conductivity through the electrolyte. This agent can be any of a long range of surfactants, both ionic and non-ionic, the only other requirement being that it has no ill effects on the performance of the cell. For low temperature applications, viscosity reducing additives may become necessary to ensure the mobility of the lithium ions is not reduced too severely, an example of which is P_2O_5 for $LiPF_6$- based electrolytes.

While the grouping might indicate that each additive has a specific function, it is important to note that that is not always the case. Some additives have several functions, e.g. the previously mentioned bis(oxalato)borate-anion, which works as both a SEI formation improver, cathode protector, overcharge protector and corrosion inhibitor. Care must therefore be taken to avoid unintended cumulative effects.

2.1.4.4 Cathodes

Numerous different cathodes for the lithium-ion battery have been researched through the years, a few examples of which are shown in Table 2. With only a few exceptions, these are made of compounds based on at least one of the transition metals. The main reason for this is that transition metals are stable at a several different oxidation states. When lithium ions are intercalated into the electrode, the transition metal atoms can accommodate the electrons arriving through the external circuit by being reduced to a lower oxidation state, thereby maintaining the charge neutrality of the compound (Fergus, 2010). While this applies for a large number of compounds, other essential criteria reduces the number of candidates markedly. The large changes in composition of the electrode during lithiation often lead to changes in the crystal structure of the material that may compromise the structural integrity of the electrode or otherwise have energetically unfavorable effects. Using a material that has a crystal structure that is stable over a wide range of compositions is therefore imperative. In addition to this, the lithium diffusivity, electronic conductivity, cost and environmental benignity of the material must be taken into account. Since the birth of the lithium-ion battery, three main groups of materials have been found to exhibit these properties.

2.1.4.4.1 Layered oxides

The first to be discovered were the layered chalcogenides, starting with the sulfides and selenides like $LiTiS_2$ and $LiVSe_2$, before moving on to the oxides, e.g. $LiCoO_2$ and $LiNiO_2$. These materials consist of an essentially close packed structure of anions, with the transition metal cations occupying the space between every other layer. The lithium can then be freely intercalated into the remaining unoccupied ones, resulting in the layered structure that gives this group its name. The structure itself is named α-$NaFeO_2$ and can be seen in Figure 5A (Whittingham, 2004). While introduced to the field of lithium-ion batteries already in 1980 (Mizushima et al., 1980), $LiCoO_2$ is still the most commonly used cathode material in current lithium-ion batteries. However, cobalt being relatively rare and thus expensive in comparison to other transition metals like iron and manganese, research in later years has been focused on development of alternative less expensive cathode materials. Inherent phase instability of the material at low lithium content that leads to severe degradation during overcharging has also prompted research into more stable alternatives (Fergus, 2010). Being far cheaper and having a higher energy density, $LiNiO_2$ is an interesting candidate, but it is also less stable and ordered than $LiCoO_2$, with nickel-ions occupying positions in the lithium plane and vice versa (Yamada et al., 2001, Rougier et al., 1996). This impedes the lithium movement in the lattice, and hence the performance of the electrode. More recent research has found that adding cobalt to $LiNiO_2$ increases the ordering, and that by using the quaternary compound $LiNi_{1-x}Co_xO_2$, the advantages of both can be utilized (Shi et al., 2009).

2.1.4.4.2 Spinels

The second group consists of materials having the spinel structure, which, in some ways, can be regarded as similar to those of the first group. However, rather than having the alternating layer structure that was described above, in the spinel structure both of the cation species are ordered throughout all of the atomic layers, as seen in Figure 5B. Due to this ordering, the spinel structure offers an interconnected matrix of interstitial positions that allows for the storage and diffusion of lithium ions, again while the transition metal atoms accommodate the electrons by changing oxidation state (Thackeray, 1997). One of the more common compounds of this group is $Li_xMn_2O_4$, which is stabile in its spinel structure to approximately $x < 1$ (Whittingham, 2004).

2.1.4.4.3 Olivines and tavorites

The last group, the olivine materials, emerged from an extensive research effort into making electrodes based on iron, being the most abundant transition metal by far. Compounds of similar composition to those proven successful for other transition metals, like $LiFeO_2$ or FeS_2, was proven to have a high lithium retention, and thus unsuitable for electrodes. It became apparent that a completely new material had to be developed, eventually resulting in $LiFePO_4$ (Whittingham, 2004). Its structure, seen in Figure 5C, consists of edge sharing octahedra of oxygen coordinated iron atoms forming layers which are bound together by tetrahedra of oxygen coordinated phosphorous atoms, between which lithium atoms can reside. Made only of materials of abundant availability and having capacities comparable to that of $LiCoO_2$, as well as very good cycle life, low toxicity and being environmental benignity, it has attracted great interest. Its defining limitation has been an extremely low electronic conductivity, for which making composites with carbon has been the most common solution (Gaberscek et al., 2007).

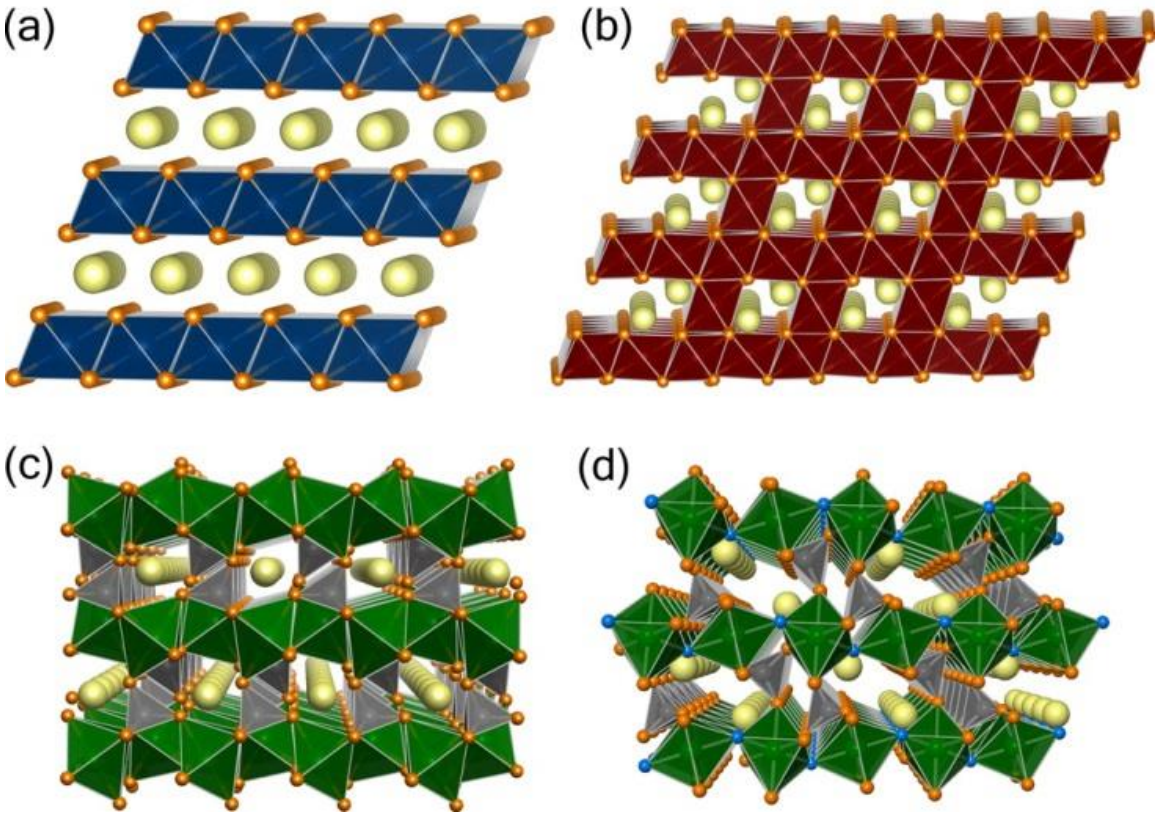

Figure 5: Illustration of the crystal structures of the best performing positive electrode materials: (a) $LiCoO_2$, (b) $LiMn_2O_4$, (c) $LiFePO_4$, and (d) the tavorite-phase of $LiFeSO_4F$. Li atoms are shown in yellow while the transition metals polyhedra for Co, Mn, and Fe are shown in blue, red, and green, respectively. The polyhedra are coordinated by oxygen atoms in orange and fluorine in blue. (Melot and Tarascon, 2013)

Although research has been focused predominantly on lithium iron phosphate, the corresponding compounds of other transition metals like manganese, nickel and cobalt have also been investigated. None of these have shown any superior electrochemical performance, however, and the materials are far more costly, hence the interest in these compounds has been limited (Whittingham, 2004). Not strictly an olivine phase, tavorite phase materials like $LiFeSO_4F$ have been found to exhibit similar properties as the olivine phases. Its structure, which can be seen in Figure 5D, also consists of layers of octahedra, but unlike in the olivine structure, these share corners and are coordinated by both oxygen and fluorine atoms, while the layers themselves are separated by tetrahedra of oxygen and fluorine coordinated sulfur atoms (Melot and Tarascon, 2013).

2.1.4.4.4 Hybrid materials

In addition to the pure materials of each group, there are several hybrid materials, including the previously mentioned $LiNi_{1-x}Co_xO_2$. $LiMnO_2$, while having a lithium content too high to be stable in the spinel structure, has been researched as an alternative layered oxide material due to the low price of manganese compared to cobalt. However, because $LiMnO_2$ is not thermodynamically stable at high temperatures, it cannot be synthesized using common high temperature processes (Armstrong and Bruce, 1996). It has been found that one solution for this is adding either or both nickel and cobalt, which stabilizes the layered oxide structure (Whittingham, 2004). This has resulted in a series of hybrids on the forms $LiNi_xMn_{1-x}O_2$, $LiMn_{1-x}Co_xO_2$ and $LiNi_xMn_{1-x-y}Co_yO_2$, which have yielded good results (Martha et al., 2009).

Table 2: Examples of cathode materials, their group and the approximate capacity ranges they have been reported to exhibit. Based on material from (Fergus, 2010)

Material	Group/structure	Reported specific discharge capacity
$LiCoO_2$	Layered oxide	100-160 mAh/g
$LiMn_2O_4$	Spinel	70-140 mAh/g
$LiFePO_4$	Olivine	80-155 mAh/g
$Li(Ni_{0.33}Mn_{0.33}Co_{0.33})O_2$	Hybrid layered oxide	80-160 mAh/g

2.1.4.5 Anodes

2.1.4.5.1 Carbon anodes

Anodes of different carbon polymorphs have traditionally been regarded as the standard for lithium-ion batteries. While the use of carbonaceous materials as intercalation electrode material was proposed as early as in the patent describing the first ever lithium-ion secondary battery (Yoshino et al., 1987), it has yet to be succeeded as the standard anode material. This can be attributed to its excellent cycle life, abundant material supply and low cost. The vast majority of the carbonaceous electrodes are made from graphite or graphitable carbons, for which the intercalation mechanism has been widely studied and is well known (Scrosati, 2000). However, lithiation into graphitic electrodes is limited by the composition of the most lithium rich phase in the Li-graphite system, LiC_6, giving rise to a relatively low theoretical maximum capacity of ~372 mAh/g, above which lithium metal is formed. This has prompted research into

alternative anode materials, including both more advanced carbon based electrodes, alloys and composites (Shukla and Prem Kumar, 2008, Zhang, 2011).

Of the alternative carbon materials, hard carbons obtained by pyrolysis of organic precursors have acquired some interest. This process forms a material with only short range ordering and various surface termination groups depending on the precursor used and pyrolization temperature. Due to the lack of long range order and varying composition, the process of lithium intercalation into such materials is not easily determined, hence the theoretical capacity limit is not known. What is known, however, is that at least some of these materials have been shown to exhibit far higher capacities than the limit for graphitic carbon. However, while the lithium insertion capacity may be very high, these materials suffer from very large irreversible capacities, severely limiting their practical applicability. Other alternative carbon polymorphs include kish graphites and multi-walled carbon nanotubes (MWCNTs) (Shukla and Prem Kumar, 2008). Compared to synthetic graphites that are formed at temperatures close to 3000 °C, kish graphite is rather cheap as it is formed at temperatures around 1500 °C in supersaturated iron melts, and is thus a common byproduct of steel production. While strictly being a member of graphitable carbons, kish graphite have proven to have capacities reaching ~20% above the theoretical limit of perfect graphite, indicating a certain degree of disorder (Lee et al., 2003). MWCNTs, on the other hand, are rather expensive, but have still attracted a fair share of attention due to the many potential mechanisms of lithium intercalation, namely in the graphene sheets constituting the tubes, in the space between the tubes formed due to imperfect packing, and inside the tubes themselves. However, as with the hard carbons, the irreversible capacity is too high for this kind of electrodes to be commercially viable (Shukla and Prem Kumar, 2008).

2.1.4.5.2 Alloying anodes

Another important group of anode materials are the alloys. These are based on the fact that many metals and metalloids are known to form well-defined intermetallic phases with lithium, including, but not limited to, Mg, Ca, Al, Si, Ge, Sn, Pb, As, Sb, Bi, Pt, Ag, Au, Zn, Cd and Hg (Winter and Besenhard, 1999). Silicon, being the theme of this thesis, will be covered in further detail in the following section, while a brief summary of the commonalities of the alloy anode materials is given here. These materials have attracted interest as mediums for energy storage since the 1971 discovery that metals can readily be alloyed with lithium by electrochemical means (Dey, 1971), and after the emergence of the lithium-ion battery, more specifically as intercalation electrode materials. Because of their availability, price and environmental benignity, Si, Sn, Sb, Al, and Mg have been most extensively researched for this purpose (Zhang, 2011). Table 3 shows a comparison between key electrode properties of these alloy anode materials and graphite, from which it is evident that the potential capacities of alloy forming electrodes are far superior to that of the graphite anode. While the specific capacities of intercalation anodes never can surpass that of the lithium metal anode due to the electrochemically inactive elements, many alloy electrodes come close. In fact, from a volumetric point of view, the amount of lithium some alloy electrodes can accommodate per volume exceed that of metallic lithium itself, e.g. $Li_{22}Si_5$ contains 88.56 mol_{Li}/L, while lithium metals only contain 76.36 mol_{Li}/L (Winter and Besenhard, 1999). The reason why this is possible

is partly because lithium is stored in ionic rather than atomic form in the alloy electrodes and partly because metallic lithium is not in a close packed crystal structure, and therefore have a potential for densification.

Alloy anodes are also superior to carbon anodes from a safety-perspective. Lithiation of the alloys happen at potentials ranging from 0.1V to 0.9V (cf. Table 3), compared to the carbon anode where lithiation typically happen around 0.05V. On one hand, this reduces the voltage of the cell, and hence the specific energy, but it also reduces the probability of accidental deposition of metallic lithium on the electrode surface during fast charging (Zhang, 2011). Safety benefits like this carries a lot of weight in many industries, e.g. in the automotive industry (Jansen et al., 1999).

However, while these materials have excellent capacity and safety benefits, there are several other characteristics that are necessary to make a suitable anode material. In two of these alloy anodes have been found to be seriously lacking; cycle stability and Coulombic efficiency. Due to the high electropositivity of lithium, many of the intermetallic phases formed by lithium and group 13-16 metals or metalloids are of highly ionic character. These are collectively known as Zintl-phases and are usually brittle. While the lithium-ions can occupy interstitial positions in the lattice, and hence cause only a limited volume expansion, the reduction of the otherwise neutral host atoms results in a substantial diameter increase, leading to an increase in volume of the material (Winter and Besenhard, 1999). This is evident from Table 3, where expansions of up to 320% are observed, compared to 12% for the graphite electrode. During cycling, this volume change introduces large stresses into the electrodes. In combination with the brittleness of many of these materials, including the Zintl-phases, these stresses can eventually lead to cracking of the electrode (Ng et al., 2006). This can lead to material losing electrical contact with rest of the electrode or the electrode itself delaminating from the current collector. Both of these effects cause electrode material to become essentially dead weight, thereby leading to an irreversible capacity fade. The pulverization is also associated with a continuous formation of new surface area. As described in section 2.1.3, this new surface area must be stabilized by forming an SEI, a process which involves irreversible loss of lithium, thereby yielding the low Coulombic efficiency observed in these materials.

Table 3: Comparison of the theoretical specific capacity, charge density, volume change and onset potential of various anode materials (adapted from (Zhang, 2011)).

Material	C	Si	Sn	Sb	Al	Mg
Density [g/cm^3]	2,25	2,33	7,29	6,7	2,7	1,3
Lithiated phase	LiC_6	$Li_{4,4}Si$	$Li_{4,4}Sn$	Li_3Sb	LiAl	Li_3Mg
Theoretical specific capacity (mAhg^{-1})	372	4200	994	660	993	3350
Theoretical charge density (mAhcm^{-3})	837	9786	7246	4422	2681	4355
Volume change (%)	12	320	260	200	96	100
Potential vs. Li (~V)	0,05	0,4	0,6	0,9	0,3	0,1

These severe effects make the volume change and associated electrode destruction arguably the biggest obstacle in the way of a successful alloy anode. However, as the potential benefits are of

such magnitudes, this is an obstacle for which there has been proposed numerous solutions. Most of these rely on composites with relatively inactive materials or dimensional stabilizing by using submicron particles or structures (Shukla and Prem Kumar, 2008). Concrete examples of this will be discussed in more detail in section 2.2 and 3.

2.2 The Silicon Anode

2.2.1 The Lithium-Silicon System

Figure 6 shows the lithium-silicon phase diagram. The stoichiometry of the four lithium rich intermetallic phases of the lithium silicon system was determined reliably by Wen (1980) and Wen and Huggins (1981). An assessment of the lithium rich part of the phase diagram from experimental and thermodynamical data was published by van der Marel et al. (1985). Based mainly on these publications, Okamoto (1990) assembled a phase diagram very similar to the one in Figure 6, but without the monosilicide phase. Because monosilicides had been reported in the other alkali-silicon systems (NaSi, KSi, RbSi and CsSi), LiSi was suspected to exist. It was not confirmed until 2003 when it was formed at pressures between 1 and 2,5GPa. The phase was reported to be stable below 470°C at ambient pressure, and that the reason for it not being observed earlier is the slow kinetics of the peritectoid reaction, rather than an inherent instability of the phase (Stearns et al., 2003).

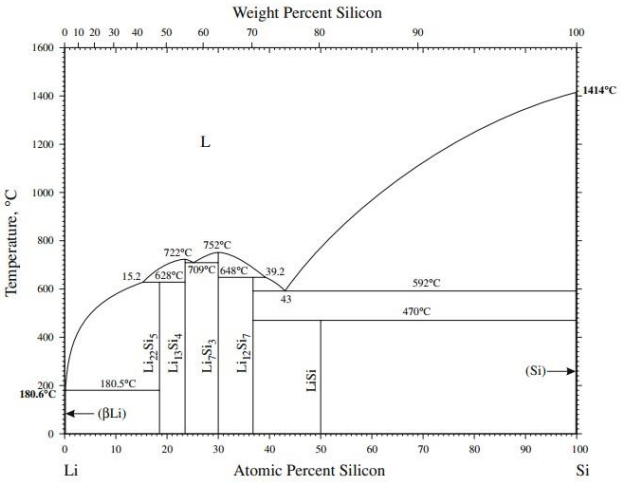

Figure 6: The lithium-silicon phase diagram

While it has been confirmed that the silicon electrode undergoes an amorphous transition during lithium intercalation, it is commonly assumed that lithiation of silicon is limited by the most lithium rich intermetallic phases; $Li_{22}Si_5$ at high temperatures and $Li_{15}Si_4$ at ambient temperature (Ge et al., 2012). This corresponds to theoretical specific capacities of 4198 mAh/g and 3578 mAh/g, respectively (cf. Appendix A).

2.2.2 Electrode Break-Down Mechanism

As mentioned in section 2.1.4.5, the break-down of the alloy anodes is mainly attributed to the volume expansion and contraction experienced by the electrode during cycling. To illustrate the magnitude of this expansion for silicon, let us first look at the bulk silicon anode and assume that this electrode goes from being elemental silicon to pure $Li_{22}Si_5$-phase during charging. Since the number of silicon atoms is constant, the relative volume increase of the anode can be established by calculating the volume of electrode per silicon atom in each of these phases. This can be expressed by

$$V_{Si\ atom} = \frac{V_C}{N_{Si}} \qquad \text{Equation 2}$$

With V_C and N_{Si} being the unit cell volume and the number of silicon atoms in the unit cell, respectively. Silicon has the cubic diamond crystal structure with 8 atoms per unit cell and a lattice parameter of 5.430Å, yielding

$$V_{Si\ atom} = \frac{(5.430\text{Å})^3}{8\ Si\ atoms} = 20.01 \frac{\text{Å}^3}{Si\ atom}$$

$Li_{22}Si_5$, on the other hand, has a more complex structure. Experiments on $Li_{22}Pb_5$, upon which the structure of $Li_{22}Si_5$ is modeled, show that the unit cell is a face centered cube containing a total of 432 atoms or 16 formula units (Fernández-Perea et al., 1999). The lattice parameter for the $Li_{22}Si_5$ unit cell is 18.75Å (Zhou et al., 2011). Again the volume per silicon atom can be calculated as

$$V_{Si\ atom} = \frac{(18.75\text{Å})^3}{16 * 5\ Si\ atoms} = 82.40 \frac{\text{Å}^3}{Si\ atom}$$

This shows that, in this idealized case, the electrode volume increases by more than 300% when going from silicon to the fully lithiated state.

Due to the limited diffusion of lithium in silicon, large concentration gradiants are readily formed in the electrode. As lithium concentration is closely related to the degree of expansion, this again leads to uneven expansion of the electrode and the associated internal stresses. Shear stress in the interface to the back contact is also formed due to the relatively constant dimensions of the back contact compared to the varying dimensions of the electrode material. Delamination can occur if the stresses between the electrode material and back contact exceed the adhesion strength of the interface.

The loss of mechanical integrity in the electrode causes fragments to loose electrical contact with the rest of the electrode, effectively deactivating a small portion of the electrode each cycle (Kasavajjula et al., 2007). In addition to this steady fade in capacity, critical failures can also occur. This happens when sharp fragments pierce the separator disk, causing a short circuiting of the battery, leading to heat build-up, which again can lead to thermal runaway and potential explosion if not controlled (Balakrishnan et al., 2006). As mentioned in section 2.1.4.5, the reactivity of the lithium leads to the formation of additional SEI. While it is common to have a surplus of lithium in battery testing, this is not the case in commercial batteries. The loss of lithium must either be accounted for by increasing the weight of the cathode, which is the lithium source, or by reducing the capacity rating of the battery. Regardless; the formation of additional SEI will indirectly decrease the specific capacity of the battery.

2.2.3 Previous Electrode Designs

Figure 7 shows the specific capacity as a function of cycle number for several different silicon anode designs. As seen from this figure the cycle stability of the silicon anodes is strongly dependent the geometrical design. This is the basis for dimensional stabilization. Through the last decades, a large number of different electrode designs have been researched, an overview of which will be given in this section.

An example of pure dimensional stabilization is electrodes made exclusively from micro or nano-scale silicon powders. The reasoning behind this design is that the small dimensions of the material reduce the stresses formed to acceptable levels. While showing some improvement over bulk silicon with respect to cycle stability, these initial attempts were far from successful

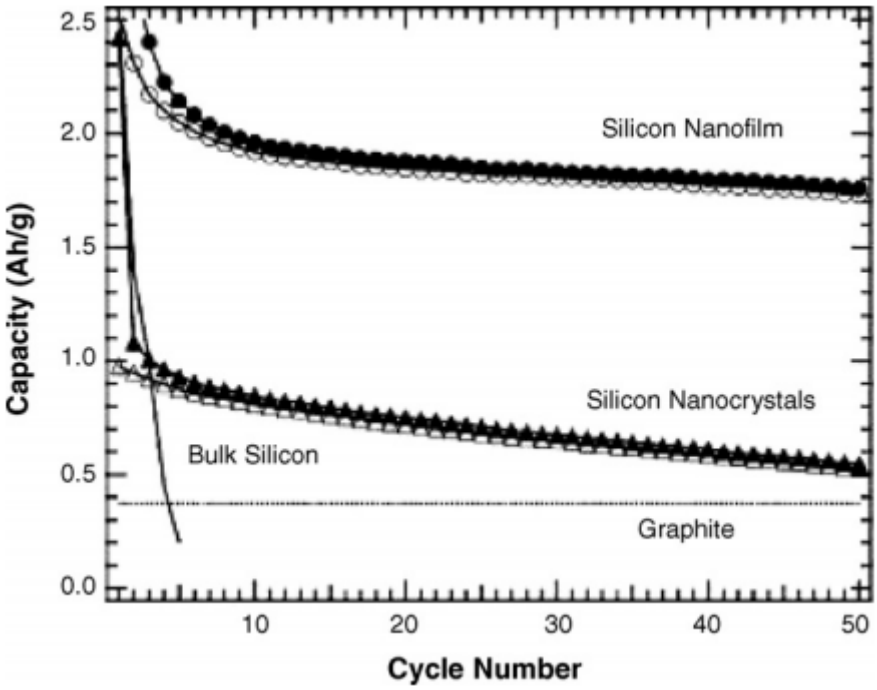

Figure 7: Specific capacity vs. cycle number for different silicon anode designs (Graetz et al., 2003)

(Ryu et al., 2004, Yoshio et al., 2005). It was quickly established that coating these particles could drastically improve the performance. Attempts were made using metals, carbon, nitrides and oxides, with carbon proving to be the most successful (Liu et al., 2005). This research eventually led to the development of silicon based composite electrodes in the early 90s (Kasavajjula et al., 2007). Presently, this is still the largest group of silicon anodes, and after more than two decades of research it has expanded to include a wide range of different constituents. The majority of this group is silicon-carbon composite electrodes, consisting of three main components; 1) silicon, 2) conductive additive, and 3) binder. The silicon is usually supplied in powder form, the size of which is an important defining parameter for the electrode, as smaller particles tend to result in better performance (Liu et al., 2005). The conductive additive has traditionally consisted of either graphite, nano-sized carbon black or a combination of the two, with carbon fibers and nanotubes having attracted some interest in later years (Zhang et al., 2006a). Of the third component, the binder, there is a wide variety of possibilities, the most common being polyvinylidene fluoride (PVdF) (Kasavajjula et al., 2007). Other alternatives include carboxyl methyl cellulose (CMC) and varieties of styrene-butadiene rubber (SBR) (Chen et al., 2006). Examples of other composite electrodes are silicon-metal composites of a wide variety. Usually based on a silicon based alloy, e.g. Mg_2Si, $CoSi_2$ and $NiSi_2$, these have performed well under some laboratory tests, but not to an extent that warrants commercialization (Kasavajjula et al., 2007).

Besides the composite electrodes, another main group of electrodes; thin-films, have received a fair share of attention. The motivation for using thin-films compared to composites is that they contain no inactive components, and thus have a higher effective specific capacity (Kasavajjula et al., 2007). Being essentially bulk silicon, the performance deteriorate quickly when film thickness approaches 1µm (Yoshio et al., 2005). However, thin films have demonstrated extremely good performance even at high charge and discharge rates, e.g. 50 nm films cycled at 30C that retain a capacity of over 2000 mAh/g even after 3000 cycles (Takamura et al., 2004). However, as a 50 nm pure silicon film is equivalent to a material loading of only 13.25 µg/cm^2

(for a silicon density of 2,65 g/cm^3). The active area would have to be immense to obtain a usable capacity and the mass of the associated current collectors would be considerable; hence the Q_m of Equation 1 would be very small, and thus also the capacity of the entire cell. On the other hand, far thicker films have been made with acceptable results, and much effort is still being put to the task. Approaches include making binary and ternary alloy thin films, and while not yet commercialized, they show much promise (Kasavajjula et al., 2007).

In later years, more advanced silicon materials have been tested both on its own and in composites, in some cases to great effect. For instance, micrometer sized pillars, nanowires and nanorods have been employed in composites (Etacheri et al., 2011a). Several of the most recent attempts have involved porous silicon, either in the form of porous films (Thakur et al., 2012b), porous particles (Zhao et al., 2012) or porous nanowires (Ge et al., 2012), which, being the theme of this thesis, will be discussed in section 3.

2.3 Fundamentals of Porous Silicon

Porous silicon was accidentally discovered in 1956 by Arthur Uhlir Jr. when trying to electrochemically polish silicon and germanium wafers. At the time, as the surface was coated in a porous film rather than polished, it was regarded as a failure and only reported as such (Uhlir, 1956). Due to this unfortunate introduction, the properties of porous silicon remained relatively unexplored for more than three decades. This ended abruptly in the eighties when the discovery of porous silicon luminescence lit a spark of interest. While issues with stability and the discovery of better performing luminescent materials caused interest in this area to wane already in the early nineties, the attention of other parts of the research community had been attracted as well. In several areas, the large surface area and controllable pore size and geometries presented unprecedented opportunities, e.g. in the solar energy field as tunable anti-reflective coatings and back side reflectors on solar cells (Kuzma-Filipek et al., 2010, Jae-Hong et al., 2007, Selj et al., 2010), or, as is the case in this work, as electrodes for lithium-ion batteries (Thakur et al., 2012b, Zhao et al., 2012, Ge et al., 2012).

In this section, the two main methods that are commonly used for fabrication of porous silicon is presented; stain etching (Dimova-Malinovska et al., 1997) and anodic etching (Halimaoui, 1997). Stain etching is a simple and scalable procedure, but allows little control over the reaction parameters in comparison to the anodic etching. As this makes it unsuitable for this research, only a brief presentation of this method will be given.

2.3.1 Stain Etching

Stain etching of silicon is based on the interworking of hydrofluoric acid and a powerful oxidizing agent, e.g. nitric acid or hydrogen peroxide (Dimova-Malinovska et al., 1997, Huang et al., 2011). The process relies on the oxidation of silicon by reaction with the oxidizing agent and subsequent dissolution of silicon oxide by HF, and can be described as a closed circuit electrochemical reaction with both anode and cathode reaction happening on the silicon surface. A reaction mechanism for nitric acid is proposed by Coffer (1997) to be

Cathode: $HNO_3 + 3H^+ \rightarrow NO + 2\,H_2O + 3h^+$

Anode: $n\,h^+ + Si + H_2O \rightarrow SiO_2 + 4H^+ + (4-n)e^-$

$SiO_2 + 6HF \rightarrow H_2SiF_6 + 2H_2O$

Overall: $3\,Si + 4\,HNO_3 + 18\,HF \rightarrow 3\,H_2SiF_6 + 4\,NO + 8\,H_2O$

(Assuming continuous recombination of holes (h^+) and electrons (e^-))

There are several variations of this method, the most notable in later research being metal assisted stain etching. The basis for this variation is the catalysis of the etching process by a metal coating or particles on the substrate surface. The etching is thus far more rapid in the metal-substrate interface than elsewhere, causing the metal to sink into the material. Patterning of the metal coating can thus be used to create nanostructures on the silicon surface in a process called template-based metal-assisted stain etching (Huang et al., 2011).

2.3.2 Anodic Etching

Anodic etching, or anodization, of silicon is by far the most commonly used method for porous silicon production (Liu et al., 2003). In this etching method silicon is submerged in an externally biased etching cell filled with HF solution. This cell is usually one of three different cell designs; the conventional single tank cell, the lateral anodization cell, and the double tank cell, sketches of which are shown in Figure 8a to c, respectively. In the two former, the silicon substrate is directly connected as the cell anode. The cathode can be made of any HF-resistant and conductive material, with platinum being the most common material of choice. In the double tank cell, the silicon substrate, most commonly in the form of a wafer, is placed in a sample holder separating two isolated chambers of electrolyte. In each of the chambers there is placed an electrode, and as a biased is applied between these, current passes through the electrolyte and the wafer separating the two chambers. The surfaces of the wafer will thus act as a secondary anode and cathode in the primary cathode and anode chambers, respectively. (Halimaoui, 1997)

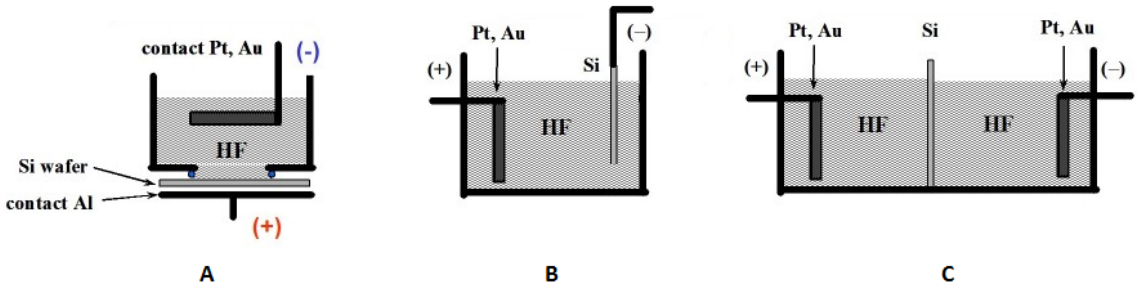

Figure 8: Different cell set-ups for anodic etching of silicon; a conventional single tank cell (A), a lateral anodization cell (B) and a double tank cell (C).

2.3.2.1 Etching chemistry

The reaction mechanism has been a matter of discussion and several different mechanisms have been proposed, of which the proposition by Turner (1958) has been recurring most often (Halimaoui, 1997);

$$\lambda\, h^+ + Si + 2\,HF \rightarrow SiF_2 + 2H^+ + (2-\lambda)e^-$$

$$SiF_2 + 2HF \rightarrow SiF_4 + 2H_2$$

$$SiF_4 + 2\,HF \rightarrow\ H_2SiF_6$$

Analogous to the reaction mechanism for stain etching, it is observed that holes are necessary to facilitate the current driven etching process; hence the electrochemical etching will happen when the silicon is anodized (Halimaoui, 1997). While the reaction mechanisms presented in this and the previous section can explain the removal of the silicon itself, the reason why pores are formed is far more complicated. The large number of theories that have been presented on this matter reflects the number of variable process parameters and the complexity of their interaction, as well as the fact that the parameter space is far from thoroughly researched. Parameters that have proven to have a great impact on the size and morphology of the pores include doping type and level, current density, electrolyte composition and the presence and

intensity of front or back side illumination (Föll et al., 2002). None of the presented theories have yet been confirmed and a thorough examination of all of them is far beyond the scope of this work. However, an overview of the main theories will be given.

Typical I-V curves for conventional single tank etching of n- and p-type silicon in aqueous HF can be seen in Figure 9. As might be expected for a semiconductor-electrolyte junction due to its similarity with a semiconductor metal junction, some of the characteristics of the Schottky diode can be recognized. For instance, the junctions exhibit photo-induced currents when reverse biased, that is; at cathodic bias for p-type silicon and anodic bias for n-type silicon (Smith and Collins, 1992). However, the there are some fundamental differences. In the I-V curves at anodic potentials for p-type silicon and n-type silicon with illumination, two characteristic peaks are observed that are anomalous. These are of great importance to porous silicon etching, as they represent the borders between different etching regimes. At potentials below the first peak porous silicon is formed. In this area, the current increases exponentially with the potential, a behavior that is analogous with the Schottky junction, indicating that the etching process is limited by the supply of charge from the electrode bulk to its surface rather than any electrolyte effects (Lehmann and Gosele, 1991). In the range between the peaks the silicon surface is electropolished as the surface is continuously oxidized and the oxide is dissolved. At potentials above the second peak, the current tends to destabilize and oscillations may occur, the reason for which is largely unknown (Smith and Collins, 1992). The case is quite different for non-illuminated n-type silicon. The reason for this is that the dissolution reaction taking place on the electrode surface requires holes regardless of the doping type of the material. As the number of holes is the material is very low, the etching happens very slowly up to a certain potential, when the etching rate increases drastically. Above this potential, it is believed that avalanche breakdown of the junction occurs and holes are produced at a rapid rate, facilitating the etching process (Föll et al., 2002).

2.3.2.1.1 Formation models

While the peaks aid in the determination of proper current densities and potentials for porous silicon formation, the underlying mechanisms that cause pores to be formed has yet to be explained. There are three theories for the pore formation that have received the most attention in the last couple of decades; the Beale model, the diffusion limited model and quantum model (Smith and Collins, 1992). In addition to these, a fourth model, called the current burst model, has attracted some attention since the early 1990s. This is a far more extensive model which is still under development and is not yet fully understood, but on the other hand claims to be a complete description of the electrochemistry of silicon; “There is little doubt in the opinion of the authors that the current burst model has the potential to explain most if not all phenomena encountered in Si electrochemistry” (Föll et al., 2000).

The Beale model

The Beale model is based on a premise recurring in electrochemistry; that field lines focus on surface irregularities and that this, under the proper circumstances, can enlarge the irregularities already present, forming pores. It was experimentally observed that the conductivity of porous silicon was comparable to the intrinsic conductivity of pure silicon, regardless of dopant concentration (Beale et al., 1985). This apparent lack of free charge carriers led Beale to the assumption that the distance between the pores is always less than two times the depletion

width, making the structure a continuous depletion zone. The resulting low conductivity of the pore walls serves to further focus the electric field lines to the pore tips, enhancing the dissolution there. In this model, the depletion width is thus the characteristic parameter describing the pore size, inter-pore distance and morphology. And, as it is a function of doping level, etching potential etc., it provides a link between these parameters and the obtained pore structure. While this model is convenient in the way it uses familiar solid-state principles like the band structure, depletion regions etc., it does use some assumptions that are not consistent with experimental data. One of these is the assumption of Fermi level pinning at the surface of the material, which is in contradiction to the low recombination rate observed on HF-treated surfaces (Smith and Collins, 1992). Still, this is one of the more commonly and readily used models, and several of its aspects have been reused in later models.

The diffusion limited model

The diffusion limited model is based on the "random walk" of charge carriers through the silicon. During etching, holes diffuse through the bulk of the material to the surface where they oxidize silicon atoms. If the movement is random, as is the nature of this model, the pore tips represent the most probable points on the surface for this oxidation to happen. The characteristic length defining the pore structure in this model is therefore the diffusion length. This models is essentially equivalent with the Beale model, as shown by Smith and Collins (1992), however, it has one primary advantage over the Beale model in that it makes no assumptions of the state of the silicon-electrolyte interface with regard to Fermi level pinning. Rather it only assumes a complete consumption of holes on the surface, which is the case for all but the smallest current densities, hence avoiding the contradictions mentioned above (Smith and Collins, 1992).

The quantum model

As mentioned in the introduction to section 2.3, porous silicon attracted a lot of interest due to its high intensity visible photoluminescence. However, silicon, being a 1.1 eV, indirect band gap semiconductor, is not expected to exhibit such properties. Due to this it was postulated that the pore structure is of sufficiently fine dimensions to act as quantum wires and wells (Lehmann and Gosele, 1991). This behavior emerges when one or more dimensions are smaller than the wavelength given by the electron wave function in that area, forming structures with quantum confinement in one, two or three directions called quantum wells, wires and dots, respectively (Cahay, 2001). One of the effects of quantum confinement is that the band gap of the semiconductor increases. This result in both higher probability of direct band-gap recombination events and energy of emitted photons, thus accounting for intense visible photoluminescence observed. However, what is more important in this context is that the increased band gap also drastically decreases the charge carrier density. This leads to depletion regions in a similar manner as in the Beale model, however, without the inconvenient assumption of surface Fermi level pinning. Quantum confinement is expected for structures below a certain size limit, which therefore is the characteristic length for this model. For silicon this is only around 1nm. Moderately doped p-type silicon is known to form pores of this size, and quantum confinement is therefore believed to play a role for such materials. For p^+ or n-type silicon, however, where pore wall thicknesses of several µm are observed, it is unlikely that quantum confinement is a limiting factor, making this model unsuitable. (Smith and Collins, 1992)

The current burst model

The three models described above are based on common principles, either in solid state or electrochemistry, and therefore may have a sense of familiarity. That is not necessarily the case for the current burst model. This model is based on the "removal" of a common assumption in electrochemistry; that current flow is homogenous in space and time. The reasoning behind this is that the dissolution of silicon happens by a sequence of four reactions (Föll et al., 2002):

1) Direct dissolution: $Si + xh^+ - ye^- \rightarrow Si^{4+}$
2) Oxidation: $Si + 4h^+ + 2O^{2-} \rightarrow SiO_2$
3) Oxide dissolution: $SiO_2 + 4F \rightarrow SiF_4 + O_2$
4) Hydrogen coverage: $SiX + H \rightarrow SiH + X$

As these cannot all occur at the same time at the same place, homogenous current is intrinsically impossible. At a given point on the surface there is a probability that the reaction will start by nucleation of a "current burst", hence the method name. This is the first of three postulates sited in this theory. The second is that the reaction happens in a logical sequence, i.e. the sequence given above. The third is that the current bursts on the surface of the material interact in both space and time. This means that the probability of a current burst happening is dependent on what is currently happening in and the history of the surrounding area. For instance; because passivation by oxidation increase with time, interaction in time tends to entail that the probability of a current burst occurring is higher when there is a short time since the last one. Different interaction processes in space can lead to the formation of domains of points that are more or less synchronized, the size of which is the characteristic length of this model. This can eventually lead to clusters of current bursts that form pores (Föll et al., 2000). While this might be an oversimplification of this model, it illustrates the principles from which it is developed.

2.3.2.1.2 Chemical etching

In addition to the electrochemical etching process where the oxidation happen by supplying holes electrically, additional natural oxidation of the silicon happened due to the presence of water and dissolved oxygen in the electrolyte. While silicon itself is resistant to HF, its oxide is not; hence the material undergoes a slow but steady chemical etching. This happens regardless of the electrochemical etching and is roughly proportional to the surface area of the sample (Selj

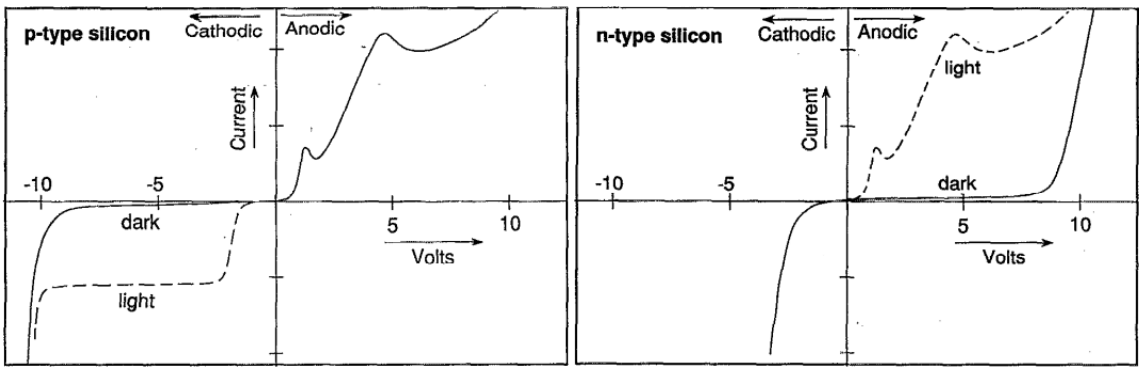

Figure 9: The characteristic I-V curves for electrochemical etching of p-type and n-type silicon (left and right, respectively) (Smith and Collins, 1992)

et al., 2011). The porous structures are thus especially vulnerable to this chemical etching, due to their high specific surface area, resulting in increased pore diameter and eventual complete removal of the porous layer if left in the HF solution (Navarro-Urrios et al., 2003). This will often result in a maximum thickness of a porous layer, as a balance between the electrochemical formation and chemical dissolution is established.

2.3.2.2 Morphology and its dependence on formation parameters

There are a vast number of different structures that can be obtained by anodic etching of silicon. Pore sizes ranging from 1nm to 10 µm that vary from perfect cylinders to seemingly random sponge structures. While a description of all the possible structure would be beyond the scope of this thesis, the main groups of structures that are usually formed will be given, as well as the parameters that control their formation.

Pore sizes are defined in three groups by the IUPAC standard as micropores, mesopores and macropores, describing pores or pore distances smaller than 10 nm, between 10 nm and 50 nm and larger than 50 nm, respectively. Pore size is obviously an important parameter for porous structures, and together with the porosity of the material as a whole it can say much about what properties to expect. However, to make a complete description of the morphology, the pore orientation, branching and filling, as well as how these parameters vary with depth must be known. Extensive work has been performed by Xiaoge Gregory Zhang in reviewing these structures. This work has been published in his 2001 book "Electrochemistry of Silicon and Its Oxide" and further in a 2004 journal article, which will constitute the basis of this section.

Pore size is naturally a very important parameter for porous silicon, and, as mentioned, a wide range of pore sizes can be obtained by anodic etching. The pore size is largely dependent on doping concentration, and the general trend is that the pore size increases with increasing doping level for p-type and decreases for increasing doping level for n-type silicon. For the latter, illumination also has a large impact on the pore size. For some doping concentrations, two distinct ranges of pore sizes have been observed. This applies particularly to low doped p-type silicon, with pore sizes ranging from 1-10 nm and >1µm, and n-doped silicon under illumination, with pore sizes of 1-10 nm and 50 nm- 10 µm. Heavily doped silicon usually have a pore distribution from 10-100 nm regardless if the material is p or n-type. Moderately doped p-type silicon has pores sizes from 1-10 nm, and lowly and moderately doped n-type from 10 nm to 10 µm. The pore size ranges generally expected for different doping levels are summarized in Table 4. While doping is the primary parameter determining the pore size, others, such as current

Table 4: General pore size dependence on doping type and level. Data collected from (Zhang, 2004).

Doping type	Doping level	No illumination	Illumination
N-type	High (10^{19})	10-100 nm	1-10 nm + 50 nm-10 µm
	Moderate (10^{15}-10^{18})	10 nm-10 µm	
	Low (<10^{15})		
P-type	High (10^{19})	10-100 nm	Negligible effect
	Moderate (10^{15}-10^{18})	1-10 nm	
	Low (<10^{15})	1-10 nm + >1 µm	

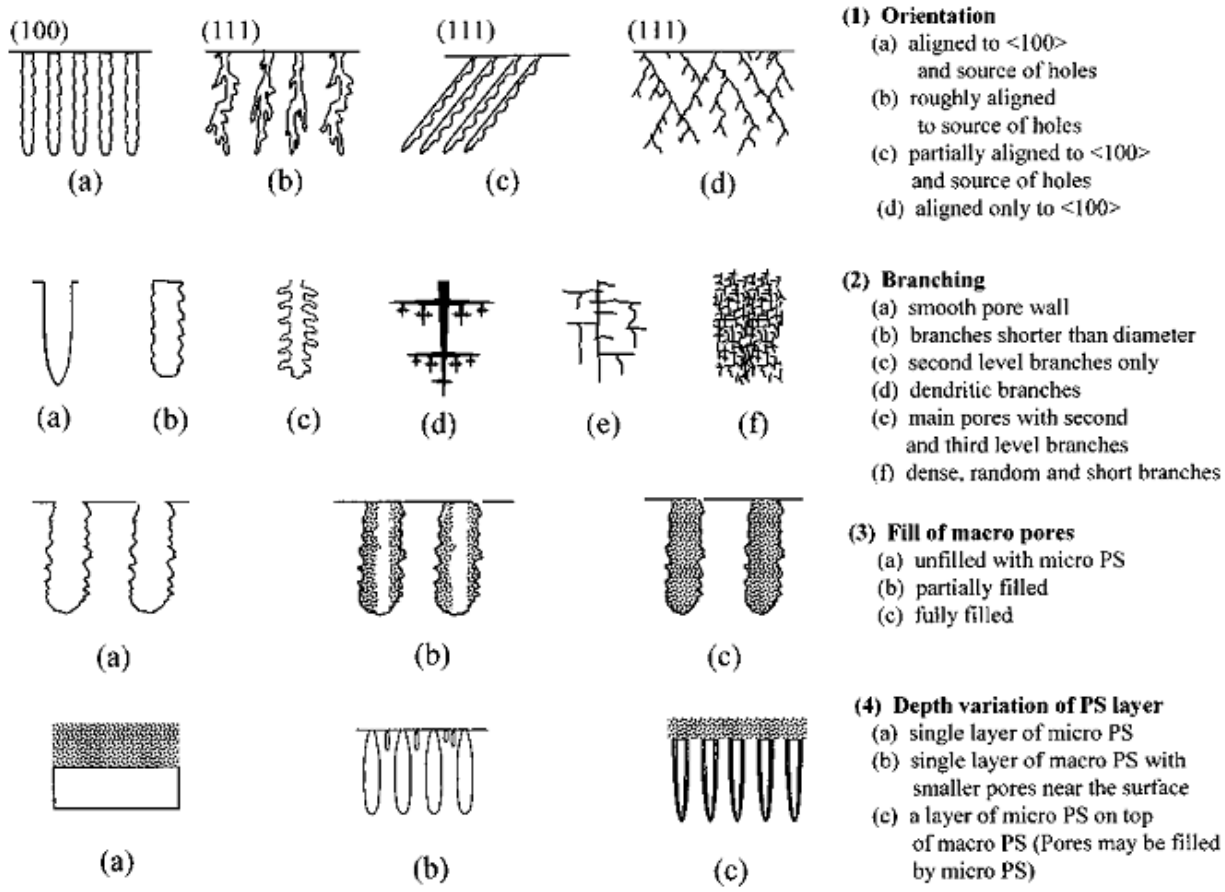

Figure 10: Morphological characteristics of porous silicon (Zhang, 2004)

density and HF concentration, also carry some weight. For these parameters, the trends are towards increasing pore size for increasing current density and decreasing HF concentration.

While important for the properties of the material, the pore size alone cannot describe a porous structure. Figure 10 shows a presentation of different morphologies that have been obtained during anodic etching in terms of orientation, branching, filling and depth variation. The orientation of the pores is believed to be controlled by mainly two factors. It has been observed that the pores tend to line up with the <100> directions for both n- and p-type silicon. This has been attributed to differences in activity of the different crystallographic surfaces, and hence the kinetics of passivation (Smith and Collins, 1992). The other factor is the direction from which holes are supplied. Under normal etching circumstances the current travels through the wafer, hence promoting pore formation perpendicular to the surface. For wafers with (100) orientation, these factors therefore work in unison, resulting in pores that are both in the <100> direction and perpendicular to the surface. For any other surface orientation, <100> is not perpendicular to the surface, hence there is a balance between these factors. This results in three different classes depending on which effect is the more prominent; 1) alignment with the source of holes, 2) partial alignment with both effects and 3) alignment with <100> direction. Which of these is obtained depends on wafer orientation, electrolyte composition, current density and doping level.

Different types and degrees of branching have been obtained by anodic etching. These can be classified in the manner shown in the second row of figures in Figure 10; smooth walled, i.e. no

branching; only second level braches, either smaller or larger than the primary pore diameter; dendritic branches; secondary and ternary branches of similar diameter; and lastly, seemingly random, dense structure of short branches, with no clear primary structure. Which of these structures is made is mainly dependent on the pore size, which again has dependencies that were accounted for above. Smaller pore sizes tend to have a higher degree of branching than large pores. The orientation of the substrate also affect the branching, with larger deviation from <100> increasing the degree of branching. The orientation of the branches themselves is controlled by the same factors as the primary pore orientation.

As mentioned above, pore sizes can occur in two distinct ranges or otherwise vary greatly in a single sample. How these different pore sizes are distributed throughout the sample is an important part of the morphology, and takes on mainly two forms. The first is structures which consist of macropores that are filled to different degrees with micropores; Figure 10.3a-c shows this for empty, partially filled and full macropores, respectively. The second is structures where the pore size changes with the depth in the sample. Different cases of this can be seen in Figure 10.4a-c. The first shows a single layer of homogenous pore size, hence no depth variation. The second structure has a transition layer constituting small pores closest to the surface, the pore size increases with depth until it reaches a value that is constant throughout the rest of the bulk porous structure. The last consists of two distinct layers, each more or less homogenous in pore size, with a microporous or mesoporous layer closest to the surface and a macroporous layer below. While the two former can be obtained from any doping type and level, the latter has only been observed for low doped p-type and n-type with illumination.

3 Porous Silicon Anodes; the State of the art

As mentioned in section 2.2.3, recent efforts in silicon anode research have included different varieties of porous silicon. This section will provide an overview of the most recent work performed by a number of prominent research groups on this subject. Emphasis is placed on the procedure used for producing the porous silicon, how the material is made into electrodes and what results are obtained. The methods used for producing porous silicon vary greatly from one group to another, ranging from electrochemical etching and stain etching to reduction of naturally occurring porous diatomaceous earth. Hence, it should be kept in mind that the obtained results are not necessarily comparable.

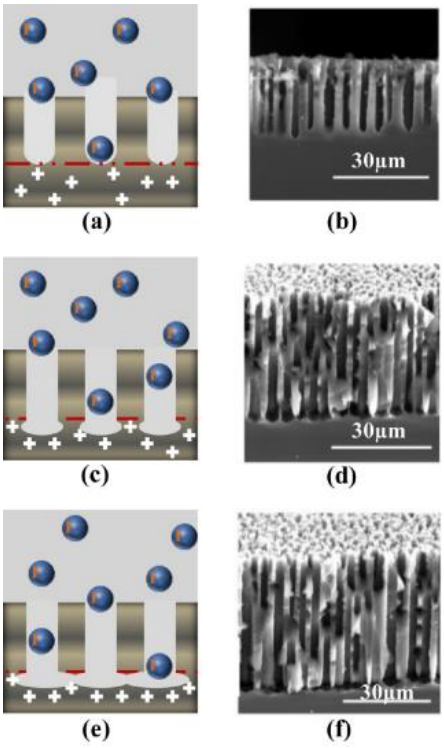

Figure 11: Schematic and SEM images of the formation of a freestanding porous silicon film. A) and b) showing etched porous material, c) and d) after current increase, and e and f) after lift of is accomplished. (Thakur et al., 2012b)

A collaboration group consisting of researchers from Lockheed Martin and Rice University, Huston TX, have published several articles in this field in recent years. Recurring in the work from this group is the formation of films of porous silicon obtained by anodic etching of p-type silicon in HF. Three different pathways are taken after this film formation. The first involves gold coating of the porous film on the wafer (Thakur et al., 2012a). This is performed using electron beam evaporation, forming a 20 nm thick gold layer on the porous material. The gold coated porous silicon was tested electrochemically, using the bulk wafer as current collector. The films were reported to retain a capacity of 3000 mAh/g for 50 cycles, and 2500 mAh/g for 75 cycles.

In the two next methods, freestanding films were obtained by first etching the porous layer on the surface of a wafer, then increasing current density above the limit for electropolishing, effectively cutting the porous material from the substrate. This is shown schematically and in SEM images in Figure 11. In the first of these methods, the films are carbon coated by covering in polyacrylonitrile (PAN) and subsequent pyrolization (Thakur et al., 2012b). They are then tested directly as electrodes, both with and without PPAN coating. The reported results are that the PPAN coated films are stable over 1200 mAh/g for 20 cycles, whereas the non-coated films fail after only a few cycles. The last method involves ultrasonically fracturing the films into porous particles (Thakur et al., 2012c). After fracturing, the particles are mixed with a PAN solution at different ratios and drop cast onto a current collector. The electrodes are then pyrolyzed to form porous silicon/PPAN composite electrodes. During electrochemical testing, these cells were discharge limited to 1000 mAh/g to maximize cycle life, with the best performing silicon/PAN holding 170 cycles at this capacity. One of the best performing samples was also tested using a fluorinated electrolyte, holding 1000 mAh/g for over 600 cycles.

Another group working out of the National Institute of Advanced Industrial Science and Technology (AIST), Japan, has researched the production and use of hierarchical porous particles

as anode material. The starting particles are produced from mechanically milling boron doped silicon wafers. These particles are then etched in two steps to produce the hierarchical pore structure. First a mixture of HF and silver nitrate ($AgNO_3$) is used to etch mesopores, and then a mixture of HF and hydrogen peroxide (H_2O_2) is used to etch micropores in the remaining material. The particles were then carbon coated by dispersing them in a formaldehyde/resorcinol gel, which is then dried and subsequently pyrolyzed. Electrodes were manufactured by mixing the carbon coated silicon particles with carbon black and PVdF binder. The electrodes were tested with a discharge limitation of 1500 mAh/g and were reported to retain this capacity for over 50 cycles. (Zhao et al., 2012)

A comparable technique has been developed at a group at Tsinghua University, Beijing. In this case, <200 nm silicon particles were doped using boric acid and annealed at 900 °C in argon before etching. The etching process is similar to the first step of the AIST process; stain etching using a mixture of HF and $AgNO_3$. The particles were carbon coated using an unspecified CVD process and mixed with reduced graphene oxide, carbon black and alginate binder to form electrodes. These electrodes were reported to deliver a stable capacity over 1400 mAh/g and 1000 mAh/g for 200 cycles at 1/4C and 1/2C rates, respectively. (Ge et al., 2013)

Yan Yu of the Max Planck Institute for Solid State Research, Stuttgart, has reported the formation of porous silicon by reduction of mesoporous silica, using it as both a silicon source and a template for porous silicon formation. This was achieved using a magnesiothermal process by the reaction

$$2\,\mathrm{Mg} + \mathrm{SiO_2} \rightarrow 2\,\mathrm{MgO} + \mathrm{Si}$$

Powders of magnesium and porous silicon oxide were mixed and heated to 650 °C under Ar-5vol% H_2. The resulting material was cleaned of MgO and remaining SiO_2 using HCl and HF, respectively. The resulting particles were silver coated using a wet chemical method described in the article. Electrodes were manufactured using porous particles, both with and without silver coating, carbon black and PVDF binder. Capacities of 2122, 1610, and 800 mAh/g were obtained for the silver coated particles after 10 cycles for 1, 2, and 4C rates, respectively. The corresponding capacities for the non-silver coated particles were 1930, 1430, and 590 mAh/g. At 0.2C capacities of ~2500 and ~2000 mAh/g were obtained after 100 cycles for the coated and non-coated particles, respectively. (Yu et al., 2010)

A similar process has been investigated by researchers at Key Laboratory for Renewable Energy, Chinese Academy of Sciences, Beijing. The fabrication procedure was essentially the same as that introduced by Yu et al. (2010), but instead of the synthetic porous silica, diatomaceous earth, a naturally occurring porous siliceous rock, was used as template. Diatomaceous earth consists largely of porous silica, and is a commercially available and cheap alternative to its synthetic counterparts. Rather than silver-coating, these particles were carbon coated using argon/toluene based CVD. Electrodes were manufactured from porous silicon particles with or without carbon coating, carbon black and an alginate binder. The reversible capacity was reported to be 633 mAh/g for the carbon coated particles and 376 mAh/g for the non-coated particles after 30 cycles. (Shen et al., 2012)

A research team at the University of Southern California has studied the production and use of porous silicon nanowires as anode material. The porous nanowires were synthesized directly by etching of boron doped silicon wafers, accomplished using a mixture of HF and $AgNO_3$. The wires were washed in HNO_3 to remove silver that precipitated during the etching process, and then rinsed in deionized water. These wires were made into electrodes by mixing with carbon black and alginate binder to form a slurry, which were spread on a copper current collector and dried. The electrodes were tested at various rates, the most impressing results being a capacity retention of 1000 mAh/g for 2000 cycles at 1C and 1000 mAh/g for 250 cycles at 4.5C. (Ge et al., 2012)

4 Experimental

The experimental part of this work is divided in three phases. The first was begun during the fall of 2012, and involves the production of lithium-silicon binary alloys for use in composite electrodes. The second phase is the formation of porous silicon by anodic etching and characterization of these structures. The last involves electrochemical testing of both the composite electrodes and the formed porous structures to determine their applicability in lithium-ion batteries.

4.1 Lithium-Silicon Composite Electrodes

4.1.1 Alloy Preparation

Due to the reactive nature of lithium, care had to be taken to avoid contamination. Sensitive samples were therefore handled in an argon filled glove box, and all melting was done in tantalum containers, also under argon atmosphere. The absence of any intermetallic compounds in the Li-Ta systems, as well as the negligible solubility of this metal in both liquid and solid lithium (Garg et al., 1990) effectively reduces contamination to acceptable levels.

The melting was conducted in a tube furnace, with the samples inside sealed tantalum tubes filled with argon. As starting lithium material a 99.9% pure rod supplied by Sigma Aldrich was used. The starting silicon grain is of unknown origin, but its composition has been accurately determined by neutron activation analysis (NAA) in the JEEP II reactor facilities at IFE. The results, which are seen in Appendix C confirm that the grains are of high purity, with titanium constituting the largest contamination at only 39 ppba. In preparation of the procedure, silicon was crushed in a mortar and sieved with a No. 35 mesh, keeping the small sized fraction. This was done in air at ambient conditions and the finished powder was moved into an argon filled glove box. In the glove box, silicon and small pieces of freshly cut lithium (ca. 1mm pieces) were weighed out to obtain 1 gram samples of the desired compositions. The materials were put layer by layer in 6mm tantalum tubes. These tubes were themselves put inside larger leak-proof stainless steel sample tubes with VCR fittings. All preparation was done and the tubes sealed inside the glove box to retain the argon atmosphere during melting.

Three samples were made with target compositions of three intermetallic compounds; the two congruently melting compounds Li_7Si_3 and $Li_{13}Si_4$, and the peritectoidally formed LiSi. The samples were heat treated by the procedures outlined in Table 5. All samples were heated to 850°C which is above the liquidus line for all these compositions, as can be seen in the phase diagram in Figure 6. It is not, however, above the melting temperature of pure silicon, leading to the assumption that the lithium forms a melt into which the silicon gradually dissolves. It has been reported that this dissolution is a slow reaction (van der Marel et al., 1985) and the samples were therefore held at 850°C for 3 hours. Since Li_7Si_3 and $Li_{13}Si_4$ are formed by congruent solidification, they were cooled directly to room temperature. LiSi, on the other hand, is formed by the peritectoid reaction:

$$Li_{12}Si_7(s) + 5\ Si\ (s) \rightarrow 12\ LiSi$$

The kinetics of this reaction is reported to be slow, and the sample was therefore held at 400°C for 12 hours before cooling to room temperature.

After melting, the tubes were returned to the glove box, where the samples were removed. Rather than being in one solid piece, the samples were in an agglomerated powder form, easily broken up during removal from the tubes. A small amount was used for X-ray diffraction analysis and the rest was put in into glass sample bottles, which were sealed thoroughly with Parafilm®.

Table 5: Heat treatment procedure for the different samples

Sample	Target Composition	Heat treatment procedure
1	LiSi	RT-850°C (10 °C/min) – 850°C 3 hrs. – Cool to 400 °C (3 °C/min) – 400°C 12 hrs. – Cool in furnace
2	Li_7Si_3	RT-850°C (10 °C/min) – 850°C 3 hrs. – Cool in furnace
3	$Li_{13}Si_4$	RT-850°C (10 °C/min) – 850°C 3 hrs. – Cool in furnace

4.1.2 Alloy Characterization

The samples were analyzed by X-ray diffraction (XRD) and SEM. The XRD was conducted using a Bruker AXS D8 Advance diffractometer, equipped with a LynxEye detector and capillary sample holder. The samples were prepared inside an argon filled glove box by grinding them to a fine powder in a mortar and putting powdered samples into capillary tubes. These have the advantage over conventional flat plate sample holders in that they can be sealed, preventing oxidation during transport and the analysis itself.

Scanning electron microscopy (SEM) and energy dispersive spectroscopy (EDS) analysis were also employed to analyze the particle morphology and composition of the resulting powders. The SEM used for this work was as Zeiss Supra 55 VP, using a backscatter electron detector, 10 kV acceleration potential, and a working distance of 14 mm. The preparation of samples for the SEM analysis proved to be a challenge due to their sensitivity to oxygen. There is presently no equipment available at NTNU that allows sensitive samples to be moved from an inert environment, e.g. a glove box, to a SEM without being exposed to air, and some oxidation therefore had to be tolerated. The samples were prepared in the glove box by putting a small amount of the powder on carbon tape on a flat plate sample holder. The sample holder was transported to the SEM in an air tight box that was sealed inside the glove box, trapping the argon atmosphere, and only opened when the SEM was ready for the sample to be mounted on the stage. The samples were exposed to air only from the box was opened to the vacuum was established.

4.1.3 Li-Si Composite Electrode Preparation

An evaluation of the quality of the alloys was made based on the results obtained from the XRD characterization. Sample 1 was determined to consist of a mixture of $Li_{12}Si_7$ and elemental silicon, sample 2 of mainly its target phase Li_7Si_3, and sample 3 of a mixture of $Li_{22}Si_5$ and $Li_{13}Si_4$. Sample 2 was deemed the most suitable for further use due to its superior phase purity. Again,

extraordinary measures had to be taken to prevent contamination. The major part of the preparation was therefore done in an argon filled MBraun Labmaster SP glove box. This glove box is equipped with an antechamber with heating capabilities, and had an impurity level of <5 ppm O_2 and <0.1 ppm H_2O. Some problems were encountered with finding a solvent that was stable in relation to lithiated silicon, while also being easy to remove by evaporation during drying and dissolve a known binder. While not a commonly used combination for electrode preparation, it was decided that DMF was the best of the available alternatives, with PAN as binder.

The initial step of composite electrode manufacturing involves the making of a slurry (cf. section 3). In addition to the Li_7Si_3 as active material and PAN as binder, Super C65 carbon black (CB) was chosen as conductive matrix, employing a mass ratio of 8:1:1 (Li_7Si_3:PAN:CB). The slurry was made by the process detailed in Appendix B. The finished slurry was then cast in titanium coins (marked F in Figure 15), which had been weighed accurately beforehand. Having a 13 mm in diameter and 1 mm deep indentation, the coins act both as current collector and mold. These were dried in the glove box for two hours to allow most of the solvent to evaporate before being put under vacuum at 100 °C in the heated antechamber and dried overnight. The finished electrodes were cooled to room temperature inside the glove box and then weighed before being mounted in cells. The total amount of electrode material could be calculated by taking the difference between the weight before and after casting and drying. From this and the recorded mass ratio of the constituents, the amount of active material could be accurately determined.

In addition to the Li_7Si_3-based electrodes, a reference electrode was made by the exact same procedure using pure silicon grain (Elkem 141) as starting material rather than Li_7Si_3. The main purpose of this reference was to rule out the effects of the unconventional binder/solvent combination.

4.2 Fabrication and Characterization of Porous Silicon

4.2.1 Silicon Wafers

As starting material for the porous silicon etching 4" mono-crystalline silicon wafers were used. One batch of wafers were primarily used; 275-325 µm thick double side polished wafers supplied by Siltronix that were n-doped by phosphine to a resistivity rating of 0.01-0.05 Ω*cm. In addition to the supplier-provided resistivity values, resistivity measurements of each wafer were conducted using a CMT SR-2000PV four point probe supplied by *Advanced Instrument Technology (AIT).* The orientation of the wafer was stated by the supplier to be [100] ± 0.5°. In addition to these wafers, p-doped material of unknown origin was obtained from Junjie Zhu at IFE's solar department. These wafers were [100] oriented, unpolished and had emitter doping on both sides.

4.2.2 Etching Process

The etching process was conducted in the Solar Cell Laboratory at IFE using a *MPSB Porous Silicon System* (PSB 100) supplied by *Advanced Micromachining Tools* (AMMT). This double tank etching cell (cf. section 2.3.2), which can be seen in Figure 13, was connected to a *Porous Silicon Power Supply* (PS2-12A), also from AMMT. The power supply has a working range from 0-36 volts and 0-12 amperes, and programmable with a resolution of 10 mV and 3 mA. Due to the hazards associated with using and handling HF, several safety measures were taken. While the cell has a built-in fume handling system, it was itself mounted inside a dedicated fume hood with an HF sensor mounted on the outside. All activity inside the fume hood was conducted using safety glasses, lab coat, clogs and nitrile rubber gloves and apron. When emptying and filling the etch bath, a full face mask was used as well. The laboratory was equipped with the proper first aid equipment necessary in case of accident, most importantly *HF-antidot gel®* and *Calciium-Sandoz®* effervescent tablets.

The etching bath was filled with a mixture of 48 wt% hydrofluoric acid (Sigma Aldrich) and absolute ethanol in a 1:5 volume ratio. Given the densities of the constituents as 1,15 g/cm^3 and 0,789 g/cm^3, respectively, this corresponds to a HF concentration of approximately ~11 wt%. Ethanol was used as it is known to reduce the formation of hydrogen bubbles on the porous surface, thus promoting a more homogenous etching. Two sample holders were available, both sized for 4" wafers, one which exposes the entire wafer to the electrolyte and another which exposes a 4 cm^2 circle eccentrically placed on the wafer, allowing for several etchings to be conducted on a single wafer. In all experiments conducted in this work, the latter was used in order to conserve material. The disassembled sample holder can be seen in Figure 12, together with two quarter wafers, one before and one after etching. Even though the sample holder

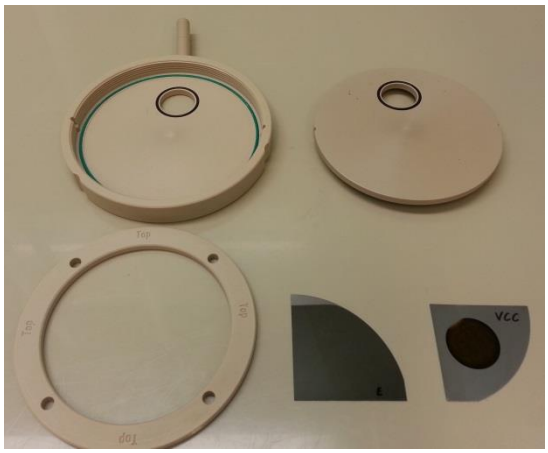

Figure 12: Disassembled sample holder for HF etching, including two quarter wafers, one non-etched (left) and one etched (right).

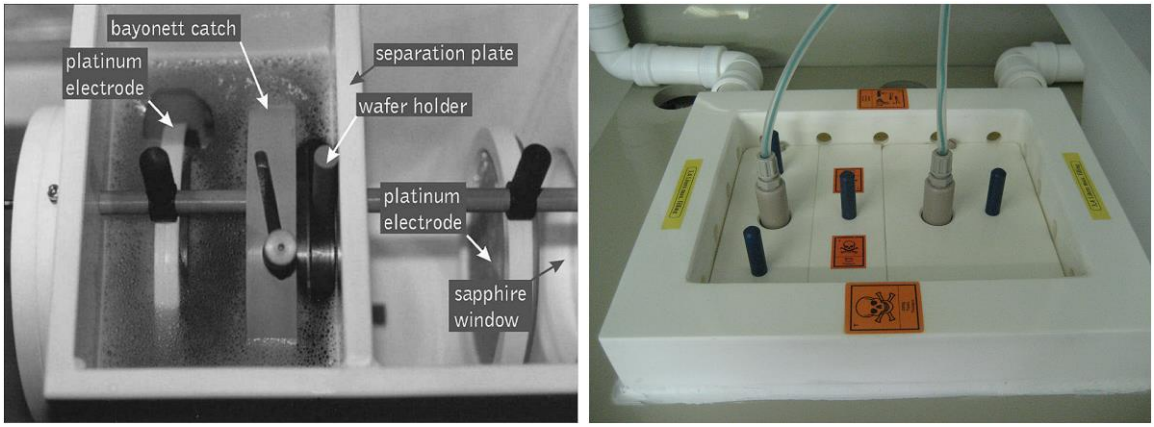

Figure 13: The etching cell. Left: the wafer is in place, dividing the two chambers so that the current has to pass through the wafer. Right: Etching cell with the lids on. (Courtesy of Josefine Selj)

could accommodate the entire wafer, it was decided that the wafers should be parted in four to limit the damage in the case of a leak. The etching itself was conducted without illumination by the procedure detailed in Appendix B. As is the case when working with fine pores and liquids, capillary forces are expected to arise during drying. For this reason, ethanol was used as for the last cleaning before drying the sample, as it has approximately one third of the surface tension of water.

In addition to several calibration and test runs, a total of 16 successful etching sessions for sample production were conducted at different current densities and etching times. The samples were generally made from the n-type wafers described in section 4.2.1. For comparison, two additional samples were made using the emitter doped p-type wafers. The parameter space is shown in Table 6, with the samples named by the following convention; *"doping type"_"current density"_"etching time"*. Due to the limited running time of this project, the parameter space was not fully explored. However, effort was made to span the space in a manner that produces the widest range of structures, while leaving as few holes as possible.

As a result of the different volatilities of ethanol, HF and water, the concentration of HF changes as the electrolyte ages. The samples were therefore made in two series; the first consisting of the 30 and 60 minute samples (blue in the table); the second of the 120 and 240 minute samples (red in the table). The latter was mainly focused at current densities of 9 and 12 mA/cm^2 after an evaluation of SEM images of the first series. To keep the concentration reasonably steady, each of the series was conducted in as short calendar time as possible and the cell was filled with new electrolyte before the start of both.

Table 6: Parameter space for porous silicon etching. The first series is written in blue and the second in red.

		Current density [mA/cm^2]				
		4	**6**	**9**	**12**	**24**
Etching time [min]	30	N_04_30	N_06_30	N_09_30	N_12_30	N_MAX_30
	60	N_04_60	N_06_60	N_09_60	N_12_60	
	120			N_09_120 P_09_120	N_12_120	
	240		N_06_240	N_09_240 P_09_240	N_12_240	

4.2.3 SEM Characterization

SEM characterization of the etched samples was conducted to determine if porous silicon was formed, and if so; which of the multitude of possible structures was obtained and how it depended on the etching parameters. The samples were transported from IFE to NTNU by plane in suitable wafer cases, and they suffered no visible damage underway. The analysis was performed in the EM-lab at the Institute for Materials Technology using a Hitachi SU-6600. All images were taken using a secondary electron detector, an acceleration voltage of 10 kV and a nominal working distance of approximately 10mm.

In the first sample series, images were taken of the surface structure of all samples, while cross section images were taken of those etched at 4 mA/cm^2 and 12 mA/cm^2. For the second series, both surface and cross sectional images were taken of all samples. To fully view the complex structures, images were taken at several magnifications. With some deviations depending on the structures observed, the surfaces were usually imaged at x150, x500, x1k, x2k, x10k, x20k and x50k, and cross sections at x500, x1k, x2k[1], x5k, x10k, x20k and x50k[2]. The cross sections were made by initiating a fracture aimed so that it divides the wafers through the center of the etched area. The fracture was made to travel along the <110> directions hence forming a cross sections with (110) orientation.

In addition to the SEM analysis performed at NTNU, two samples, N_09_60 and N_12_60, were sent for further analysis to Dr. Fermin Cuevas, Dr. Michel Latroche and Dr. Stéphane Bastide; a group working out of *East Paris Institute of Chemistry and Material Science* (ICMPE) who are in collaboration with IFE. While details of the equipment and conditions are not available, the acceleration voltage and working distance used for this analysis was 3 kV and approximately 3.0 cm, respectively.

[1] Only for the first series of samples
[2] Only for the second series of samples

4.3 Porous Silicon Electrode Preparation

4.3.1 Cutting of Porous Silicon Samples

For electrochemical testing of porous silicon, the optimal case would be to have free-standing material, rather than wafer bound material, as the effects of the underlying wafer could be difficult to distinguish from that of the porous material. However, the thickness of the formed porous layer rendered it virtually impossible to collect sufficient amounts to make pure porous electrodes. The best alternative was determined to be to cut out sections of the etched part of the wafer to be used as electrodes directly. While mono-crystalline wafers are extremely fragile and easily cut along the crystal directions by hand, it was crucial that the area of the sample were known if accurate measurements of the capacity were to be made. This was achieved by using a PowerLine E 20 laser cutter supplied by *Rofin Sinar Laser*, which is programmable with a resolution of 1µm. Four square pieces of 5x5mm^2 were cut from each etched sample, as well as from a non-etched n-type wafer of the same stock as was etched to be used as reference.

4.3.2 Determination of Mass of Porous Material

To be able to make accurate measurements of the materials electrochemical properties, it is necessary to know the amount of porous material. As this cannot be measured directly due to the relatively large amount of solid base material, other methods had to be used. Attempts to do this nondestructively by a combined analysis of sample weight and SEM images failed due to insufficient accuracy. A destructive approach was then deemed necessary. The method used is based on weighing the sample before and after selective etching of the porous layer using 2 wt% potassium hydroxide (KOH) aqueous solution, and from that determining the porous layer mass. While KOH is known as an effective silicon etchant, it was assumed that at the dilution and temperature used the effect on the bulk silicon wafer would be negligible compared to the high specific surface area porous structures. Through a rough calculation using the formula provided by Rai-Choudhury (1997) for 2wt% KOH at 30 °C, the maximum etch rate was determined to be approximately 4 nm/minute. While only an approximation, this result provides an indication of the low etch rate at these conditions. This hypothesis was readily confirmed by trial on a non-porous reference sample.

One of the four laser-cut pieces from each sample was used for the mass measurements. As the method is destructive, there is no guarantee that the mass of porous material is identical on all four samples. However, from the high accuracy of the cutting process and assumed homogeneity of the etching, this was deemed sufficient. The 2 wt% KOH solution was prepared on site by mixing the appropriate amounts of solid KOH (Sigma Aldrich) and deionized water. For the weight measurements, a Sartorius BT 125D scales was used, which has an accuracy of 0.01 mg in the range used. The detailed procedure was as follows; the sample was weighed dry, then put in the KOH bath and left there for several minutes, until no reaction was observed and the surface appeared polished, after which it was transferred to deionized water to halt the etching process. The sample was then dried at 50 °C for 15 minutes before being weighed once more. This was conducted for all samples etched at 9 and 12 mA/cm^2.

4.3.3 Carbon Coating

Carbon has been determined to be an important addition to most silicon anodes, both as a coating and as a conductive matrix for composite electrodes. To examine the effects of carbon coating on the porous structures, some of the samples were carbon coated using a PAN-based method adapted from the one used by Thakur et al. (2012c) at Rice University (cf. section 3). Precursor solution was prepared by mixing PAN (Sigma Aldrich, M_w = 150,000) and dimethylformamide (DMF, Sigma Aldrich, anhydrous, 99.8%) in a weight ratio of 1:80. The solution was mixed and stored under argon atmosphere. The samples designated for carbon coating was separately submerged in this solution and left there for several days to ensure that the solution had fully penetrated into the pores. Before pyrolization, the samples were removed from the solution and excess solution was removed using a lint free cloth. The samples were then dried under argon flow at room temperature for 2 hours.

The pyrolization was conducted using a Brother Furnace XD-1600MT vacuum tube furnace with gas flow capabilities. The samples were initially heated under argon flow to 250 °C at a ramp rate of 10 °C/min and held at that temperature for 60 minutes. The purpose of this step was to melt the PAN before pyrolization to achieve an homogenous carbon coating. For pyrolization, the temperature was raised to 700 °C at the same ramp rate and held there for two hours before cooling to room temperature at a controlled cooling rate of 10 °C/min, still under argon flow (nearing room temperature, it is assumed that the cooling rate is smaller). The treatment program can be seen in can be seen in Figure 14.

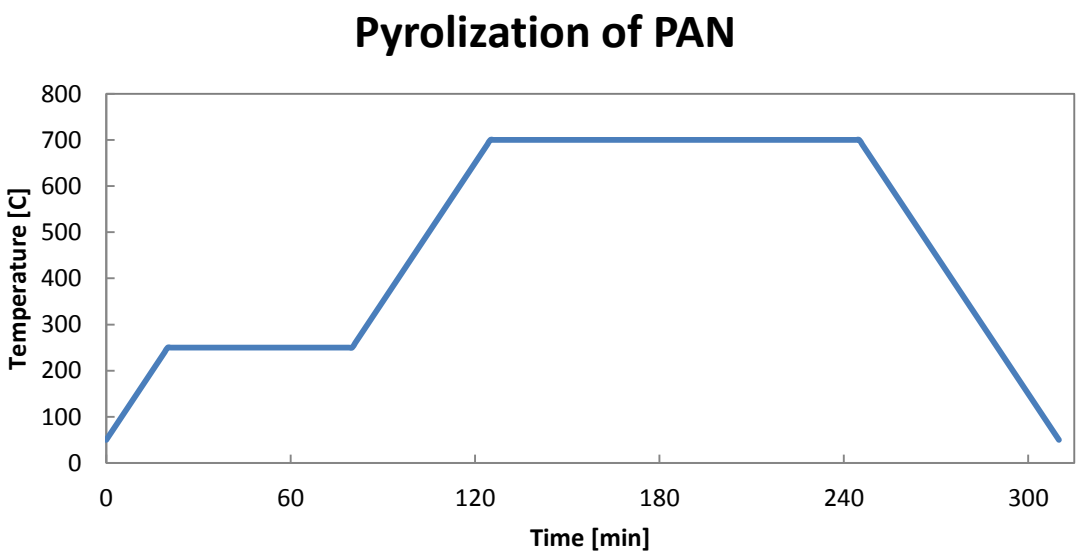

Figure 14: PAN Pyrolization program

4.4 Electrochemical Testing

Electrochemical testing was performed on a selection of the electrodes using an Arbin BT-2000 battery tester. Due to the time intensive nature of such testing and limited number of simultaneous tests, it was not possible to test all the porous structures made in the first phase of this work. A total of 10 electrodes were tested, including the composite electrodes and references, of which three are composite electrodes and seven are wafer-based. This section contains a description of the cells used for the testing and a detailed overview of the testing parameters used for the different electrodes.

4.4.1 Cell Design and Assembly

The cells used for the electrochemical testing are custom made. Figure 15 shows an image of the disassembled cell and a sketch showing a cross section of an assembled cell with the corresponding components marked by letters. When the cell is properly assembled, components A) and D) form a sealed compartment with the plastic ring (H) constituting the washer. Inside this compartment, the electrochemically active parts of the cell is contained in a plastic cylinder (E). In normal operation, the test electrode is in the titanium coin (F) and lithium foil attached to the bottom side of the titanium current collector (G) act as counter electrode. To obtain a controllable reaction, a separator is put between the electrodes together with the electrolyte. The spring and ball mechanism (I) ensures that the electrodes are pressed together with a suitable force, as well as connecting the counter-electrode to the shell of the cell. Regardless if an anode or cathode material is tested, the use of a lithium counter-electrode makes the test electrode always act as a cathode. Hence the shell of the cell is always the negative pole while the tip of the cylinder (C) is the positive pole.

In this work, there are two types of electrodes; composite and wafer-based. The composite electrodes are prepared directly in the titanium coin (cf. section 4.1.3). Despite their differences, the cell assembly process is more or less the same. To prevent the deterioration of the lithium counter electrode, the assembly was done inside the glove box. First a counter-electrode was

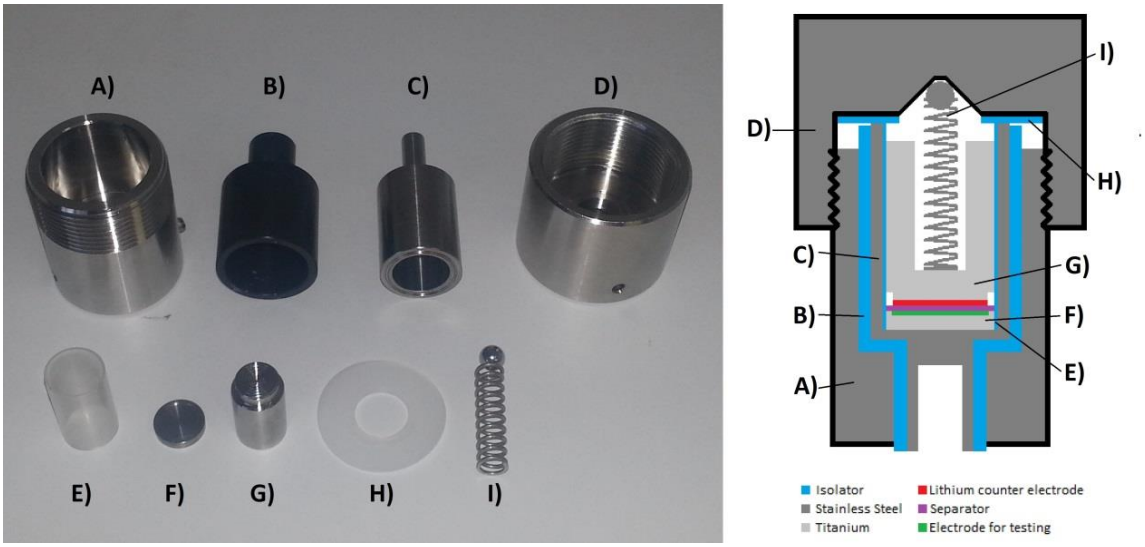

Figure 15: (Left) Picture of disassembled test cell showing the components and (right) a sketch of the assembled cell. The letters mark the corresponding components in the picture and the sketch.

prepared by stamping out a 13 mm lithium disk from 0.38 mm thick lithium ribbon (Sigma Aldrich, 99.9% trace metal basis) and attached to the counter electrode current collector (G). The base of the cell was then assembled, consisting of parts A, B and C. The core of the cell was assembled by lowering the plastic cylinder (E) with the electrode-containing titanium coin (F) into the cell. Then inserting a 15 mm diameter Celgard® 2400 separator and adding 0.2 ml 1M $LiPF_6$ EC:DMC 1:1 (BASF) electrolyte using a syringe. After making sure the electrode was centered and completely covered by the separator, the counter-electrode (G) was lowered into the plastic cylinder. Finally, the spring and ball (I) was put into the hole in the current collector and the washer (H) centered on top of the cell before the top part of the container attached and hand tightened.

After cycling, the cells were first disassembled in a glove box, where the electrode could be removed for post-cycling analysis. As the cells are made for multiple uses, the components were removed from the glove box and thoroughly cleaned after each test. The individual components were washed using water and dishwashing liquid. After drying by hand they were then rinsed in ethanol before being wiped off and dried at 60 °C for at least two hours before being assembled with a new electrode.

4.4.2 Testing Methods and Parameters

Electrochemical testing is a wide term which can entail a variety of tests yielding different results depending on test parameters and conditions. While enabling different properties of the material to be established, it also makes the proper choice of parameters essential to obtain the desired information. The tests performed in this work involved a series of charge/discharge cycles to determine the capacity and cycle stability of the electrodes. The lithiation step is denoted the charge step and, consequently, the delithiation step is denoted the discharge step. This is by the convention explained in section 2.1.2, even though lithium spontaneously travels from the lithium metal counter electrode and into the test electrode, this would not be the case when coupled with a cathode material. During cycling voltage and current were closely monitored, regulated and recorded for later analysis. In addition, dedicated open circuit voltage (OCV) and internal resistance (IR) measurements were made and recorded at rest between cycles. This section will give an account of the samples chosen for testing, the tests that were conducted for each sample and their purpose, as well as which parameters were used.

4.4.2.1 Porous silicon cells

Based on analysis of the SEM structures, samples N_12_120 and P_09_120 were selected for electrochemical testing, in addition to one of the non-porous n-type reference samples that were made (cf. section 4.3.1). These samples were chosen due to their clearly defined structures and very different morphology, the assumption being that these would give the best defined results. All the wafer based electrodes that were tested are presented in Table 7. Six of the samples, two electrodes from each of the samples, one with and one without carbon coating, were tested using the same program and parameters in order to be able to compare the results. The detailed program can be found in Appendix B.

In short this program entails that the electrodes were run at a rate of C/20 for three cycles and then at C/10 until it was stopped or failed, with OCV and IR measurements taken between each charge and discharge step. Due to kinetic effects in the cell, voltage profiles from slow cycles often show details that fast cycles do not, hence, three initial slow cycles were made to better describe what happens in the cell during this important initialization phase; surface oxide removal, SEI formation etc. It also serves to demonstrate how the cell performs at different current rates. The cycling was conducted with a charge limitation of 3000 mAh/g (with a 50 mV cut-off as redundancy) based on the mass of porous material determined by the process described in section 4.3.2, not including the mass of the underlying wafer. While the bulk silicon of the wafer is in fact active material, it was reasoned that using a capacity-limitation would limit the cycling to the porous layer due to its large surface area and slow diffusion kinetics of lithium in silicon. The reference electrode, while not having a porous layer, was cycled as if it had the same assumed active mass as the electrodes made from N_12_120. This was done to determine the difference between cycling a porous layer and solid layer of the same mass.

An additional non-coated electrode from sample N_12_120 was run for a single cycle at C/20. The purpose for this electrode was post-cycle analysis in SEM to determine the structural changes in the porous layer during the initial cycle. An electrode from N_12_120 was chosen due to the more clearly defined pore structure of this sample compared to that of P_09_120, and thus best possibility of observing a structural change.

Table 7: An overview showing the wafer based electrodes that have been electrochemically tested, As well as whether the sample was coated or not and the cycle program each sample was run at (n being an unlimited number of cycles)

Electrode	Source Sample ID	Coating	Cycle program
N-SEM	N_12_120	None	1 x C/20
N-type	N_12_120	None	3 x C/20 + n x C/10
N-type with PPAN	N_12_120	PPAN	3 x C/20 + n x C/10
P-type	P_09_120	None	3 x C/20 + n x C/10
P-type with PPAN	P_09_120	PPAN	3 x C/20 + n x C/10
Reference	N_ref	None	3 x C/20 + n x C/10
Reference with PPAN	N_ref	PPAN	3 x C/20 + n x C/10

4.4.2.2 Li-Si composite cells

Three composite electrodes were made and tested; two electrodes using Li_7Si_3 as base material and one reference electrode using pure silicon. The main purpose of these electrodes was to demonstrate the difference between prelithiated electrode and a silicon electrode. It was determined that the best way to do this was to first delithiate the electrodes, and then run a cycling program with a charge capacity limitation of 2200 mAh/g. This charge limitation was chosen based on the primed capacity of the prelithiated electrodes, calculated as being 2226 mAh/g (Appendix A), thus cycling the electrode between complete delithiation and the primed capacity. The program, which can be seen detailed in Appendix B, consisted of three cycles run at C/20 and 50 cycles at C/10, all with a charge capacity limitation of 2200 mAh/g and voltage cut-off at 50 mV and 1 V for charge and discharge, respectively. The reference sample was tested using the exact same program. Being already delithiated, the initial delithiation was skipped as the start OCV was over 1 V and the cut-off criterion thus immediately fulfilled.

However, during testing it was rather surprisingly discovered that the lithium was not readily removed from or inserted into the prelithiated electrodes, and the voltage cut-offs was engaged virtually immediately for both the charge and discharge cycles. To examine this further, one of the prelithiated electrodes was moved to a program where it was tested with a discharge cut-off at 2 V and extremely low current rates at C/200 and C/100 for the slow and fast cycles, respectively. Before the program change, the electrode ran for the initial delithiation and the following five cycles, however, as the reaction was so limited, it was assumed that the effect of these cycles would be negligible. An overview of the composite electrodes can be seen in Table 8.

Table 8: An overview showing the composite electrodes that have been electrochemically tested, as well as the cycle programs and cut off voltages used for each.

Electrode	Base material	Cycle program (After initial delithiation)	Charge voltage cut-off	Discharge voltage cut-off
Li7Si3 C/200	Li_7Si_3	(2 x C/20 + 3 x C/10) 3 x C/200 + 50 x C/100	0.05 V	2 V
Li7Si3 C/20	Li_7Si_3	3 x C/20 + 50 x C/10	0.05 V	1 V
Reference C/20	Si	3 x C/20 + 50 x C/10	0.05 V	1 V

4.5 Post-Cycling Characterization

In preparation of the post-cycling characterization, the sample was carefully removed from the cell as described in section 4.4.1. As the delithiation generally is incomplete at the cut-off voltage of 5 mV, the electrode was still very reactive and had to be handled accordingly. All handling was therefore done inside the glove box, and drying was done at 50 °C overnight using the heated antechamber. The characterization was in a large part conducted using the SEM-instrument at NTNU which was used to do the initial characterization of the porous structures. The electrode was therefore carefully packed in a sealed sample glass, fastened as not to be harmed during transport. To make comparison as accurate as possible, images were taken at the same magnifications as for the pre-cycling characterization, using as close to same conditions as was feasible.

In addition, the sample surface was analyzed using the energy dispersive spectroscopy (EDS) detector on the SEM. While this detector is not able to detect atoms as light as lithium, it was useful in order to analyze the SEI formation, which in addition to the silicon and lithium is assumed to consist of mainly fluorine, phosphorous and carbon.

5 Results

5.1 Characterization of Lithium-Silicon Alloys

The spectra obtained from the XRD analysis can be seen in Figure 17 and complete interpreted spectra with reference peaks in appendices D, E and F. These show that sample 1, rather than forming LiSi, consisted mainly of $Li_{12}Si_7$ and elemental silicon. This is in agreement with current theory, in which the formation of LiSi has only been reported at high pressures due to its negative volume of formation (Stearns et al., 2003). Sample 3 consisted partly of the target phase, $Li_{13}Si_4$, but also of $Li_{22}Si_5$ and elemental silicon. This indicates that some of the silicon did not dissolve, thus forming a melt richer in lithium that solidifies as the two former phases. The figure also shows a magnified section of the diffractogram for sample 2, in which peaks of $Li_{13}Si_4$, elemental silicon and lithium can be distinguished. However, the intensities are sufficiently low for sample 2 to be regarded as consisting mainly of the target phase, Li_7Si_3.

SEM images were taken of all three alloys at different magnifications, examples of which can be seen in Figure 16. It is observed that the roughness of the particles increase with lithium content. This is consistent silicon rich samples forming smooth facets due to its brittleness. While the samples consist of particles of relatively dissimilar morphology, all of them show particles of wide size distributions. A particulate morphology is inconsistent with what might be expected from a solidified mass. And while it may be caused by the volume expansion silicon undergoes when solidifying, it can also indicate an alternative process mechanism altogether. The results from the EDS was not able to shed any light on this, as it could not detect atoms as light as lithium, and thus proved to be less than reliable. The degree of oxidation could give an indication of the lithium content, but no tangible results. Regardless, the XRD spectrum confirmed the formation of the predicted phases, and the morphology of the particles is of secondary importance, prompting continuation with electrochemical tests. As stated above, sample 2 was determined to have the purest phase composition, and was therefore used as the source material for the later electrochemical experiments for the sake of reproducibility.

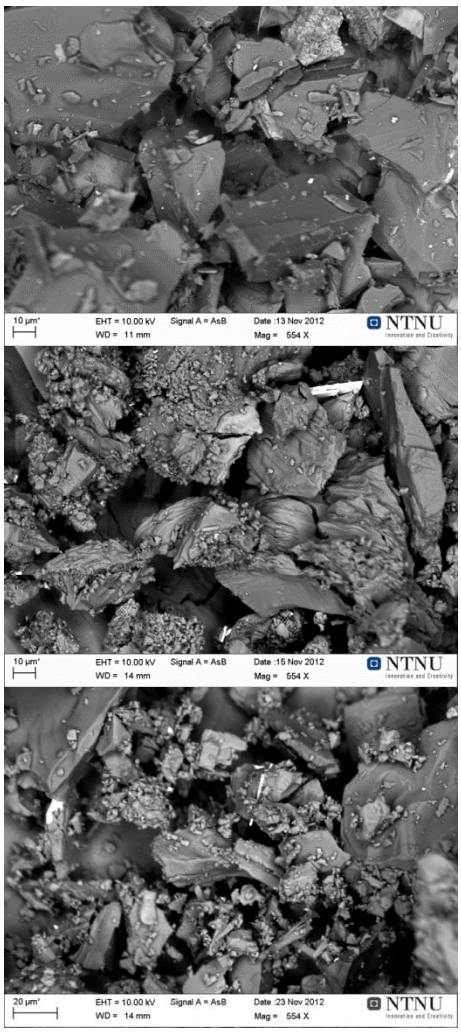

Figure 16: SEM micrographs of sample 1 (top), 2 (middle) and 3 (bottom) at 554x magnification.

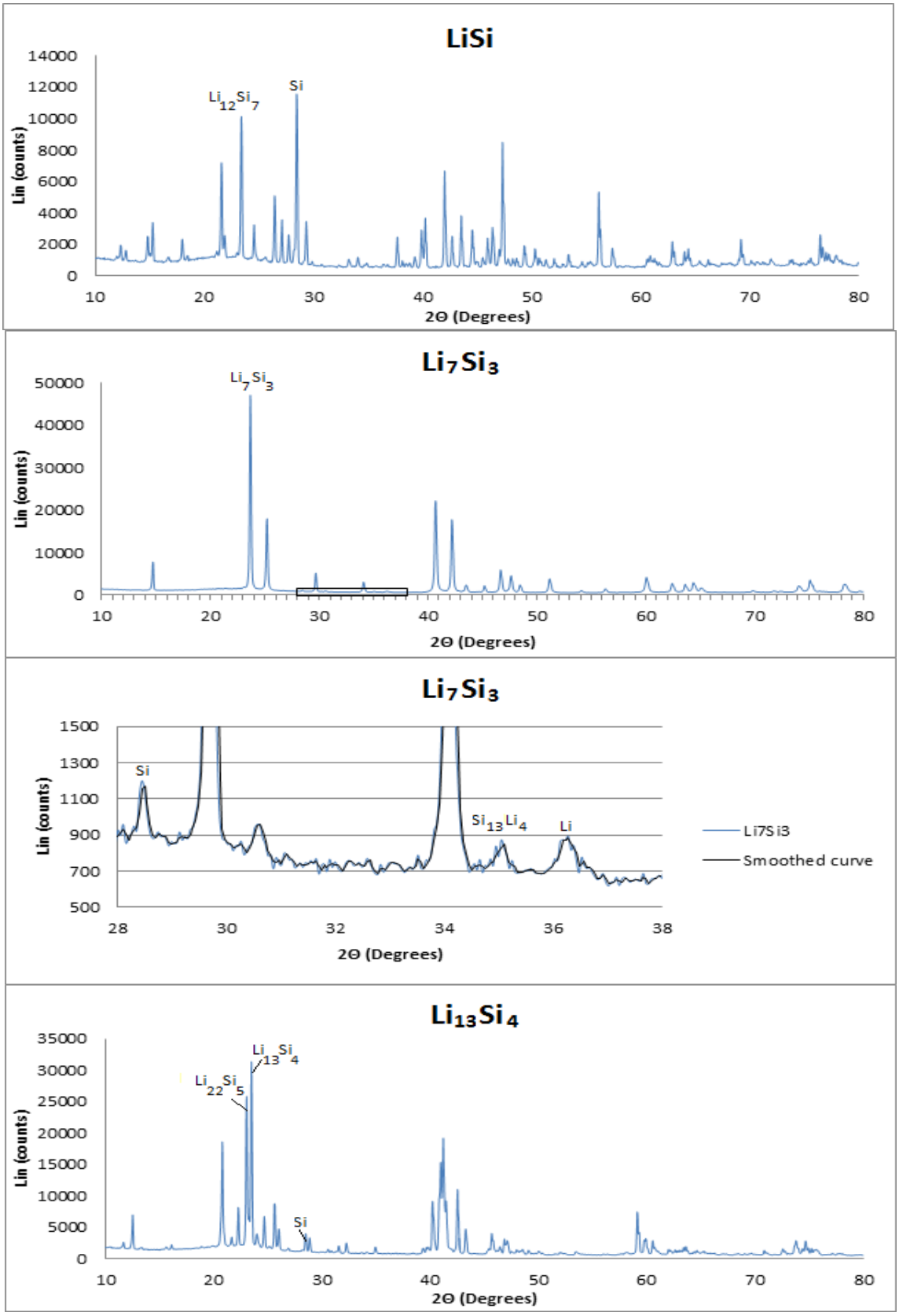

Figure 17: X-ray diffractograms for the samples marked by their target phase, with the top peak of each major constituent phase marked. For samples 2 (Li_7Si_3) both a full and magnified spectrum is shown, the black square in the full spectrum showing the position of the magnified section.

5.2 Porous Silicon

5.2.1 Resistivity Measurements

Five individual measurements were taken at random spots on the wafer and an average was then calculated. These results can be seen in Table 9, in addition to an overview of the samples that were made from each wafer. The resistivity of the p-type wafers can be seen to be approximately 50 times that of the n-type wafers. However, due to the higher mobility of electrons than holes, this corresponds to similar doping levels; approximately $1x10^{18}$ and $6x10^{18}$ for the n and p-type wafers, respectively.

Table 9: Resistivity measurements

Wafer ID	N1	N2	N3	N4	N5	P1	P2
Used for samples	N_04_30 N_07_30 N_09_30 N_12_30	N_04_60 N_07_60 N_09_60 N_12_60	N_12_240 N_MAX_30	N_09_240 N_12_120 N_07_240	N_09_120	P_09_120	P_09_240
R1 [mΩ*cm]	7,99	7,27	8,24	7,85	8,36	374,00	374,00
R2 [mΩ*cm]	7,80	7,29	8,07	7,86	8,29	375,00	377,00
R3 [mΩ*cm]	7,97	7,57	8,30	7,88	8,29	372,00	386,00
R4 [mΩ*cm]	7,78	7,58	8,42	8,04	8,47	374,00	386,00
R5 [mΩ*cm]	7,93	7,63	8,19	7,93	8,53	387,00	384,00
R avg [mΩ*cm]	7,89	7,47	8,24	7,91	8,39	376,40	381,40

5.2.2 SEM Characterization

During the course of this study, several hundred SEM images have been taken, all of which cannot be displayed in this section. Instead, the general trends seen in the pictures will be described using suitable examples. However, a complete collection of the images can be found in Appendix G and Appendix H, showing the surface structures and cross sections, respectively. In these, images of each sample at different magnifications are displayed together. This is done to give a better visualization of the complex structures that emerges at different magnifications.

5.2.2.1 Surface structure of n-type silicon samples

The surface structure of the n-type samples was seen to be dependent on both etching time and etching current density, creating a range of different structures. However, there are some common traits that are shared by all of these. Figure 18 shows the surface structure of the samples etched at 9 and 12 mA/cm^2 for 30, 60, 120 and 240 minutes at x500 magnification. As can be seen from these images, all the samples have a cracked structure with formations with a characteristic size of tens of microns. It is also observed that the morphology of this structure is very different depending on the duration of the etching, while being very similar for the samples etched for the same duration, showing virtually no variation with changing current density.

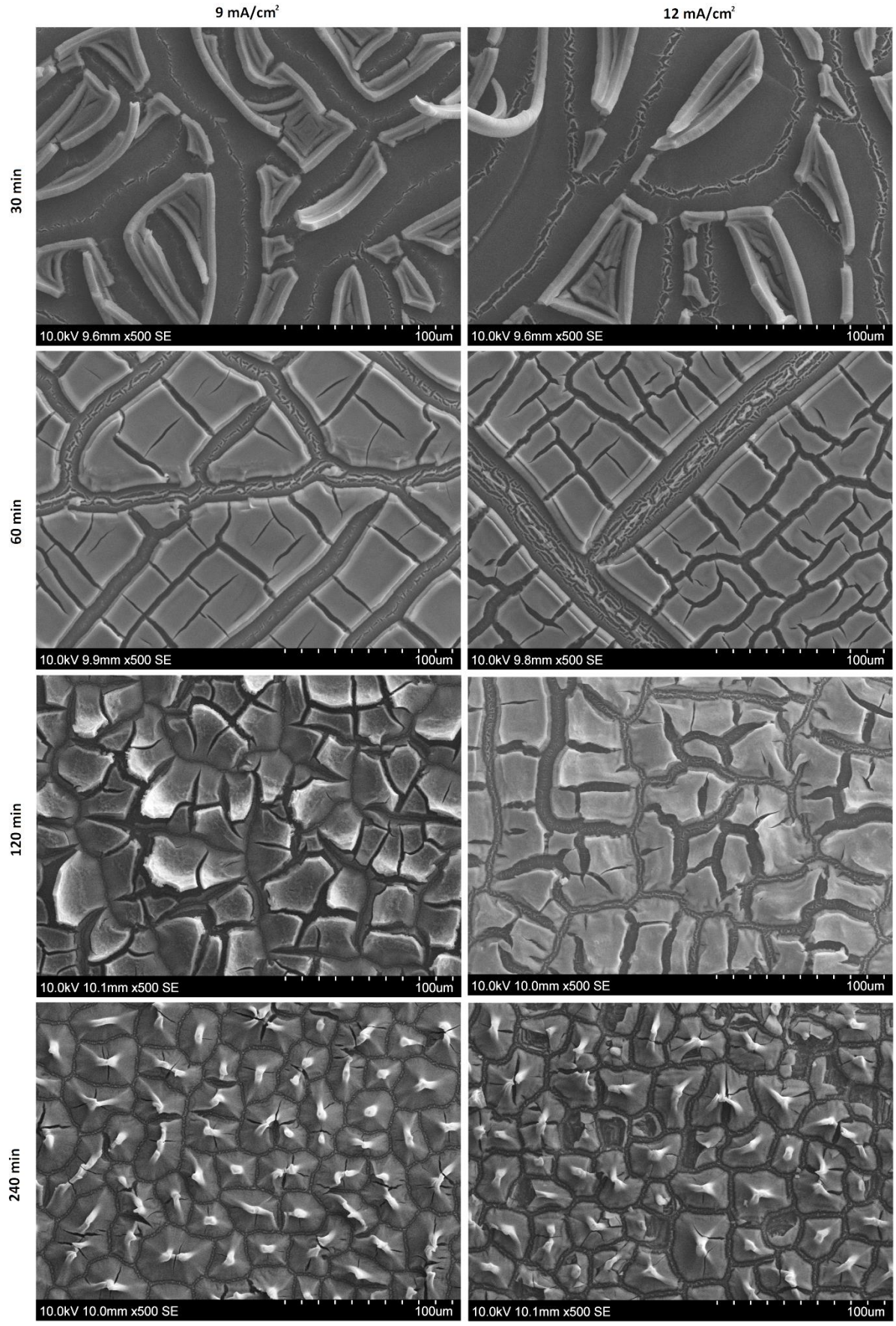

Figure 18: SEM images of the surface structure of the n-type samples etched at 9 and 12 mA/cm^2 taken at x500 magnification

On the surface of the samples etched for 30 minutes at all current densities and those etched for 60 minutes at 4 and 6 mA/cm^2, several peculiar structures were observed, most notably a number of “curls”, seemingly peeled off the surface. Two examples of this is shown in Figure 20, the left image showing how the top layer peel off the sample to form wide cracks and the right showing a fully formed “curl”.

When increasing the magnification, a second structure is revealed in the bottom of the cracks themselves. This is seen for the samples etched for 30 minutes in Figure 19 and in Figure 22 for the same samples as Figure 18. The images show that the structure consists of a large number of holes, which, while it cannot be concluded from these images alone, seems to form porous material. It is observed that the size of the holes increase with both etching time and current density, but the latter seems to have the largest influence. Regardless of the etching parameters, this distinct two-level structure is observed on all samples. N_MAX_30, which was etched at the maximum current density that could be achieved with the power supply that was used, had a slightly anomalous structure in this regard. The structure, which is shown at different magnifications in Figure 21, also had the multi-level structure. However, the lower level was not a continuous porous material, but a seemingly random structure of larger micrometer-sized pores, which itself was microporous. This structure is also observed to a lesser degree in the other samples (see Figure 22), the amount varying with a clear dependence on current density.

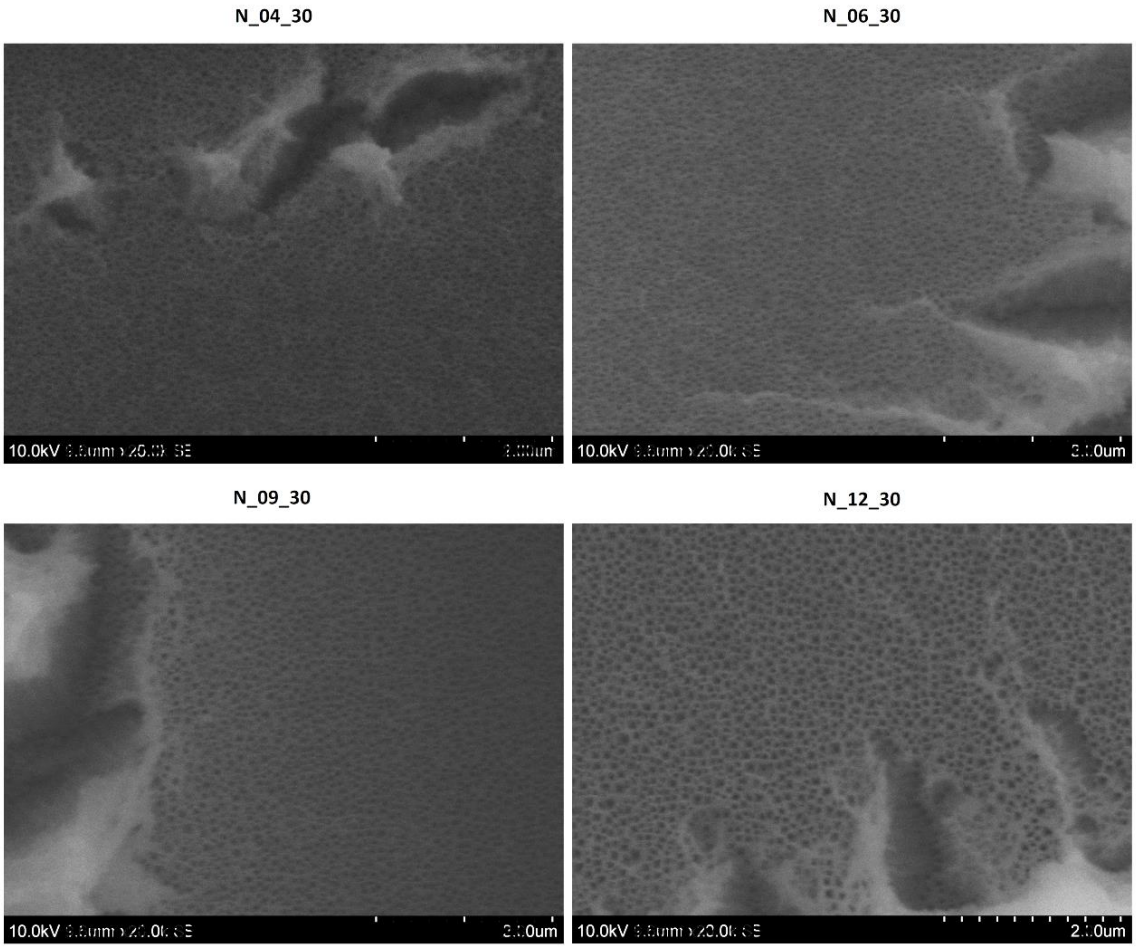

Figure 19: SEM images of the surface structure of the n-type samples etched for 30 min, taken at x20k magnification

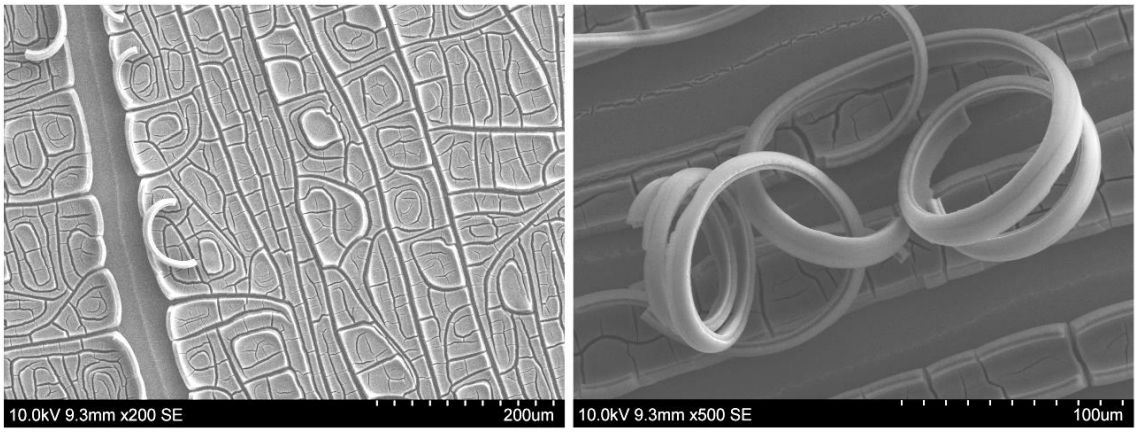

Figure 20: SEM images of the surface of N_04_60, showing the peel phenomenon (left) and a fully formed "curl" (right).

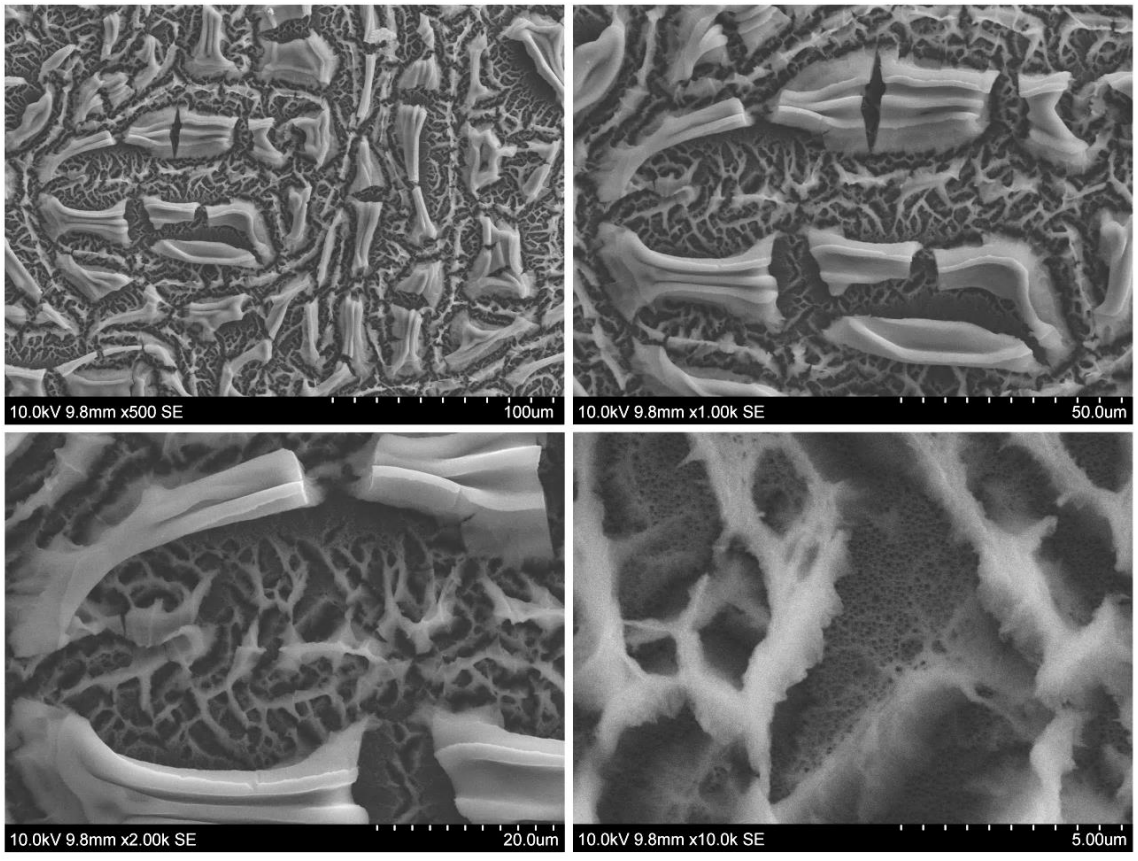

Figure 21: SEM images showing the surface structure of N_MAX_30, taken at x500, x1k, x2k and x10k magnifications

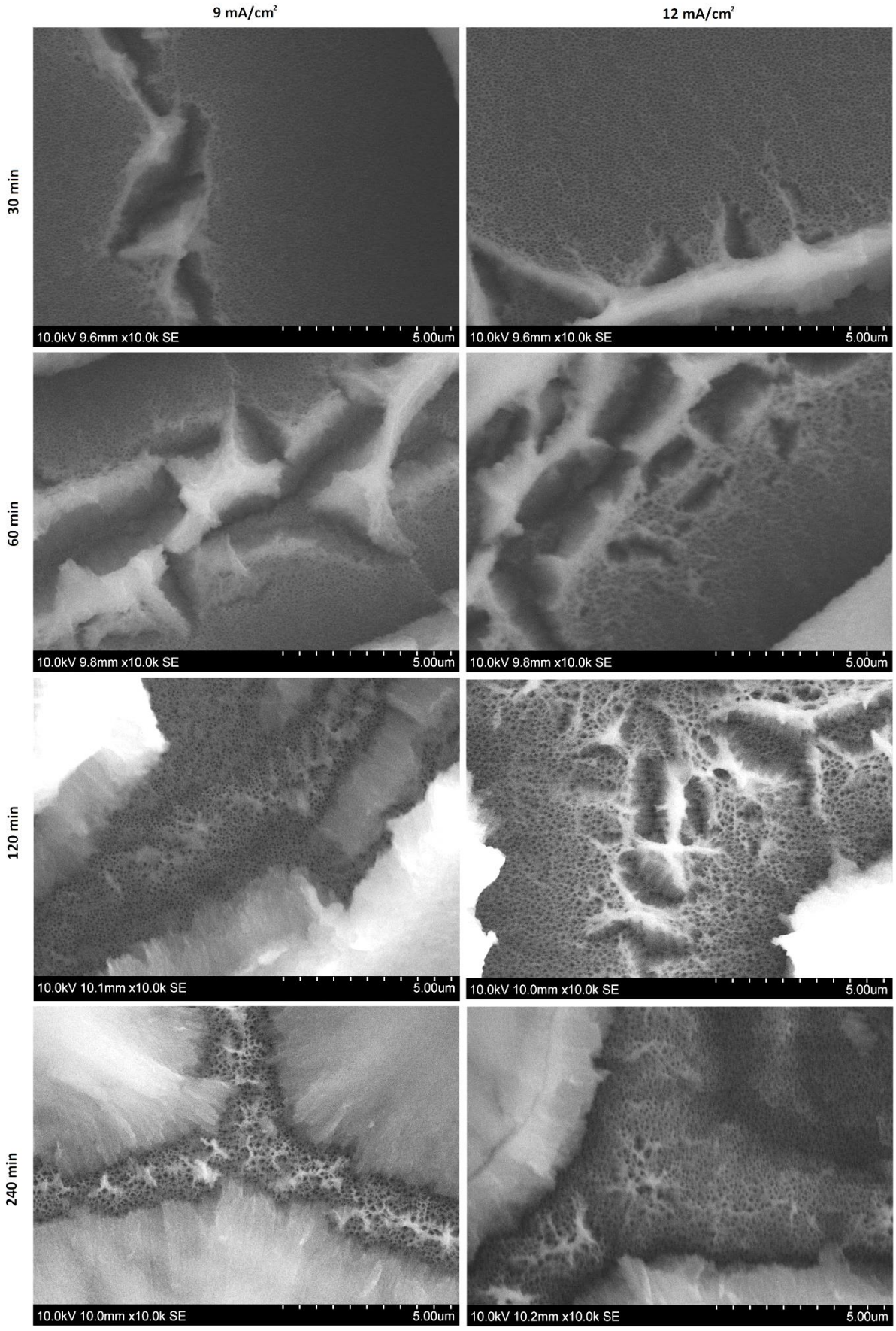

Figure 22: SEM images of the surface structure of the n-type samples etched at 9 and 12 mA/cm2 taken at x10k magnification

5.2.2.2 *Cross sections of n-type silicon samples*

The cross section images of the n-type samples confirm the observations made of the surface structures. Figure 23 shows images taken at x1000 magnification of the cross sections of n-type samples etched at 4 and 12 mA/cm^2 for 30 and 60 minutes. From these images it is evident that the "curl" effect is far less extensive on the sample etched at 12 mA/cm^2 for 60 minutes than the three others. The images also give a better view of the two-level structure that was seen from above. This is further seen in Figure 24, which shows the cross sections of the four samples etched at 12 mA/cm^2 imaged at x5k. At this magnification it is also possible to discern the structure of pores that were viewed as holes from above. It is now seen that the pores are oriented perpendicular to the surface and penetrate to a depth on the order of 10 µm, with little dependence seen on the etching time or current density. In the same figure images of the samples taken at x20k magnification are seen as well, now clearly showing the vertical pore structure. The pore size dependency on current density and etching time observed in the surface images should now be visible, but due to the rough pore walls, a quantitative measurement cannot be reliably performed. At the highest magnification that yielded clear images on the instrument used, it is revealed that the pore walls are not only rough, but show clear branching. This is shown for the samples etched at 9 and 12 mA/cm^2 for 120 and 240 minutes in Figure 25.

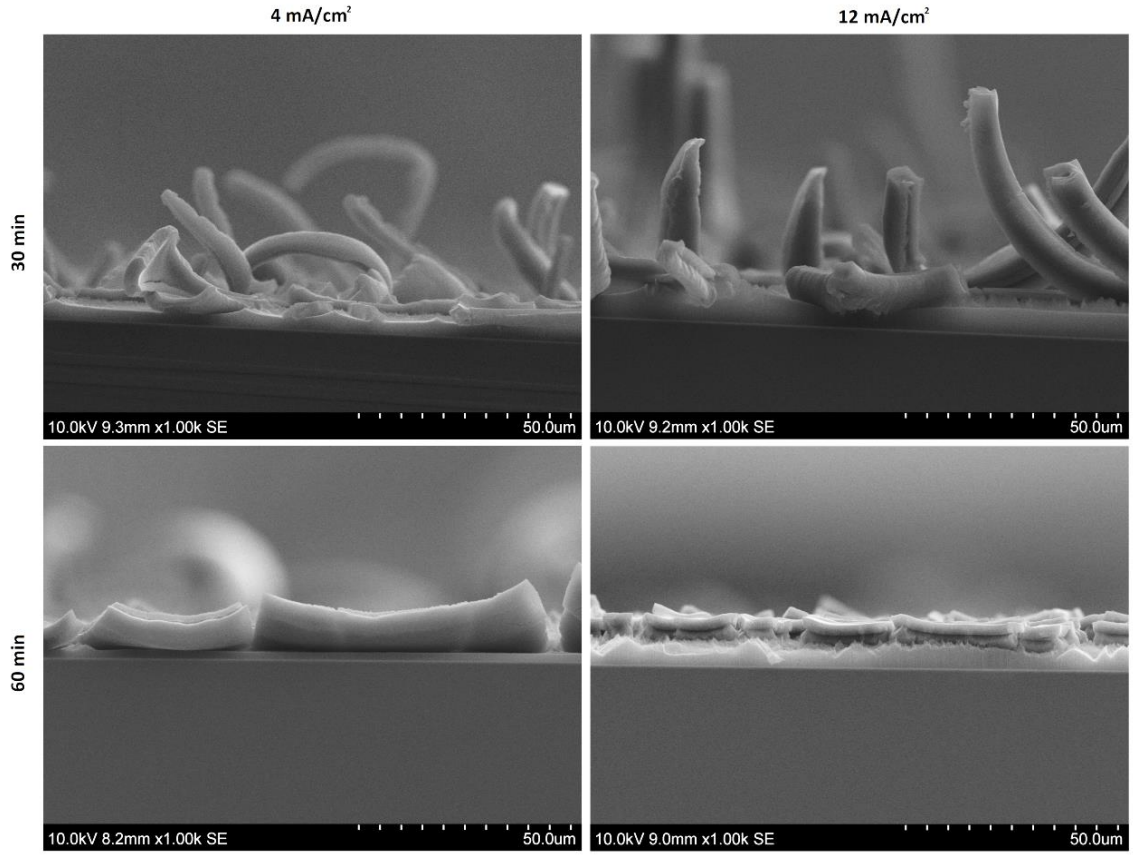

Figure 23: SEM images of the cross sections of the n-type samples etched at 4 and 12 mA/cm2 for 30 and 60 minutes taken at x1k magnification

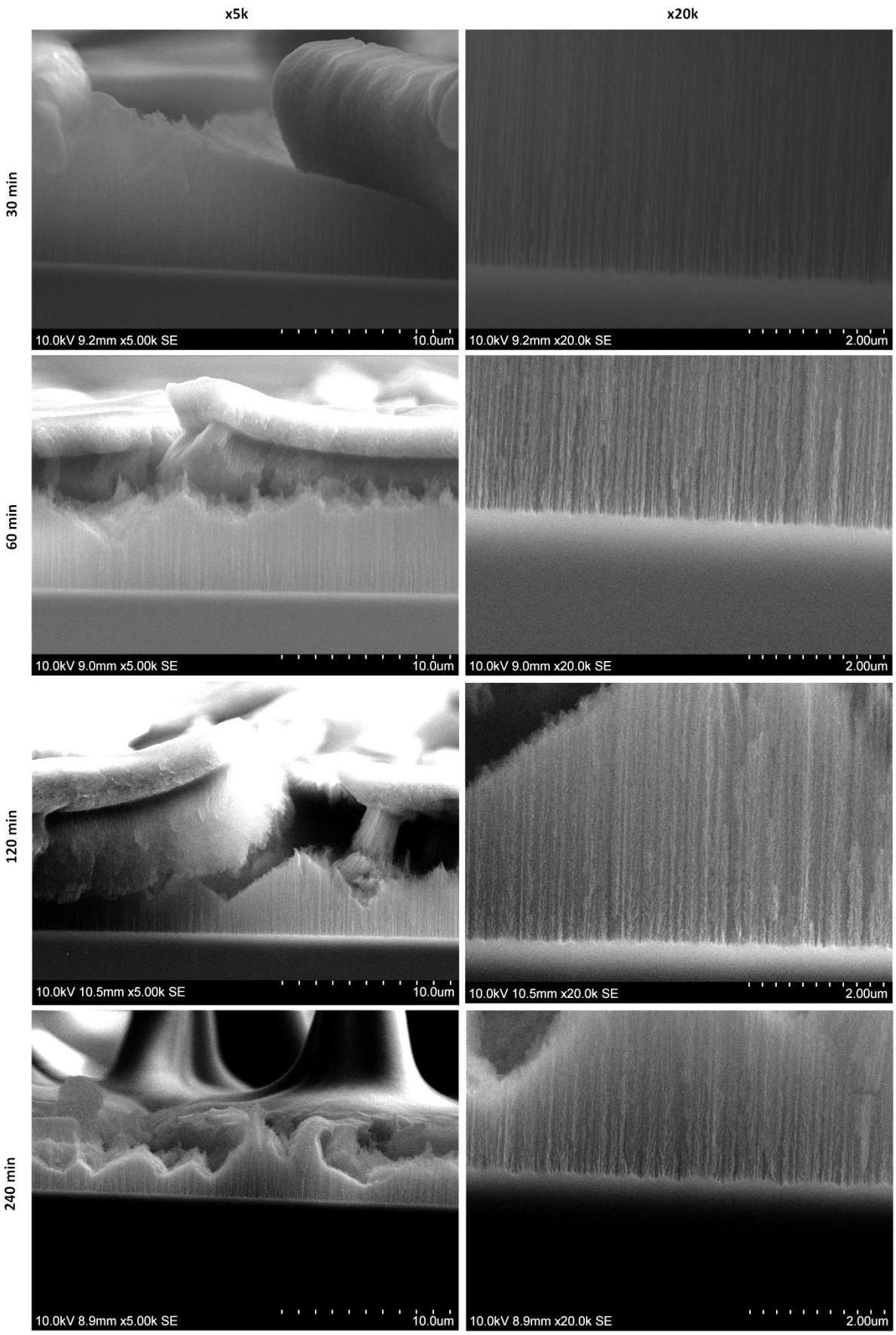

Figure 24: SEM images of the cross sections of the n-type samples etched at 12 mA/cm2 taken at x5k and x20k magnifications.

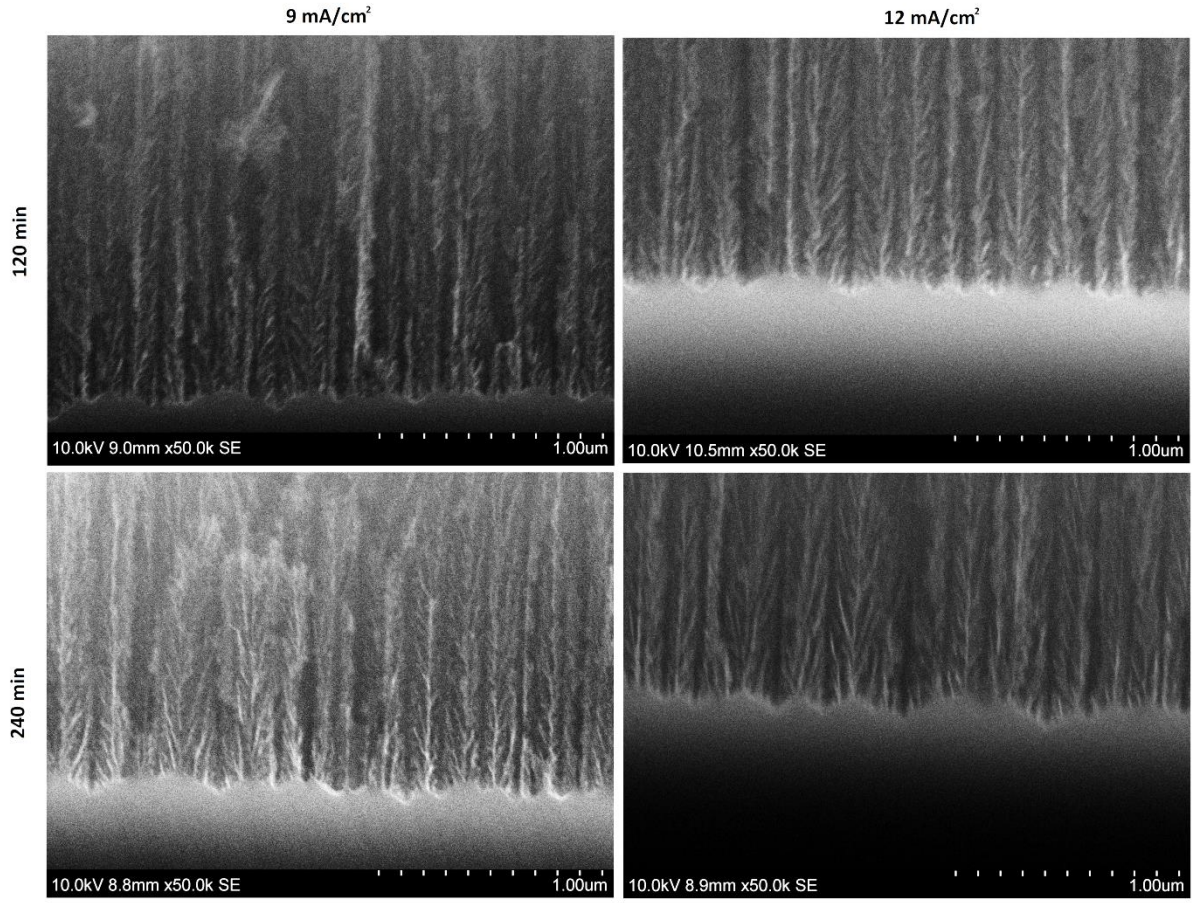

Figure 25: SEM images of the cross sections of the n-type samples etched at 9 and 12 mA/cm^2 for 120 and 240 minutes taken at 50k magnification

5.2.2.3 Results from ICMPE

For sample N_09_60, the thickness of the porous layer was determined to be 9.5 µm in the middle of the sample and 8.1 µm ~5 mm from the edge. It consisted of two parts;

- a top microporous Si layer. Thickness: ~3.1 µm (middle) and 2.7 µm (edge)
- a bottom mesoporous Si layer with strongly branched mesopores. Thickness: ~6.4 µm (middle) and 5.4 µm (edge)

The mesopores were determined to follow the <100> direction and exhibit diameters between 20-50 nm. For sample N_12_60, the thickness of the porous layer was ~10 µm, with the top microporous layer being ~2.7 µm and the bottom mesoporous layer ~7.3 µm. It was determined that capillary forces resulting from the drying are responsible for the cracking of the layers.

Images from the analysis conducted at ICMPE are shown in the figures below. These images revealed that the top layer consisted of a microporous structure, clearly seen in the top right image in Figure 27, which is of the cross section of N_09_60. The remaining images of this figure show the vertical pore structure of the second layer, appearing much as in the images from NTNU, but at a higher quality. The same is the case for Figure 28 and Figure 29, which show the surface structure of N_09_60 and cross section of N_12_60, respectively.

5.2.2.4 Surface and cross sections of the p-type samples

The structure formed from the p-type samples was discovered to be quite different from those made from n-type silicon, but some similarities were also observed. Figure 30 shows the surface structure of the two samples at different magnification, from which it can be seen that p-type samples surface consist of what looks like twisting pillars. However, at high magnification, no second porous layer is observed. The pillar structure shows some resemblance to the structures formed on the n-type samples etched for 240 minutes. To illustrate this, Figure 31 shows a comparison between the cross section of the n-type and p-type samples etched at 9 mA/cm^2 for 240 minutes. From this comparison, it is seen that the scale of the p-type structure is approximately half that of the n-type structure (note the different magnification used in the comparison). While the surface structure shows clear resemblance, the porous structure which is visible in the borders between the pillars in n-type sample cannot be seen in the p-type sample.

In Figure 31, which shows the cross section of the sample etched for 120 minutes, the pillar structure is evident, but still no secondary pores can be distinguished. On the other hand, the surface between the pillars show the roughness and “furry” texture that would be expected from a porous structure, indicating the existence of pores too small to be distinguishable.

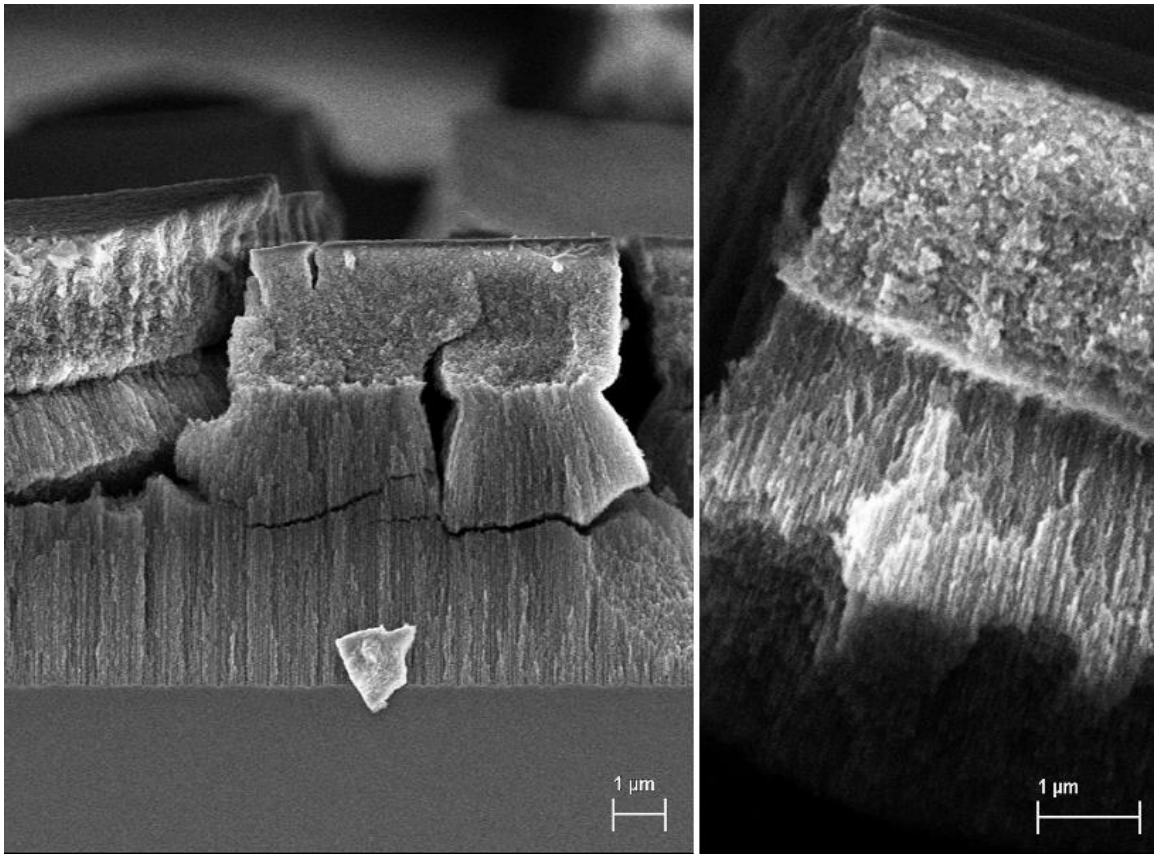

Figure 26: SEM images of the cross section of sample N_09_60 at x5k (left) and x10k (right)

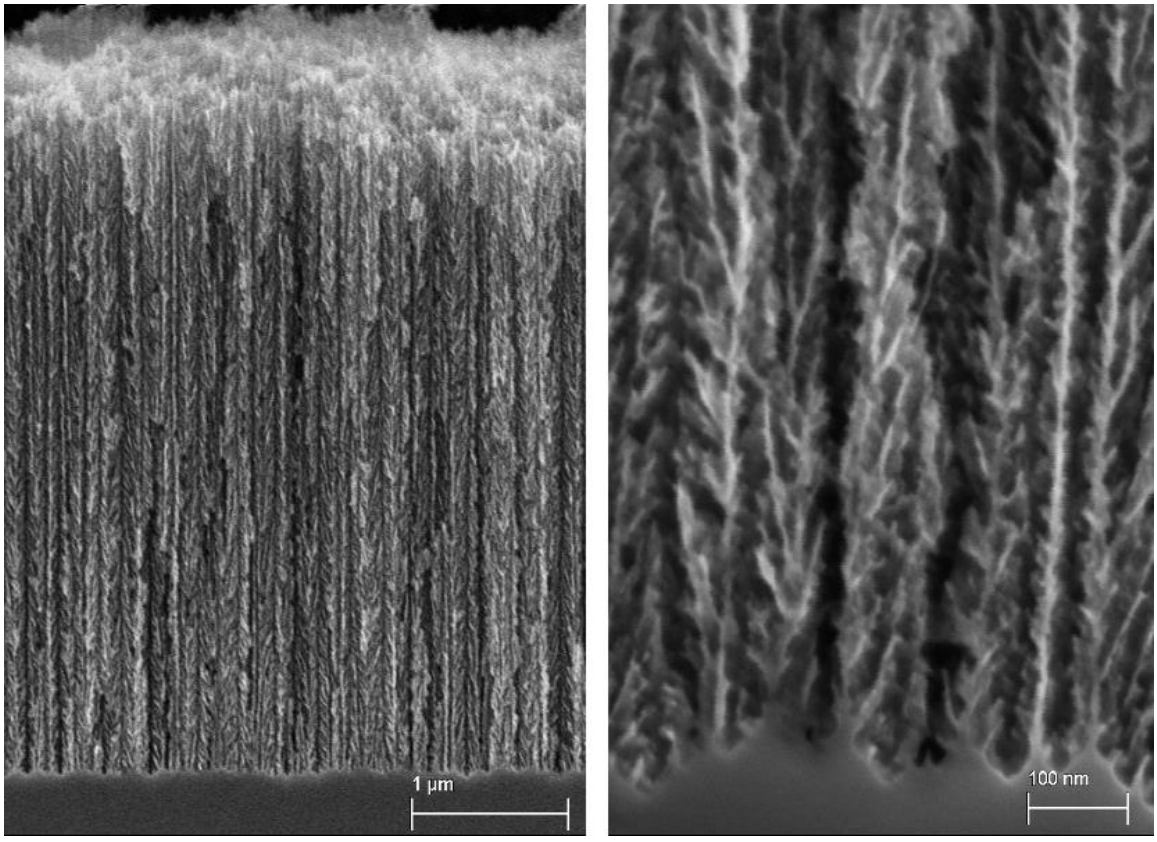

Figure 27: SEM images of the cross section of sample N_09_60 at x15k (left), and x100k (right).

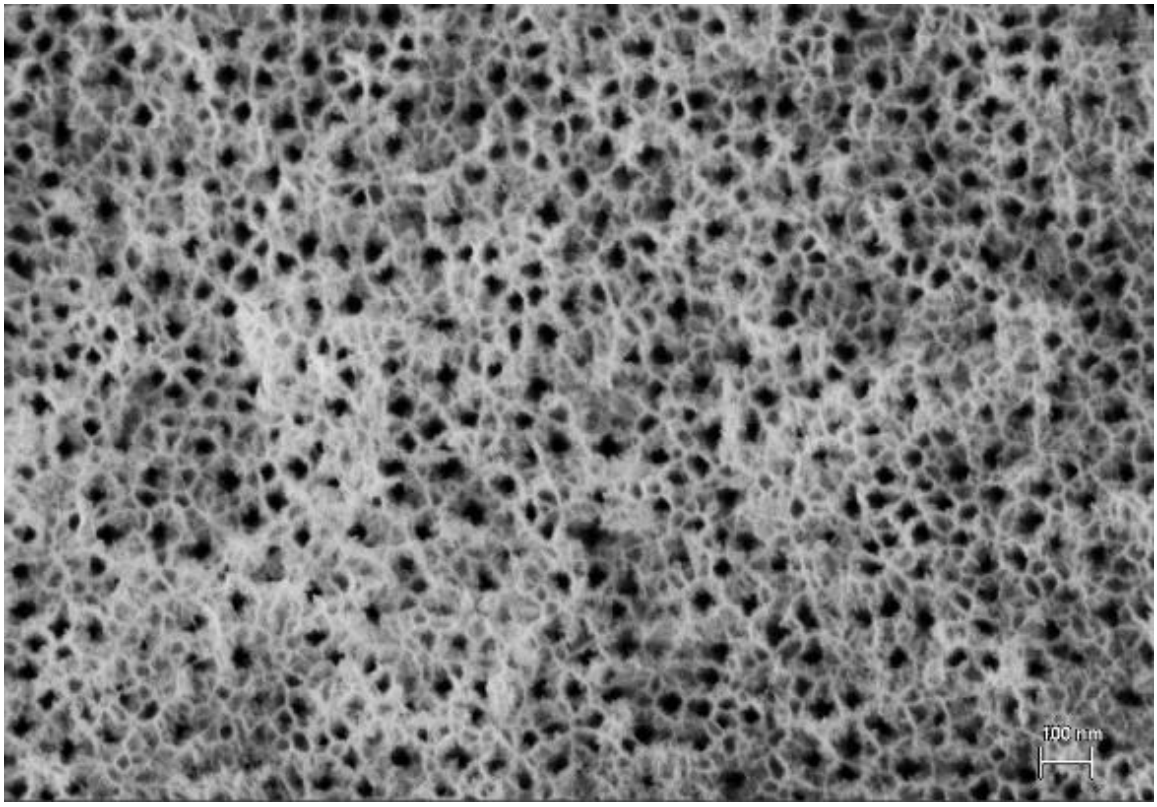

Figure 28: SEM image of the surface of N_09_60 at x50k magnification.

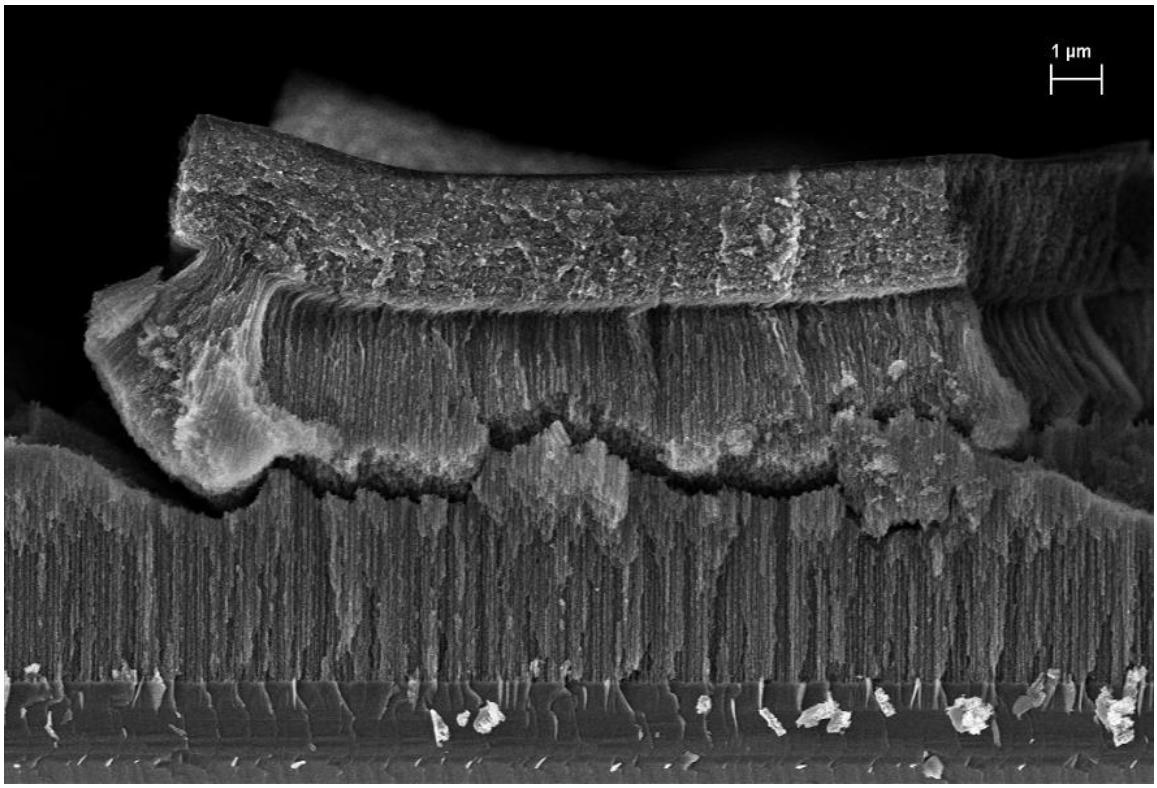

Figure 29: SEM image of the cross section of N_12_60 at x5k magnification.

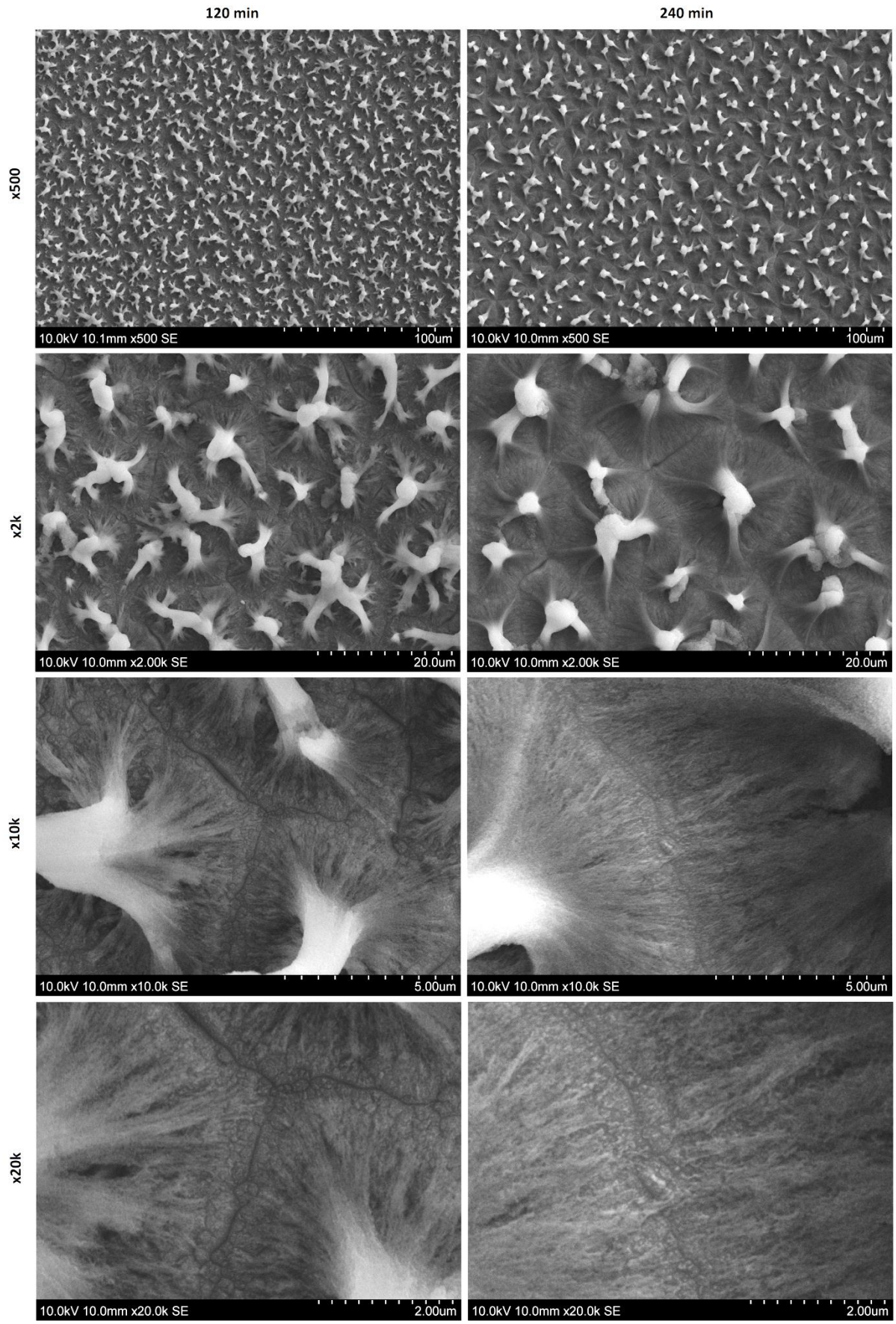

Figure 30: SEM images of the surface structure of the p-type samples etched at 9 mA/cm2 for 120 and 240 minutes, taken at x500, x2k, x10k and x20k magnifications

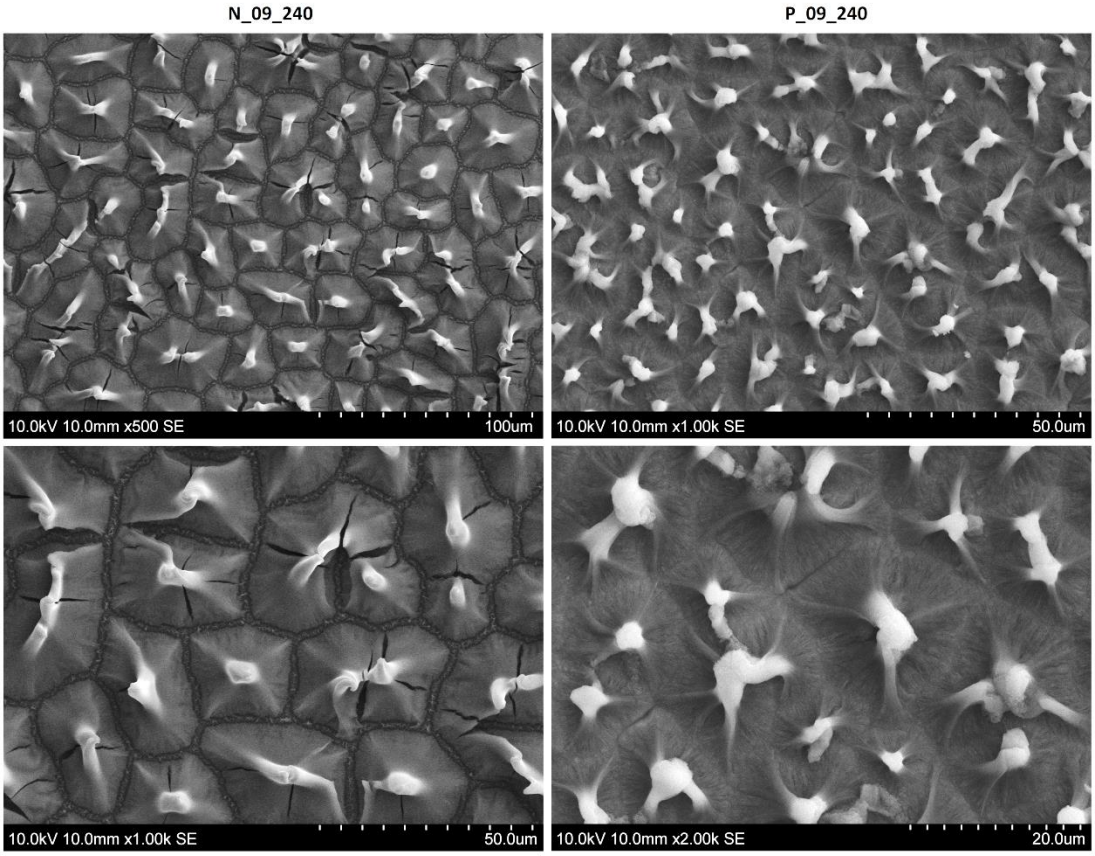

Figure 31: Comparison of SEM images taken of the surface structure of N_09_240 and P_09_240. Note the different magnification used in the comparison, illustrating the structures scale difference

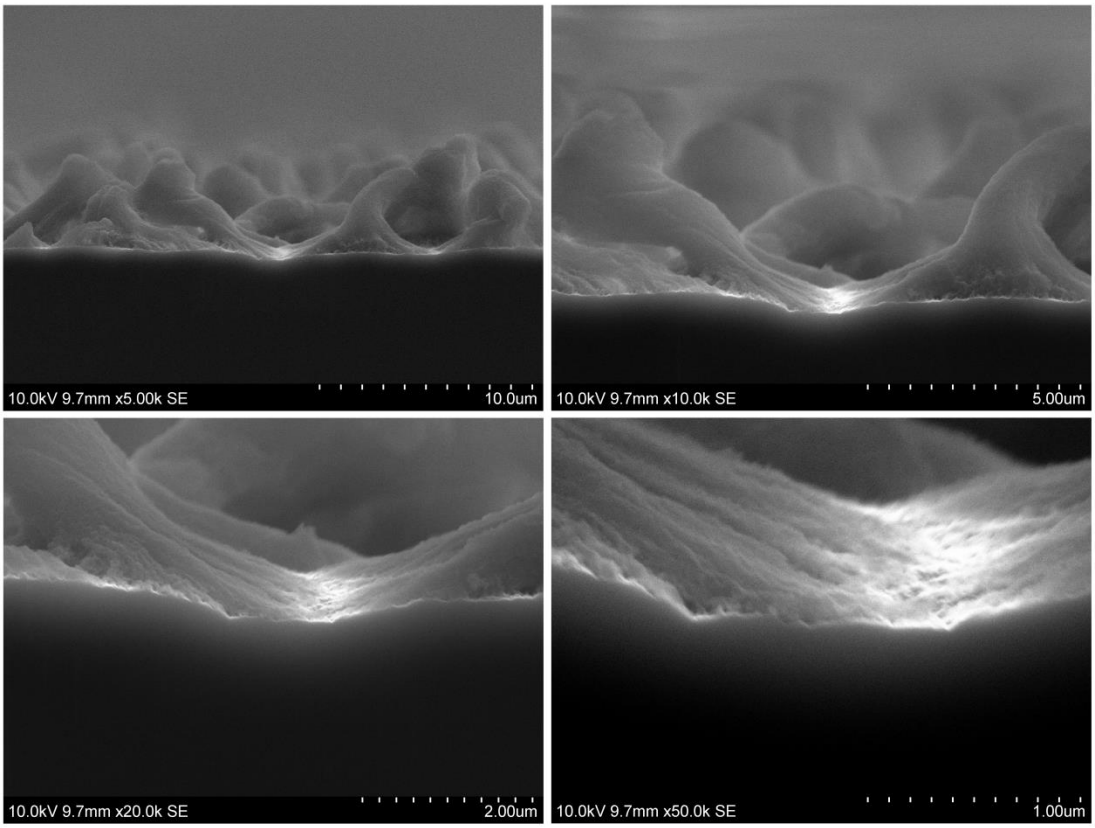

Figure 32: SEM images of the cross section of P_09_120 at x5k, x10k, x20k and x50k magnifications

5.3 Electrochemical Testing

5.3.1 Determination of Mass Porous material

Table 10 shows the mass of the samples before and after KOH etching, as well as the mass of porous material determined by calculating the difference between these measurements. The reference measurement (N_ref) shows that the bulk silicon is not affected to a measurable degree, hence it is reasonable to assume that only the porous structure was removed. As seen from this table, there is a slight increase in the mass of porous material with increased etching time. However, the relationship is not proportional, e.g. for N_12_30 and N_12_240 increasing the etching time by a factor of 8 only increased the porous mass by a factor of ~1.4. It is also noted that the mass of porous material on the p-type samples is approximately half that on the corresponding n-type samples.

Table 10: Results from the determination of mass porous material. The weight measurements are of a 0.25 cm^2 section of each sample.

Sample ID	Weight before [mg]	Weight after [mg]	Mass porous material [mg]
N_09_30	17,88	17,80	0,08
N_12_30	17,55	17,47	0,08
N_09_60	17,10	17,02	0,08
N_12_60	16,88	16,80	0,08
N_09_120	15,62	15,54	0,08
N_12_120	15,45	15,35	0,10
N_09_240	13,24	13,13	0,11
N_12_240	12,62	12,51	0,11
P_09_120	12,54	12,50	0,04
P_09_240	9,55	9,50	0,05
N_ref	18,32	18,32	0,00

Figure 33 shows the measured mass loss, obtained by subtracting the mass of the etched sample from the mass of the reference sample and dividing by the area of the weighed sample to obtain the weight loss per unit area.

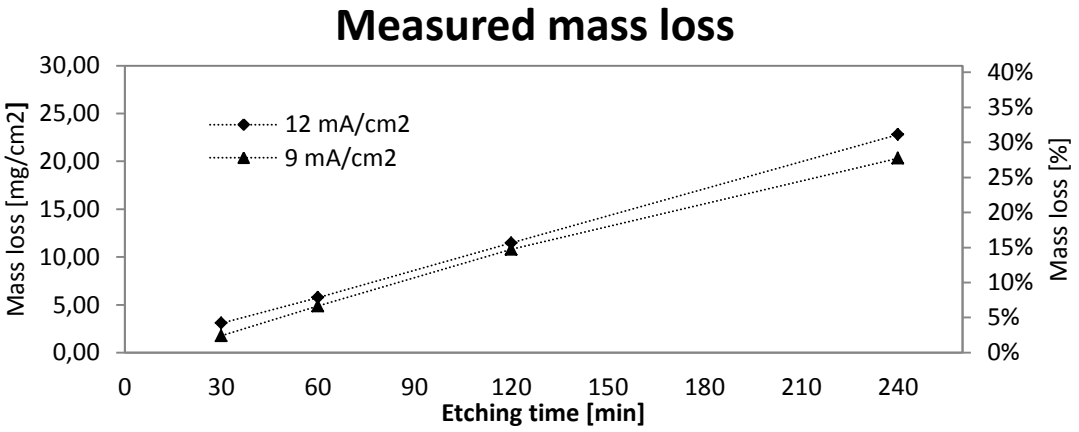

Figure 33: Mass loss of the samples during etching as a function of etching time

5.3.2 Cycling of Porous Silicon Electrodes

The electrochemical cycling of the porous silicon electrodes continued as long as possible, meaning that dependent on when the electrode was started, some were run for a few weeks and other for several months, accumulating vast amounts of data. In this section, a selection of these data will be displayed.

5.3.2.1 Charge and discharge capacity vs. cycle number

The following figures display the discharge capacity of the non-coated and coated electrodes. The non-coated electrodes were run for more than 40 cycles and the PPAN-coated were run for 16. As the charge was cut off at 3000 mAh for all cycles, the charge capacities are not included in the charts.

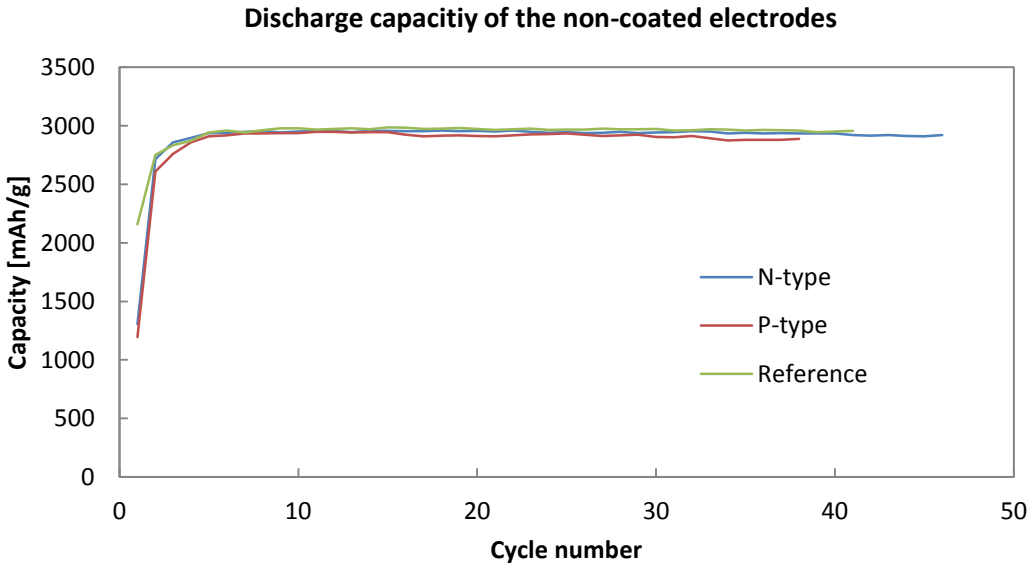

Figure 34: Discharge capacity vs. cycle number for the non-coated electrodes.

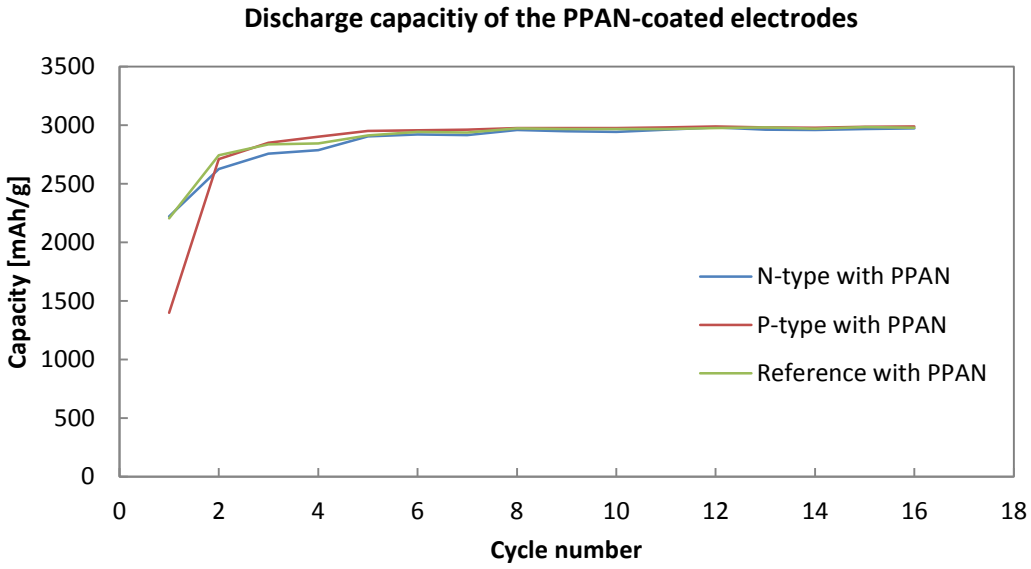

Figure 35: Discharge capacity vs. cycle number for the PPAN-coated electrodes.

5.3.2.2 *Coulombic efficiency*

The figures below show the Coulombic efficiency of the samples. As the coated samples ran for 16 cycles, all the graphs are limited to this number to provide a better comparison. Figures 36 and 37 compare all the non-coated and carbon coated electrodes, respectively, while figures 37, 38 and 39 compare the n-type, p-type and reference electrodes, respectively.

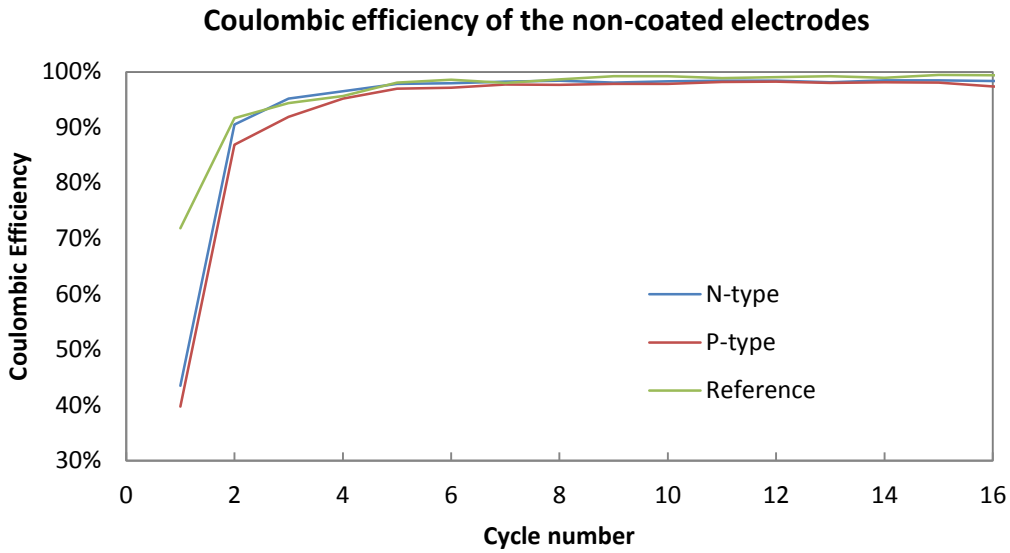

Figure 36: Chart showing the Coulombic efficiency of the initial 18 cycles for the non-coated electrodes.

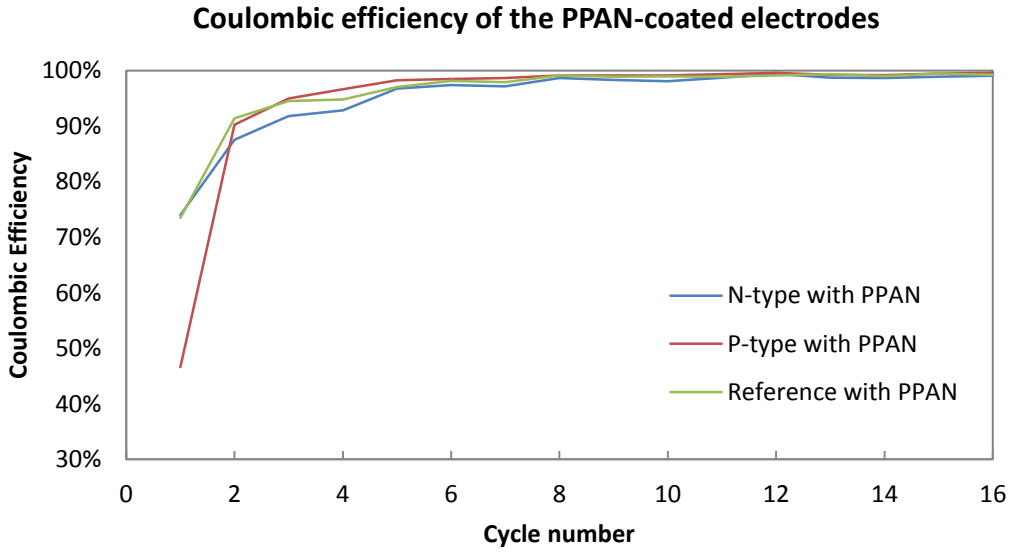

Figure 37: Chart showing the Coulombic efficiency of all the cycles for the PPAN-coated electrodes.

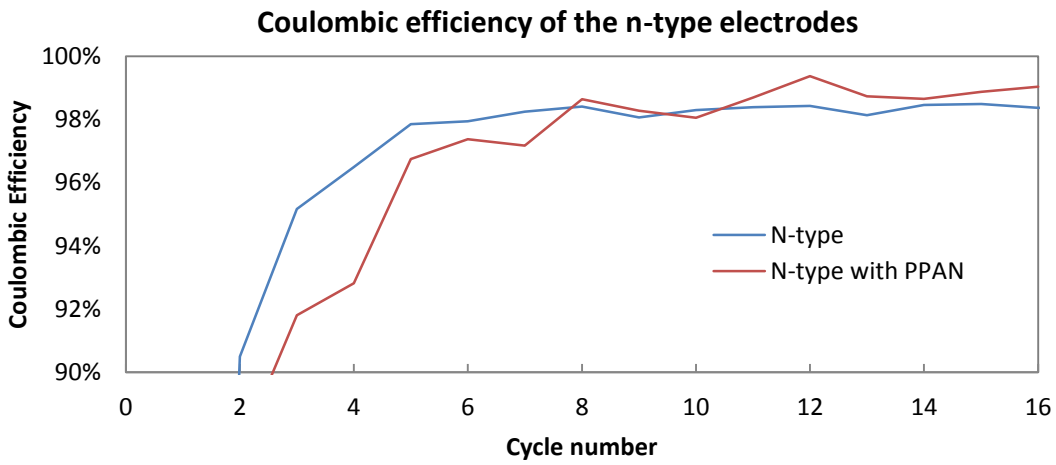

Figure 38: Chart showing a comparison between the Coulombic efficiency of the non-coated and PPAN coated n-type electrodes.

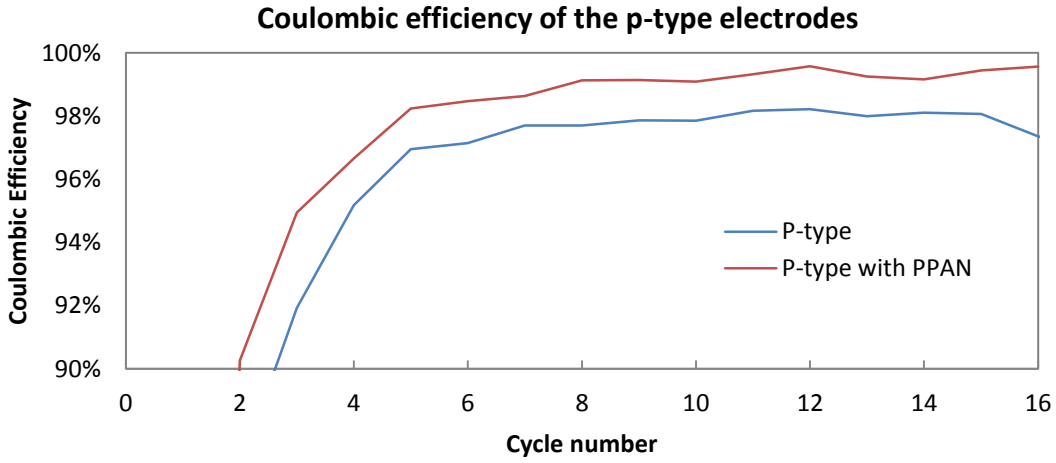

Figure 39: Chart showing a comparison between the Coulombic efficiency of the non-coated and PPAN coated p-type electrodes.

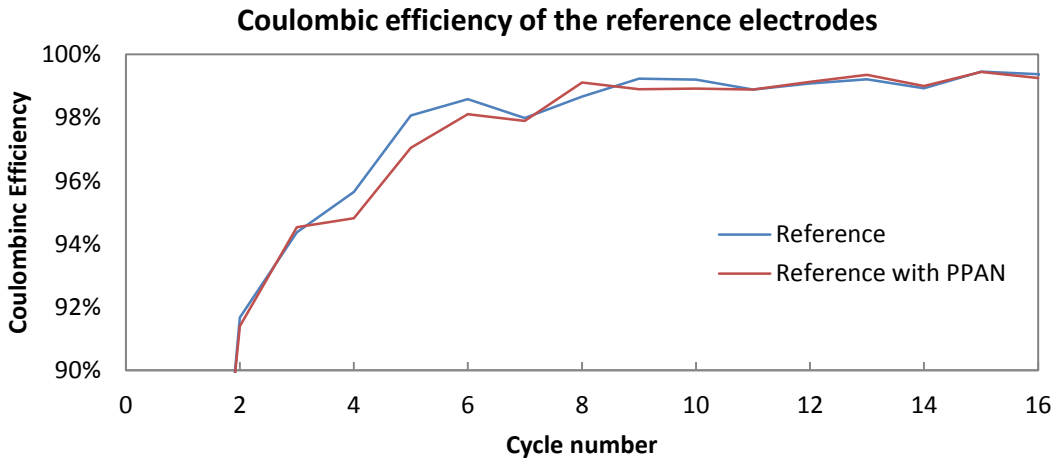

Figure 40: Chart showing a comparison between the Coulombic efficiency of the non-coated and PPAN coated reference electrodes.

5.3.2.3 Voltage curves of the initial cycle

The following charts show the voltage-time curve of the initial charge-discharge cycle. During this cycle a number of processes occur, most notably the initial SEI formation. Due to the charge (lithiation) limitation at 3000 mAh/g, none of the samples reach the voltage cutoff, hence the charge part of the cycles are of the same duration. During the discharge cycle, all samples reach the cutoff voltage sooner or later as the amount of lithium in the electrode is limited. The time it takes for this to happen reflects the amount of lithium that can be removed from the electrode, and hence also the Coulombic efficiency of the cycle. Figure 41 shows the voltage curve for all the porous electrodes together, while figures 42, 43 and 44 compare the different versions of the n-type, p-type and reference samples, respectively, separately.

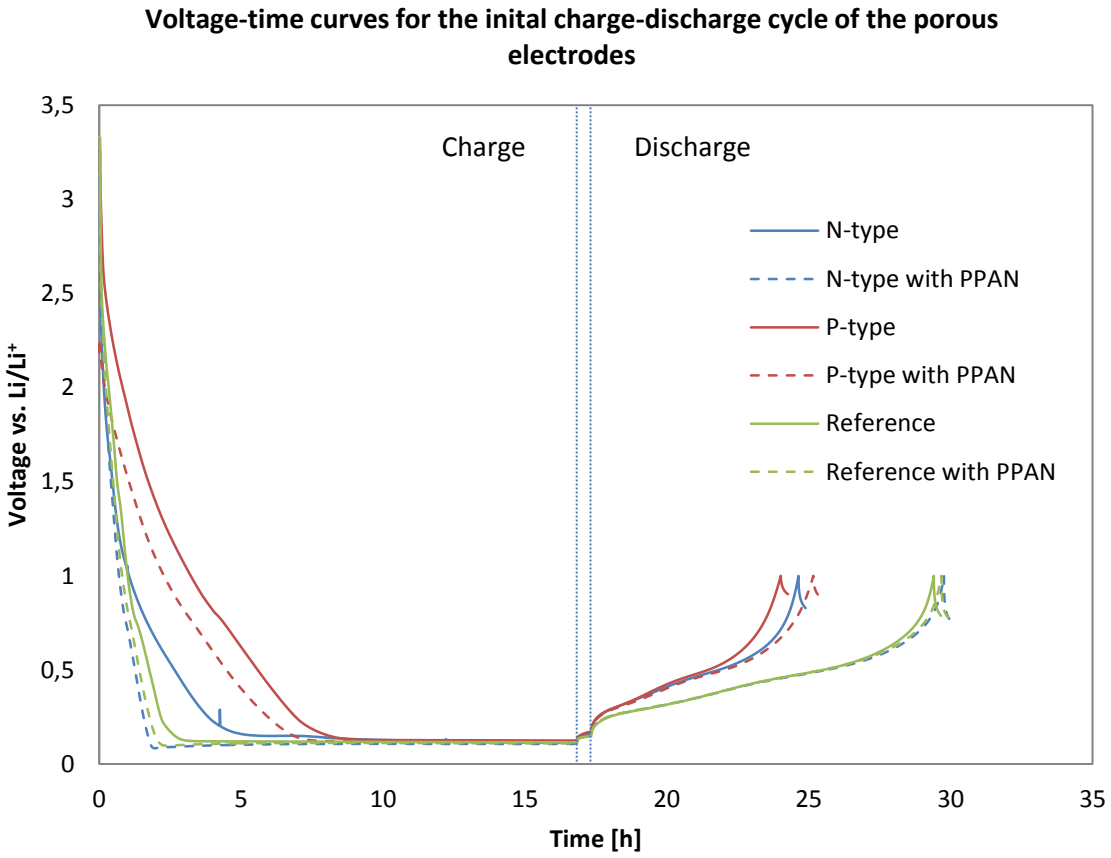

Figure 41: Voltage-time curves for the initial cycle of all the porous electrodes. The vertical lines separating the charge and discharge steps, the gap representing the post-charge rest step.

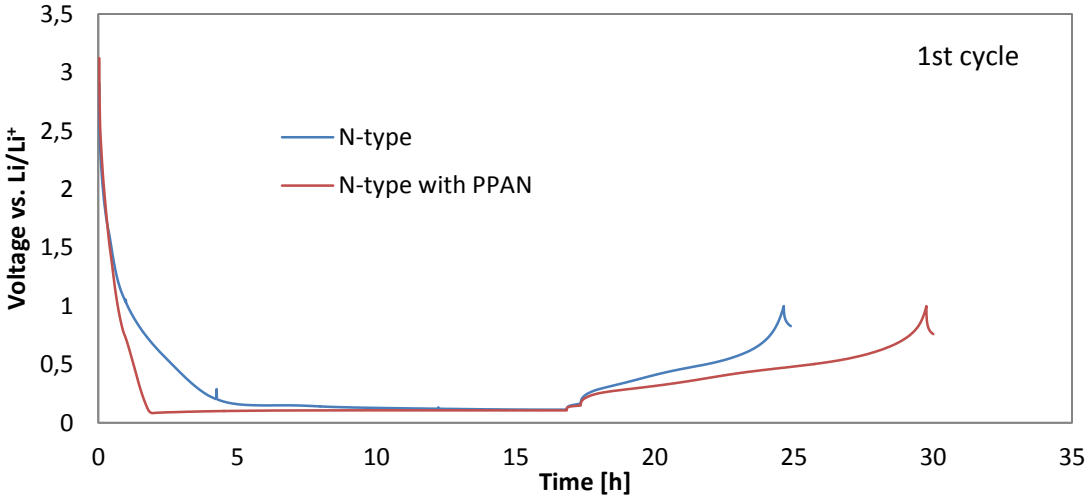

Figure 42: Voltage-time curve for the initial cycle of N_12_120 with and without carbon coating.

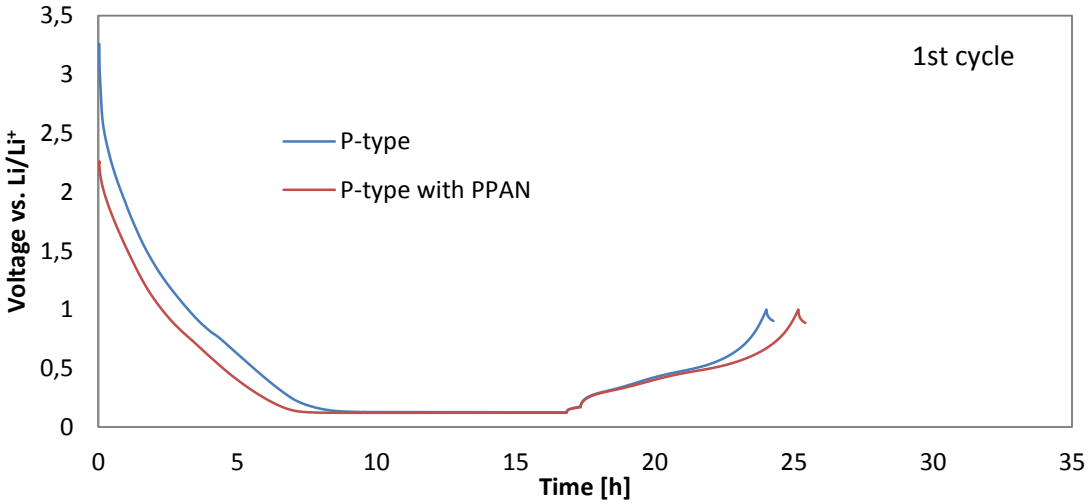

Figure 43: Voltage-time curve for the initial cycle of P_09_120, with and without carbon coating.

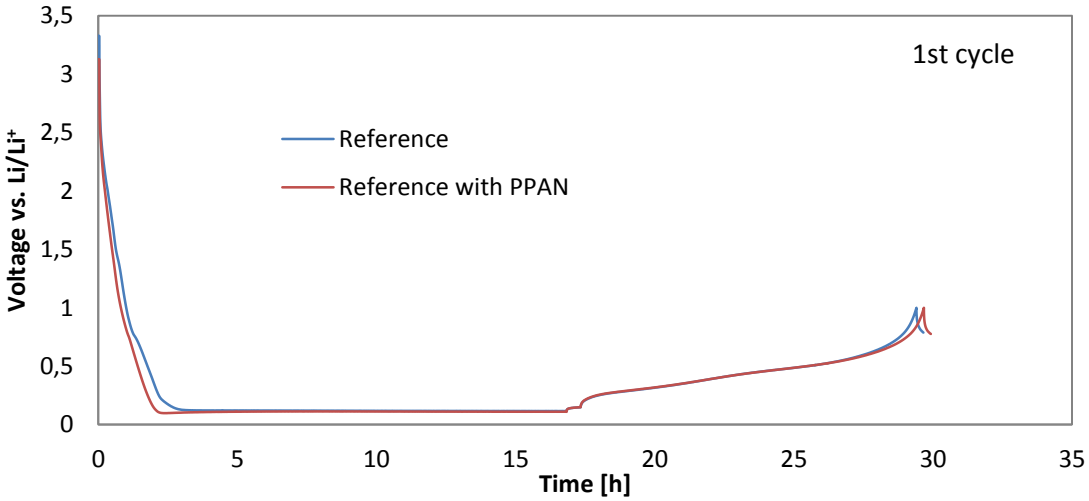

Figure 44: Voltage-time curve for the initial cycle of N_ref, with and without carbon coating.

5.3.2.4 *Voltage-time curves for the 8th cycle*

After 8 cycles, it is believed that the start-up processes have finished and that the cells are more or less stable from this point to their eventual failure. Figures 45 and 46 compare the voltage-time curves of the non-coated and PPAN-coated electrodes, respectively, while figures 47, 48 and 49 compares the non-coated and PPAN-coated electrodes from each sample.

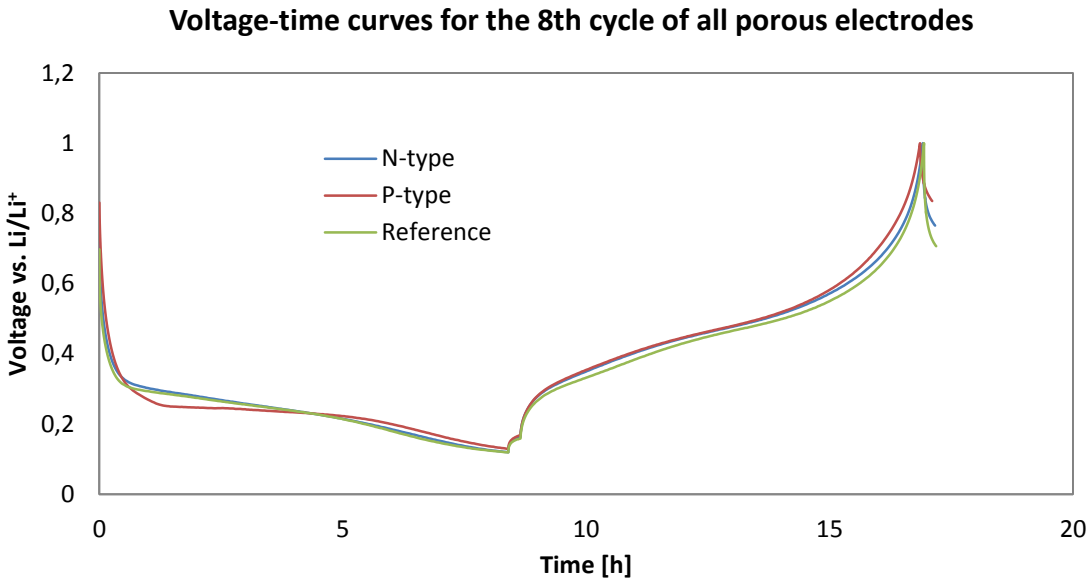

Figure 45: Voltage-time curve for the 8th cycle of the non-coated electrodes.

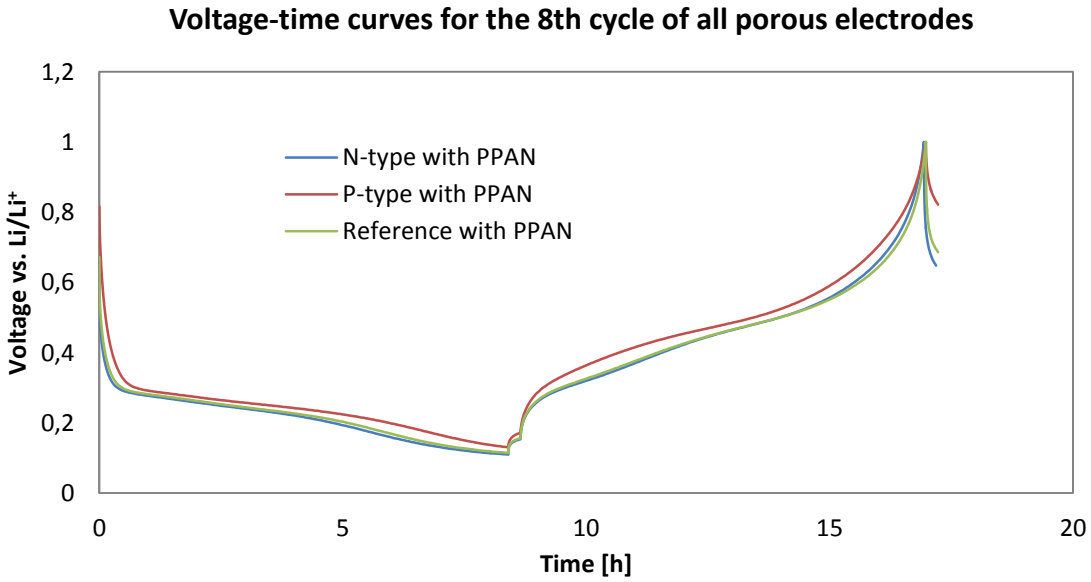

Figure 46: Voltage-time curve for the 8th cycle of the PPAN-coated electrodes.

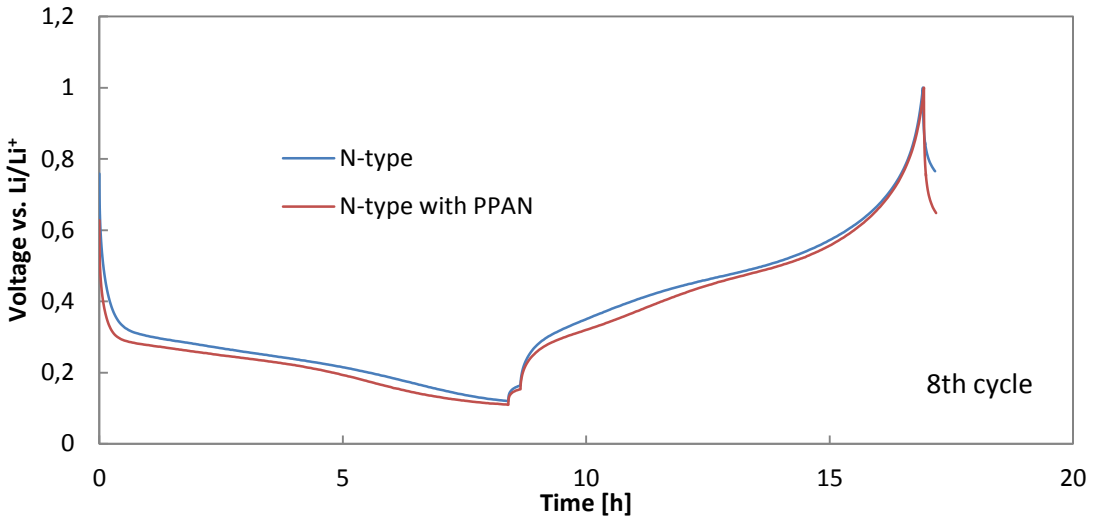

Figure 47: Voltage-time curve for the 8th cycle of N_12_120, with and without carbon coating.

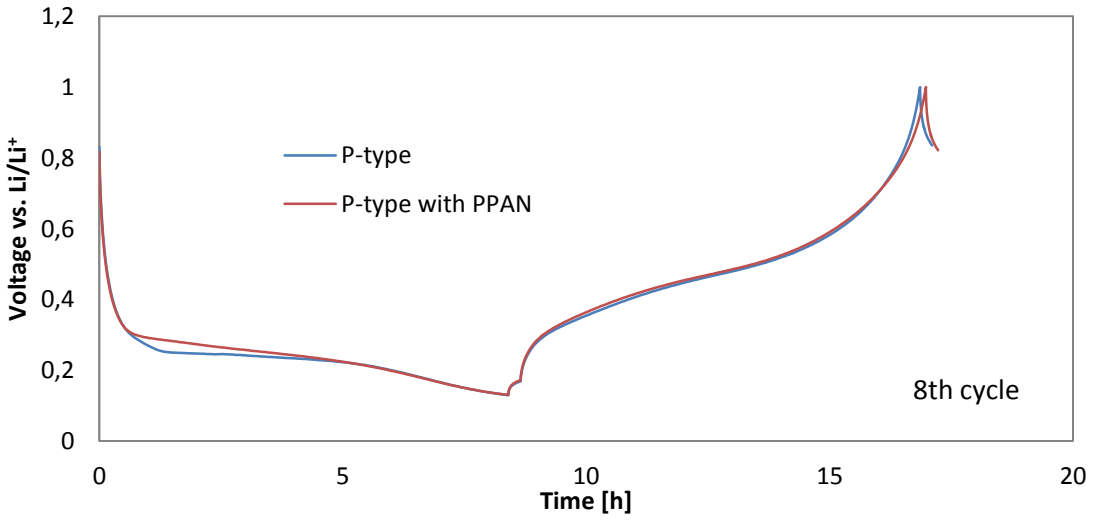

Figure 48: Voltage-time curve for the 8th cycle of P_09_120, with and without carbon coating.

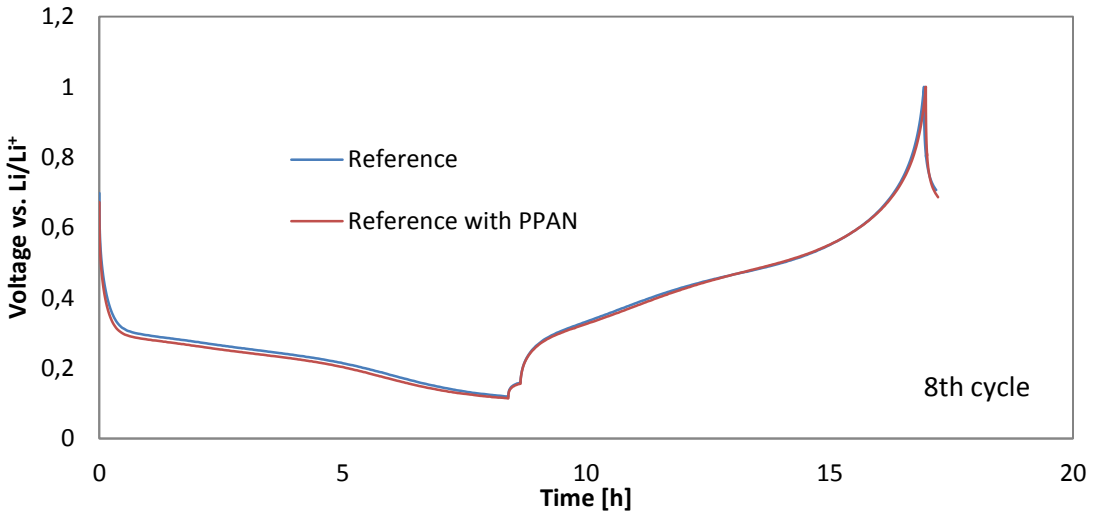

Figure 49: Voltage-time curve for the 8th cycle of N_ref, with and without carbon coating.

5.3.2.5 *Overvoltage evolution*

The figures below show the voltage at the end of the post-delithiation rest step as a function of cycle number. As the cut-off voltage was 1 volt for the delithiation step, the voltage after the 30 minute rest step is a good indication of the overvoltage with which the lithium was deintercalated from the electrode. The closer the end-of-rest voltage is to 1 volt, the closer the deintercalation happened to equilibrium, and vice versa.

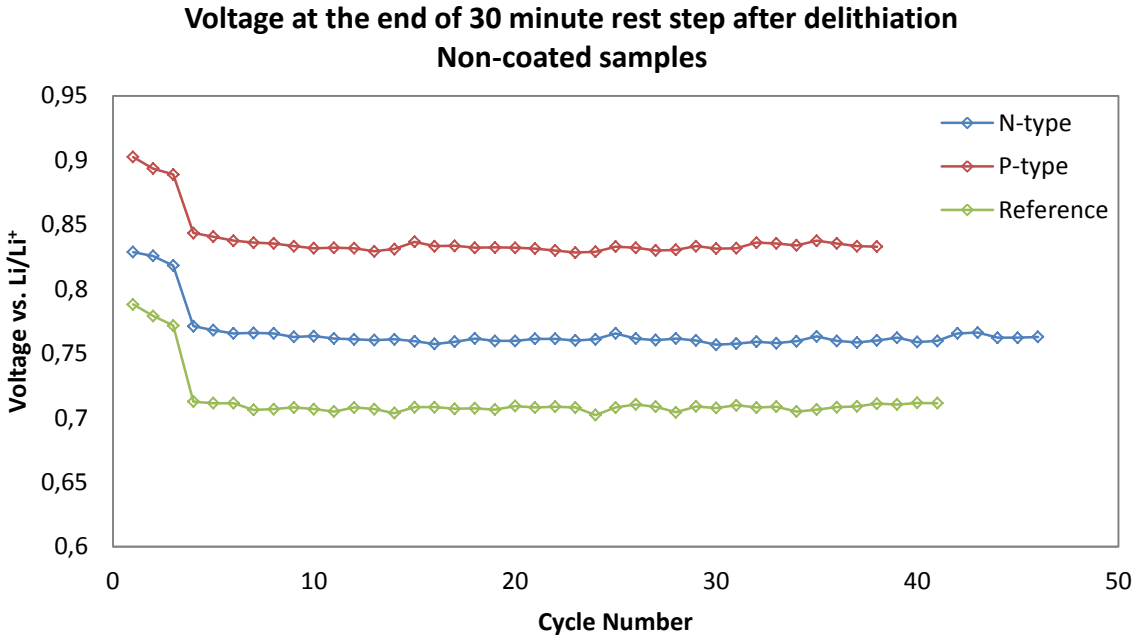

Figure 50: Voltage at the end of 30 minute rest step after delithiation as a function of cycle number for the non-coated samples

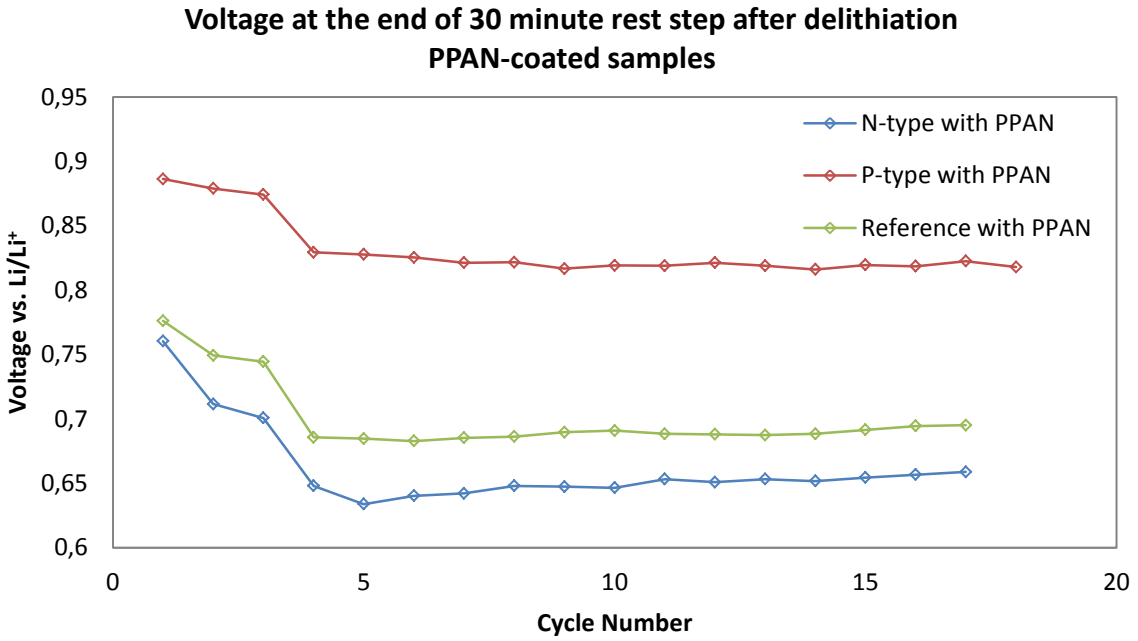

Figure 51: Voltage at the end of 30 minute rest step after delithiation as a function of cycle number for the PPAN-coated samples

5.3.3 Cycling of Composite Electrodes

5.3.3.1 Initial cycle voltage-time curves

The curves below show the voltage-time curves for the initial delithiation of the electrode and the initial cycle of each of the composite electrodes. For the electrode run at C/20 the cycle is dominated by the rest steps, showing only rapid increase or decrease to the cut-off voltages. The electrode run at C/200 exhibit a behavior more close to that of a composite electrode, however, the capacity is extremely low, despite the increased discharge cut-off voltage. The silicon reference starts directly at the post-delithiation rest step, as its start OCV is above the cut off, then proceeds to complete a typical initial cycle for a composite electrode.

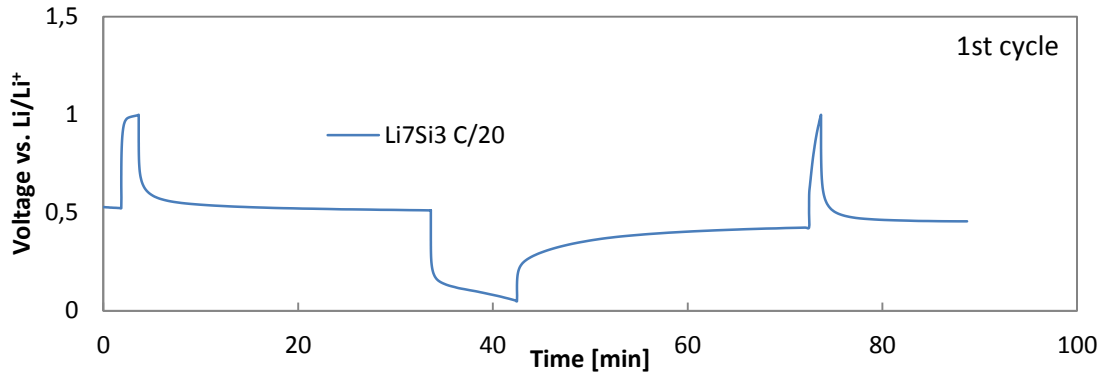

Figure 52: Voltage-time curve for the first cycle of the Li_7Si_3-composite electrode cycled at C/20

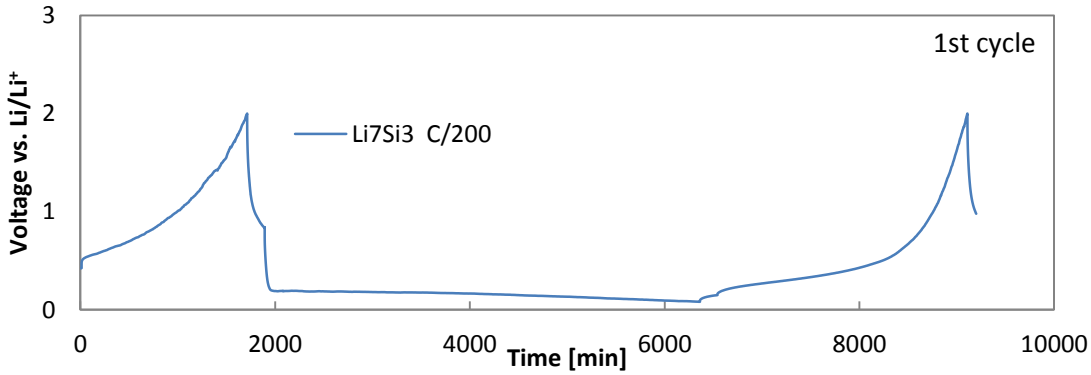

Figure 53: Voltage-time curve for the first cycle of the Li_7Si_3-composite electrode cycled at C/200

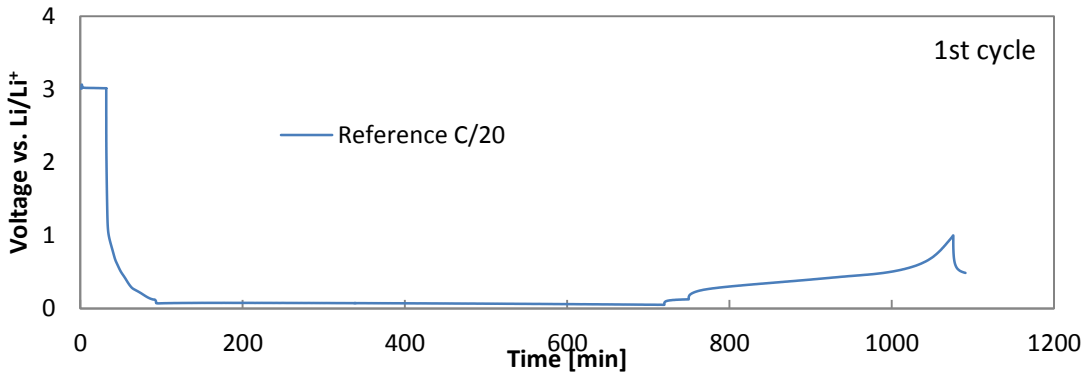

Figure 54: Voltage-time curve for the first cycle of the silicon-composite reference electrode cycled at C/20

5.3.3.2 *Charge and discharge capacity vs. cycle number*

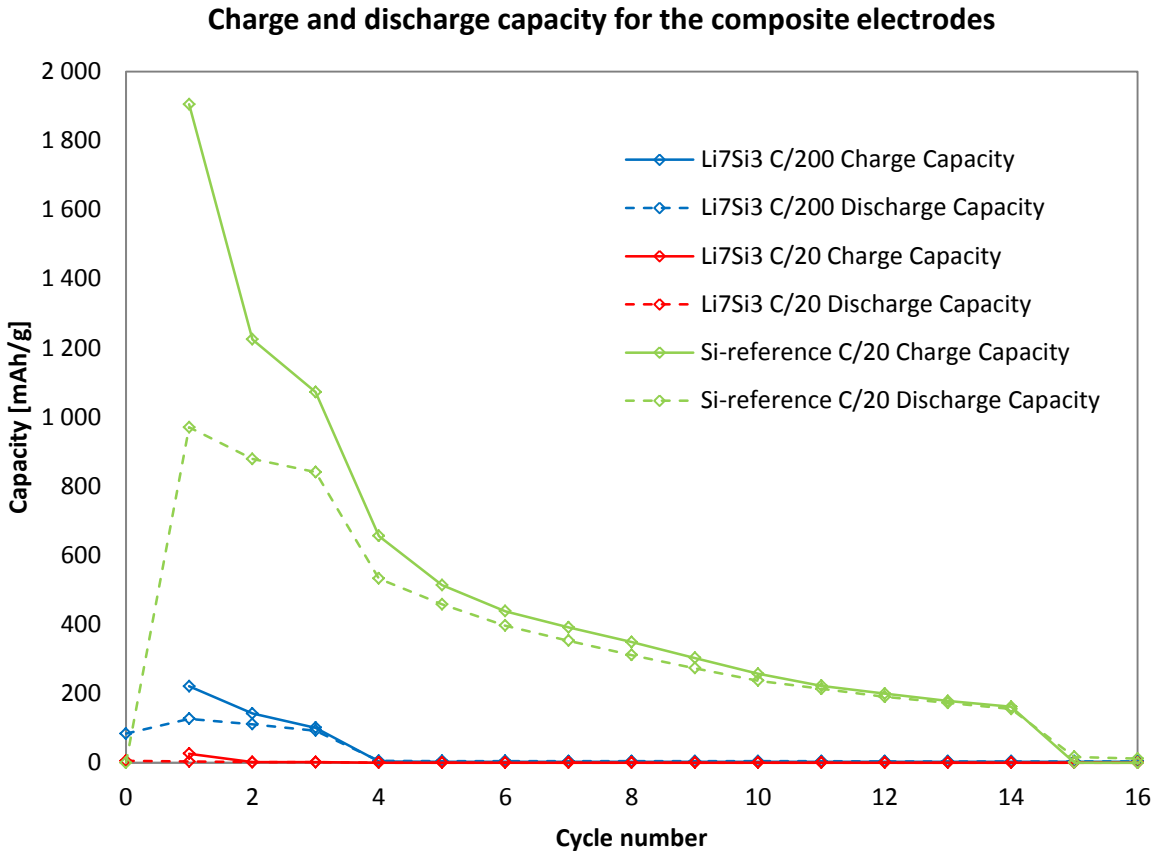

Figure 55: Charge and discharge capacity as a function of cycle number for the composite electrodes

5.3.4 Post-Cycling SEM Characterization

Figure 57 shows the surface images taken of the N_12_120 electrode before and after being cycled for one full cycle. These show that much of the microporous upper layer has been preserved; however, the macroporous structure that was present before cycling is either removed or has been replaced by a dense structure of what can be described as packed particulates. These images also show that whole sections of the upper layer have fallen off the electrode. Figure 58 displays a comparison between the cross sections of the cycled and un-cycled electrodes. These show that much of the macroporous material has in fact disintegrated, and that what is left has become too dense for pores to be discernible.

Figure 56 shows an EDS map of the same section as shown in Figure 57. This shows that fluorine and phosphorous are present in far higher quantities on the surface of the lower layer than on the surface of the upper layer. The surface of the upper layer is instead dominated by oxygen, while in the cracks that have been formed in the lower layer, only silicon is observed.

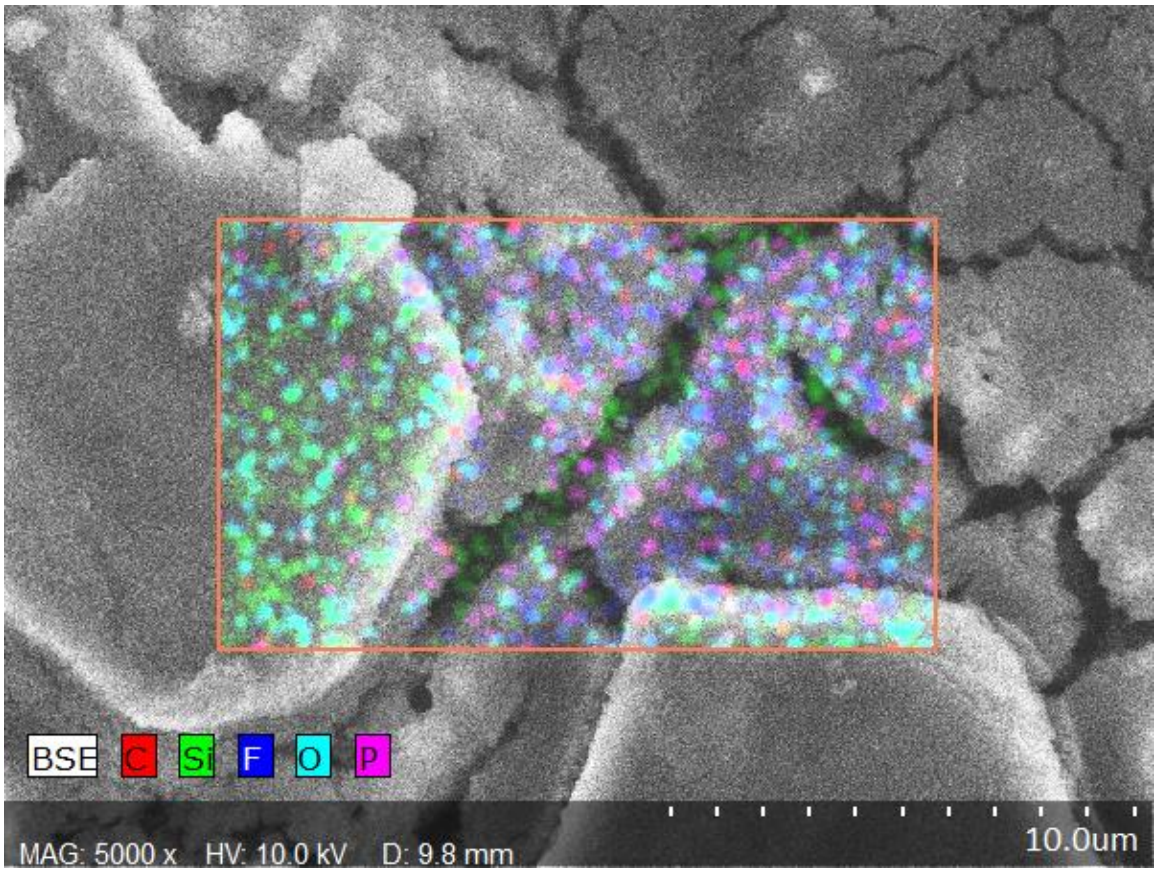

Figure 56: An EDS map superimposed on a SEM image of a section of the surface of N_12_120 after cycling

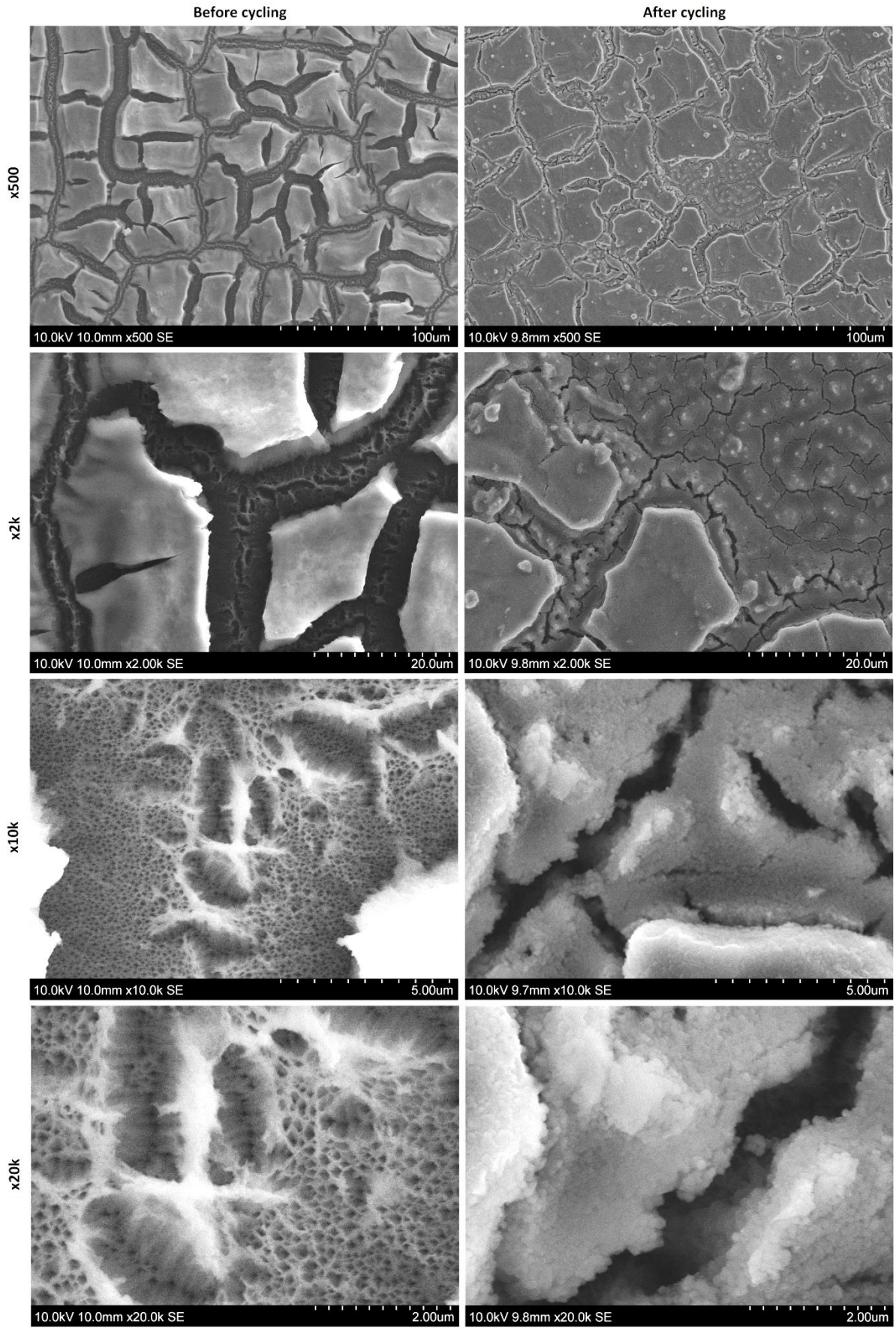

Figure 57: SEM images comparing the surface structure of N_12_120, before (left) and after (right) being cycled for one full cycle

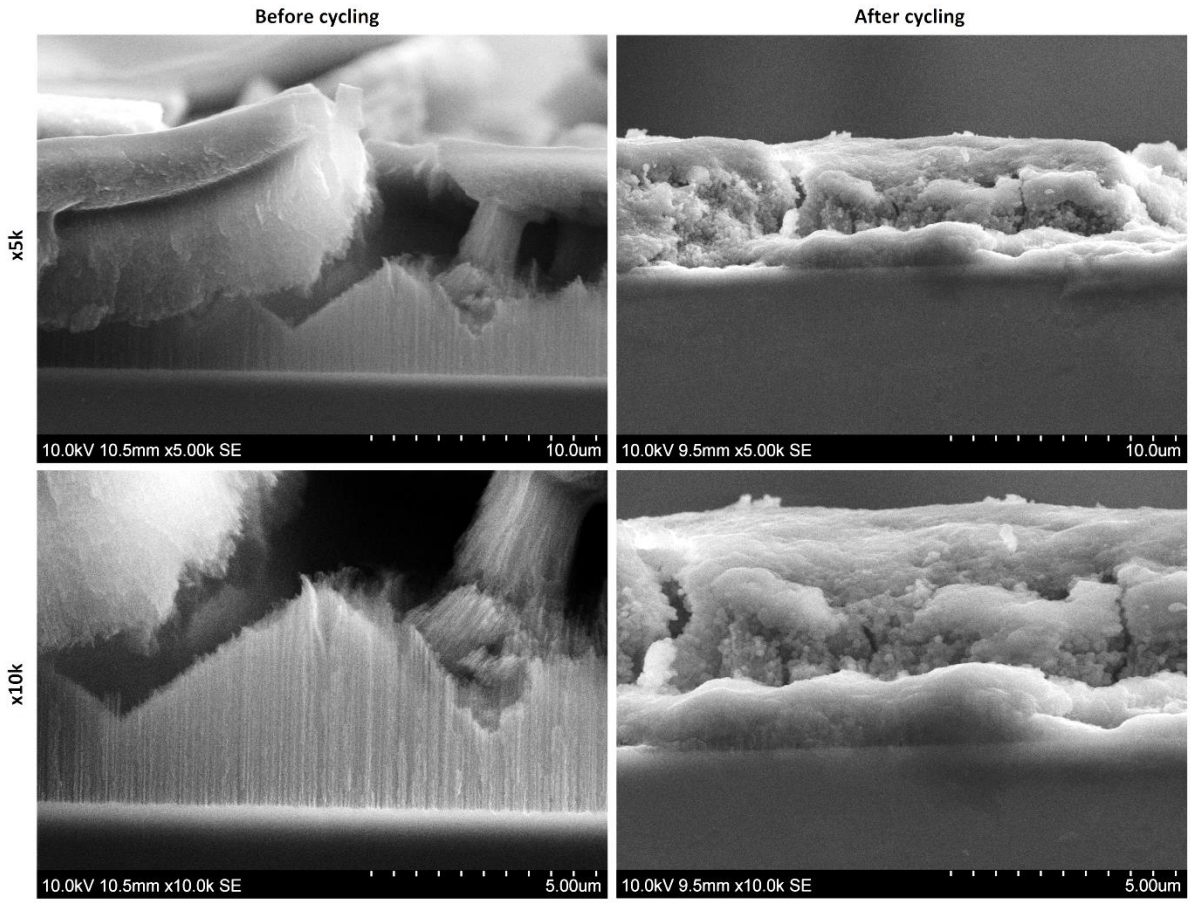

Figure 58: SEM images comparing the cross section of N_12_120 before (left) and after (right) being cycled for one full cycle

6 Discussion

6.1 Porous Silicon

From the images presented in the experimental section and appendices, it is confirmed that porous material is formed on all of the n-type samples. In this section, the different trends that are observed for the formed structures will be commented on, and where reasonable hypotheses for the formation mechanism can be made, they are presented as well. But first a general description and classification of the structures that have been formed are made.

All of the n-type samples consist of a two layer structure; a layer of randomly oriented micropores over a layer of vertical macropores with a high degree of branching. By the classification system presented in Figure 10, this structure clearly belongs to group 4c, which is describes as a layer of microporous silicon on top of macropores. As would be predicted from a (100)-wafer, the macropores are oriented by the <100> direction, that is vertically to the surface, and thus classified in group 1a, whereas the micropores show no clear orientation. The level and type of branching are also different in the two layers; the macroporous layer consist of second level branching, and thus classified as 2c, while the microporous layer consists of a dense structure of short randomly oriented branches, thus classified as 2f. The microporous layer is seemingly limited to the surface of the material, and does not extend into the macropores themselves, which then is classified as 3a. This classification can be seen schematically in Figure 59.

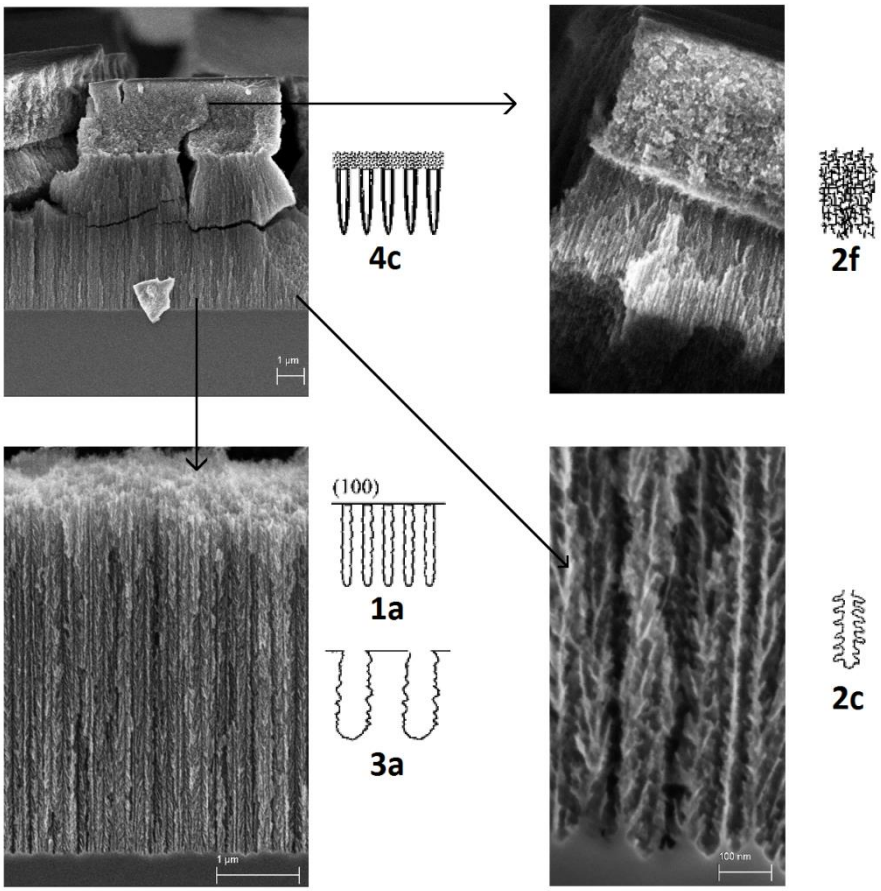

Figure 59: Schematic presentation of the classification of the n-type porous structure. Comparing SEM images of the structure with the classification matrix seen in Figure 10, showing the two-layer structure (4c), dense randomly branched structure of the top layer (2f), and empty (3a) and branched (2c) mesopores of the bottom layer, vertically aligned in the <100> direction (1a).

It has been thoroughly established that the n-type samples have a two-layer structure. This kind of structure is only expected for samples made of low doped p-type silicon or n-type silicon under illumination. The structures observed fit remarkably well with the pore sizes expected from n-type samples under illumination, which usually have two ranges of pore sizes; 1-10 nm and 30 nm–10 µm. As all samples in this study were etched without illumination, this structure is surprising. However, the cell is equipped with the necessary sapphire window to provide illumination, and as this window is located under the cell mounting table behind a glass door, a possibility is that diffuse radiation from the ambient lighting was able to reach the samples inside the cell. While this light would have to be reflected by several dull surfaces and thus have an extremely low intensity, it cannot be ruled out. On the other hand, the parameter space for anodic etching is far from explored, and it is thus quite possible that this was the first time these exact parameters were employed.

For these two-layer structures, the top layer is seen to crack or peel off the surface of the samples. Even though ethanol was used as the last soaking medium before drying after etching, it is postulated that the cause of the cracking and peeling is capillary pressure formed when the sample was dried. The “curly” structures were observed mainly on the samples etched for 30 minutes and 60 minutes at low current densities. From Figure 19 these samples are also seen to have the smallest pore sizes. As the nature of capillary pressure is that it increases with decreasing pore size, these observations are in agreement. It should also then be expected that the coverage of the microporous layer should increase with increasing etching time. When looking at the images in figure 18, it is seen that this is in fact the case for the samples etched for 30, 60 and 120 minutes. However, when the etching time reaches 240 minutes, the coverage is reduced to a point where the topmost layer only exists in the form of pillars, rather than a layer. The conical shape of the pillars is hypothesized to be a result of chemical etching; as the topmost part of the pillars are formed first, they have suffered from chemical etching the longest time and therefore are thinnest. As to why they form no hypothesis is proposed, however, from their height above the rest of the surface structure, the pillars are seemingly more resistive to the chemical etching than the surrounding structure. This indicates that they consist of a structure having a lower specific surface area, and might in fact be solid pillars rising above an underbrush of macroporous material.

While the structure of the porous layers changes with increased etching time, the thickness of the layer remains approximately the same and the mass lies in the 0.1 mg region for all samples. Due to the low mass and small thickness of the porous layer, most of the measured mass loss during etching is related to the reduction of thickness of the samples itself. As seen from Figure 33, the mass loss exhibit a close-to linear relationship with etching time, however, the mass loss is only slightly higher for the samples etched at 12 mA/cm^2 than those etched at 9 mA/cm^2. If only electrically driven etching occur, the amount of etched material should be approximately proportional to the total charge transferred through the system, and thus proportional to both the etching time and the current density. As this is not the case, and the mass loss, and thus thickness reduction, is seen to be only slightly dependent on current density, chemical etching is believed to play a major role. It is therefore hypothesized that the etching speed is more or less constant for the system, and that the formed structure is relatively quickly dissolved by chemical etching, hence the proportionality with etching time and apparent low dependence on current density. The balance between the electrochemical production of porous material and chemical

removal of it creates a moving etching front, where the porous material constitutes a transition zone between the solid silicon and the electrolyte, thus resulting in the similar mass of porous material for all samples.

Operating with a constant etching speed implicates that a higher current density creates a higher porosity material, simply because more material is removed in the same volume. It is seen from Table 10 that the mass of porous material is similar on the samples etched for the same duration at different current densities. Logically, this must mean that the porous layers on the high current density samples must be thicker, as they have a higher porosity. As the etching speed is approximately the same, this must also mean that the chemical etching is slower on the high current density samples. While it may be natural to assume that a high porosity material is more vulnerable to chemical etching, its vulnerability is, as mentioned above, in fact decided by the specific surface area, which therefore instead must be higher in the low current density samples. This means that the low current density samples must have smaller pores and thinner pore walls than the high current density materials. The conclusion from this line of reasoning is that, while an increased current density creates a higher porosity material, a lower current density results in a denser but still higher specific surface area material.

The thinning of the sample also presents a rather peculiar problem; how does the two-layer structure occur at all etching times, when the topmost layer has the smallest pores? For this several possible explanations are proposed, but no conclusions are drawn: 1) The macroporous layer is etched away from underneath the microporous layer, which then only lies loosely on the surface; 2) the microporous structure is formed from the macroporous structure through a process which is not understood; 3) the topmost layer is formed after the etching process itself, e.g. by capillary action during drying or oxidation; or, 4) the layers are formed in an alternating manner. When looking at the cross-section images, the microporous layer is seen to pull away parts of the macroporous layer when it peels off, hence the first hypothesis seems unlikely. Due to the lack of evidence either way, no conclusions are drawn, and this is left as a note.

The structure observed on the p-type samples is quite different. Although they share some similarities with the n-type samples etched for 240 minutes, the second level of macropores is not observed, as can be seen in Figure 31. In fact, no pores are observed at all, with only a pillar structure being discernible in the SEM images. However, from the doping level of the sample calculated in section 5.2.1 and pore size dependence on doping seen in Table 4 , a pore size of 1-10nm would be expected, which is below what could be observed in the SEM that was used. From the determination of the active mass by KOH etching, it was determined that the samples had an active mass of only approximately half of that of the corresponding n-type samples. Despite this, the extremely low etch rate of the KOH would make virtually no measurable impact if there was no porous structure on the surface, supporting the presence of very small pores. In addition, as mentioned above, chemical etching by HF is more potent on structures with smaller pore diameters due to the increased surface area, which is in correlation with the smaller measured mass. As the pores are not visible on the SEM images, there is no way of classifying them as was possible on the n-type samples. However, it is concluded that these samples do in fact have a porous structure on their surfaces, and that this structure consists of micropores. Figure 60 shows an overview of how the structures of typical n-type and p-type samples evolve with etching time.

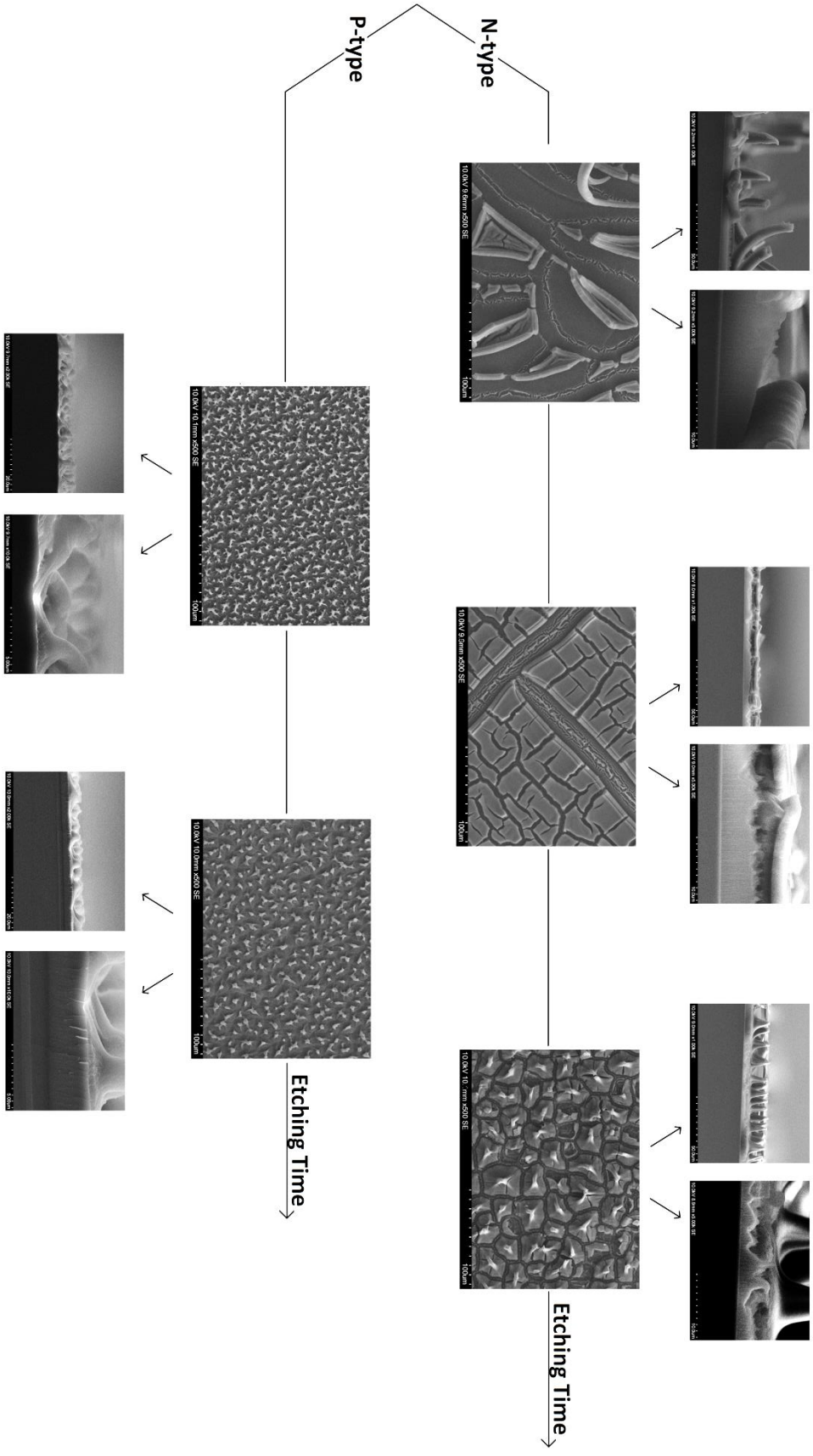

Figure 60: An overview of representative samples showing the evolution of the surface structure and cross sections of the n and p-type samples. (N-type: N_12_30, N_12_60 and N_12_240, and p-type: P_09_120 and P_09_240)

6.2 Electrochemical Testing of Porous Silicon Electrodes

Due to the low mass of porous material compared to that of the underlying material, it was expected that this would have some influence on the electrochemical testing. As it turned out, this effect was much larger than anticipated. When comparing the charge cycle stability of the samples, it can be seen from figures 34 and 35 that the performance of the electrodes, including the reference, is very similar in this regard, as none of the samples failed during the test period. It is reasoned that this is because the electrodes were tested using a capacity limitation based on the mass of porous material, which, compared to the mass of the underlying silicon, is negligibly small. As the breakdown mechanism mainly is based on the loss of active material, the electrodes could easily use several hundred cycles to break down due to the virtually unlimited supply of silicon, which, for the C-rate used in these experiments, could take several years.

Because of the long cycle life, the cycle stability cannot be used as a measure of the performance enhancing effect of a porous layer on the electrodes. But, while the cycle stability is one of the most easily interpreted measures of performance, there are a number of more subtle differences that also can give indications of what occurs inside the cells. These will be explained thoroughly in the following paragraphs.

The primary purpose of the porous silicon is to prevent cracking of the material during lithiation and delithiation. As the cracking is associated with the formation of additional SEI, the irreversible binding of lithium in this process should be reflected in the Coulombic efficiency. Figures 36 and 37 show the Coulombic efficiency of the initial 16 cycles for the non-coated and PPAN-coated samples, respectively. As can be seen, the Coulombic efficiency of the first cycle of the non-coated porous samples are approximately 40% and 43% for the p and n-type samples, respectively, versus 72% for the reference, reflecting the large surface area of these samples and the formation of the initial SEI. The low efficiency of the p-type electrode indicates that it has a higher surface area, and thus a more extensive pore structure than was observed in the SEM analysis, as hypothesized in the structural analysis. Another possible explanation is that the pillar structure of this sample could not handle the stresses formed during deintercalation of lithium, causing the pillars to break and the lithium bound in them to be lost, thus lowering the Coulombic efficiency.

The corresponding values for the PPAN coated electrodes was 74%, 47% and 73% for the n-type, p-type and reference, respectively, showing that carbon coating yields a clear improvement for the n-type porous electrode, while only having a moderate effect on the p-type and references samples. This can be seen in the comparisons of the Coulombic efficiency of the non-coated and carbon coated versions of the n-type, p-type and reference electrodes found in figures 38, 39 and 40. Carbon coating is known to facilitate the formation of a thinner and more stable SEI, binding less lithium. The effect of the carbon coating should therefore be more evident on the high surface area porous structure. While the lack of effect on the reference electrode was expected due to the limited surface area, the limited change on the p-type electrode was not. However, while limited, the effect on the p-type electrode lasted throughout the cycling. The positive effect on the n-type electrode, on the other hand, while large, was only evident in the first cycle. This varying effect of carbon coating on the two structures indicates that some additional mechanism has affected one or both of these electrodes.

The voltage-time curves of the first charge-discharge cycle of the electrodes are seen in Figure 41. As most of the processes occurring in the cell are electrochemically driven and therefore happen at certain potentials, these curves contain a lot of information about passivation phenomena occurring, most notably SEI formation. Lithium intercalation into silicon happens in the area around 0.1 V, and is seen as the plateau at this voltage, forming at various times for the different samples. In the time before this plateau is reached, a range of higher potential reactions are believed to occur, together forming the SEI. As the current is constant, the time it takes before the voltage levels out is therefore an indication of how much lithium is irreversibly bound in the SEI formation. Or the other way around; the longer the sample is at the plateau, the more lithium is stored reversibly. The latter should be reflected in the duration of the delithiation, and thus also in the Coulombic efficiency of the cycle. A comparison of figure 41 with figures 36 and 37 show this correlation clearly, with one exception; the uncoated n-type sample, which reaches the plateau relatively quickly but still has a low Coulombic efficiency, indicating some additional loss mechanism. To compare the results without these effects, figures 42 to 44 show comparisons between the V-t curves for the initial cycle of the non-coated and carbon-coated versions of the n-type, p-type and reference samples, respectively. These show that all the carbon coated samples approach the plateau more quickly than their non-coated counterparts, as well as releasing more lithium during delithiation. Again, the effect is more pronounced for the n-type sample, but is also clearly evident in the p-type and reference samples.

While the initial cycle is important for the initial SEI formation, the Coulombic efficiency for the continuing cycles is an important measure on the SEI stability, which is known to be an issue with silicon anodes. When comparing the Coulombic efficiency of the uncoated samples, the general trend is that the reference performs better than the n-type electrode, which again performs better than the p-type electrode. This is in correlation with the assumed surface area of the samples, indicating the failure to form a stable SEI, causing a continuous irreversible loss of lithium. For the PPAN coated electrodes, on the other hand, the results are very different. For the n-type electrodes, the initial cycle saw an immense improvement with the PPAN coating. However, for the continuing cycles, the efficiency was seen to fall below that of the uncoated electrode. The p-type electrode on the other hand, while showing only a modest improvement on the initial cycle, continued to show an improved efficiency in the following cycles as well. With the reference showing only a minute change, this results in the p-type sample performing better than the reference, which again is better than the n-type. Why the p-type electrode exhibit such a large performance enhancement from carbon coating while the n-type does not is obviously a complicated issue.

Another issue presented by the large amount of solid silicon relative to porous silicon, is that the porous silicon layer could disintegrate without any immediate alarming effects. Whether or not this happens is therefore an important determination to make, and if so; when. As the porous material should ideally be better at handling the large volume change of lithium intercalation, ideally, this could be seen from the Coulombic efficiency, which would degrade in parallel with the porous material. However, due to the good performance of the reference, this becomes a more complicated task. In fact, for the uncoated electrode, the reference was seen to have a higher Coulombic efficiency than the porous electrodes, rendering this method useless. It is hypothesized that the reason why the reference behaves better than bulk silicon generally does,

is the very small degree of lithiation the electrode actually goes through. An assumed active mass of 0.1 mg silicon was used to limit the current on the reference samples as well, an amount which is equivalent to a 1.5 µm thick layer on a 0.25 cm^2 electrode. This is only slightly thicker than the upper working limit for a thin film electrode. Even though it is assumed that diffusion limitations keep the lithium in the surface region of the electrode, the large volume of silicon underneath will most certainly accommodate at least some of the lithium, as well as absorb some of the stresses formed. As this renders analysis of the Coulombic efficiency inaccurate in this regard, another method must be employed to detect the presence of porous material. One tool which can reveal some information about this is the voltage-time curves, more specifically overvoltage.

Overvoltage can in many cases be a good measure of the resistance the system provides against the intercalation and deintercalation of lithium in and out of the electrode. The overvoltage can be seen in the voltage-time curves as the "recoil"-like behavior of the voltage during the rest steps after the electrode reaches the cut-off voltages or capacities. Several processes affect the overvoltage; an immediate voltage drop is expected as the current is stopped, due to the disappearance of the ohmic voltage drop in the cell. However, even though the ohmic resistance in the cells used in this study is considerable, the low currents used render the ohmic voltage drop as too small to be of any consequence. Since the connection between the silicon wafer and titanium coin is made purely by pressing them together, there is also the possibility of a Schottky barrier forming in this junction. However, silicon-titanium Schottky diodes have been reported to have barrier height of 0.5 and 0.61 volts for n and p-type silicon, respectively (Cowley, 1970). As overvoltages of this magnitude are not observed in these samples, it is assumed that conduction is facilitated through alternative interphases.

The overvoltage for these cells is thus assumed to be caused mainly by limited diffusion rate of lithium into the silicon structure. The porous structure is believed to greatly increase the diffusion kinetics of the intercalation process due to the high specific surface area and smaller required diffusion distance relative to the solid reference electrode. This is the same reasoning that was employed when determining that the porous silicon would be preferentially lithiated compared to the underlying wafer. For the same current densities, a larger concentration gradient would have to be established in the solid reference than in the pore walls of the porous structure. Formation of this concentration gradient is associated with an overvoltage, which therefore should be far higher for the reference electrodes. The diffusion-limited contribution to the overvoltage is distinguished from the ohmic contribution by its temporal dependency; as it is caused by concentration gradients, when the current is stopped, it gradually diminishes as the lithium distributes itself in the electrode. The V-t curve for the 8^{th} cycle for the non-coated electrodes is seen in figure 45, shifted so that they start simultaneously. As the cut-off voltage is the same for all samples, the overvoltage is approximated from the voltage fall during the rest cycle; the longer the fall, the higher the overvoltage. This figure shows that the overvoltage is most evident in the rest step after the delithiation, as the delithiation happens further from the equilibrium voltage than the lithiation. It also shows that the overvoltage increases markedly from the p-type electrode to the n-type, and further to the reference. Figure 50 displays the evolution of the post-rest voltage of the non-coated samples during cycling, showing that this order stays the same throughout the cycling, indicating that the porous layer is maintained. This

is in agreement with the assumed pore sizes, and thus also the diffusion distance of the lithium during lithiation.

Figure 46 and 51 show the corresponding data for the PPAN-coated samples. For these samples, the order of performance is different, with the n-type porous sample working at the highest overvoltage. This result is quite interesting, as it indicates that the diffusion kinetics of the n-type porous sample is even lower than the non-porous reference. With this in mind, a second look at the 1st cycle voltage-time curves immediately draws attention to the similarities between this sample and the non-porous references. In fact, the PPAN coated reference and n-type electrodes exhibit an almost improbable similarity, considering the different treatments they have been subject to. It is thus hypothesized that the pore structure of the n-type sample was destroyed during the carbon coating process, e.g. by capillary action during the evaporation of the DMF used to dissolve the PAN. The rapid SEI formation and high Coulombic efficiency of the initial cycle would be thus caused by the low active surface area of the underlying wafer. This would also explain the high Coulombic efficiency of the initial cycle and, in addition to the diffusion barrier expected to form from the porous silicon/PPAN deactivated layer, the high overvoltage.

It was previously mentioned that the non-coated n-type sample exhibited an inconsistency with regard to the length of the voltage plateau during lithiation and the Coulombic efficiency, indicating an additional loss mechanism to SEI formation. This loss is consistent with a part of the porous layer loosing electrical contact with the rest of the electrode at some time during the first cycle. This also agrees with the overvoltages observed, where the uncoated n-type electrode performed better than the reference, but worse than the p-type. It is thus concluded from the electrochemical testing that the n-type electrodes seem to be too fragile for both carbon coating and uncoated cycling.

This might seem surprising with regard to the p-type electrodes, which are assumed to have a far finer pore structure than the n-type electrodes. It could be explained, however, by the latter electrode's two layer structure. As seen from the cross sectional SEM-images of the n-type samples, the underlying macroporous structure consist of pores several tens of micrometers in diameter. The pore walls, however, are far thinner, consisting of nanometer-sized branched structures. The upper, seemingly denser layer is supported exclusively by these, which then also is responsible for the electric conduction to and from this layer. Both the structural end electrical soundness of the structure could therefore be called into question. Post-cycle SEM characterization was performed in the n-type sample in order to establish the effect of cycling on the porous structure. The surface structure and cross sections seen in figures 57 and 58 show the severe degradation the macroporous lower layer has undergone after only one cycle. These images also show that entire sections of the upper layer have fallen off the sample, confirming the suspicion that the lower layer compromises the structural stability of the sample. The sample was also mapped using EDS, seen in figure 56, which revealed that fluorine and phosphorous were almost exclusively found on the surface of the lower layer. This is a clear indication that SEI only form on the macroporous structure, and that the upper layer therefore is inactive. This could be caused by the proposed fragility of the lower layer causing failure in the electrical connection between the upper layer and the wafer, or by passivation of the top layer caused by excessive oxidation. The latter is supported by the considerable amount of oxygen

seen on the upper layer in the EDS, but as the lower layer is proven to be very fragile, it is most probably a combination of the two. The EDS mapping also showed that the cracks seen on the sample surface was pure silicon. The lack of SEI components indicates that they were formed after the lithiation, and thus not a part of the initial structure. The formation of these cracks is most probably the cause of the reduced Coulombic efficiency of the porous sample.

6.3 Electrochemical Testing of Composite Electrodes

The composite anodes made from lithium-silicon alloy were expected to perform similarly or better than their pure silicon counterparts. Casting the electrode in its lithiated state, thus starting with a volume decrease rather than increase, was believed to result in a structure more suited to handle the consecutive volume expansion and contractions of the silicon particles. The results obtained from the testing, however, turned out to be quite different. The first Li-Si electrode was tested at a rate of C/20, similarly to the three first cycles of the porous electrodes. The voltage-time curve for the initial delithiation and the first consecutive cycle for this electrode is seen in Figure 52. The initial capacity of the electrode was assumed to be approximately 2200 mAh/g_{Si}, as this corresponds to the Li_7Si_3-phase used in its production. At C/20, the initial delithiation, if completed, would then take approximately 11 hours. As seen from the figure, the electrode reached its cut-off voltage of 1 V after only just over 100 seconds, corresponding to a discharge capacity of only 5.3 mAh/g_{Si}. This is for all intents and purposes negligible, as can be seen in the capacity curves in Figure 55. The following lithiation managed to reach 26.3 mAh/g_{Si} before triggering its cut off at 50 mV, which is still negligibly low. Due to the quick failure of the electrode, little information was yielded to establish the mechanisms behind this low capacity.

Three main hypotheses were then made. The first based on the fact that during lithiation, crystalline Li_7Si_3 is not formed. Instead, silicon loses its crystallinity and becomes amorphous, as the temperature is too low to allow for the recrystallization of new phases (cf. section 2.2.1). The effect of Li_7Si_3 itself on the cell chemistry is thus untested, and could for instance have a severely limited lithium diffusion. It was found in literature that lithium diffusion in all the intermetallic phases was several times better than in pure silicon at 415 °C (Wen and Huggins, 1981), however no literature could be found for diffusion at ambient temperature and it could therefore not be ruled out. The second hypothesis was that the unconventional PAN binder could work as a lithium diffusion barrier, and the third; that the lithiated silicon reacted with the DMF/PAN mixture during the electrode production, and thus deactivated the active material by the formation of inactive lithium compounds.

The second Li_7Si_3 electrode was cycled at an extremely low current rate and discharge cut-off at 2 volts instead of 1 volt. The purpose of this test was to determine if the electrode was diffusion limited or if the active material had in fact been deactivated during electrode production. The voltage-time curve for the initial delithiation and first cycle for this electrode is seen in Figure 53, and the capacity vs. cycle number in Figure 55. While performing slightly better at low current rates, it did not meet the expectations, having a max charge and discharge capacity of 221 mAh/g_{Si} and 127 mAh/g_{Si}, respectively, both on the first cycle. In addition to these electrodes, a reference pure silicon composite electrode was made by the exact same procedure as the first electrode, in order to establish the performance of the PAN. The voltage and capacity data for this electrode, as seen in the figures 54 and 55, shows that this electrode performs much as expected from an electrode based on hand ground silicon particulates; a high initial charge capacity of approximately 1900 mAh/g followed by a relatively quick degradation and complete failure after 15 cycles. This text-book behavior confirms that PAN performs acceptably well as binder, and thus rules out the second hypothesis. While the performance of the Li_7Si_3-composite electrode cycle at C/200 does not completely rule out the possibility of low diffusion of lithium in

Li_7Si_3, it is regarded as highly likely that some reaction between the lithiated silicon occurred in a way that deactivated the material.

6.4 Evaluation of the Experimental Procedure and Proposal for Further Work

There are several factors that contribute to reduce the robustness of the experimental procedure in this study, the most notable being the limited number of studied samples. This is a weakness that runs through the entire experimental procedure, starting with the porous silicon formation, for which only one sample were made at each parameter set. Each of these samples were cut into four electrodes, one of which was used for mass determination, one for testing without carbon coating, one for testing with carbon coating and one in reserve. To increase the robustness of the research, several samples would have to be made for each of these purposes. On the other hand, due to the time intensive nature of the etching process, SEM characterization and battery testing, this would place unrealistic demands on the limited time allotted to this work. The scope of the thesis could have been narrowed to allow for a more robust approach. However, the primary purpose of this work was to act as an introductory investigation into the formation and use of porous silicon, hence a wider scope was prioritized over robustness.

In addition to the experimental fragility, the small amount of porous material obtained on each sample compared to the underlying non-porous silicon presents a potentially major source of error. In order to remove this in future studies, it is strongly recommended that free-standing porous material be made instead of wafer-bound material, preferably in larger amounts than was obtained in this study.

For future research, other possible alterations to the experimental procedure that would be beneficial to the analysis are SEM characterization of electrodes in different stages of production; e.g. after PPAN coating, short term cycling and long term cycling. This would provide a firmer base for the conclusions drawn from the purely electrochemical data. Other characterization techniques include ellipsometry, which could be employed for a more accurate characterization of the porous structures than was possible in SEM, and Brunauer–Emmett–Teller (BET) analysis, which could be used to determine the specific surface area of the sample. TEM could also be useful, due to its higher resolution and electron energy loss spectroscopy (EELS) capabilities, which in contrast to EDS can detect lithium. While these methods of characterization were deemed too time consuming for this study, they would provide a more thorough understanding of the structures formed.

This field of research is in its infancy, hence there are a number of possible routes for further research. While structures of different pore size were formed in this study, the morphology of the structures themselves was too different to attribute the difference in performance to a single parameter. This research could therefore be continued by making porous structures of similar morphology, but with a single clearly determined and changing parameter, e.g. pore size or porosity, to study the effects of this parameter independently. Another possibility is a study of the effect of SEI stabilizing agents or different surface coatings, which, due to the very large surface area of the structures formed, is expected to be substantial.

7 Conclusions

From the analysis of the results described in the previous section, a number of conclusions can be drawn. As this study was meant to be an introductory part of a broader research effort, conclusions related to the experimental procedure are regarded as equally important as those related to the results themselves.

Formation of porous structures:

- It has been determined that a two-layer structure consisting of a top microporous layer and a bottom mesoporous layer is formed during etching of the n-type wafers at the etching conditions used. The mesopores were vertically oriented and heavily branched, while the micropores were dense and seemingly random. From the p-type wafers etched under similar conditions, a single layer of microporous material was formed, the layer itself shaped in a pillar structure.
- The pore size of the material increased following an increase in current density and etching time, with a more pronounced dependency on the former.
- The thickness of the porous layer was similar for all the samples, resulting from a balance between the electrochemical and chemical etching processes; the former producing porous material and the latter dissolving it.
- This balance results in a moving of the etching front, the speed of which is constant throughout the etching, as well as exhibiting only a minor dependency of the current density.
- The independency of the etching speed of current density means that the porosity of the material must necessarily increase with the current density.
- The specific surface area of the structures decreases with increasing current density. As this is in contrast to the porosity, by using a lower current density, a denser material with higher specific surface area is obtained, which is beneficial for an electrode material.

Electrochemical testing of porous electrodes:

- The electrochemical discharge capacity of all the wafer-based electrodes stabilizes at a high value of 3000 mAh/g within 8 cycles, and does not notably decrease during the rest of the cycling (46 cycles for the longest running electrode).
- The overvoltage of the lithium extraction showed that there was a higher barrier for the extraction of lithium from the solid electrodes than from the porous electrodes. This indicates faster diffusion kinetics for the materials with a higher surface area. Thus, the porous structure is sustained in the electrode during the cycling.
- The effect of the PPAN-coating was primarily seen in an increased Coulombic efficiency. The magnitude of the effect depended on the surface area of the samples; it was largest for the p-type sample and negligible for the compact wafer. The n-type porous material was destroyed during the coating process and this electrode thus behaved much like the reference.
- The Coulombic efficiency of the initial cycles was very low for the porous electrodes, which is attributed to the large SEI that had to be formed. After stabilization, the wafer reference electrode had the highest Coulombic efficiency of the non-coated electrodes

at 98.5-99.5%, with the n and p-type the porous electrodes following at 98.0-98.5 and 97.0-98.0%, respectively. For the carbon coated electrodes, the reference electrode did not change, the n-type was similar to the reference, and the p-type had improved to a stable efficiency above 99%.

- From the post cycling SEM-analysis of the n-type sample, we conclude that at least some of the porous material is lost during the initial cycle. It was also observed that the SEI formation was mostly confined to the lower layer of the two-layer structure, indicating a partial deactivation of the top layer. It is believed that this is caused by the poor electrical connection between this layer and the wafer. In combination with its inability to be carbon coated, this leads to the conclusion that the n-type two-layer structure is unsuitable for use as electrodes in the manner employed in this study.
- The reason for the good performance of all the electrodes, even for the compact reference wafer, is attributed to the easy access to the solid silicon, both under the porous structures and in the solid reference electrodes. Compared to the low proportion of the porous material, the compact base constitutes a virtually unlimited supply of silicon. It is strongly recommended that a free-standing porous material will be used in future studies.

Electrochemical testing of composite electrodes:

- The composite electrodes based on Li_7Si_3 performed rather poorly during the cycling. This has been attributed to the active alloy being compromised during electrode preparation, rendering the electrochemical charge-discharge.
- The precise mechanism of contamination has not been clearly determined. However, due to the highly controlled manner in which the electrodes were made, we believe that DMF/PAN is not inert with respect to the alloy as it was initially anticipated.
- For future studies it is recommended that one of the solvents making up the electrolyte of the lithium ion battery is used instead of DMF, as the stability of these have already been successfully proved.

Finally, both n-type and p-type Si with variable doping compared to the materials used in the current research should be tried to further probe the mechanism of electrochemical etching of silicon, and to propose an efficient technology for synthesis of porous silicon.

8 References

ARMSTRONG, A. R. & BRUCE, P. G. 1996. Synthesis of layered LiMnO2 as an electrode for rechargeable lithium batteries. *Nature,* 381**,** 499-500.

AURBACH, D., TALYOSEF, Y., MARKOVSKY, B., MARKEVICH, E., ZINIGRAD, E., ASRAF, L., GNANARAJ, J. S. & KIM, H.-J. 2004. Design of electrolyte solutions for Li and Li-ion batteries: a review. *Electrochimica Acta,* 50**,** 247-254.

BALAKRISHNAN, P. G., RAMESH, R. & PREM KUMAR, T. 2006. Safety mechanisms in lithium-ion batteries. *Journal of Power Sources,* 155**,** 401-414.

BARD, A. J., PARSONS, R. & JORDAN, J. 1985. *Standard potentials in aqueous solution*.

BEALE, M. I. J., BENJAMIN, J. D., UREN, M. J., CHEW, N. G. & CULLIS, A. G. 1985. An experimental and theoretical study of the formation and microstructure of porous silicon. *Journal of Crystal Growth,* 73**,** 622-636.

BRUCE, P. G., SCROSATI, B. & TARASCON, J.-M. 2008. Nanomaterials for Rechargeable Lithium Batteries. *Angewandte Chemie International Edition,* 47**,** 2930-2946.

CAHAY, M. L., J. P.; LOCKWOOD, D. J.; BANDYOPADHYAY, S.; HARRIS, J. S. 2001. *Quantum Confinement VI: Nanostructured Materials and Devices : Proceedings of the International Symposium*, Electrochemical Society.

CHAN, C. K., PENG, H., LIU, G., MCILWRATH, K., ZHANG, X. F., HUGGINS, R. A. & CUI, Y. 2008. High-performance lithium battery anodes using silicon nanowires. *Nat Nano,* 3**,** 31-35.

CHEN, L., XIE, X., XIE, J., WANG, K. & YANG, J. 2006. Binder effect on cycling performance of silicon/carbon composite anodes for lithium ion batteries. *Journal of Applied Electrochemistry,* 36**,** 1099-1104.

COFFER, J. 1997. Porous silicon formation by stain etching. *Properties of Porous Silicon,* 18**,** 223.

CONNOLLY, D., LUND, H., MATHIESEN, B. V., PICAN, E. & LEAHY, M. 2012. The technical and economic implications of integrating fluctuating renewable energy using energy storage. *Renewable Energy,* 43**,** 47-60.

COWLEY, A. M. 1970. Titanium-silicon Schottky barrier diodes. *Solid-State Electronics,* 13**,** 403-414.

CUI, L.-F., RUFFO, R., CHAN, C. K., PENG, H. & CUI, Y. 2008. Crystalline-Amorphous Core−Shell Silicon Nanowires for High Capacity and High Current Battery Electrodes. *Nano Letters,* 9**,** 491-495.

CUI, L.-F., YANG, Y., HSU, C.-M. & CUI, Y. 2009. Carbon−Silicon Core−Shell Nanowires as High Capacity Electrode for Lithium Ion Batteries. *Nano Letters,* 9**,** 3370-3374.

DEY, A. N. 1971. Electrochemical Alloying of Lithium in Organic Electrolytes. *Journal of The Electrochemical Society,* 118**,** 1547-1549.

DIMOVA-MALINOVSKA, D., SENDOVA-VASSILEVA, M., TZENOV, N. & KAMENOVA, M. 1997. Preparation of thin porous silicon layers by stain etching. *Thin Solid Films,* 297**,** 9-12.

DUNN, B., KAMATH, H. & TARASCON, J.-M. 2011. Electrical Energy Storage for the Grid: A Battery of Choices. *Science,* 334**,** 928-935.

ETACHERI, V., HAIK, O., GOFFER, Y., ROBERTS, G. A., STEFAN, I. C., FASCHING, R. & AURBACH, D. 2011a. Effect of Fluoroethylene Carbonate (FEC) on the Performance and Surface Chemistry of Si-Nanowire Li-Ion Battery Anodes. *Langmuir,* 28**,** 965-976.

ETACHERI, V., MAROM, R., ELAZARI, R., SALITRA, G. & AURBACH, D. 2011b. Challenges in the development of advanced Li-ion batteries: a review. *Energy & Environmental Science,* 4**,** 3243-3262.

FERGUS, J. W. 2010. Recent developments in cathode materials for lithium ion batteries. *Journal of Power Sources,* 195**,** 939-954.

FERNÁNDEZ-PEREA, R., BERMEJO, F. J., MARTÍNEZ, J. L., ENCISO, E. & VERKERK, P. 1999. Collective dynamics on a crystal composed by disparate-mass particles: Li_{22}Pb_{5}. *Physical Review E,* 59**,** 3212-3222.

FÖLL, H., CARSTENSEN, J., CHRISTOPHERSEN, M. & HASSE, G. 2000. A new view of silicon electrochemistry. *Physica Status Solidi (a),* 182**,** 7-16.

FÖLL, H., CHRISTOPHERSEN, M., CARSTENSEN, J. & HASSE, G. 2002. Formation and application of porous silicon. *Materials Science and Engineering: R: Reports,* 39**,** 93-141.

GABERSCEK, M., DOMINKO, R. & JAMNIK, J. 2007. Is small particle size more important than carbon coating? An example study on LiFePO< sub> 4</sub> cathodes. *Electrochemistry Communications,* 9**,** 2778-2783.

GARG, S., VENKATRAMAN, M. & KRISHNAMURTHY, N. 1990. The Li--Ta(Lithium--Tantalum) System. *Journal of Alloy Phase Diagrams,* 6**,** 8-9.

GE, M., RONG, J., FANG, X., ZHANG, A., LU, Y. & ZHOU, C. 2013. Scalable preparation of porous silicon nanoparticles and their application for lithium-ion battery anodes. *Nano Research***,** 1-8.

GE, M., RONG, J., FANG, X. & ZHOU, C. 2012. Porous doped silicon nanowires for lithium ion battery anode with long cycle life. *Nano letters,* 12**,** 2318-2323.

GERSSEN-GONDELACH, S. J. & FAAIJ, A. P. C. 2012. Performance of batteries for electric vehicles on short and longer term. *Journal of Power Sources,* 212**,** 111-129.

GNANARAJ, J. S., LEVI, M. D., GOFER, Y., AURBACH, D. & SCHMIDT, M. 2003. LiPF3 (CF 2 CF 3) 3 : A Salt for Rechargeable Lithium Ion Batteries. *Journal of The Electrochemical Society,* 150**,** A445-A454.

HAAS, O. & CAIRNS, E. J. 1999. . Electrochemical energy storage. *Annual Reports Section" C"(Physical Chemistry),* 95**,** 163-198.

HALIMAOUI, A. 1997. Porous silicon formation by anodisation. *Properties of porous silicon,* 18**,** 12-22.

HUANG, Z., GEYER, N., WERNER, P., DE BOOR, J. & GÖSELE, U. 2011. Metal-Assisted Chemical Etching of Silicon: A Review. *Advanced materials,* 23**,** 285-308.

JAE-HONG, K., SOO-HONG, L. & BYEONG-KWON, J. 2007. Screen-printed multicrystalline silicon solar cells with porous silicon antireflective layer formed by electrochemical etching. *Journal of Applied Physics,* 101**,** 104515-104515-4.

JANSEN, A. N., KAHAIAN, A. J., KEPLER, K. D., NELSON, P. A., AMINE, K., DEES, D. W., VISSERS, D. R. & THACKERAY, M. M. 1999. Development of a high-power lithium-ion battery. *Journal of Power Sources,* 81–82**,** 902-905.

KASAVAJJULA, U., WANG, C. & APPLEBY, A. J. 2007. Nano-and bulk-silicon-based insertion anodes for lithium-ion secondary cells. *Journal of Power Sources,* 163**,** 1003-1039.

KUZMA-FILIPEK, I., NIEUWENHUYSEN, K. V., HOEYMISSEN, J. V., PAYO, M. R., KERSCHAVER, E. V., POORTMANS, J., MERTENS, R., BEAUCARNE, G., SCHMICH, E., LINDEKUGEL, S. & REBER, S. 2010. Efficiency (>15%) for thin-film epitaxial silicon solar cells on 70 cm2 area offspec silicon substrate using porous silicon segmented mirrors. *Progress in Photovoltaics: Research and Applications,* 18**,** 137-143.

LEE, Y. H., PAN, K. C., LIN, Y. Y., PREM KUMAR, T. & FEY, G. T. K. 2003. Lithium intercalation in graphites precipitated from pig iron melts. *Materials Chemistry and Physics,* 82**,** 750-757.

LEHMANN, V. & GOSELE, U. 1991. Porous silicon formation: A quantum wire effect. *Applied Physics Letters,* 58**,** 856-858.

LEWANDOWSKI, A. & ŚWIDERSKA-MOCEK, A. 2009. Ionic liquids as electrolytes for Li-ion batteries—An overview of electrochemical studies. *Journal of Power Sources,* 194**,** 601-609.

LIU, W.-R., GUO, Z.-Z., YOUNG, W.-S., SHIEH, D.-T., WU, H.-C., YANG, M.-H. & WU, N.-L. 2005. Effect of electrode structure on performance of Si anode in Li-ion batteries: Si particle size and conductive additive. *Journal of Power Sources,* 140**,** 139-144.

LIU, Y., XIONG, Z. H., LIU, Y., XU, S. H., LIU, X. B., DING, X. M. & HOU, X. Y. 2003. A novel method of fabricating porous silicon material: ultrasonically enhanced anodic electrochemical etching. *Solid State Communications,* 127**,** 583-588.

MANUEL STEPHAN, A. 2006. Review on gel polymer electrolytes for lithium batteries. *European Polymer Journal,* 42**,** 21-42.

MARANCHI, J. P., HEPP, A. F. & KUMTA, P. N. 2003. High Capacity, Reversible Silicon Thin-Film Anodes for Lithium-Ion Batteries. *Electrochemical and Solid-State Letters,* 6**,** A198-A201.

MARTHA, S. K., SCLAR, H., SZMUK FRAMOWITZ, Z., KOVACHEVA, D., SALIYSKI, N., GOFER, Y., SHARON, P., GOLIK, E., MARKOVSKY, B. & AURBACH, D. 2009. A comparative study of electrodes comprising nanometric and submicron particles of LiNi0.50Mn0.50O2, LiNi0.33Mn0.33Co0.33O2, and LiNi0.40Mn0.40Co0.20O2 layered compounds. *Journal of Power Sources,* 189**,** 248-255.

MELOT, B. C. & TARASCON, J. M. 2013. Design and Preparation of Materials for Advanced Electrochemical Storage. *Accounts of Chemical Research,* 46**,** 1226-1238.

MIZUSHIMA, K., JONES, P., WISEMAN, P. & GOODENOUGH, J. 1980. Li< sub> x</sub> CoO< sub> 2</sub>(0< x<-1): A new cathode material for batteries of high energy density. *Materials Research Bulletin,* 15**,** 783-789.

NAVARRO-URRIOS, D., PEREZ-PADRON, C., LORENZO, E., GABURRO, Z., OTON, C. J. & PAVESI, L. Chemical etching effects in porous silicon layers. Microtechnologies for the New Millennium 2003, 2003. International Society for Optics and Photonics, 109-116.

NG, S.-H., WANG, J., WEXLER, D., KONSTANTINOV, K., GUO, Z.-P. & LIU, H.-K. 2006. Highly Reversible Lithium Storage in Spheroidal Carbon-Coated Silicon Nanocomposites as Anodes for Lithium-Ion Batteries. *Angewandte Chemie International Edition,* 45**,** 6896-6899.

OKAMOTO, H. 1990. The Li-Si (Lithium-Silicon) system. *Bulletin of Alloy Phase Diagrams,* 11**,** 306-312.

RAI-CHOUDHURY, P. 1997. *Handbook of Microlithography, Micromachining and Microfabrication: Handbook of Microlithography*, Spie Optical Engineering Press ; Institution of Electrical Engineers.

ROUGIER, A., GRAVEREAU, P. & DELMAS, C. 1996. Optimization of the Composition of the Li1 − z Ni1 + z O 2 Electrode Materials: Structural, Magnetic, and Electrochemical Studies. *Journal of The Electrochemical Society,* 143**,** 1168-1175.

RYU, J. H., KIM, J. W., SUNG, Y.-E. & OH, S. M. 2004. Failure Modes of Silicon Powder Negative Electrode in Lithium Secondary Batteries. *Electrochemical and Solid-State Letters,* 7**,** A306-A309.

SCROSATI, B. 2000. Recent advances in lithium ion battery materials. *Electrochimica Acta,* 45**,** 2461-2466.

SELJ, J., THØGERSEN, A., FOSS, S. & MARSTEIN, E. 2011. Ellipsometric study of the influence of chemical etching on thin porous silicon structures. *Thin Solid Films,* 519**,** 2998-3001.

SELJ, J. H., TH, XF, GERSEN, A., FOSS, S. E. & MARSTEIN, E. S. 2010. Optimization of multilayer porous silicon antireflection coatings for silicon solar cells. *Journal of Applied Physics,* 107**,** 074904-074904-10.

SHEN, L., GUO, X., FANG, X., WANG, Z. & CHEN, L. 2012. Magnesiothermically reduced diatomaceous earth as a porous silicon anode material for lithium ion batteries. *Journal of Power Sources,* 213**,** 229-232.

SHI, X., WANG, C., MA, X. & SUN, J. 2009. Synthesis and electrochemical properties of LiNi0.9Co0.1O2 cathode material for lithium secondary battery. *Materials Chemistry and Physics,* 113**,** 780-783.

SHUKLA, A. & PREM KUMAR, T. 2008. Materials for next-generation lithium batteries. *Current Science,* 94**,** 314-331.

SMITH, R. L. & COLLINS, S. D. 1992. Porous silicon formation mechanisms. *Journal of Applied Physics,* 71**,** R1-R22.

STEARNS, L. A., GRYKO, J., DIEFENBACHER, J., RAMACHANDRAN, G. K. & MCMILLAN, P. F. 2003. Lithium monosilicide (LiSi), a low-dimensional silicon-based material prepared by high

pressure synthesis: NMR and vibrational spectroscopy and electrical properties characterization. *Journal of Solid State Chemistry,* 173**,** 251-258.

TAKAMURA, T., OHARA, S., UEHARA, M., SUZUKI, J. & SEKINE, K. 2004. A vacuum deposited Si film having a Li extraction capacity over 2000 mAh/g with a long cycle life. *Journal of Power Sources,* 129**,** 96-100.

THACKERAY, M. M. 1997. Manganese oxides for lithium batteries. *Progress in Solid State Chemistry,* 25**,** 1-71.

THAKUR, M., ISAACSON, M., SINSABAUGH, S. L., WONG, M. S. & BISWAL, S. L. 2012a. Gold-coated porous silicon films as anodes for lithium ion batteries. *Journal of Power Sources,* 205**,** 426-432.

THAKUR, M., PERNITES, R. B., NITTA, N., ISAACSON, M., SINSABAUGH, S. L., WONG, M. S. & BISWAL, S. L. 2012b. Freestanding Macroporous Silicon and Pyrolyzed Polyacrylonitrile As a Composite Anode for Lithium Ion Batteries. *Chemistry of Materials,* 24**,** 2998-3003.

THAKUR, M., SINSABAUGH, S. L., ISAACSON, M. J., WONG, M. S. & BISWAL, S. L. 2012c. Inexpensive method for producing macroporous silicon particulates (MPSPs) with pyrolyzed polyacrylonitrile for lithium ion batteries. *Sci. Rep.,* 2.

TURNER, D. R. 1958. Electropolishing Silicon in Hydrofluoric Acid Solutions. *Journal of The Electrochemical Society,* 105**,** 402-408.

UHLIR, A., JR. 1956. Electrolytic shaping of germanium and silicon. *The Bell System Technical Journal,* 35**,** 333-347.

UMMELS, B. C., PELGRUM, E. & KLING, W. L. 2008. Integration of large-scale wind power and use of energy storage in the netherlands' electricity supply. *Renewable Power Generation, IET,* 2**,** 34-46.

VAN DER MAREL, C., VINKE, G. J. B. & VAN DER LUGT, W. 1985. The phase diagram of the system lithium-silicon. *Solid State Communications,* 54**,** 917-919.

VAN SCHALKWIJK, W. & SCROSATI, B. 2002. *Advances in Lithium-Ion Batteries*, Springer.

VERMA, P., MAIRE, P. & NOVÁK, P. 2010. A review of the features and analyses of the solid electrolyte interphase in Li-ion batteries. *Electrochimica Acta,* 55**,** 6332-6341.

WEN, C. J. 1980. Chemical diffusion in lithium alloys. *Dissertation Abstracts International Part B: Science and Engineering[DISS. ABST. INT. PT. B- SCI. & ENG.],* 41**,** 1980.

WEN, C. J. & HUGGINS, R. A. 1981. Chemical diffusion in intermediate phases in the lithium-silicon system. *Journal of Solid State Chemistry,* 37**,** 271-278.

WHITTINGHAM, M. S. 2004. Lithium batteries and cathode materials. *Chemical Reviews-Columbus,* 104**,** 4271-4302.

WHITTINGHAM, M. S. 2012. History, Evolution, and Future Status of Energy Storage. *Proceedings of the IEEE,* 100**,** 1518-1534.

WIESER, M. 2006. Atomic weights of the elements 2005. *Pure Appl. Chem,* 78**,** 2051-2066.

WINTER, M. & BESENHARD, J. O. 1999. Electrochemical lithiation of tin and tin-based intermetallics and composites. *Electrochimica Acta,* 45**,** 31-50.

XU, K., ZHANG, S., JOW, T. R., XU, W. & ANGELL, C. A. 2002. LiBOB as Salt for Lithium-Ion Batteries:A Possible Solution for High Temperature Operation. *Electrochemical and Solid-State Letters,* 5**,** A26-A29.

YAMADA, A., CHUNG, S.-C. & HINOKUMA, K. 2001. Optimized LiFePO4 for lithium battery cathodes. *Journal of The Electrochemical Society,* 148**,** A224-A229.

YOSHINO, A. 2012. The Birth of the Lithium-Ion Battery. *Angewandte Chemie International Edition,* 51**,** 5798-5800.

YOSHINO, A., SANECHIKA, K. & NAKAJIMA, T. 1987. Secondary battery. Google Patents.

YOSHIO, M., TSUMURA, T. & DIMOV, N. 2005. Electrochemical behaviors of silicon based anode material. *Journal of Power Sources,* 146**,** 10-14.

YU, Y., GU, L., ZHU, C., TSUKIMOTO, S., VAN AKEN, P. A. & MAIER, J. 2010. Reversible Storage of Lithium in Silver-Coated Three-Dimensional Macroporous Silicon. *Advanced Materials,* 22**,** 2247-2250.

ZHANG, S. S. 2006. A review on electrolyte additives for lithium-ion batteries. *Journal of Power Sources,* 162**,** 1379-1394.

ZHANG, W.-J. 2011. A review of the electrochemical performance of alloy anodes for lithium-ion batteries. *Journal of Power Sources,* 196**,** 13-24.

ZHANG, X. G. 2004. Morphology and Formation Mechanisms of Porous Silicon. *Journal of The Electrochemical Society,* 151**,** C69-C80.

ZHANG, Y., ZHANG, X., ZHANG, H., ZHAO, Z., LI, F., LIU, C. & CHENG, H. 2006a. Composite anode material of silicon/graphite/carbon nanotubes for Li-ion batteries. *Electrochimica acta,* 51**,** 4994-5000.

ZHANG, Y., ZHANG, X. G., ZHANG, H. L., ZHAO, Z. G., LI, F., LIU, C. & CHENG, H. M. 2006b. Composite anode material of silicon/graphite/carbon nanotubes for Li-ion batteries. *Electrochimica Acta,* 51**,** 4994-5000.

ZHAO, Y., LIU, X., LI, H., ZHAI, T. & ZHOU, H. 2012. Hierarchical micro/nano porous silicon Li-ion battery anodes. *Chem. Commun.,* 48**,** 5079-5081.

ZHOU, Y.-N., LI, W.-J., CHEN, H.-J., LIU, C., ZHANG, L. & FU, Z. 2011. Nanostructured NiSi thin films as a new anode material for lithium ion batteries. *Electrochemistry Communications,* 13**,** 546-549.

Appendix A: Theoretical capacity calculations

The theoretical capacity of a material can be calculated from

$$Q_{max} = \frac{nF}{M}$$

Where n is the number of lithium ions per formula unit of the fully intercalated electrode, F is Faraday's constant and M is the total molar mass of the formula unit minus that of lithium.

For the carbon electrode:

$$Q_{max} = \frac{1 * 96485\ C/mole}{(6 * 12)\ g/mole} = 1340\frac{C}{g} = 372.2\frac{mAh}{g}$$

For $Li_{22}Si_5$:

$$Q_{max} = \frac{22 * 96485\ C/mole}{(5 * 28.09)\ g/mole} = 15113\frac{C}{g} = 4198\frac{mAh}{g}$$

For $Li_{15}Si_4$:

$$Q_{max} = \frac{15 * 96485\ C/mole}{(4 * 28.09)\ g/mole} = 12881\frac{C}{g} = 3578\frac{mAh}{g}$$

For Li_7Si_3:

$$Q_{max} = \frac{7 * 96485\ C/mole}{(3 * 28.09)\ g/mole} = 8015\frac{C}{g} = 2226\frac{mAh}{g}$$

Appendix B: Detailed experimental procedures

The slurry for the composite electrodes was prepared by the following procedure:

1. PAN and DMF were weighed out in a 1:80 mass ratio and mixed. The solution was sealed in a sample glass, removed from the glove box and put in a Branson 3510 ultrasonic bath for 40 minutes to ensure the complete dissolution of the PAN.
2. Li_7Si_3 was crushed by hand in a mortar to obtain a fine powder and a suitable amount was weighed out.
3. Carbon black was weighed out to obtain a 1:8 CB:Li_7Si_3 mass ratio.
4. PAN/DMF solution was weighed out to obtain a 81:8 PAN/DMF: Li_7Si_3 mass ratio.
5. The Li_7Si_3, carbon black and PAN were mixed and dispersed in the ultrasonic bath for 10 minutes.

The etching process was conducted using the following procedure:

1. Mounting a quartered wafer in the sample holder
2. Submerging the sample holder in the cell and tightening the bayonet hatch to properly seal the two tanks of the cell
3. Running the etching program
4. Removing the sample holder from the cell, immediately putting it in a bath of deionized water and letting it rest there for two minutes
5. Disassemble the sample holder; putting the etched sample in absolute ethanol and washing the parts of the sample holder in deionized water
6. Removing the sample and letting it dry in ambient conditions

Detailed test program for the electrochemical testing of the porous silicon electrodes:

1. 2 minute rest and open circuit voltage measurement (OCV)
2. Internal resistance (IR) measurement
3. The following cycle is repeated three times:
    A. Lithiation (charge) at C/20 with cut-off at 50 mV or 3000 mAh/g, whichever comes first
    B. IR measurement
    C. 30 minute rest and OCV
    D. Delithiation (discharge) at C/20 with cut-off at 1 V or 3000 mAh/g, whichever comes first
    E. IR measurement
    F. 30 minute rest and OCV

4. The following cycle is repeated until stopped:
    A. Lithiation (charge) at C/10 with cut-off at 50 mV or 3000 mAh/g, whichever comes first
    B. IR measurement
    C. 15 minute rest and OCV
    D. Delithiation (discharge) at C/10 with cut-off at 1 V or 3000 mAh/g, whichever comes first
    E. IR measurement
    F. 15 minute rest and OCV

Detailed test program for the electrochemical testing of the composite electrodes:

1. 2 minute rest and OCV
2. Delithiation (discharge) at C/20 with cut-off at 1 V
3. IR measurement
4. 30 minute rest and OCV
5. IR measurement
6. The following cycle is repeated two times:
    A. Lithiation (charge) at C/20 with cut-off at 50 mV or 2200 mAh/g, whichever comes first
    B. IR measurement
    C. 30 minute rest and OCV
    D. Delithiation (discharge) at C/20 with cut-off at 1 V
    E. IR measurement
    F. 30 minute rest and OCV
7. The following cycle is repeated for 50 cycles:
    A. Lithiation (charge) at C/10 with cut-off at 50 mV or 2200 mAh/g, whichever comes first
    B. IR measurement
    C. 15 minute rest and OCV
    D. Delithiation (discharge) at C/10 with cut-off at 1 V
    E. IR measurement
    F. 15 minute rest and OCV

Appendix C: NAA (Neutron Activation Analysis) of the starting silicon powder

< < < < < < < < MURR Nuclear Analysis Program Report > > > > > > > >							
Sample Name: **SEEDS**							
Description: Silicon BEADS							
Client Name: A. HOLT/IFE							
Treatment: Both short and long counts after etching sample							

Measured Element		PPB by Weight		Atoms/cc of Silicon		Element atoms per billion Silicon atoms	% ERR

Elements from SHORT count at 2.52 days							
As		2,7E-02		5,1E+11		1,0E-02	1,8
Au		1,9E-04		1,4E+09		2,8E-05	9,4
Br		6,4E-03		1,1E+11		2,3E-03	7,9
Ca	<	3,3E+01	<	1,2E+15	<	2,3E+01	
Cd	<	5,5E-02	<	7,0E+11	<	1,4E-02	
Cu		1,8E+00		3,9E+13		7,8E-01	0,6
Ga		2,0E-03		4,1E+10		8,1E-04	41,3
Ge	<	5,2E+00	<	1,0E+14	<	2,0E+00	
K		2,5E-01		9,0E+12		1,8E-01	34,4
La		7,0E-03		7,1E+10		1,4E-03	2,7
Mo		1,2E+00		1,7E+13		3,4E-01	2,3
Na		2,3E-01		1,4E+13		2,9E-01	1,3
Ti	<	6,7E+01	<	2,0E+15	<	3,9E+01	
U		1,4E-02		8,1E+10		1,6E-03	16,4
W		6,6E-02		5,0E+11		1,0E-02	1,6
Elements from LONG count at 16.50 days							
Ag		1,9E-01		2,5E+12		5,0E-02	1,6
Ba	<	2,5E-01	<	2,6E+12	<	5,1E-02	
Ce	<	1,9E-02	<	1,9E+11	<	3,7E-03	
Co		4,7E-02		1,1E+12		2,3E-02	1,3
Cr		1,2E+01		3,3E+14		6,6E+00	0,2
Cs	<	9,0E-04	<	9,5E+09	<	1,9E-04	
Eu		3,4E-04		3,2E+09		6,3E-05	25,3
Fe		1,3E+01		3,4E+14		6,7E+00	2,7
Hf		7,0E-03		5,6E+10		1,1E-03	5,8
Hg	<	5,6E-03	<	4,0E+10	<	7,9E-04	
In	<	5,4E-02	<	6,6E+11	<	1,3E-02	
Ir	<	3,5E-05	<	2,6E+08	<	5,1E-06	
Ni		5,7E+00		1,4E+14		2,7E+00	3,8
Pt	<	4,6E+00	<	3,4E+13	<	6,7E-01	
Rb	<	2,1E-02	<	3,5E+11	<	7,0E-03	
Sb		2,2E-02		2,6E+11		5,2E-03	3,5
Sc		3,5E-04		1,1E+10		2,2E-04	6,4

Se	<	1,6E-02	<	2,9E+11	<	5,7E-03	
Sn	<	8,3E-01	<	9,9E+12	<	2,0E-01	
Sr	<	5,1E-01	<	8,3E+12	<	1,6E-01	
Ta	<	6,2E-04	<	4,9E+09	<	9,7E-05	
Tb	<	4,4E-04	<	3,9E+09	<	7,7E-05	
Th		3,4E-03		2,1E+10		4,1E-04	15,8
Yb	<	2,0E-03	<	1,6E+10	<	3,2E-04	
Zn		2,2E-01		4,8E+12		9,6E-02	6,4
Zr	<	3,7E-01	<	5,7E+12	<	1,1E-01	

Date Reported: 01-OCT-2010							

Appendix D: Evaluated XRD pattern for alloy 1

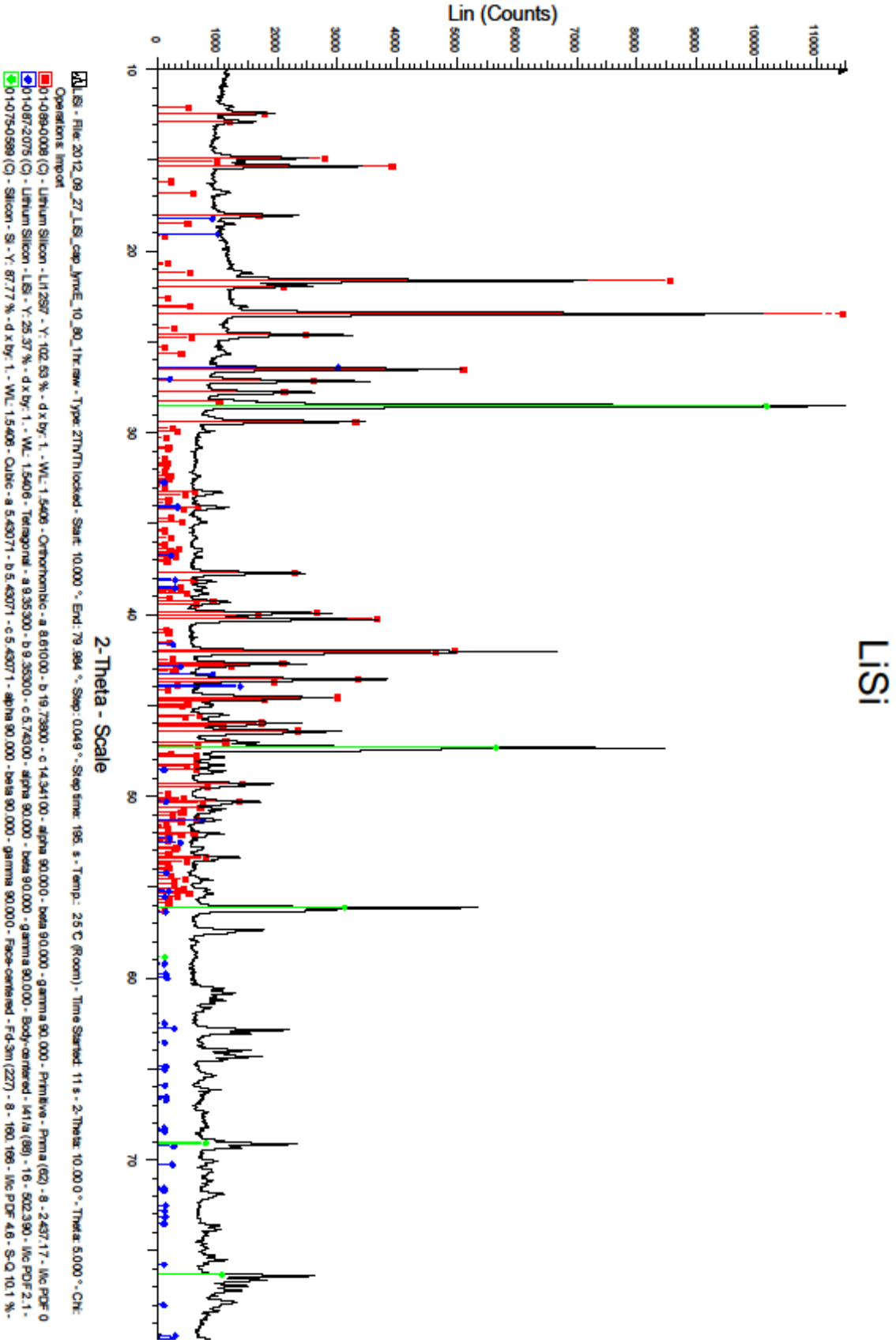

Appendix E: Evaluated XRD pattern for alloy 2

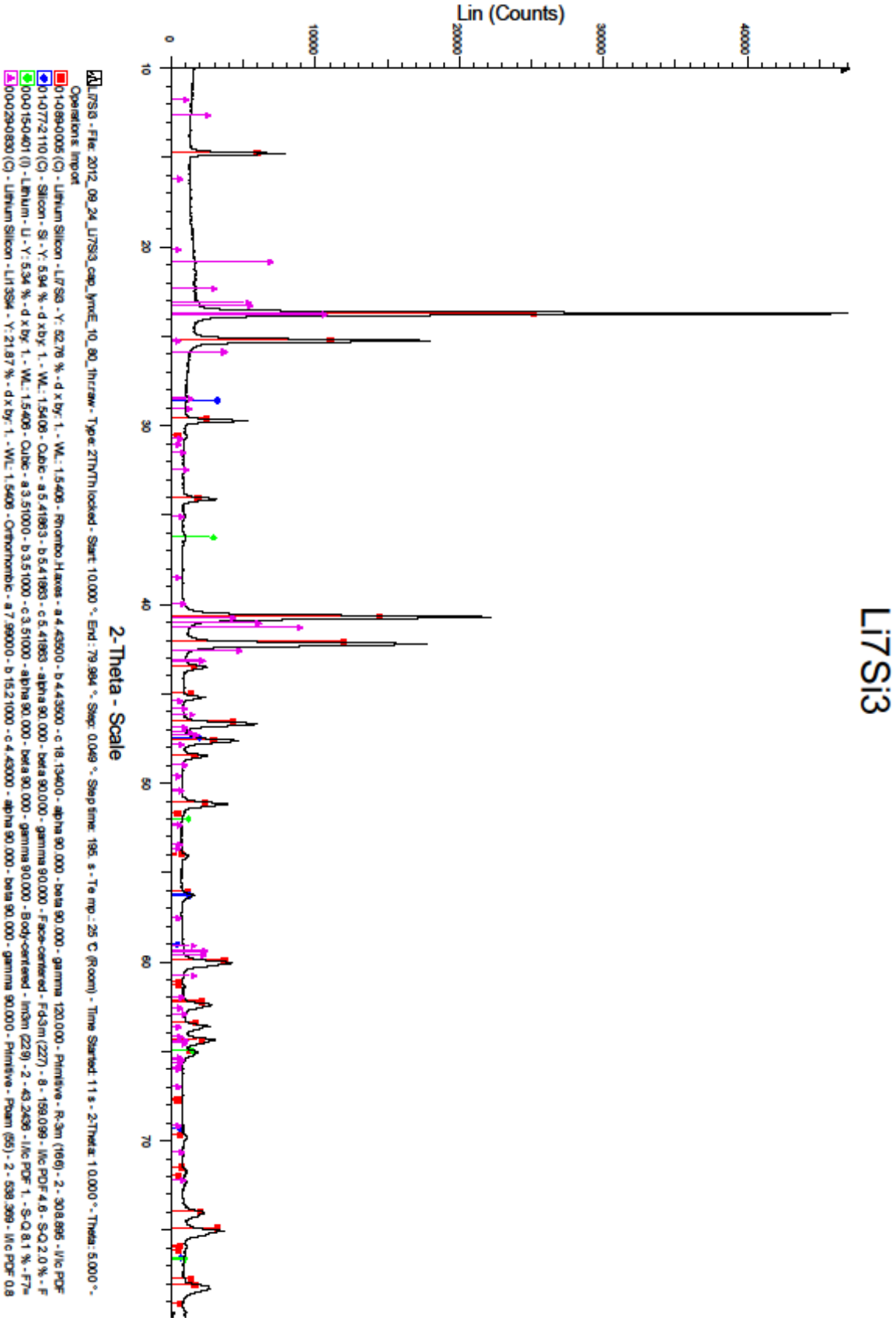

Appendix F: Evaluated XRD pattern for alloy 3

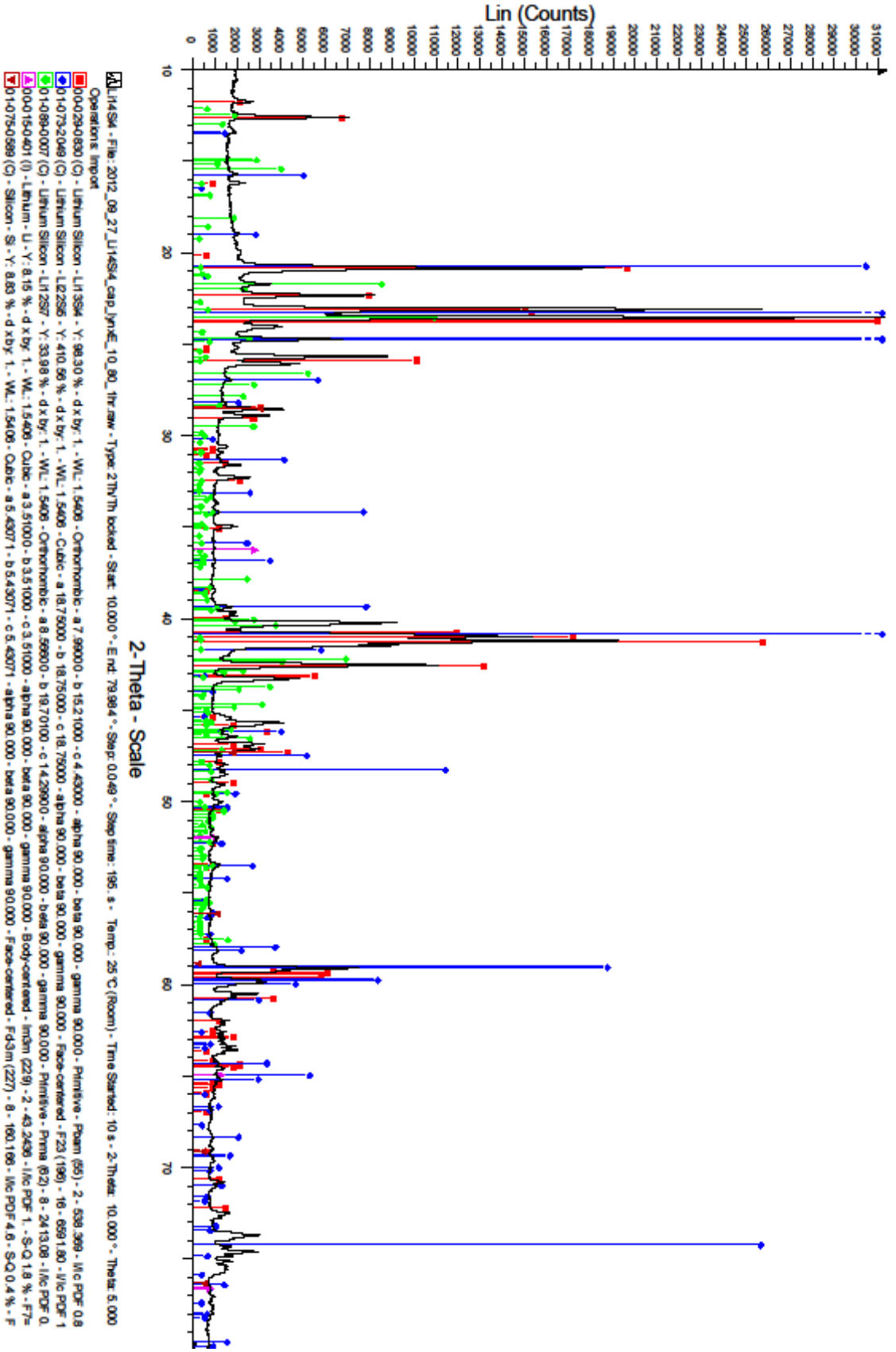

Appendix G: SEM images of the surface structure of the porous samples

Sample: N_04_30

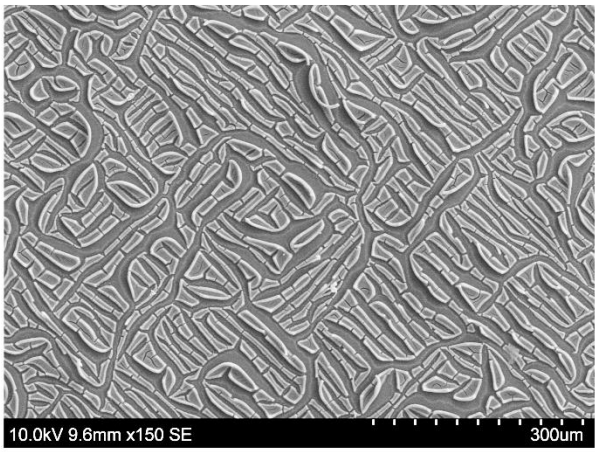

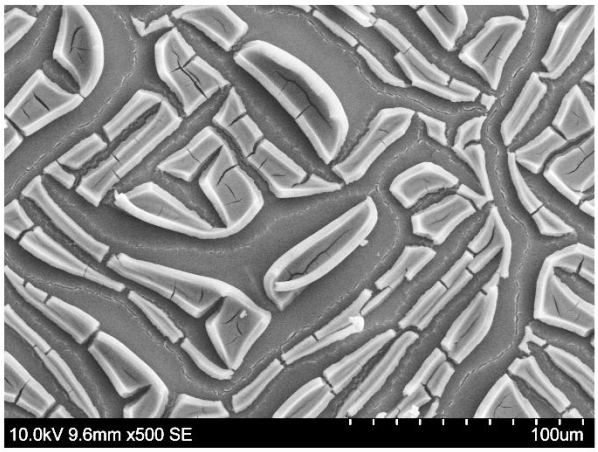

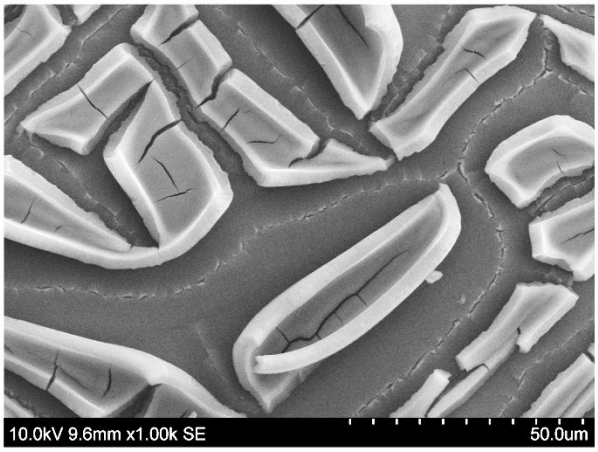

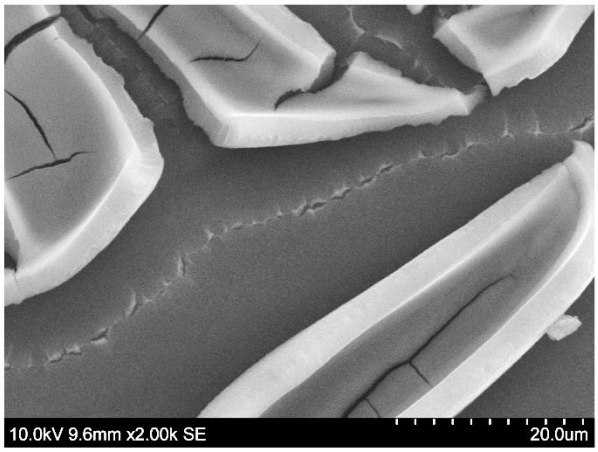

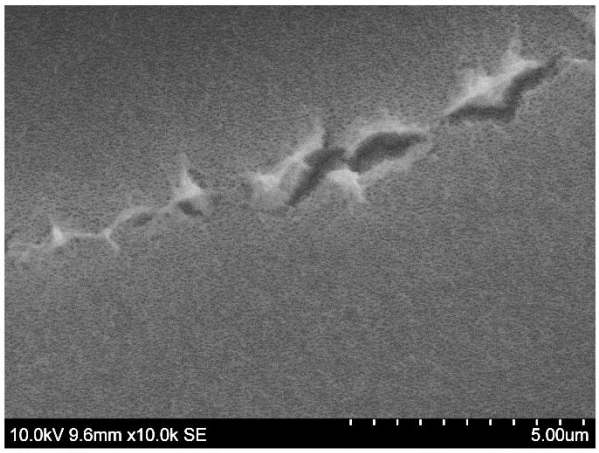

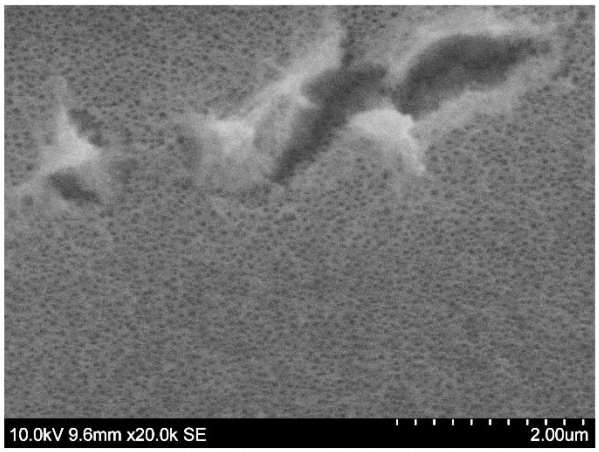

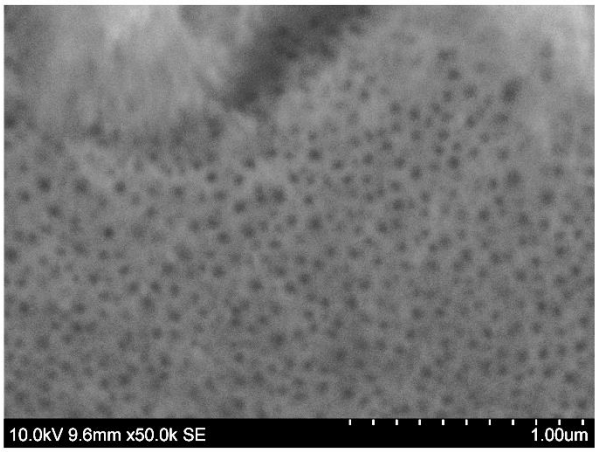

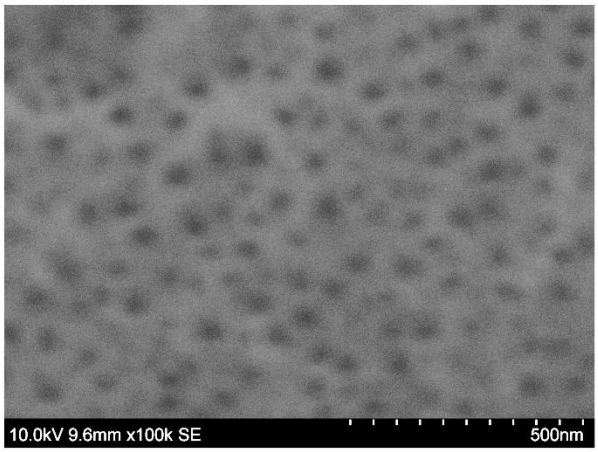

Sample: N_06_30

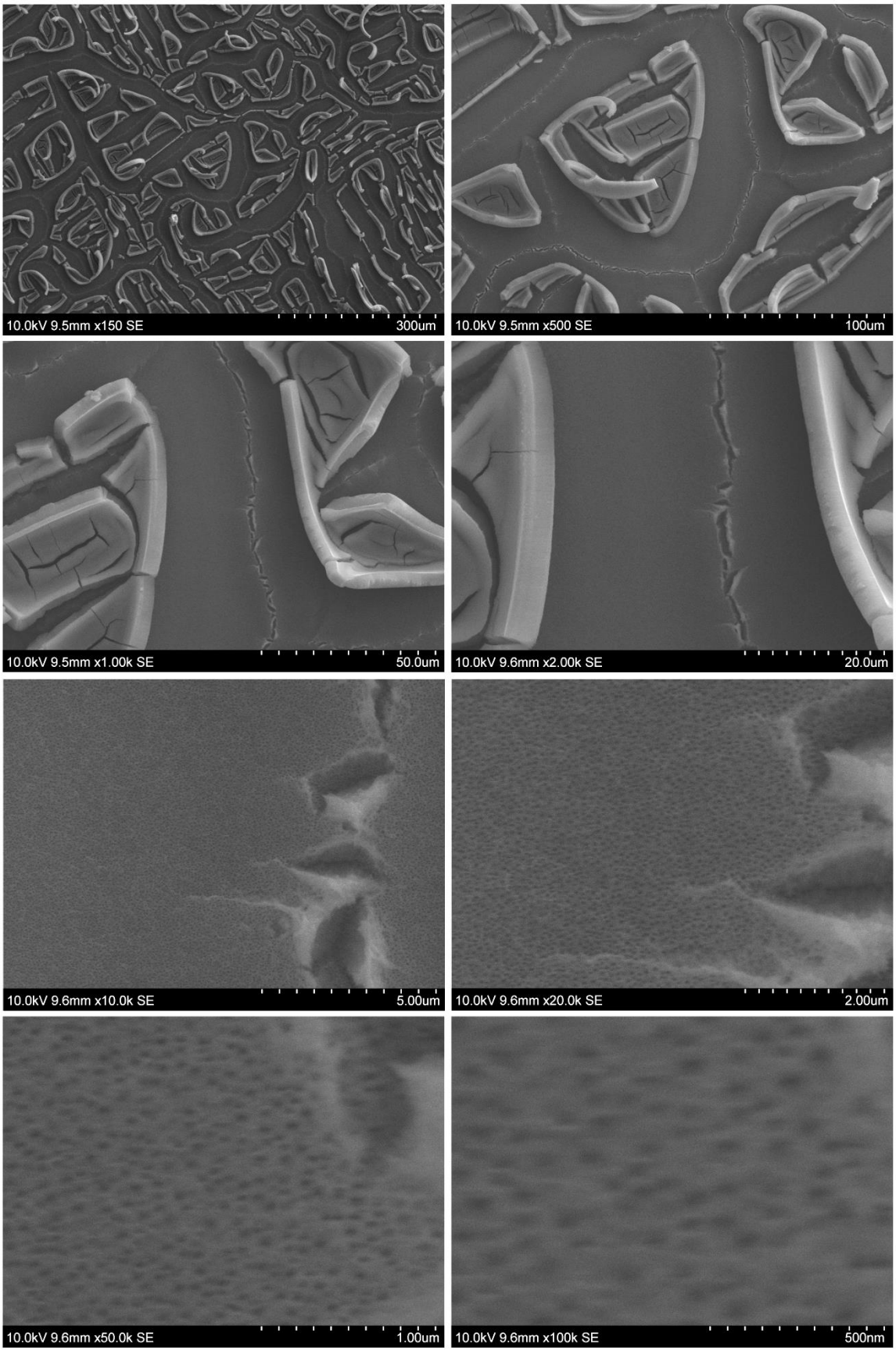

Sample: N_09_30

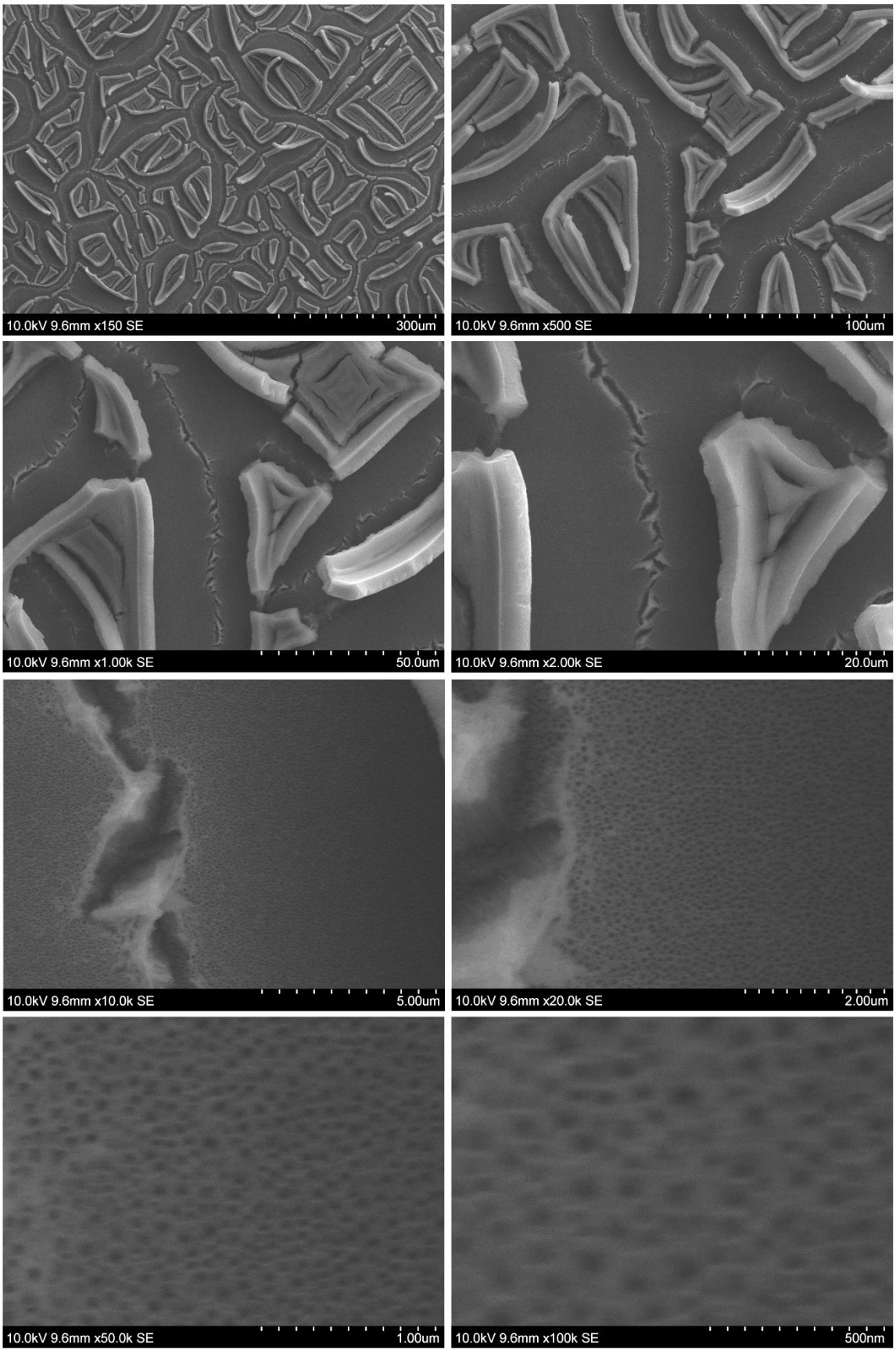

Sample: N_12_30

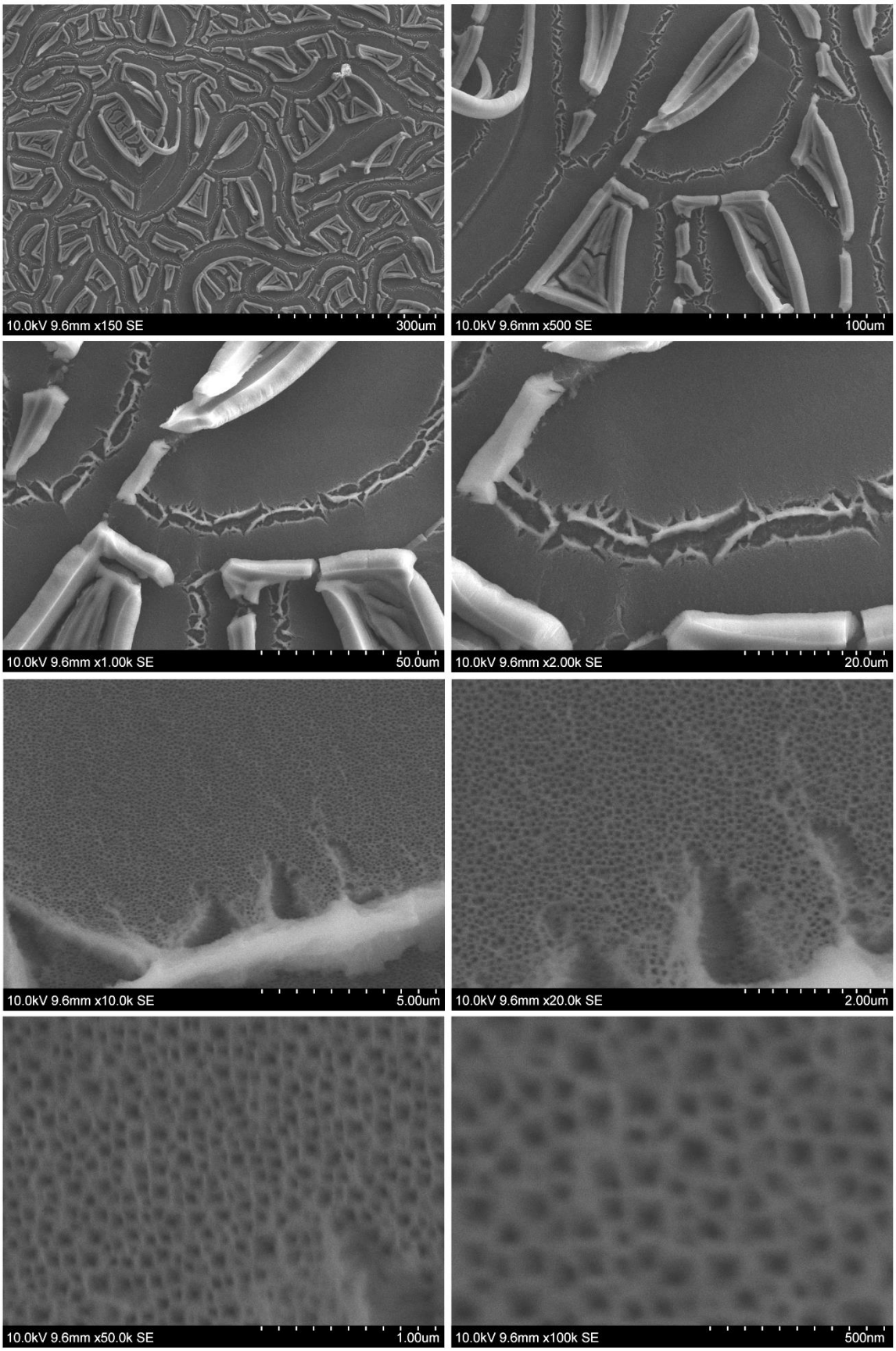

Sample: N_MAX_30

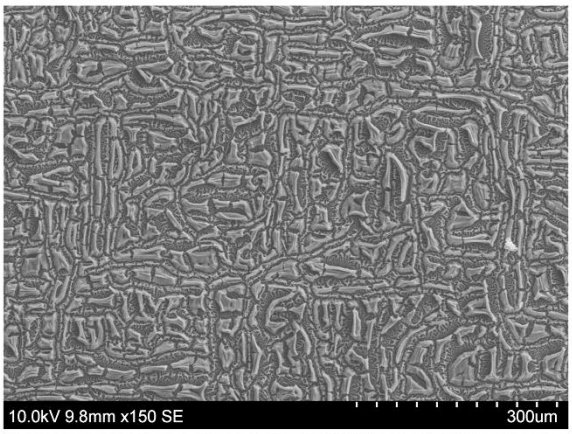

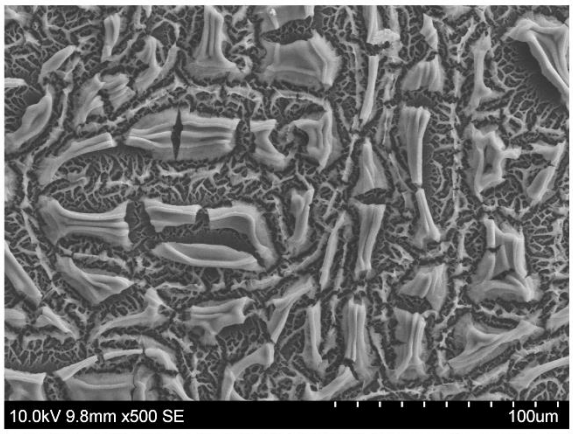

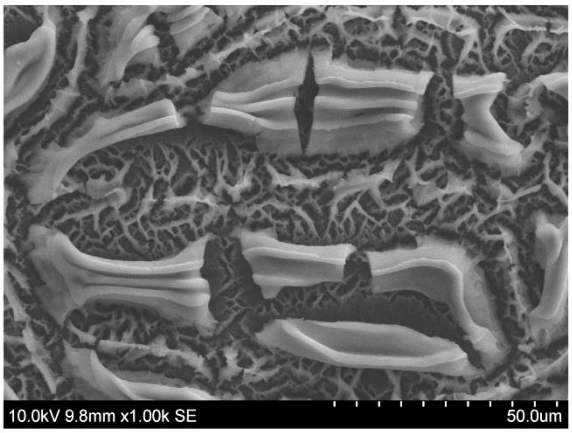

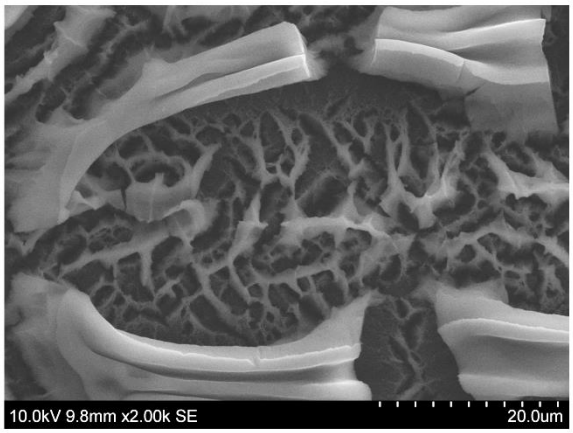

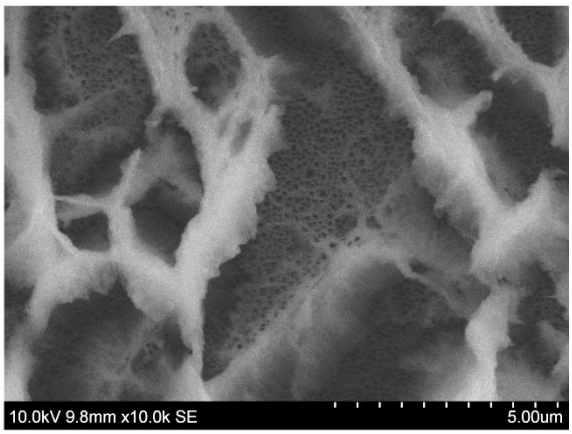

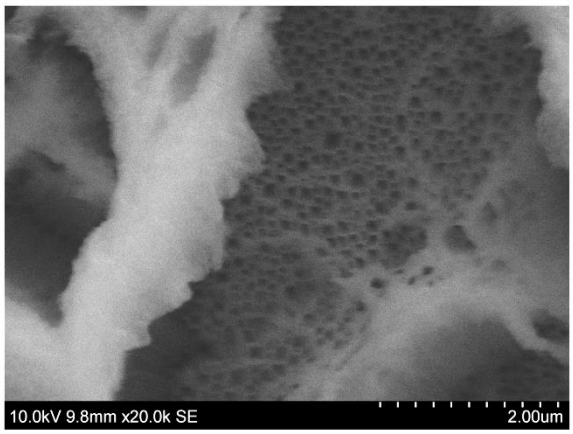

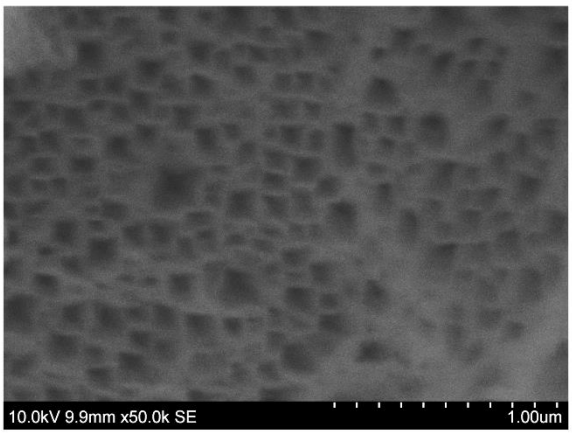

Sample: N_04_60 (First sample analyzed, hence focus was mainly on peculiar formations)

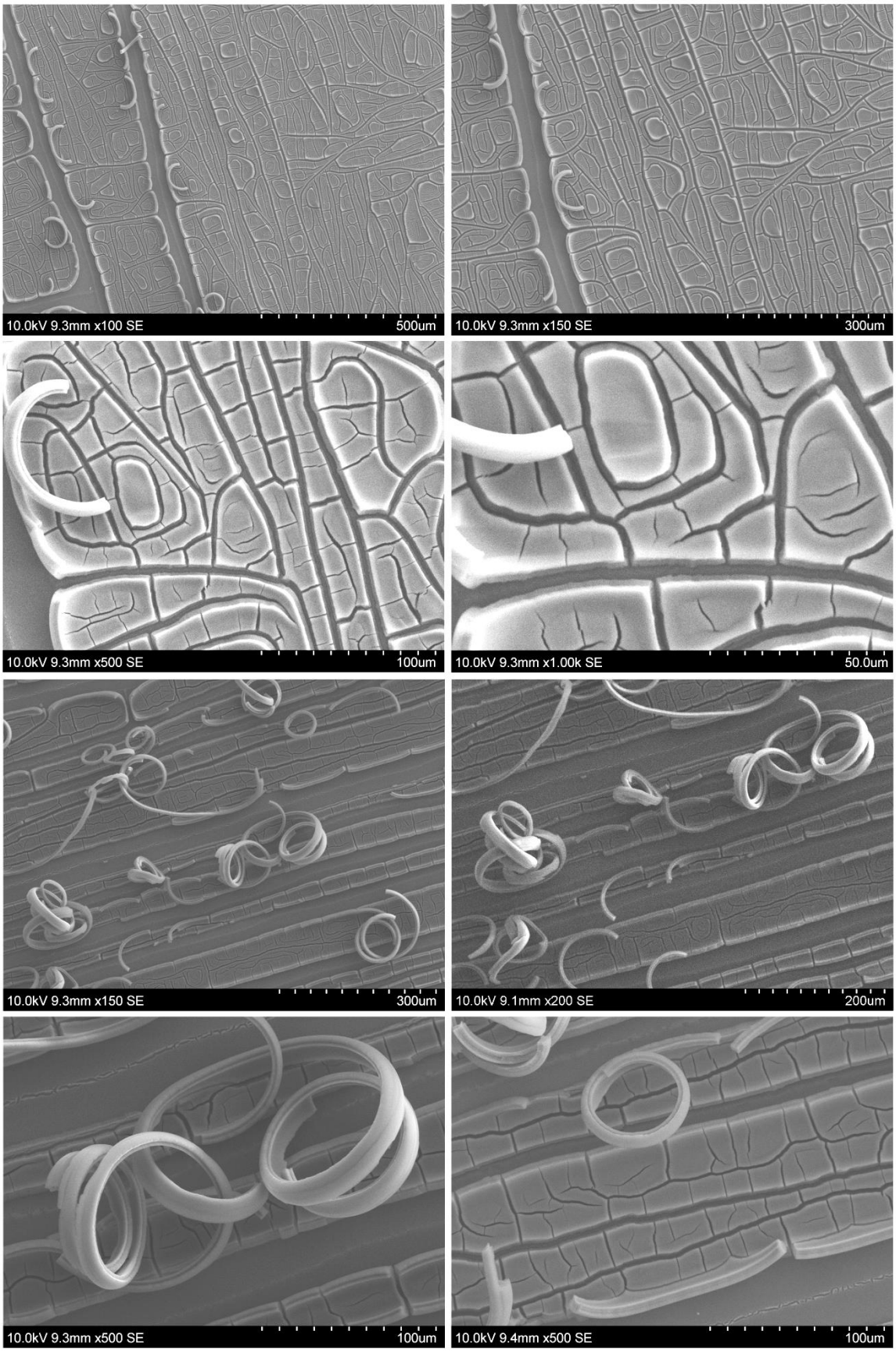

Sample: N_06_60 (Second sample analyzed, initial discovery of lower porous structure)

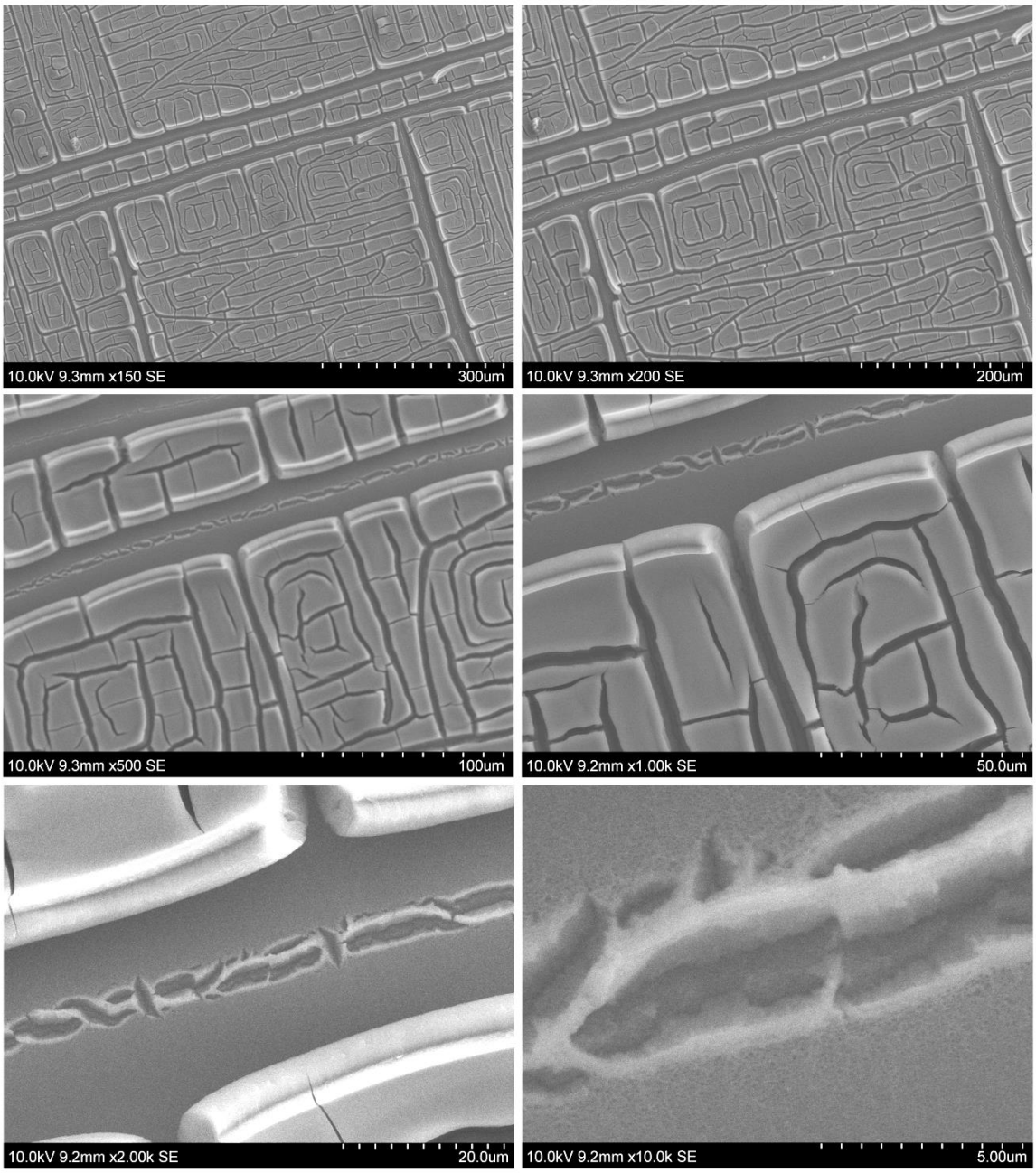

Sample: N_09_60

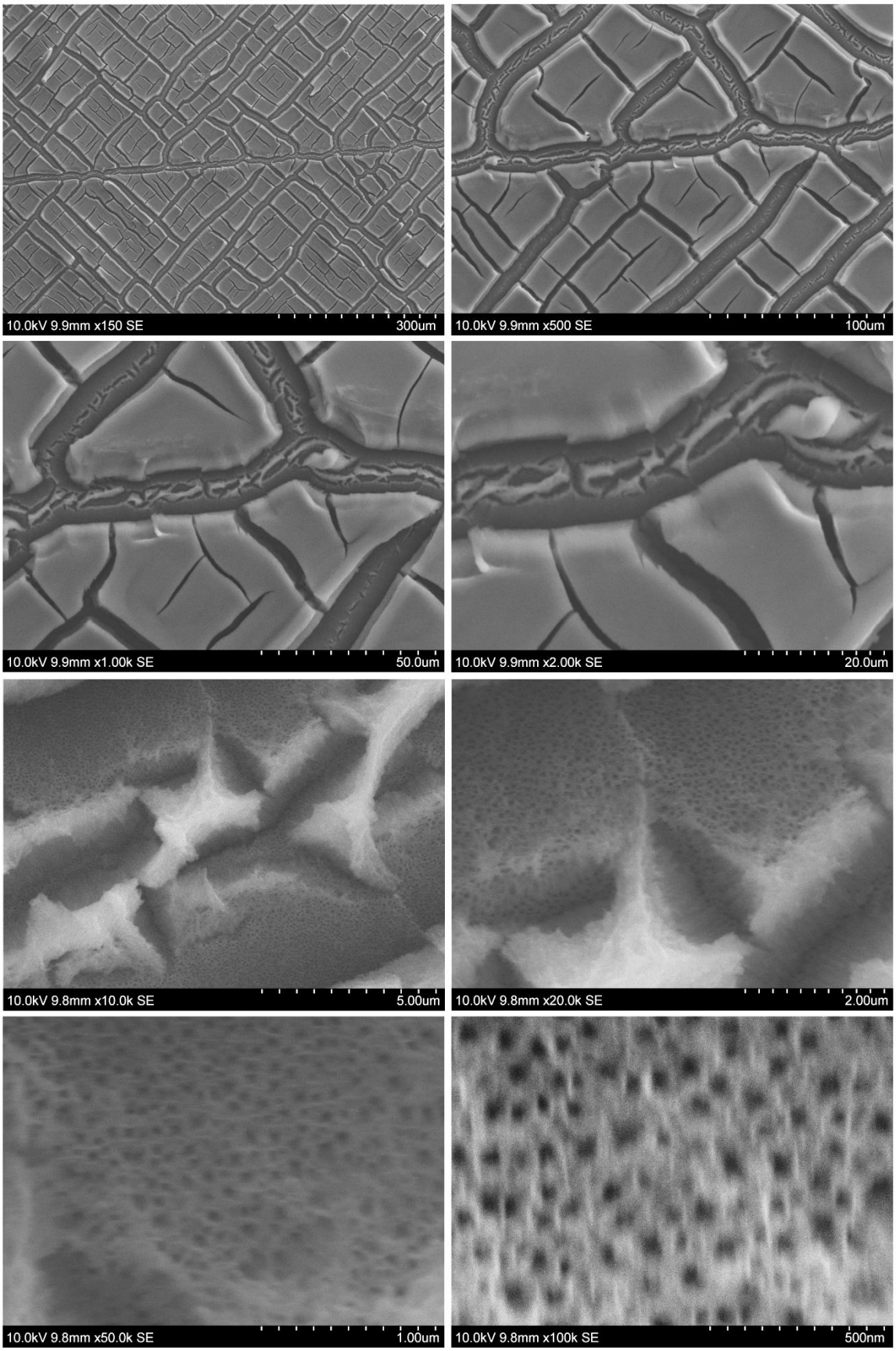

Sample N_12_60

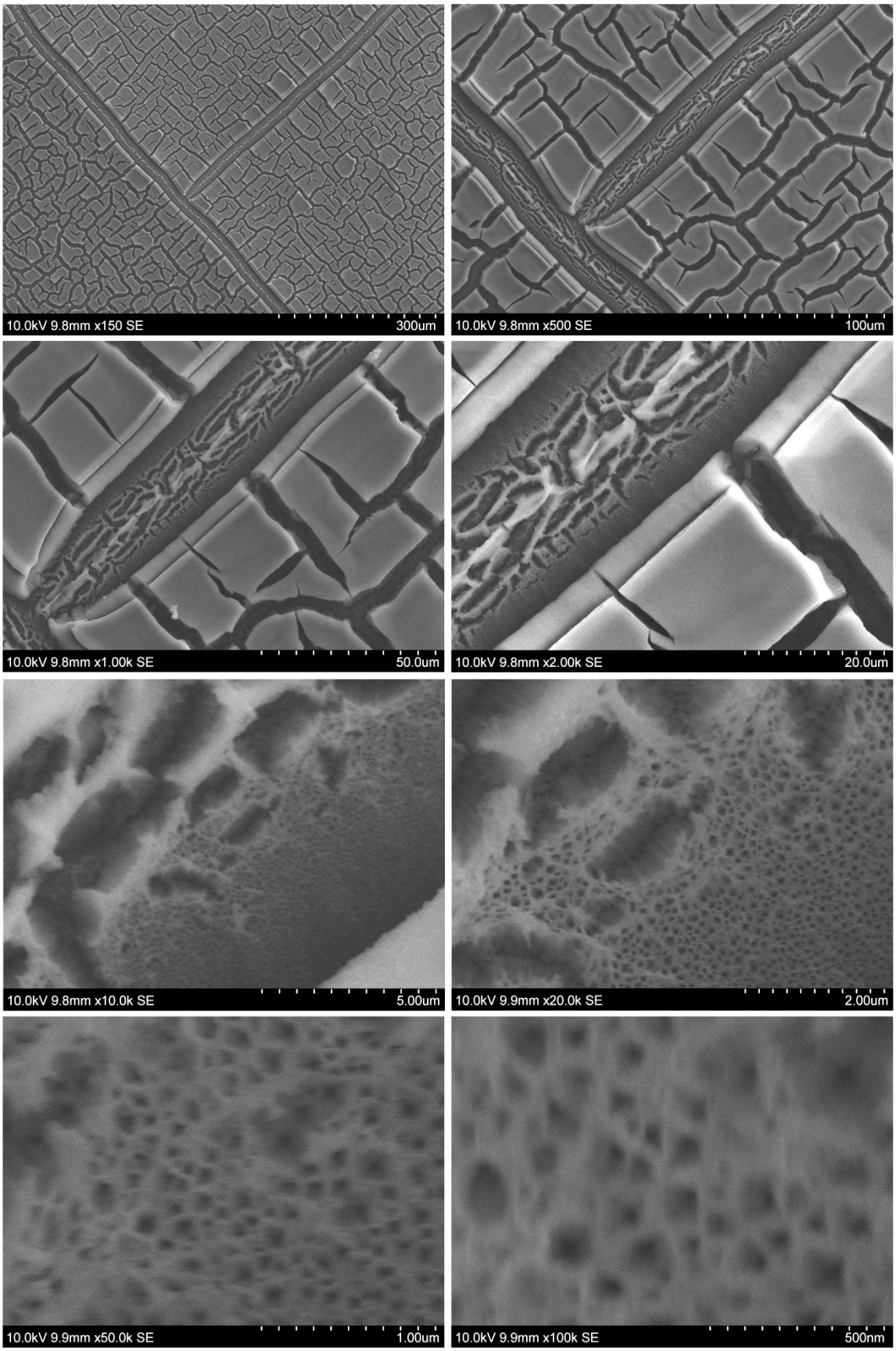

Sample: N_09_120

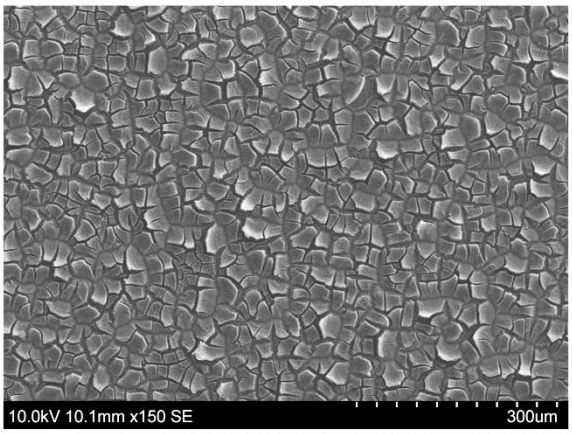

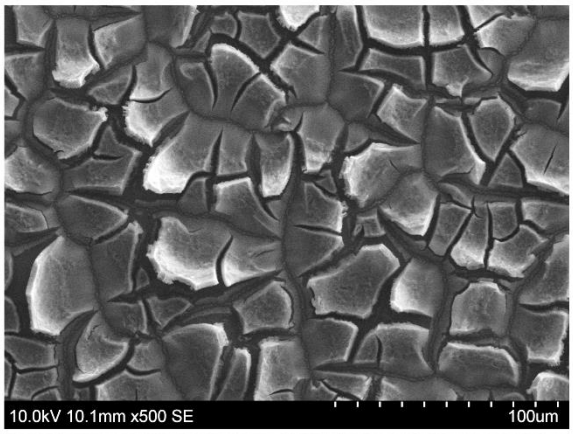

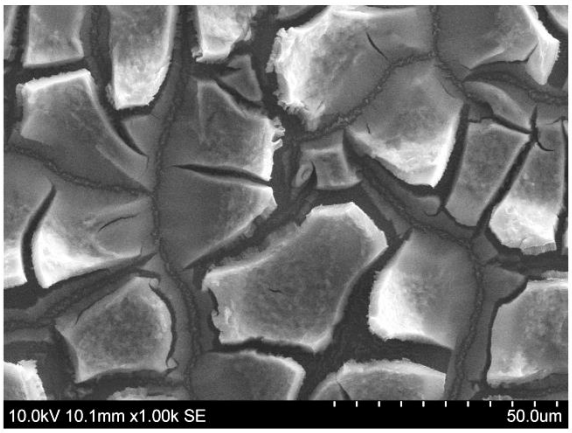

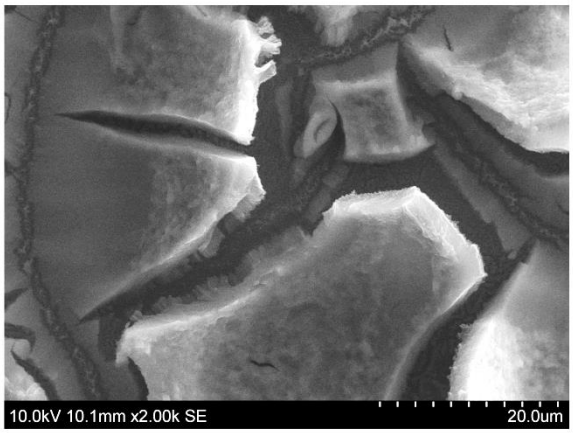

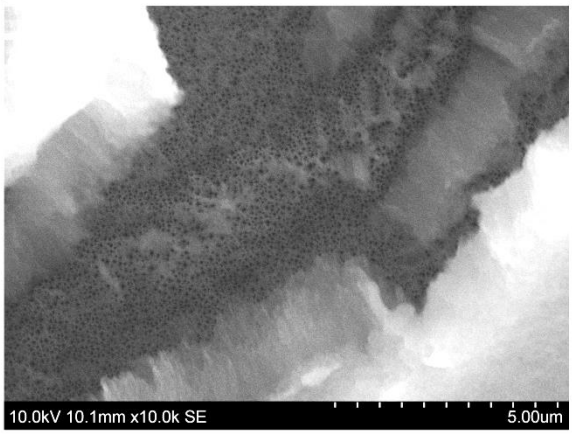

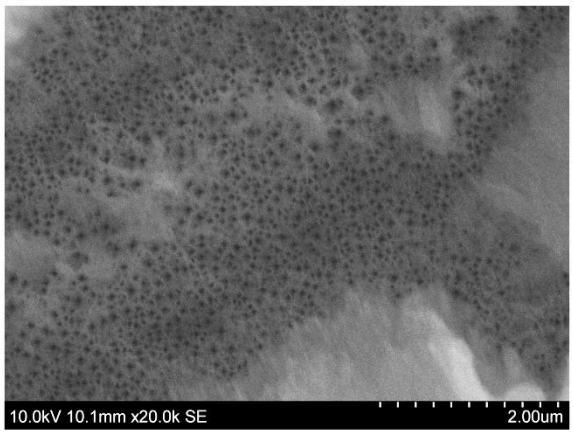

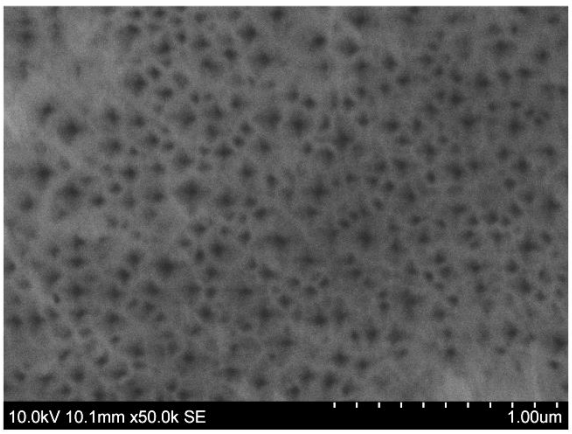

Sample: N_12_120

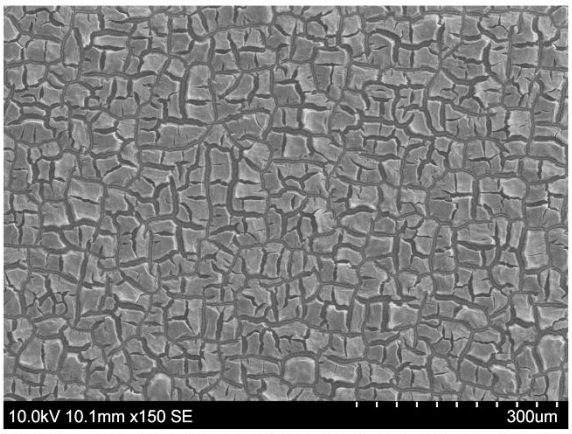

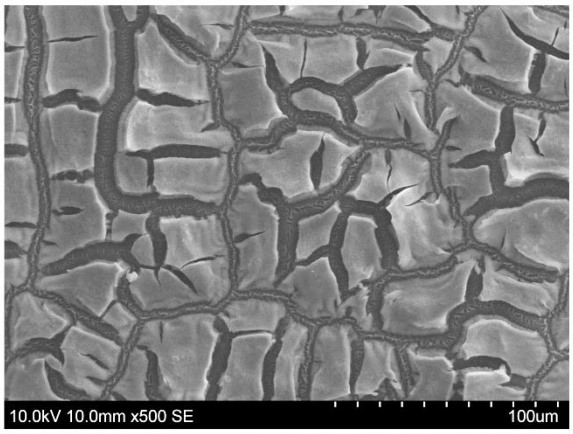

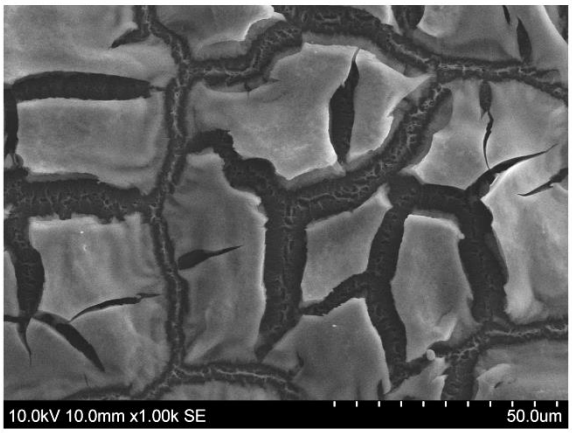

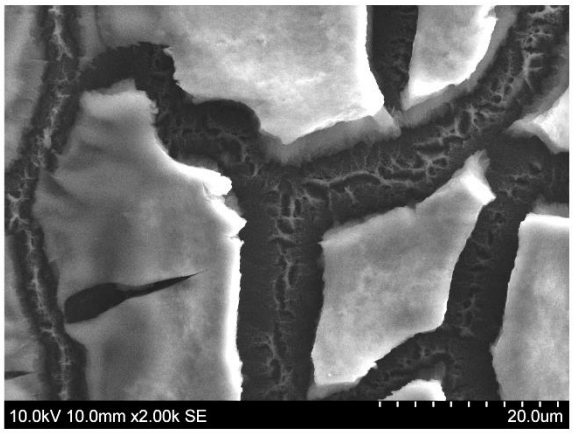

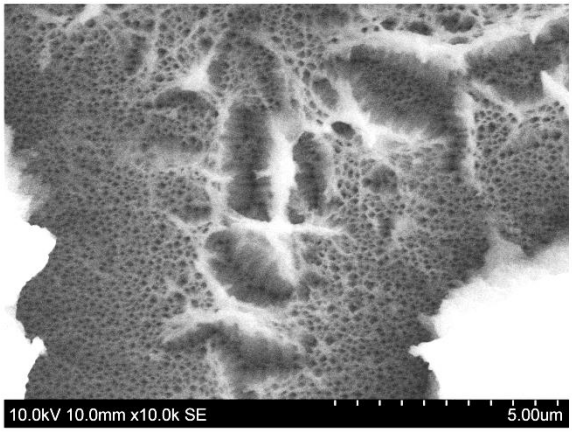

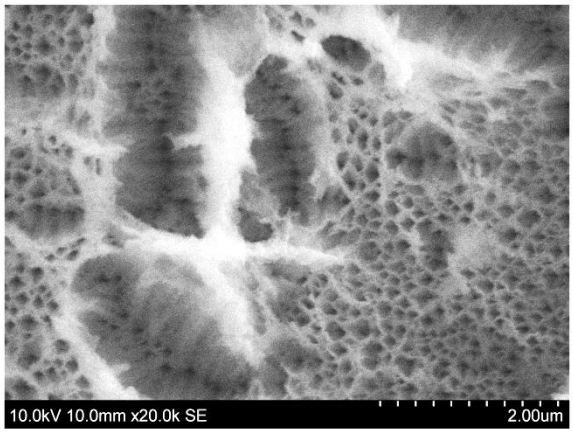

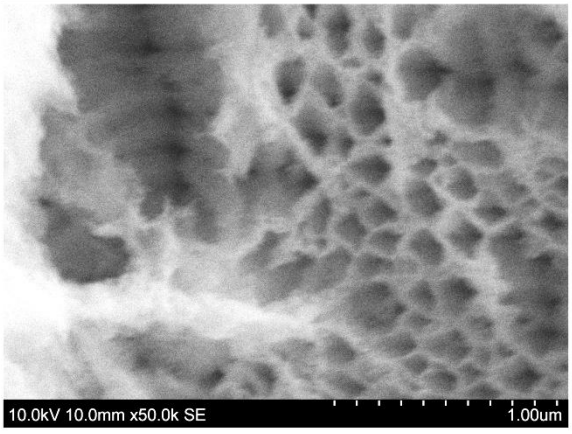

Sample: N_12_120 Post cycling

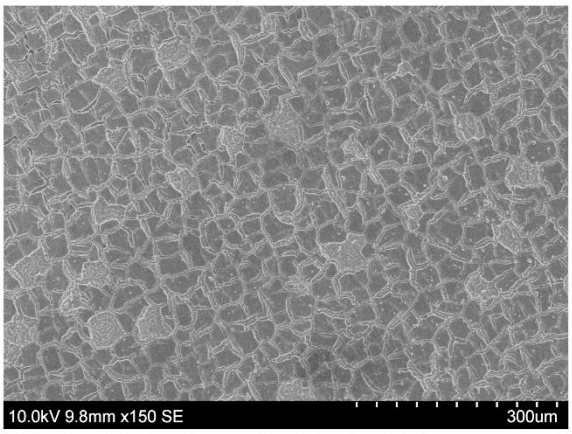

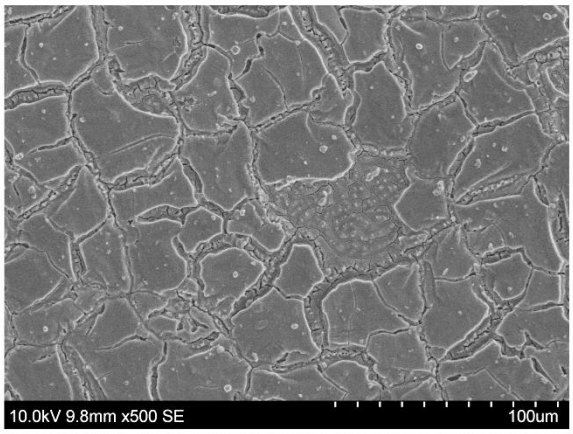

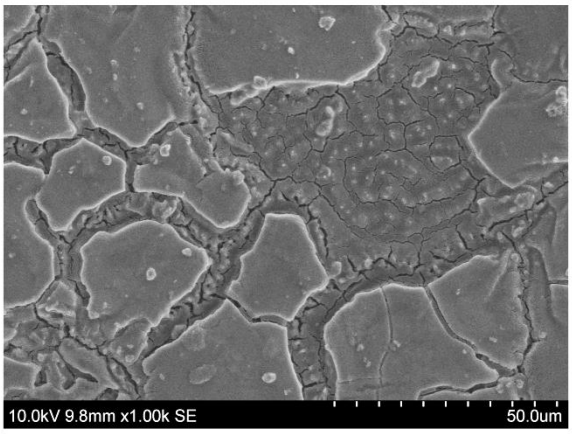

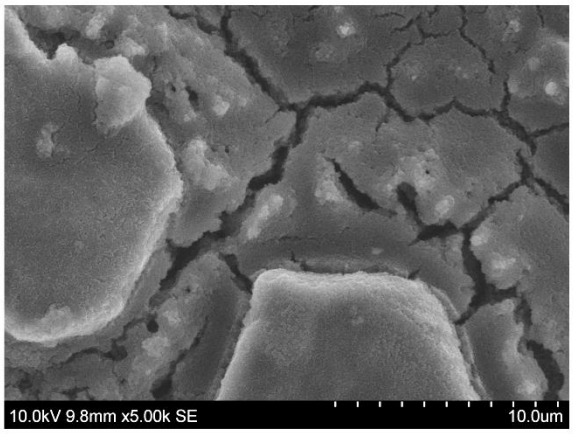

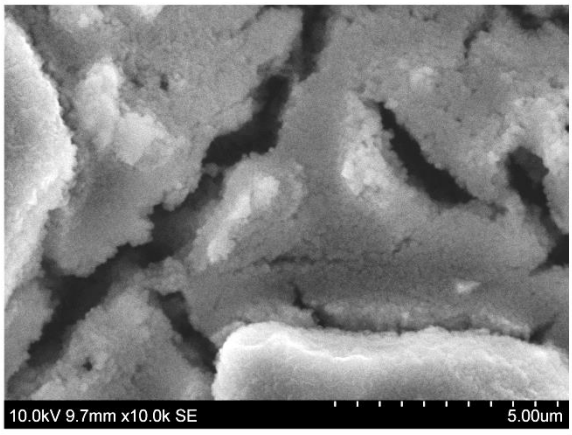

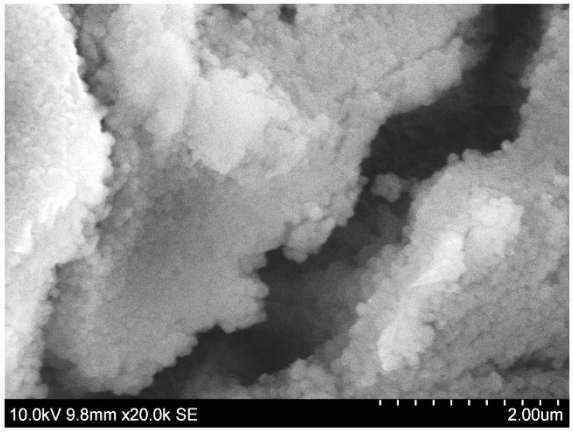

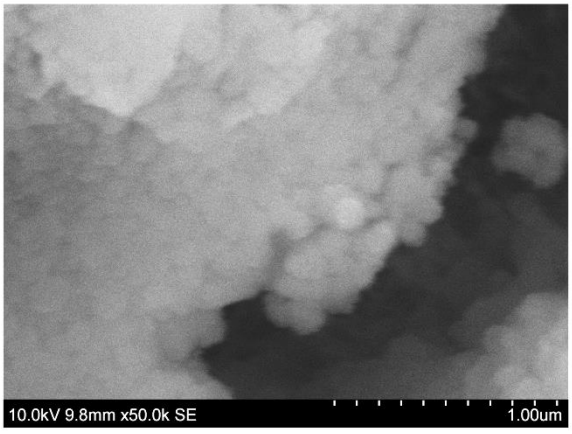

Sample: N_06_240

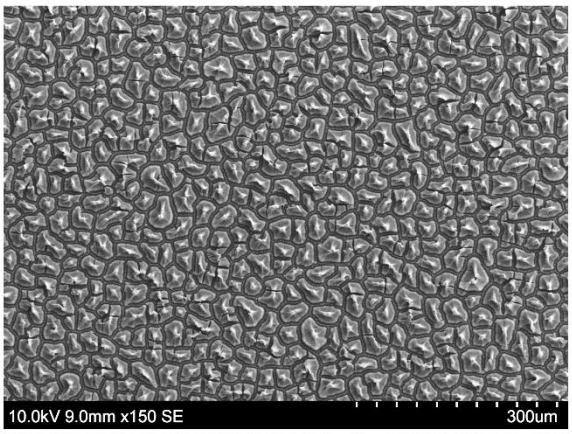

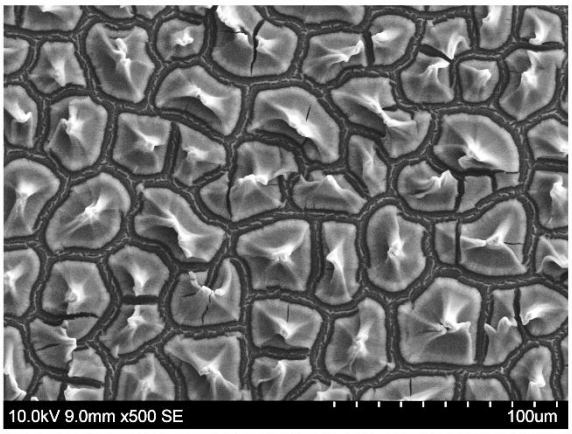

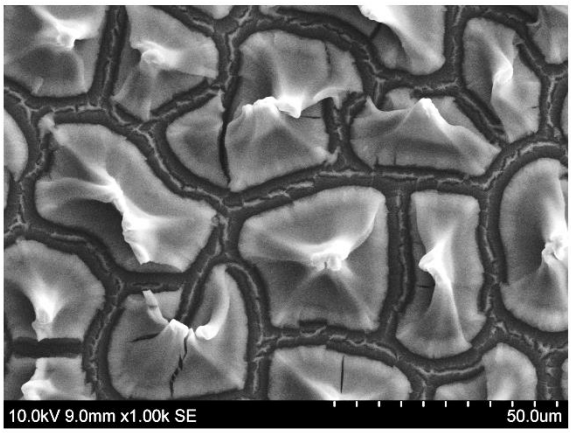

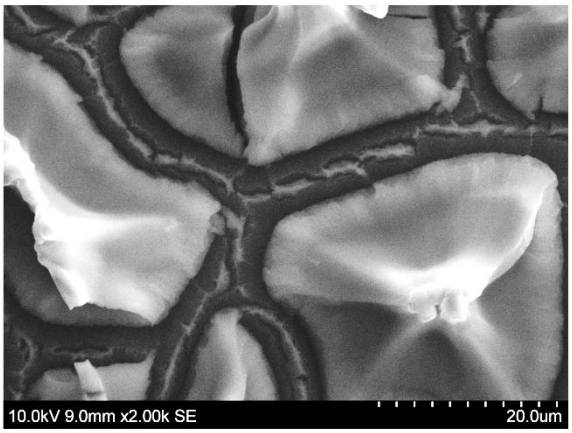

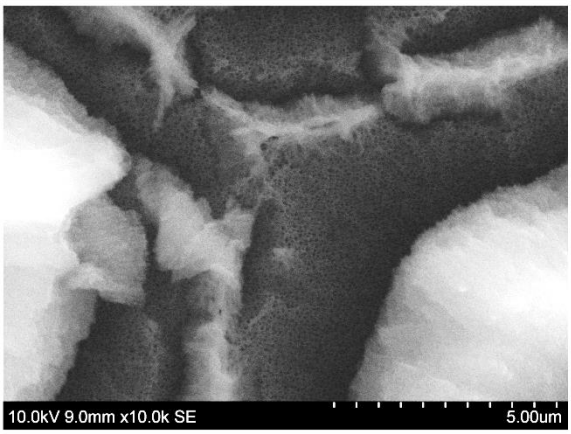

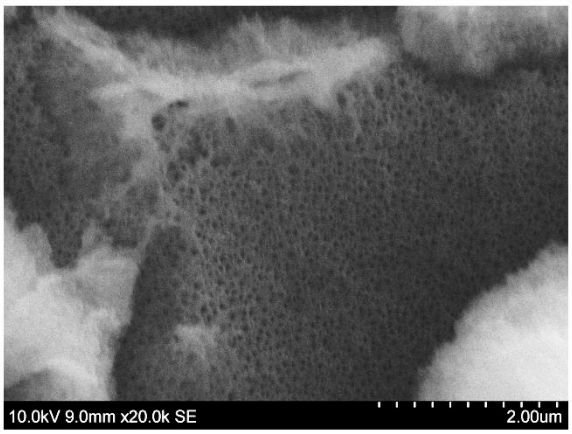

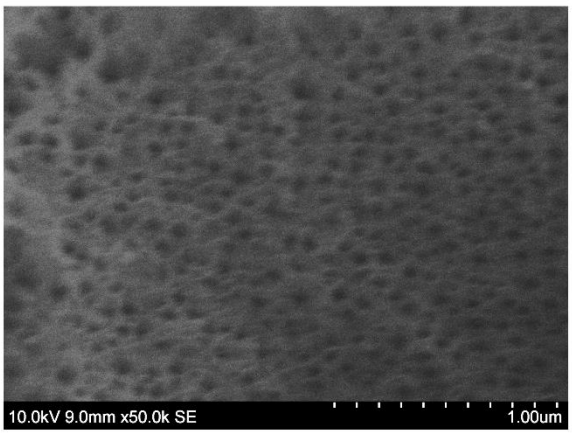

Sample: N_09_240

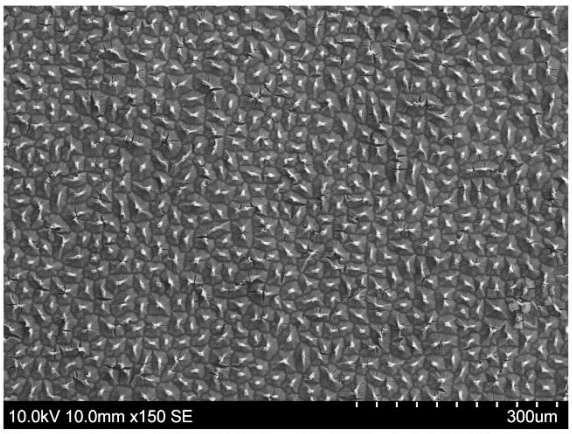

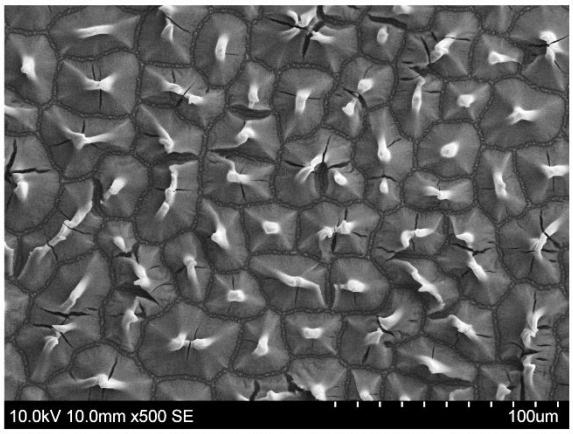

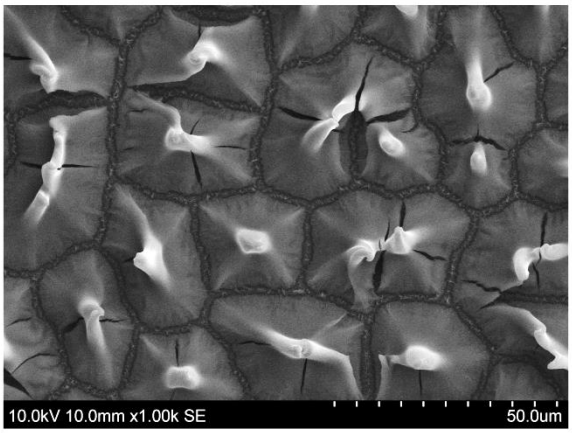

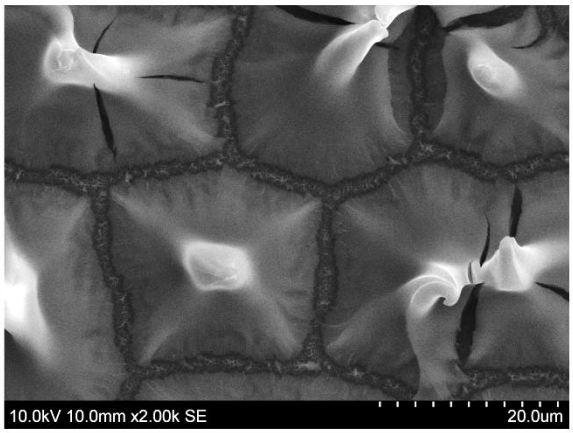

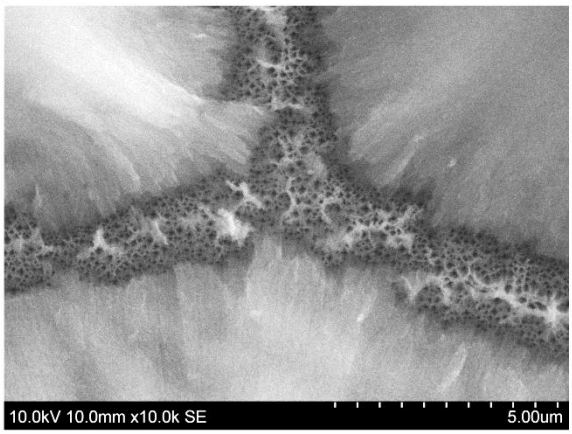

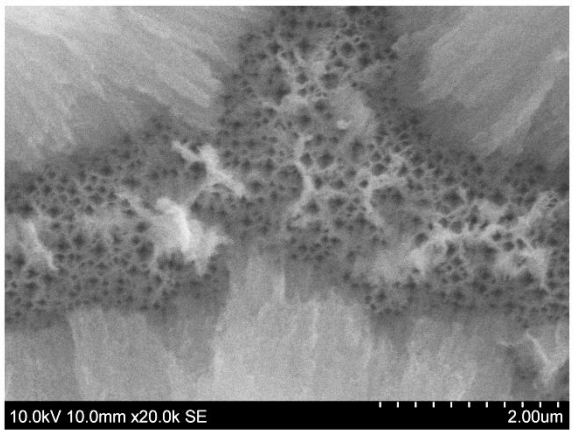

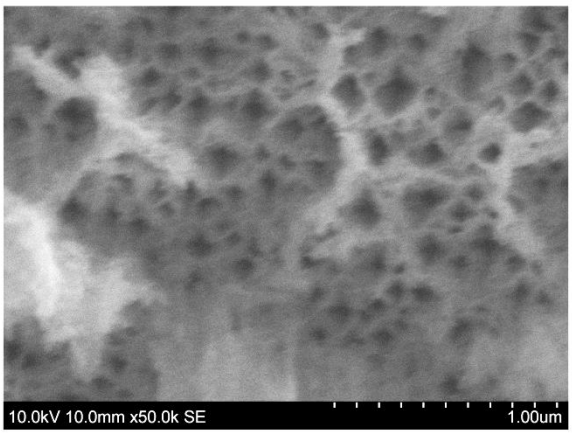

Sample: N_12_240

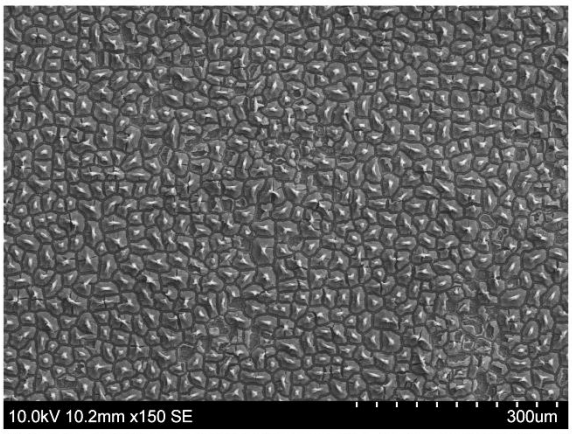

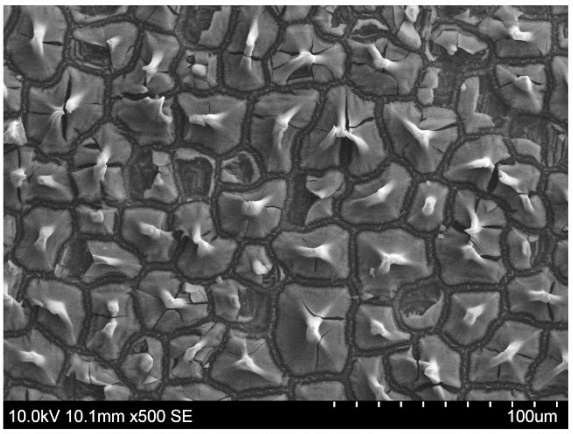

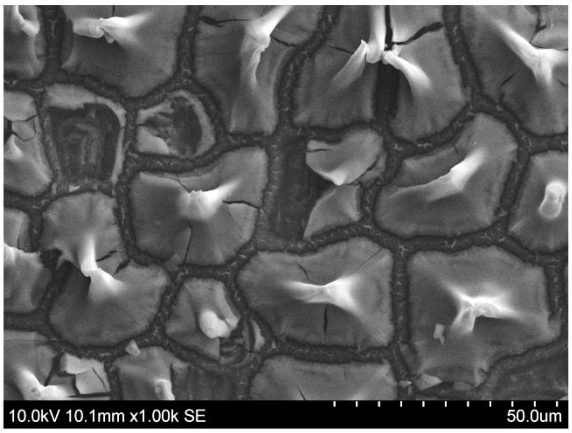

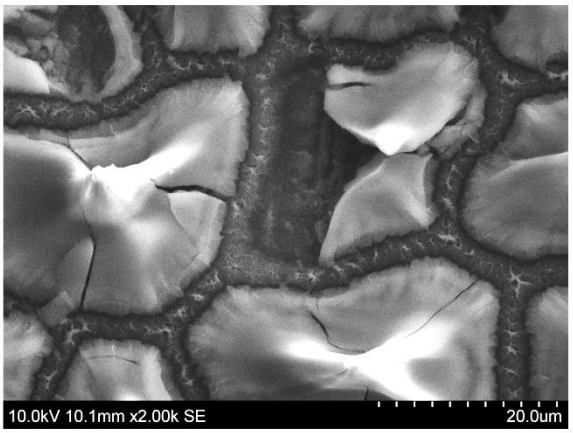

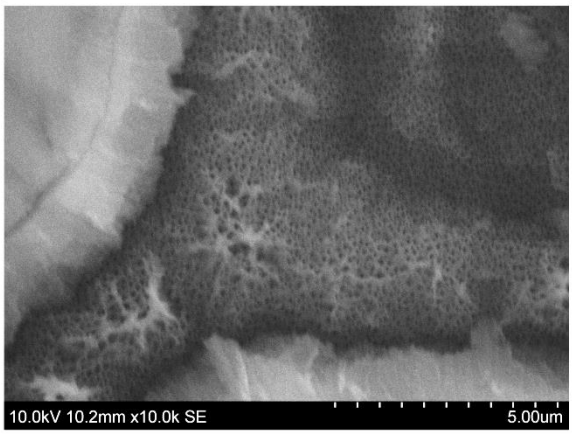

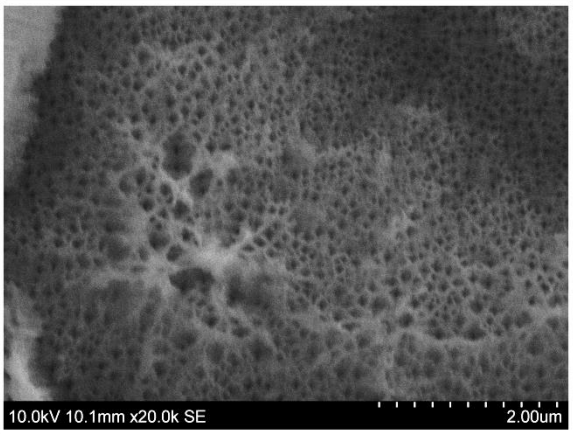

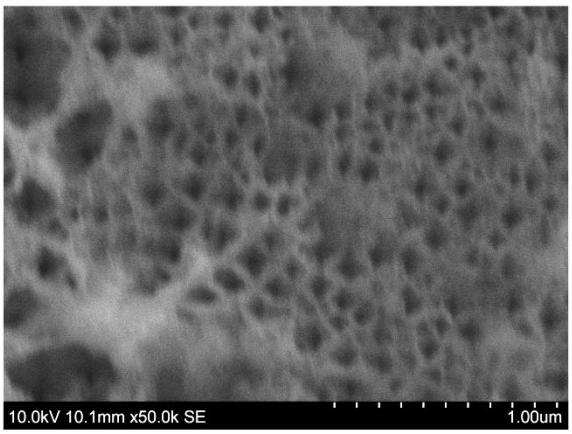

Sample: P_09_120

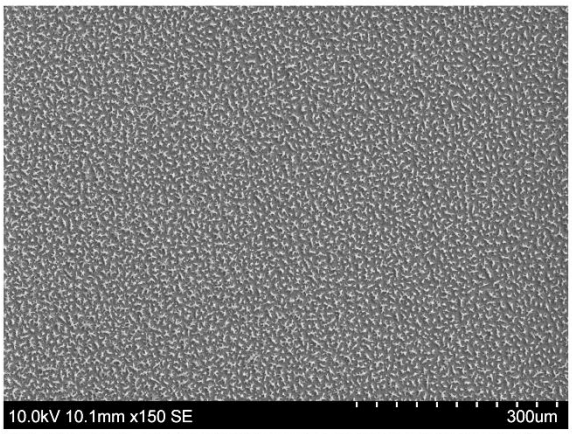

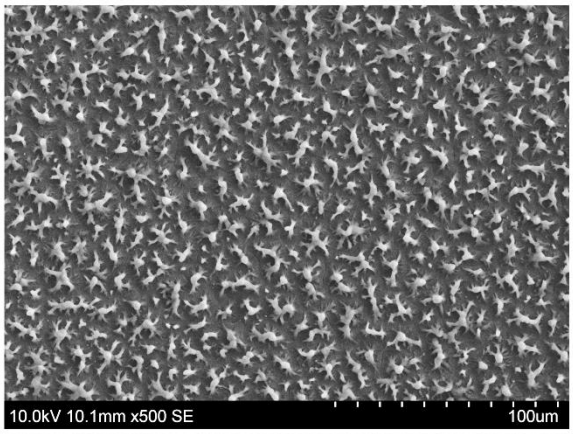

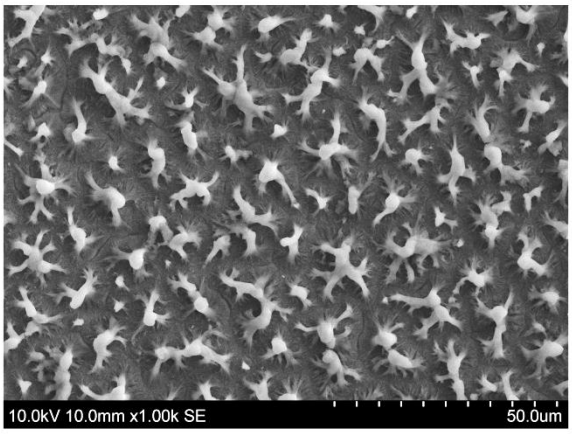

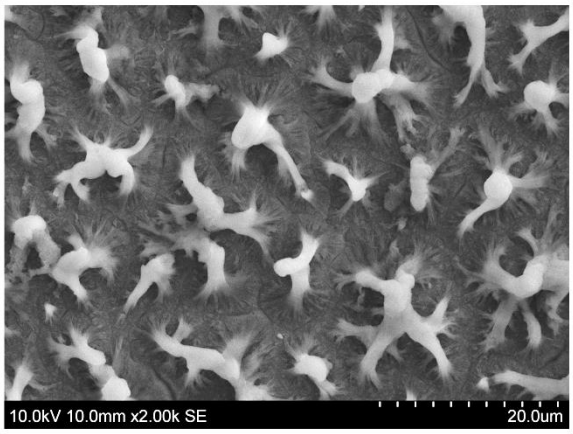

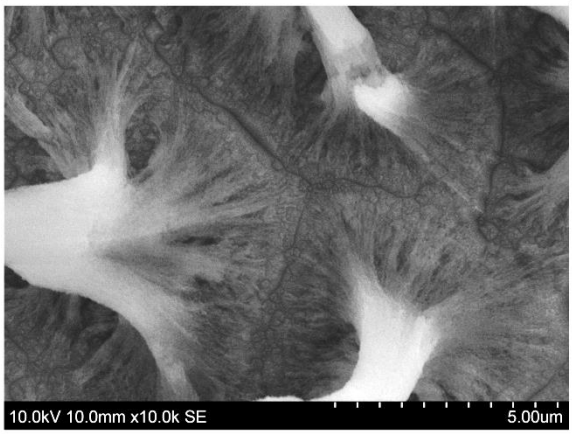

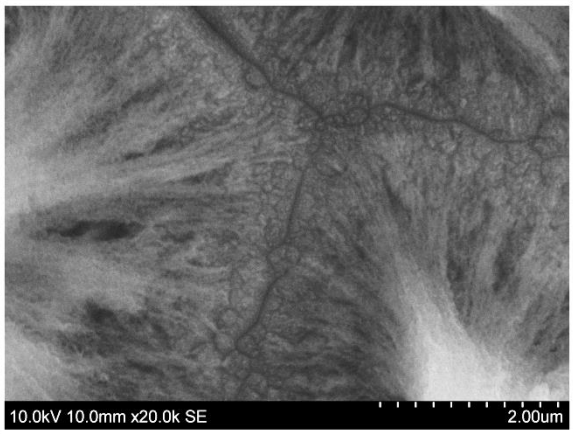

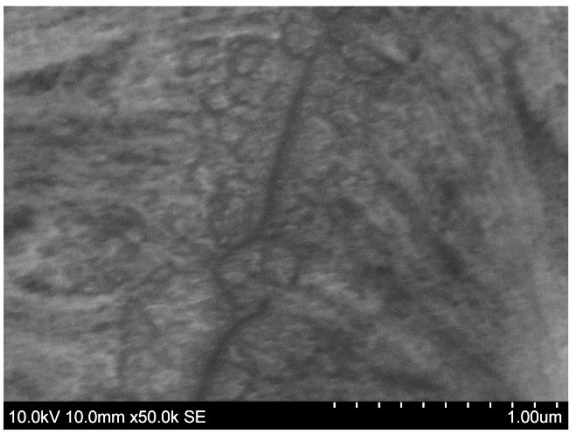

Sample: P_09_240

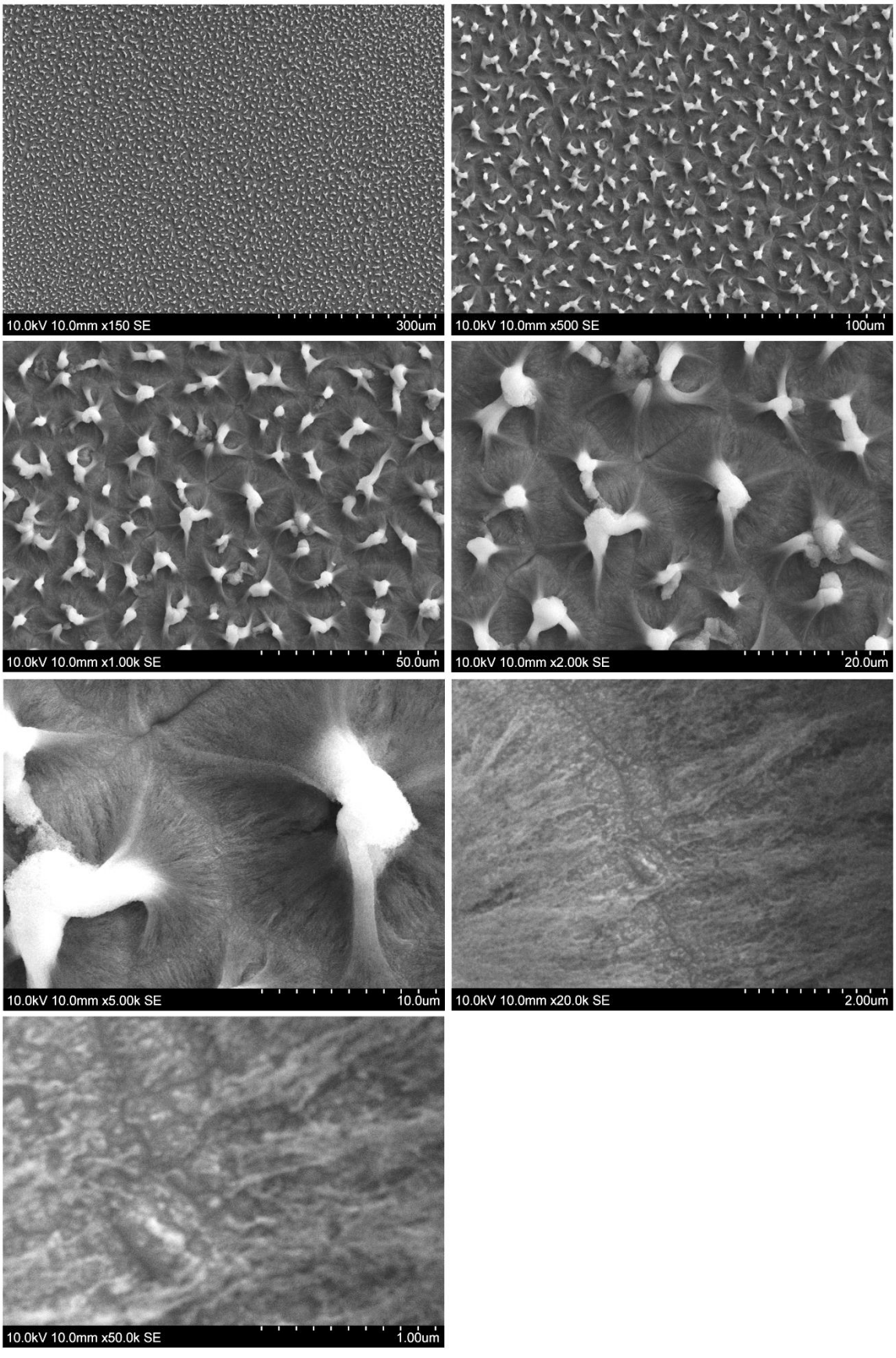

Appendix H: SEM images of the cross-sections of the porous samples

Cross section images were taken at x500, x1k, x2k, x5k, x10k, x20k, and x50k but not all magnifications were used for all samples. In order to make comparison easier, each magnification will have the same placement on the page for all the samples.

Sample: N_04_30

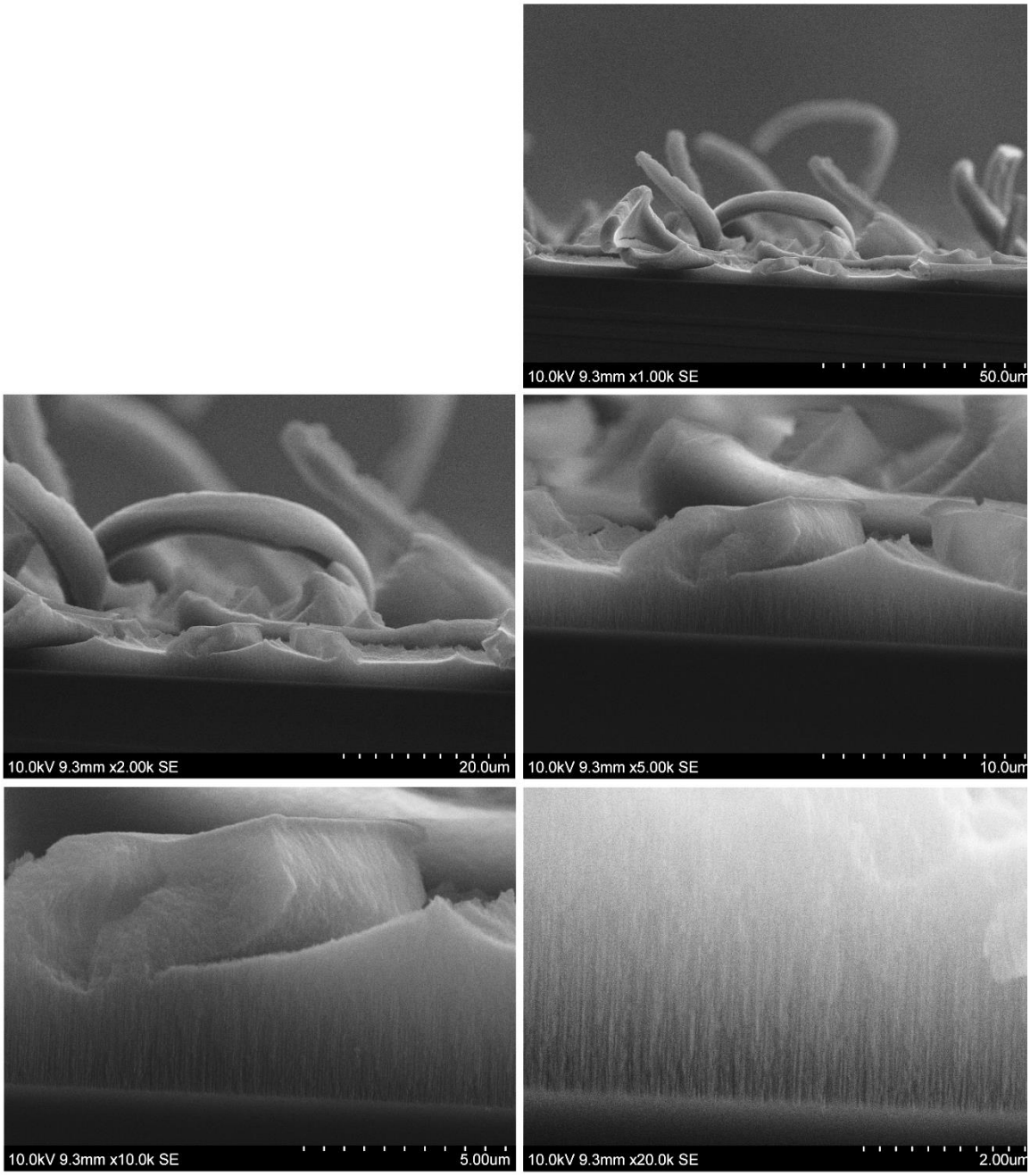

Sample: N_12_30

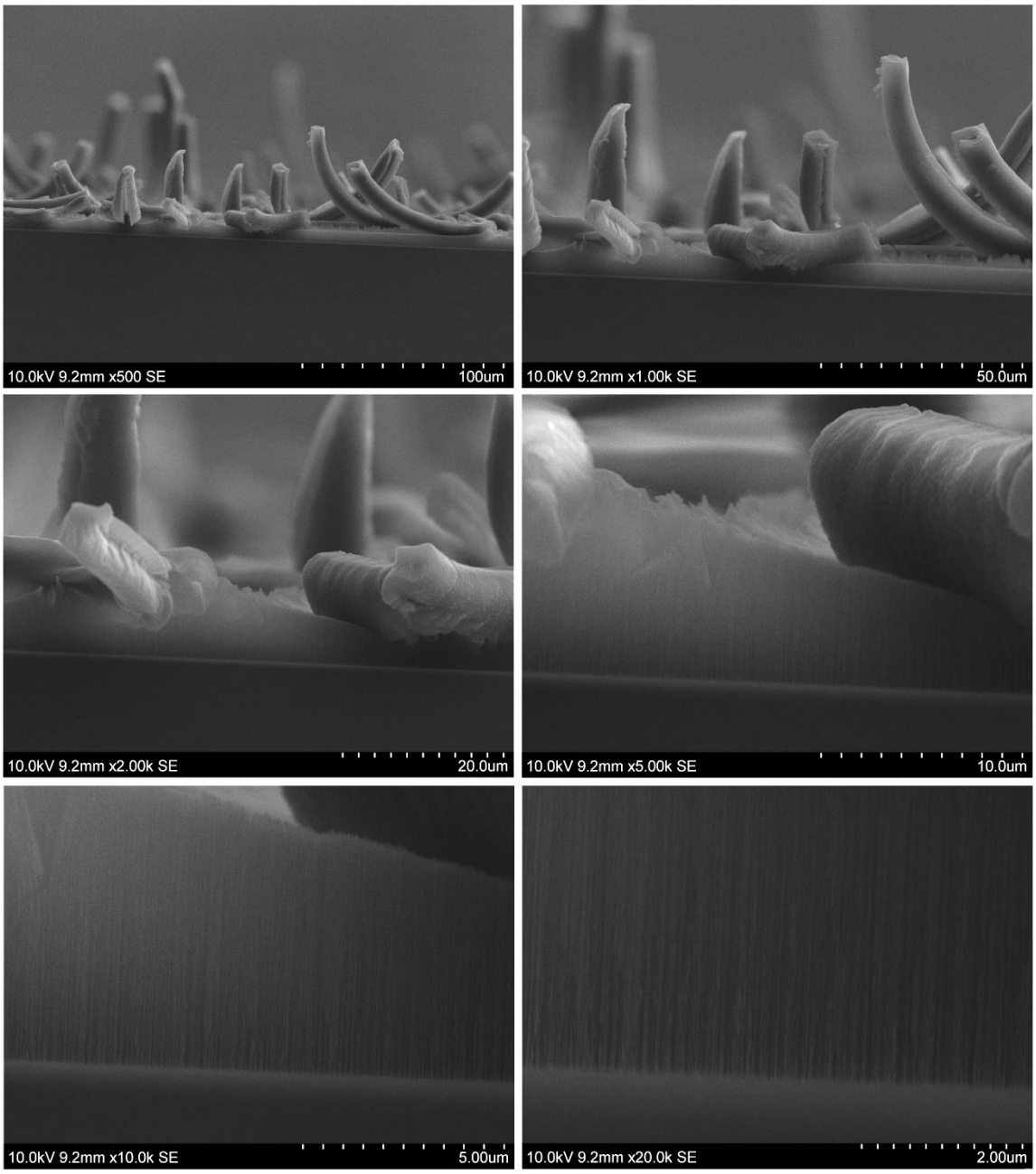

Sample: N_MAX_30

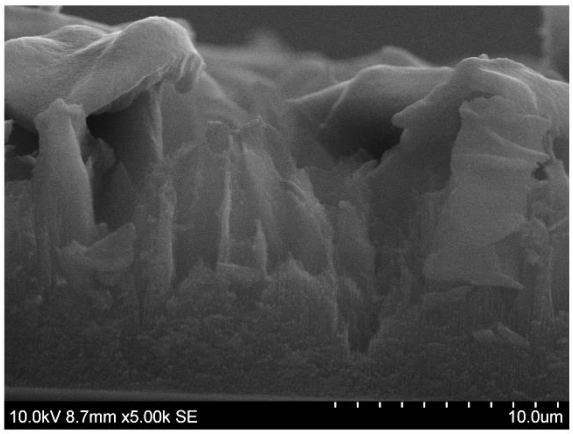

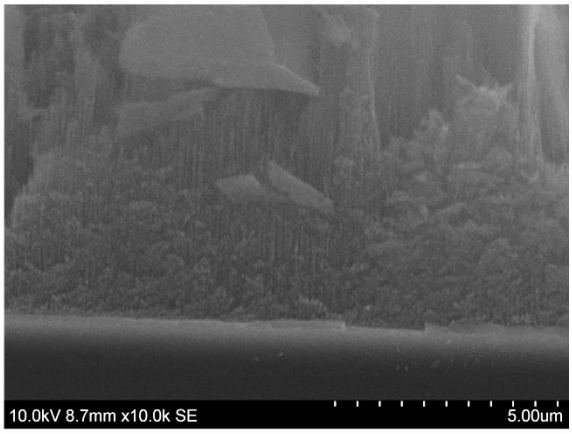

Sample: N_04_60

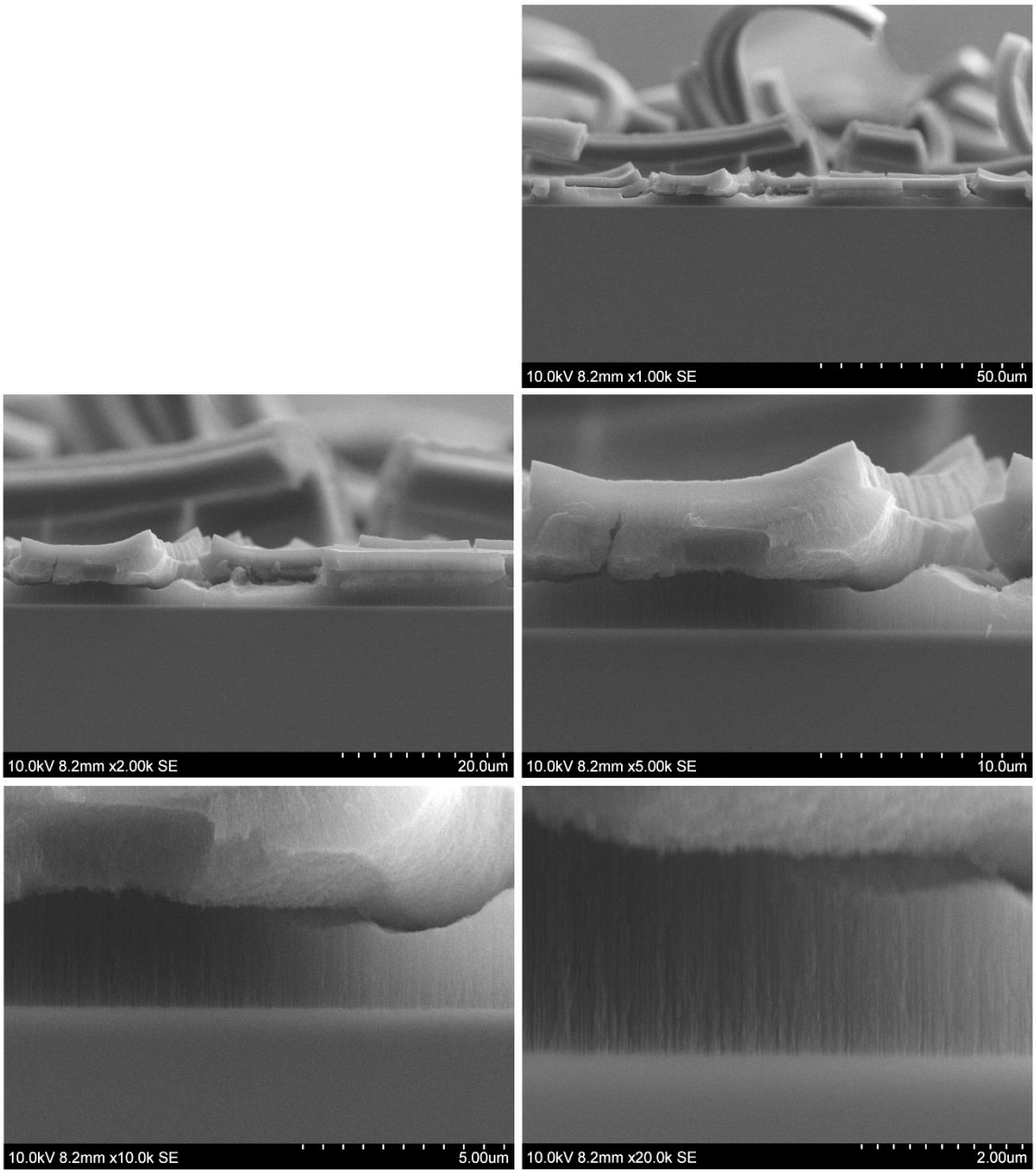

Sample: N_12_60

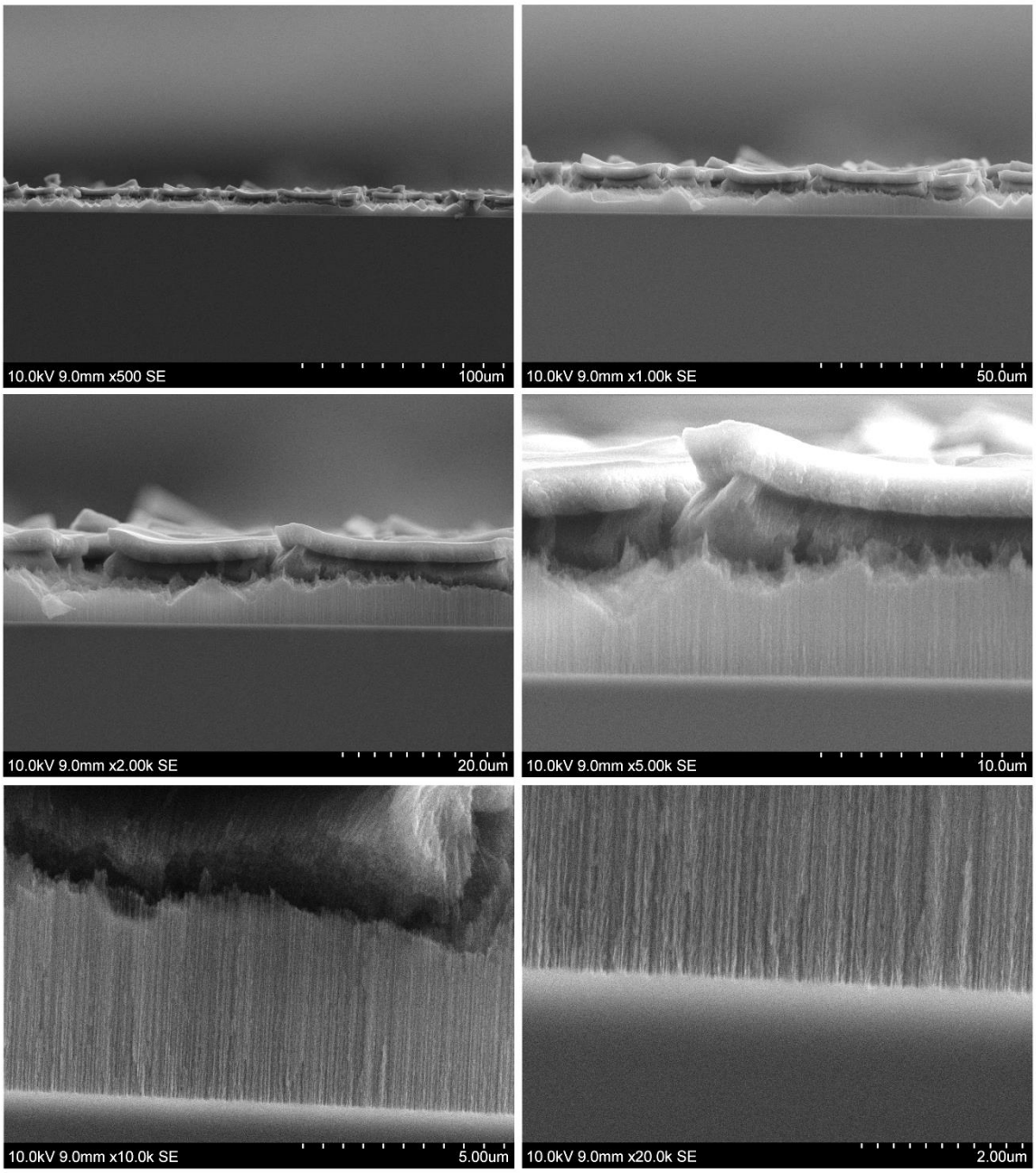

Sample: N_09_120

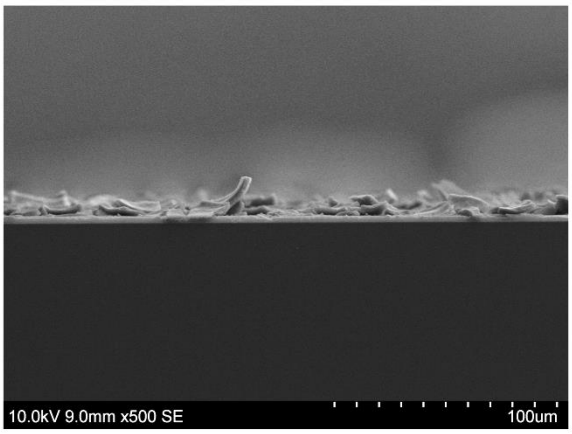

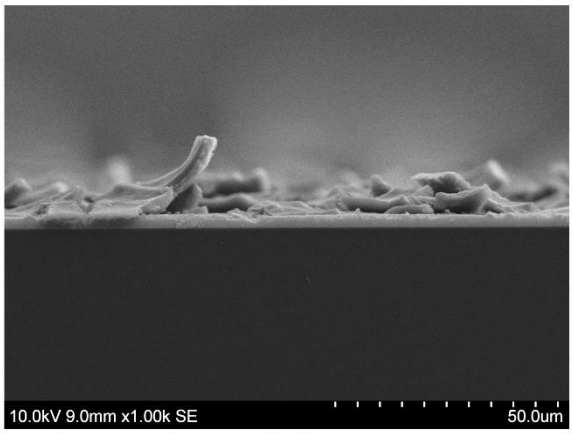

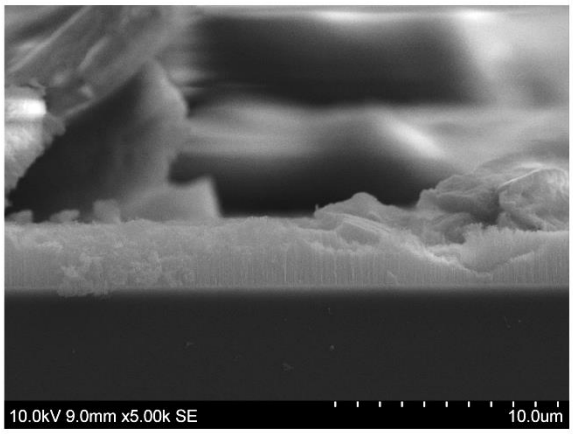

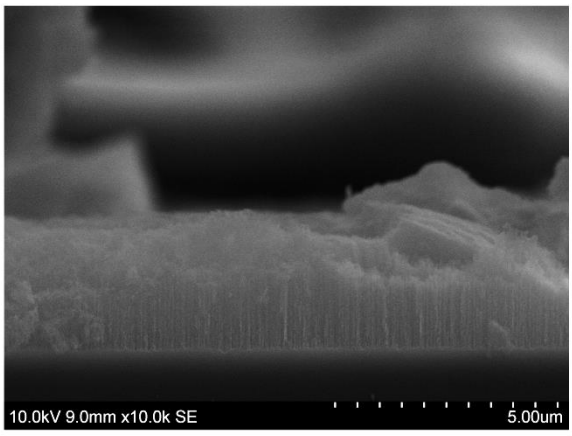

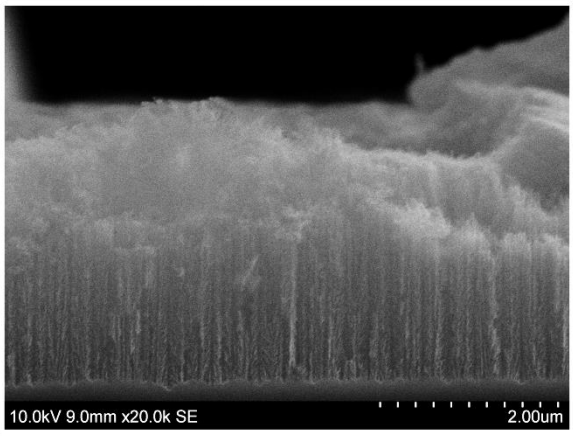

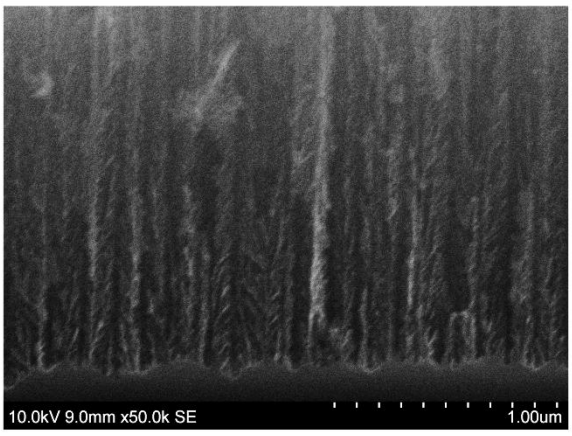

Sample: N_12_120

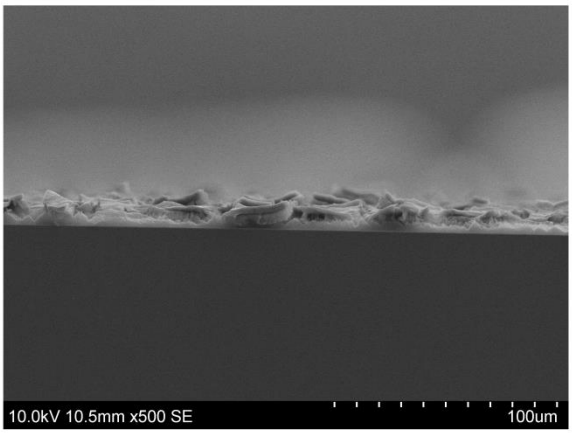

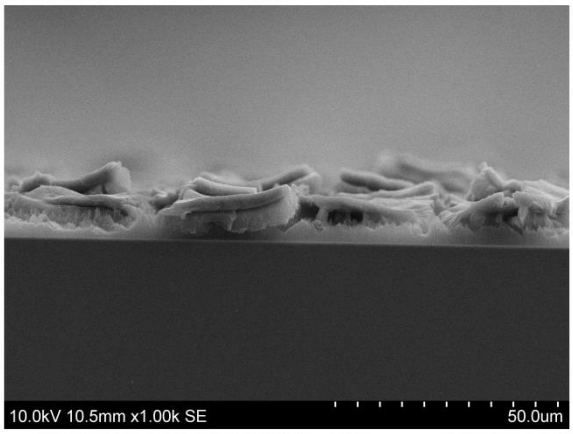

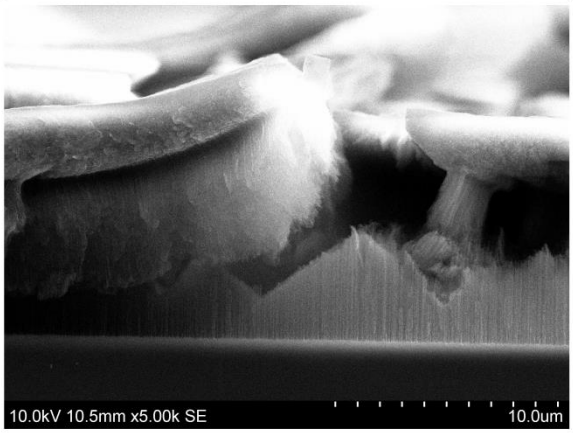

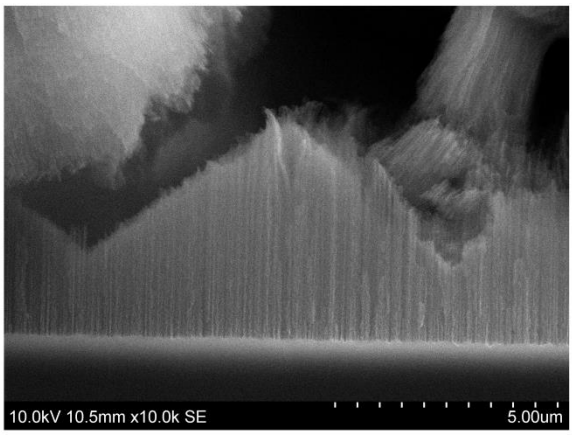

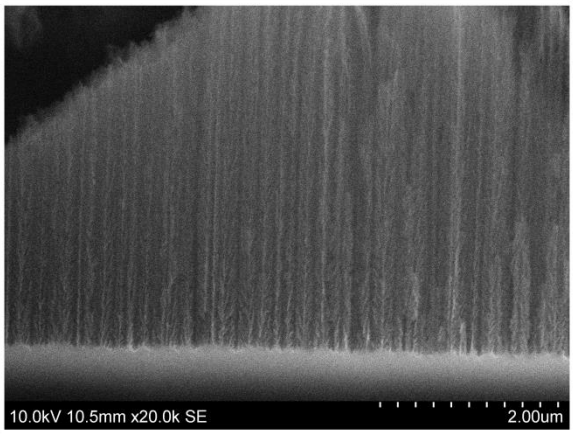

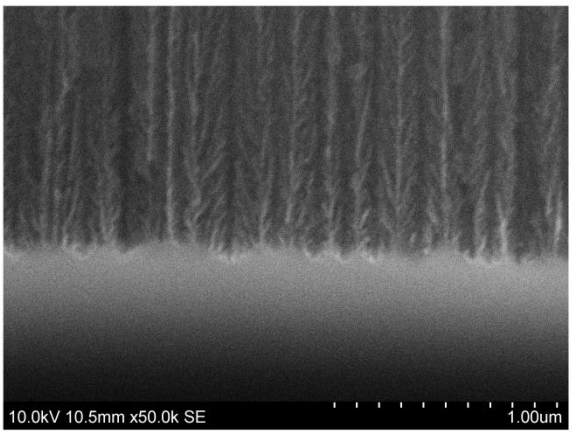

Sample: N_12_120 Post cycling

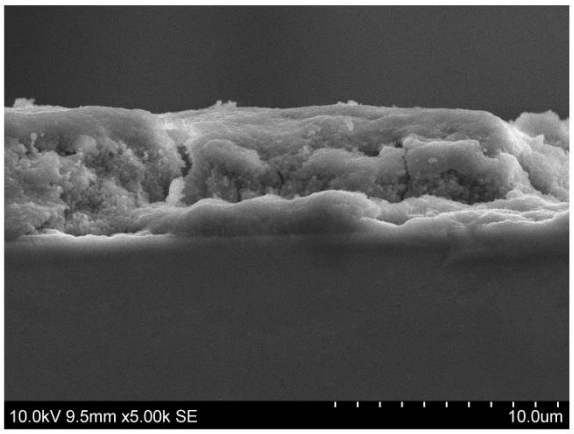

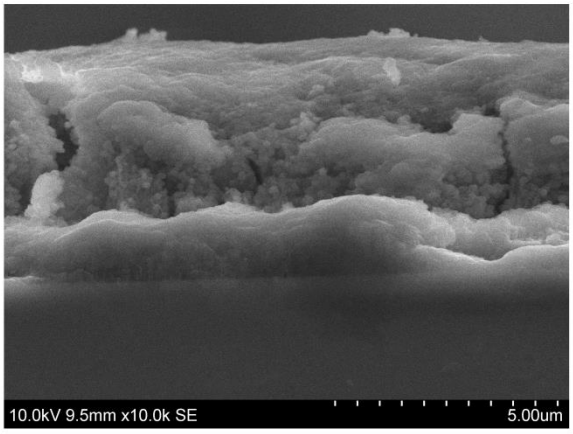

Sample: N_06_240

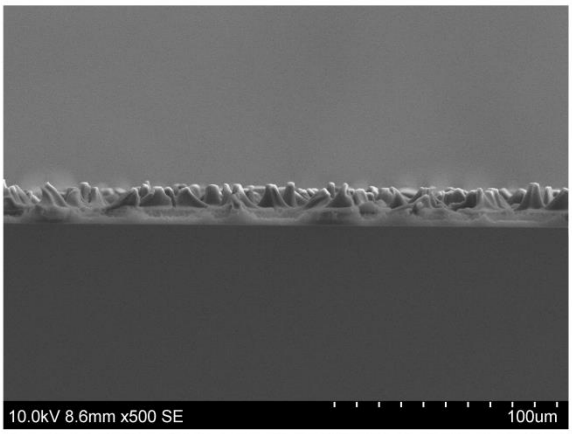

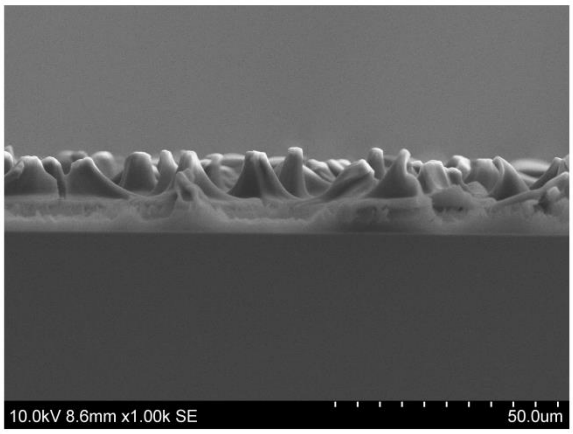

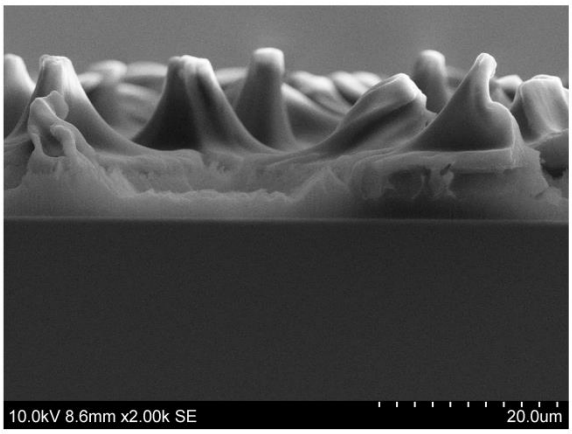

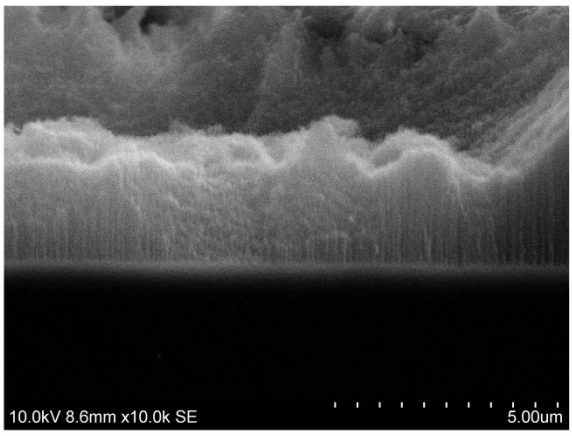

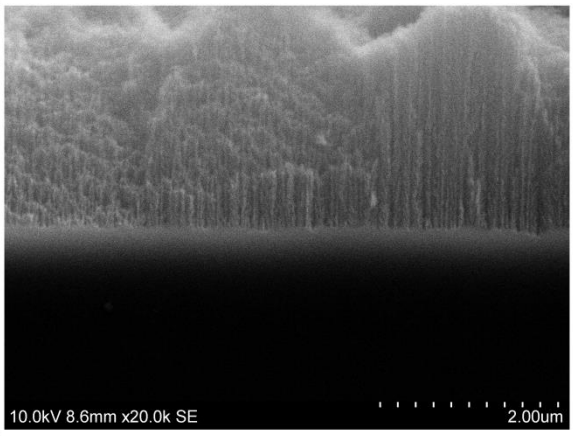

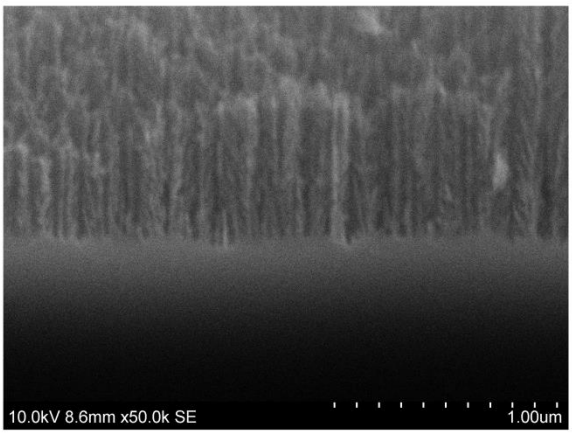

Sample: N_09_240

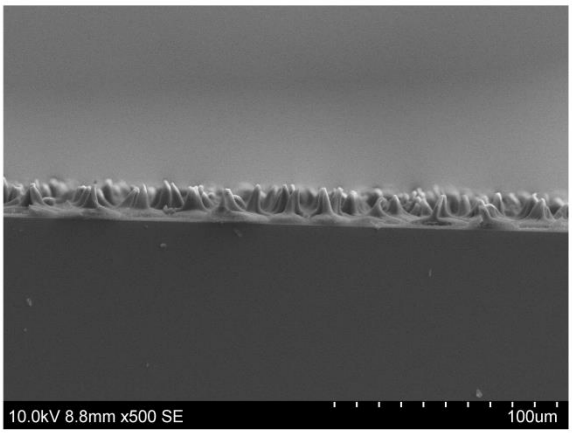

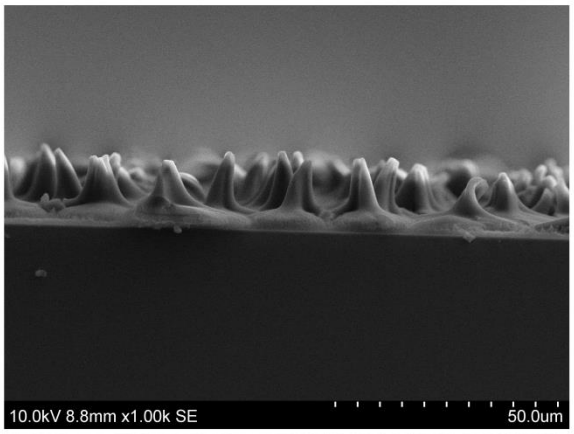

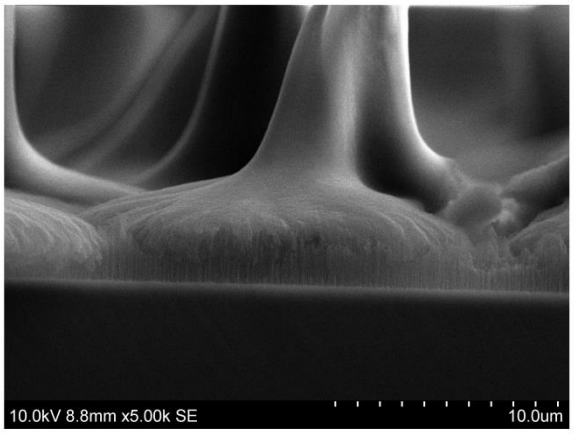

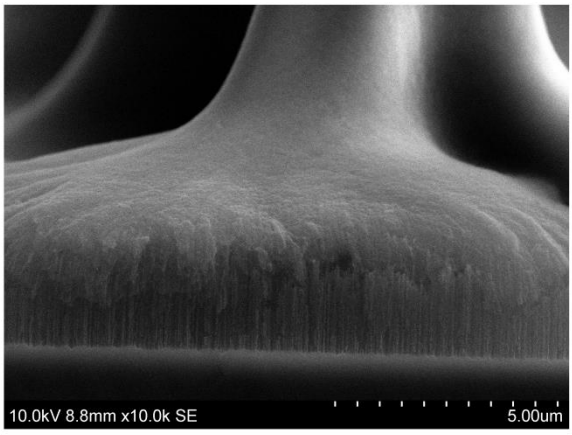

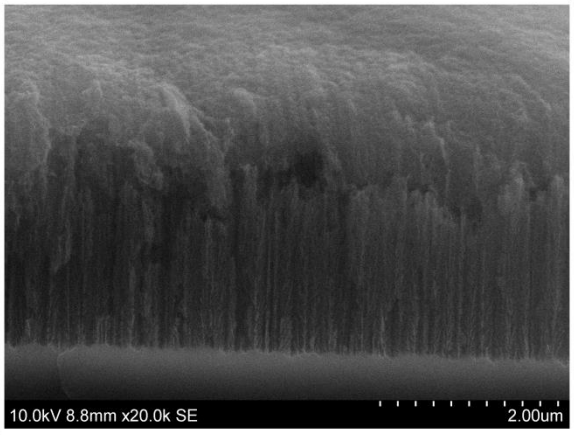

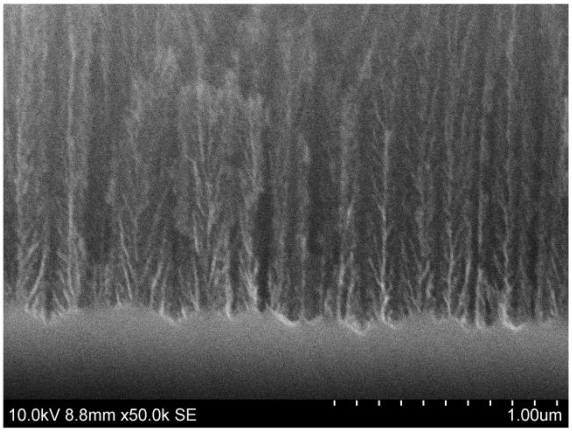

Sample: N_12_240

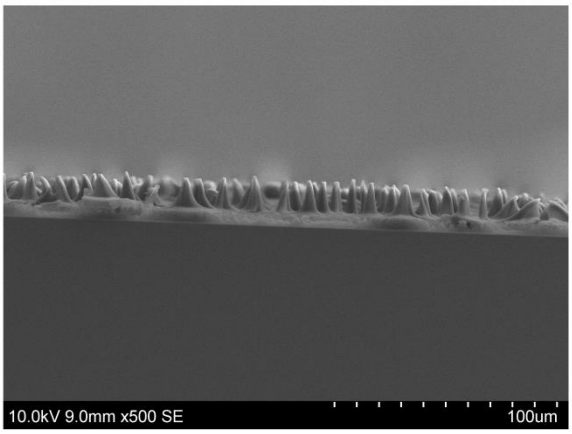

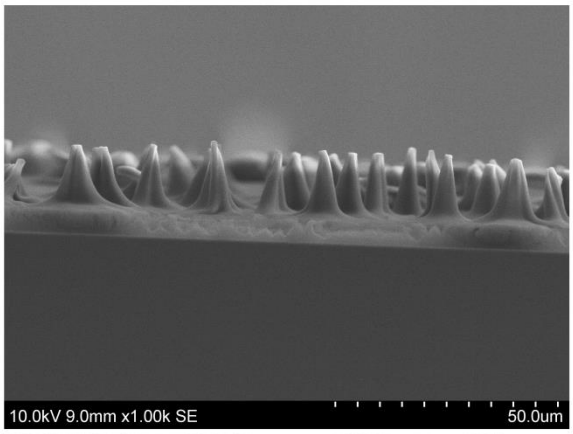

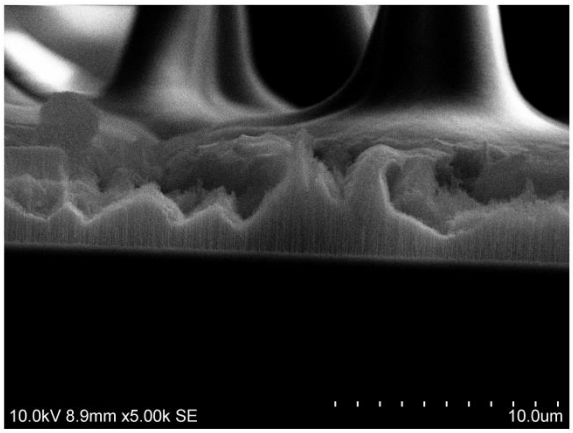

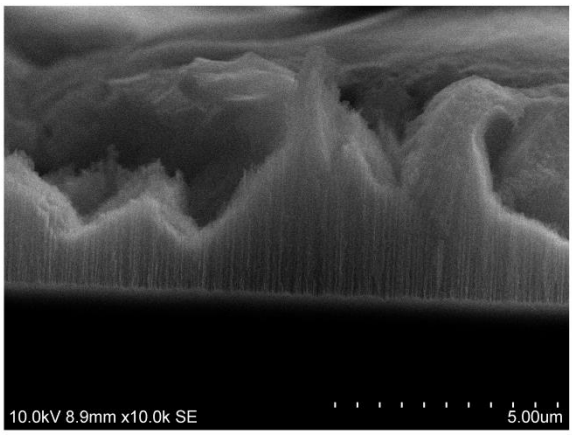

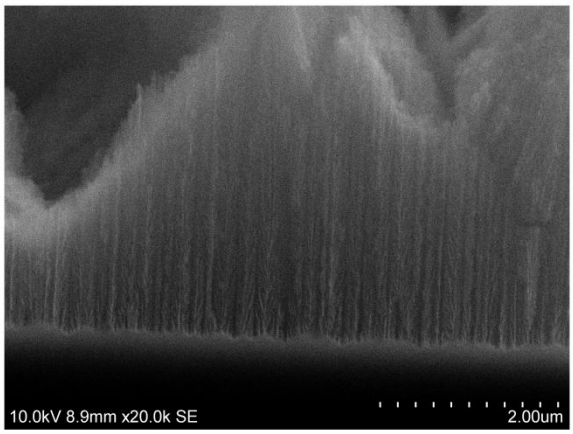

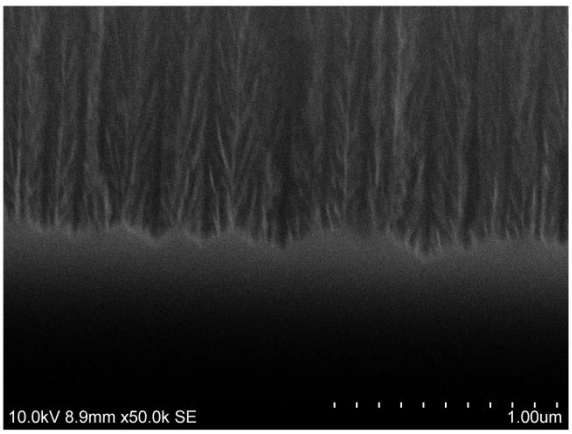

Sample: P_09_120

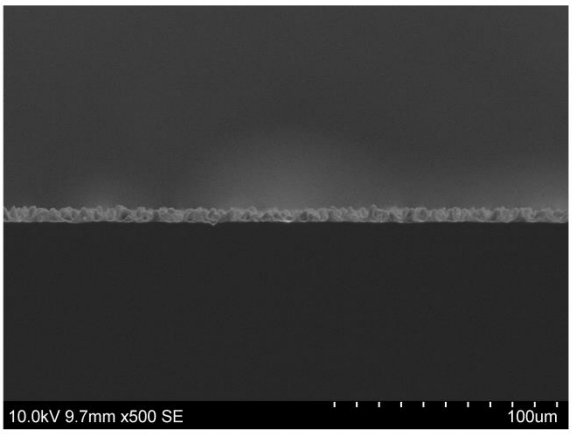

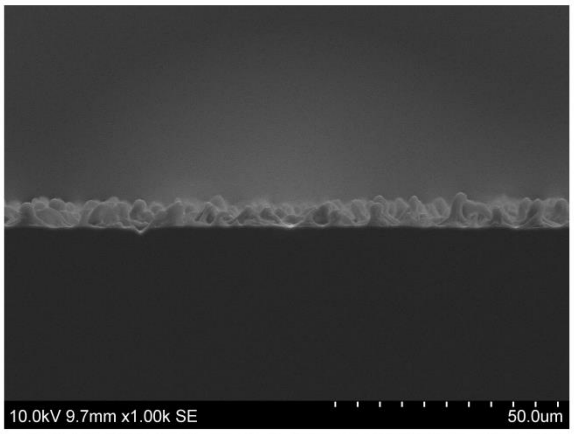

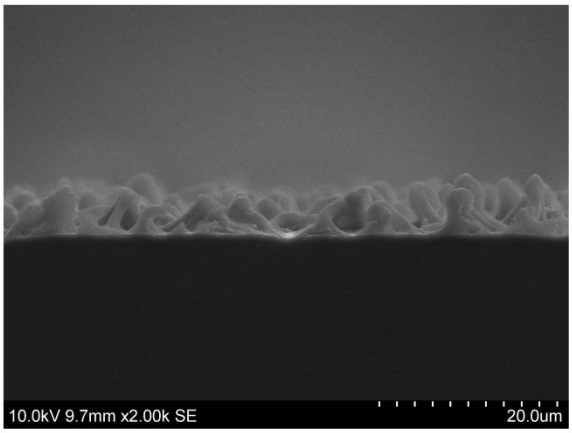

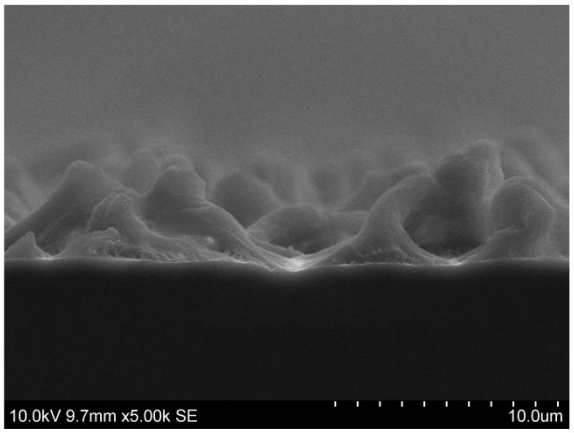

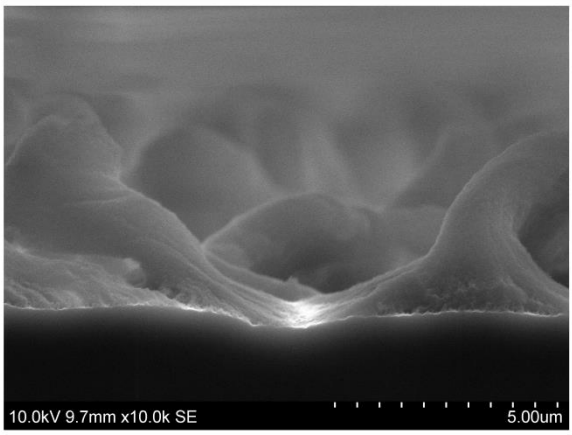

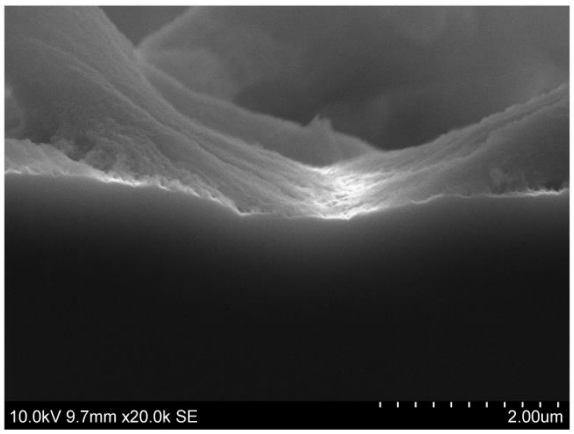

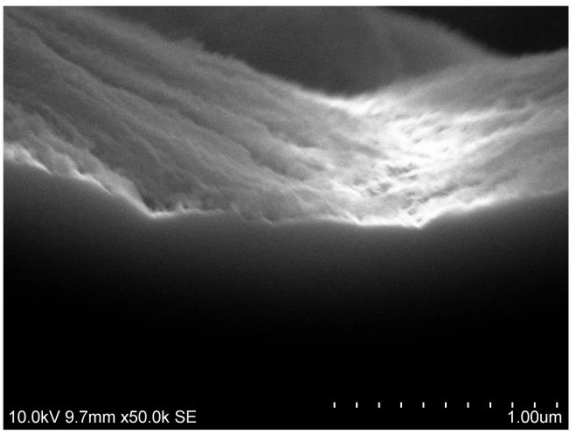

Sample: P_09_240